

# APPLIED COMPUTATIONAL ELECTROMAGNETICS SOCIETY JOURNAL

June 2022  
Vol. 37 No. 6  
ISSN 1054-4887

**The ACES Journal is abstracted in INSPEC, in Engineering Index, DTIC, Science Citation Index Expanded, the Research Alert, and to Current Contents/Engineering, Computing & Technology.**

The illustrations on the front cover have been obtained from the ARC research group at the Department of Electrical Engineering, Colorado School of Mines

Published, sold and distributed by: River Publishers, Alsbjergvej 10, 9260 Gistrup, Denmark

# THE APPLIED COMPUTATIONAL ELECTROMAGNETICS SOCIETY

<http://aces-society.org>

## EDITORS-IN-CHIEF

**Atef Elsherbeni**

Colorado School of Mines, EE Dept.  
Golden, CO 80401, USA

**Sami Barmada**

University of Pisa, ESE Dept.  
56122 Pisa, Italy

## ASSOCIATE EDITORS

**Maokun Li**

Tsinghua University  
Beijing 100084, China

**Wei-Chung Weng**

National Chi Nan University, EE Dept.  
Puli, Nantou 54561, Taiwan

**Paolo Mezzanotte**

University of Perugia  
I-06125 Perugia, Italy

**Mauro Parise**

University Campus Bio-Medico of Rome  
00128 Rome, Italy

**Alessandro Formisano**

Seconda Università di Napoli  
81031 CE, Italy

**Luca Di Rienzo**

Politecnico di Milano  
20133 Milano, Italy

**Yingsong Li**

Harbin Engineering University  
Harbin 150001, China

**Piotr Gas**

AGH University of Science and Technology  
30-059 Krakow, Poland

**Lei Zhao**

Jiangsu Normal University  
Jiangsu 221116, China

**Riyadh Mansoor**

Al-Muthanna University  
Samawa, Al-Muthanna, Iraq

**Long Li**

Xidian University  
Shaanxi, 710071, China

**Sima Noghianian**

Commscope  
Sunnyvale, CA 94089, USA

**Lijun Jiang**

University of Hong Kong, EEE Dept.  
Hong Kong

**Steve J. Weiss**

US Army Research Laboratory  
Adelphi Laboratory Center (RDRL-SER-M)  
Adelphi, MD 20783, USA

**Qiang Ren**

Beihang University  
Beijing 100191, China

**Shinishihiro Ohnuki**

Nihon University  
Tokyo, Japan

**Jiming Song**

Iowa State University, ECE Dept.  
Ames, IA 50011, USA

**Nunzia Fontana**

University of Pisa  
56122 Pisa, Italy

**Kubilay Sertel**

The Ohio State University  
Columbus, OH 43210, USA

**Toni Bjorninen**

Tampere University  
Tampere, 33100, Finland

**Stefano Selleri**

DINFO - University of Florence  
50139 Florence, Italy

**Giulio Antonini**

University of L'Aquila  
67040 L'Aquila, Italy

**Santanu Kumar Behera**

National Institute of Technology  
Rourkela-769008, India

**Yu Mao Wu**

Fudan University  
Shanghai 200433, China

**Antonio Musolino**

University of Pisa  
56126 Pisa, Italy

**Daniele Romano**

University of L'Aquila  
67100 L'Aquila, Italy

**Fatih Kaburcuk**

Sivas Cumhuriyet University  
Sivas 58140, Turkey

**Abdul A. Arkadan**

Colorado School of Mines, EE Dept.  
Golden, CO 80401, USA

**Alireza Baghai-Wadji**

University of Cape Town  
Cape Town, 7701, South Africa

**Huseyin Savci**

Istanbul Medipol University  
34810 Beykoz, Istanbul

**Salvatore Campione**

Sandia National Laboratories  
Albuquerque, NM 87185, USA

**Marco Arjona López**

La Laguna Institute of Technology  
Torreon, Coahuila 27266, Mexico

**Zhixiang Huang**

Anhui University  
China

**Ibrahim Mahariq**

American University of the Middle East  
Kuwait and University of  
Turkish Aeronautical Association  
Turkey

**Kaikai Xu**

University of Electronic Science  
and Technology of China  
China

**Amin Kargar Behbahani**

Florida International University  
Miami, FL 33174, USA

**Laila Marzall**

University of Colorado, Boulder  
Boulder, CO 80309, USA

## EDITORIAL ASSISTANTS

**Matthew J. Inman**  
University of Mississippi, EE Dept.  
University, MS 38677, USA

**Shanell Lopez**  
Colorado School of Mines, EE Dept.  
Golden, CO 80401, USA

## EMERITUS EDITORS-IN-CHIEF

**Duncan C. Baker**  
EE Dept. U. of Pretoria  
0002 Pretoria, South Africa

**Allen Glisson**  
University of Mississippi, EE Dept.  
University, MS 38677, USA

**Ahmed Kishk**  
Concordia University, ECS Dept.  
Montreal, QC H3G 1M8, Canada

**Robert M. Bevensee**  
Box 812  
Alamo, CA 94507-0516

**Ozlem Kilic**  
Catholic University of America  
Washington, DC 20064, USA

**David E. Stein**  
USAF Scientific Advisory Board  
Washington, DC 20330, USA

## EMERITUS ASSOCIATE EDITORS

**Yasushi Kanai**  
Niigata Inst. of Technology  
Kashiwazaki, Japan

**Mohamed Abouzahra**  
MIT Lincoln Laboratory  
Lexington, MA, USA

**Alexander Yakovlev**  
University of Mississippi, EE Dept.  
University, MS 38677, USA

**Levent Gurel**  
Bilkent University  
Ankara, Turkey

**Sami Barmada**  
University of Pisa, ESE Dept.  
56122 Pisa, Italy

**Ozlem Kilic**  
Catholic University of America  
Washington, DC 20064, USA

**Erdem Topsakal**  
Mississippi State University, EE Dept.  
Mississippi State, MS 39762, USA

**Alistair Duffy**  
De Montfort University  
Leicester, UK

**Fan Yang**  
Tsinghua University, EE Dept.  
Beijing 100084, China

**Rocco Rizzo**  
University of Pisa  
56123 Pisa, Italy

**Atif Shamim**  
King Abdullah University of Science and  
Technology (KAUST)  
Thuwal 23955, Saudi Arabia

William O'Keefe Coburn  
US Army Research Laboratory  
Adelphi, MD 20783, USA

**Mohammed Hadi**  
Kuwait University, EE Dept.  
Safat, Kuwait

**Amedeo Capozzoli**  
Univerita di Naoli Federico II, DIETI  
I-80125 Napoli, Italy

**Wenxing Li**  
Harbin Engineering University  
Harbin 150001, China

## EMERITUS EDITORIAL ASSISTANTS

**Khaleb ElMaghoub**  
Trimble Navigation/MIT  
Boston, MA 02125, USA

**Kyle Patel**  
Colorado School of Mines, EE Dept.  
Golden, CO 80401, USA

**Christina Bonnington**  
University of Mississippi, EE Dept.  
University, MS 38677, USA

**Anne Graham**  
University of Mississippi, EE Dept.  
University, MS 38677, USA

**Madison Lee**  
Colorado School of Mines, EE Dept.  
Golen, CO 80401, USA

**Allison Tanner**  
Colorado School of Mines, EE Dept.  
Golden, CO 80401, USA

**Mohamed Al Sharkawy**  
Arab Academy for Science and Technology, ECE Dept.  
Alexandria, Egypt

## **JUNE 2022 REVIEWERS**

**Behrokh Beiranvand  
Muhammad Bilal  
CJ  
Xiaoming Chen  
Thippesha D.  
Bernhard J. Hoenders  
Taha Imeci  
Mohamed Khalifa  
Brian LaRocca  
Zi-Liang Liu  
Matteo Bruno Lodi  
Xuesong Meng  
Anton Menshov**

**Anveshkumar Nella  
Andrew Peterson  
Chalasani Subba Rao  
Alain Reineix  
Pavel Roy Paladhi  
Kannadhasan S.  
Suganthi Santhanam  
Michael Saville  
Steven Weiss  
Yinfeng Xia  
Hany Zamel  
Qiwei Zhan**

TABLE OF CONTENTS

A New Method for Twisted Wire Crosstalk Estimation Based on GA-BP Neural Network Algorithm  
Wu Zhang, Yongji Wu, Jiafei Ding, Yang Zhao, and Mingyuan He ..... 655

Enhancement of Multifrequency Microwave Tomography Breast Imaging System using Flexible Preconditioner Based Krylov Subspace Methods  
N. Nithya and M. S. K. Manikandan ..... 664

Computational Analysis for Miniaturization of Tapered Slot Antenna using Elliptical Conducting Loaded Strips  
Bismah Tariq, Muhammad Anjad, and Abdul Aziz ..... 672

Advanced Numerical and Experimental Analysis of Ultra-Miniature Surface Resonators  
Yakir Ishay, Yaron Artzi, Nir Dayan, David Cristea, and Aharon Blank ..... 679

A Robust Algorithm for DOA Estimation of Coherent Sources with UCA  
Ye Tian, Yonghui Huang, Xiaoxu Zhang, and Meiyuan Lin ..... 692

Design of Compact Multiband MIMO Antenna Based on Ground Neutralization Line Decoupling  
Zhonggen Wang, Weidong Mu, Ming Yang, and Chenlu Li ..... 702

Compact Dual-band (28/38 GHz) Patch for MIMO Antenna System of Polarization Diversity  
Mai Abo. El-Hassan, Khalid F. A. Hussein, and Asmaa E. Farahat ..... 716

Wideband Printed Antipodal Vivaldi Antenna using Straight Slots for UHF DVB-T/T2 Applications  
Na-Rae Kwon, Seong-Hyeop Ahn, and Wang-Sang Lee ..... 726

Dual-band Dual-polarized Dipole Antenna for Gain and Isolation Enhancements  
Peng Chen, Lihua Wang, Yumeng Lin, and Dan Wang ..... 733

Stacked Metamaterial Patch Antenna Made of Low Permittivity Dielectrics  
Bei Zhang, Xiaofei Xu, Xiao Deng, Yefang Wang, and Juzheng Wei ..... 743

# A New Method for Twisted Wire Crosstalk Estimation Based on GA-BP Neural Network Algorithm

Wu Zhang, Yongji Wu, Jiafei Ding, Yang Zhao, and Mingyuan He

Department of Electrical and Automation Engineering  
Nanjing Normal University, Nanjing, 210046, China  
m13571872250@163.com, 597692488@qq.com, 2269533002@qq.com, zhaoyang2@njnu.edu.cn,  
704256104@qq.com

**Abstract** – Based on the research of genetic algorithm (GA) to optimize the BP neural network algorithm, this paper proposes a method for predicting twisted wire crosstalk based on the algorithm. Firstly, the equivalent circuit model of a multi-conductor transmission line is established, combined with the method of similarity transformation, the second-order differential transmission line equations are decoupled into  $n$  groups of independent two-conductor transmission line equations, and the crosstalk is finally solved. Then the mathematical model of the twisted wire is established and its structural characteristics are analyzed, and the GA-BP neural network algorithm is used to realize the mapping of the electromagnetic parameter matrix of the twisted wire and the position of the twisted wire. Finally, the mapping relationship is substituted into the transmission line equation, and the near-end crosstalk (NEXT) and the far-end crosstalk (FEXT) of an example three-core twisted wire are predicted based on the idea of cascade combined. By comparing with the transmission line matrix method (TLM), it can be seen that the method proposed in this paper is in good agreement with the crosstalk results obtained by the electromagnetic field numerical method, which verifies the effectiveness of the algorithm proposed in this paper.

**Index Terms** – Back propagation neural network (BPNN) algorithm, crosstalk, genetic algorithm (GA), multi-conductor transmission line (MTL).

## I. INTRODUCTION

As the main body of the car circuit network, the car wiring harness connects the various electrical and electronic components of the car and makes them function, but it also provides a carrier for the propagation of interference signals. It can increase the noise level of the adjacent equipment and wires, destroy the data, affect the conducted and radiated emissions of the system, and make the overall electromagnetic compatibility performance of the vehicle drop drastically [1]. Therefore, in

the early stage of automotive EMC performance design, crosstalk is the primary prediction target [2, 3]. However, due to the uncertainty of the parasitic parameters of the twisted wire, there is a lack of research concerning internal crosstalk.

The research method of non-uniform transmission line crosstalk is also applicable to twisted wires; the only difference is the lack of effective methods for extracting parasitic parameters of twisted wires [4, 5]. Based on the cascade concept, the non-uniform transmission line can be equivalent to the cascade of finite micro-element segments, and a single micro-element segment can be approximated as a uniform transmission line, and its transmission line equation can be characterized by its RLGC parasitic parameter matrix [6, 7]. Most of the existing literature uses computational electromagnetic numerical methods to extract the parasitic parameters of non-uniform transmission lines. Literature [8] introduced the FDTD algorithm when analyzing the transmission line system, and then obtained the time domain difference model of the transmission line, and finally extracted the parasitic parameter matrix from the field solution. In [9], the finite element method (FEM) is used to solve the problem of electromagnetic parameter extraction, and the extraction is based on the equivalent dielectric constant to deal with the layered problem of the medium. Literature [10] discusses a simple model for approximating the per-unit-length parameters of a lossy cable providing a smooth transition from low to high frequencies.

Numerical methods have both precision defects and application conditions, but modern artificial intelligence algorithms can better deal with the coexistence of computational efficiency and computational accuracy. Literature [11] is based on this idea and introduces BP neural network to construct the nonlinear mapping relationship between the twisted wire electromagnetic parameter matrix and the axial extension of the twisted wire, and finally combines the finite difference time domain algorithm (FDTD) to complete the crosstalk prediction of the twisted wire. BP neural network has a strong non-linear

mapping ability and can escape the constraint of mathematical formulas [12, 13], to complete the one-to-one correspondence between any position of the twisted wire and its RLCG parasitic parameter matrix. As the sample data stimulate it, the BP neural network adjusts the weight threshold of the hidden layer and the output layer to achieve the approximate output of the network's expected output of the sample data, and self-learning. The essence is to dynamically adjust the connection weight, so that the algorithm may fall into a local extreme value. In addition, the BP neural network relies on the initial network weight threshold. After initialization with different weight thresholds, the network will often acquire solutions with different accuracy [14–16]. To prevent the BP neural network from falling into the local optimum, this paper proposes the GA-optimized BP neural network algorithm model. A genetic algorithm can solve the problem of the BP neural network falling into local optimality. It optimizes the weights and thresholds of BP neural networks and solves the sensitivity problem of BP neural networks to initial weights.

## II. MULTI-CONDUCTOR TRANSMISSION LINE MODELING ANALYSIS

### A. Multi-conductor transmission line equation

Based on the idea of a cascade, the analysis of multi-conductor transmission lines can be micro-processed, the multi-conductor transmission line is composed of a finite length of micro-element small segments, in which the multi-conductor transmission line can be equivalent to the equivalent circuit form, which is convenient further analyze its crosstalk effect, as shown in Fig. 1. The coupling effect of the transmission line can be fully characterized by this model, with high accuracy. Among them,  $l_{ii}$ ,  $l_{jj}$  represent the self-inductance per unit length of the transmission line,  $l_{ij}$  represents the mutual inductance per unit length between the transmission lines.  $r_{ii}$ ,  $r_{jj}$  respectively represent the resistance per unit length of the transmission line.  $c_{ij}$  represents the mutual coupling capacitance per unit length between the transmission lines,  $c_{ii}$ ,  $c_{jj}$  represents the coupling capacitance of the transmission lines to the ground.  $g_{ij}$ ,  $g_{ii}$  represent the leakage conductance per unit length between the transmission lines.

Based on the above analysis, the multi-conductor transmission line equation is derived from the perspective of Kirchhoff's law. For the loop between the  $i$ -th conductor and the reference conductor, the multi-conductor transmission line equation can be obtained:

$$\begin{cases} \frac{\partial}{\partial z} \mathbf{V}(z, t) = -\mathbf{R}\mathbf{I}(z, t) - \mathbf{L} \frac{\partial}{\partial t} \mathbf{I}(z, t) \\ \frac{\partial}{\partial z} \mathbf{I}(z, t) = -\mathbf{G}\mathbf{V}(z, t) - \mathbf{C} \frac{\partial}{\partial t} \mathbf{V}(z, t) \end{cases} \quad (1)$$

Where RLCG is the parasitic parameter matrix of the transmission line.

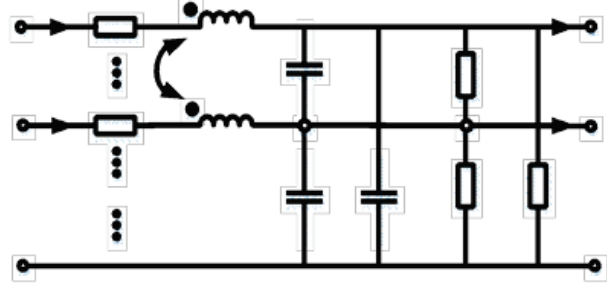


Fig. 1. The equivalent circuit of a multi-conductor transmission line per unit length.

### B. Similarity transformation decoupled MTL equations

Equation (1) removes time-domain related  $t$  parameters to form a frequency-domain multi-conductor transmission line equation:

$$\begin{cases} d\bar{\mathbf{U}}(z)/dz = -\mathbf{Z}\bar{\mathbf{I}}(z) \\ d\bar{\mathbf{I}}(z)/dz = -\mathbf{Y}\bar{\mathbf{U}}(z) \end{cases} \quad (2)$$

Where  $\mathbf{Z}$  is the impedance matrix per unit length, and  $\mathbf{Y}$  is the admittance matrix per unit length, which can be expressed by the RLCG parasitic parameters:

$$\begin{cases} \mathbf{Z} = \mathbf{R} + j\omega\mathbf{L} \\ \mathbf{Y} = \mathbf{G} + j\omega\mathbf{C} \end{cases} \quad (3)$$

Differentiating the position  $z$  of the transmission line on both sides of the first-order coupling differential equation (2) and substituting them for each other can be converted into a decoupled second-order ordinary differential equation:

$$\begin{cases} d^2\bar{\mathbf{U}}(z)/dz^2 = \mathbf{Z}\mathbf{Y}\bar{\mathbf{U}}(z) \\ d^2\bar{\mathbf{I}}(z)/dz^2 = \mathbf{Y}\mathbf{Z}\bar{\mathbf{I}}(z) \end{cases} \quad (4)$$

The idea of similar transformation method is used to further decoupling [17], removing the coupling between the cable voltage and the current. Through similar transformation,  $\mathbf{Z}\mathbf{Y}$  and  $\mathbf{Y}\mathbf{Z}$  are diagonalized at the same time, so as to realize the decoupling of the above second-order equation, there are:

$$\begin{cases} \mathbf{T}_U^{-1}\mathbf{Z}\mathbf{Y}\mathbf{T}_U = \boldsymbol{\gamma}^2 \\ \mathbf{T}_I^{-1}\mathbf{Y}\mathbf{Z}\mathbf{T}_I = \boldsymbol{\gamma}^2 \end{cases} \quad (5)$$

Modulus transformation  $\Sigma U(z)$  and  $\Sigma I(z)$  can obtain the solution of homogeneous differential equations after decoupling:

$$\begin{cases} \bar{\mathbf{U}}_m(z) = \mathbf{U}_m^+ e^{-\boldsymbol{\gamma}z} + \mathbf{U}_m^- e^{\boldsymbol{\gamma}z} \\ \bar{\mathbf{I}}_m(z) = \mathbf{I}_m^+ e^{-\boldsymbol{\gamma}z} - \mathbf{I}_m^- e^{\boldsymbol{\gamma}z} \end{cases} \quad (6)$$

Where  $\bar{\mathbf{U}}_m = \mathbf{T}_U^{-1}\mathbf{U}\bar{\mathbf{I}}_m = \mathbf{T}_I^{-1}\bar{\mathbf{I}}$ .

The crosstalk after modulus transformation can be expressed as:

$$\bar{\mathbf{U}}(z) = \mathbf{Y}^{-1}\mathbf{T}_I\boldsymbol{\gamma}\mathbf{T}_I^{-1}\mathbf{I}_m^+ e^{-\boldsymbol{\gamma}z} + \mathbf{I}_m^- e^{\boldsymbol{\gamma}z}. \quad (7)$$

Combining the port conditions and reducing the undetermined coefficients, the crosstalk can be finally

obtained. It can be seen that, for a multi-conductor transmission line, only the impedance matrix  $Z$  and the admittance matrix  $Y$  need to be obtained to actually solve the parallel cable crosstalk.

### III. GA-BP NEURAL NETWORK ALGORITHM TO EXTRACT PARASITIC PARAMETERS OF TWISTED RLCG

#### A. Twisted wire structure analysis

From the perspective of the axial direction of the transmission line, the twisted wire can be seen as a combination of countless continuously rotating cross sections. Taking the three-core twisted wire shown in Fig. 2 as an example, the phase difference of the initial point of the single wire is  $120^\circ$ , and the cross-section of the twisted wire at the corresponding axial point can be obtained by continuous rotation of the initial cross-section. When  $O_1$  turns to the  $O_2$  position,  $O_2$  turns to the  $O_3$  position, and  $O_3$  turns to the  $O_1$  position, it means that the rotation angle is  $120^\circ$ . The definition of the pitch  $p$  shows that the axial extension distance of the strands is a single pitch at this time.

Figure 3 illustrates the continuous rotation of the cross-section of the three-core twisted wire within a single pitch and the axial extension of the wire. It can be seen from Fig. 3 that the initial cross-section of the three-core twisted wire is rotated through the angle to obtain a cross-section consistent with the initial cross-sectional shape, only the difference in the serial number of the transmission line is artificially defined. In this paper, the position of the axial extension of the three-twisted wire at this time is defined as the transposition of the three-core twisted wire, which defines the axial coordinate of the transposition point as  $mp/3, m = 0, 1, 2, \dots$ . By analogy, the corresponding axial length of the twisted wire transposition and its corresponding rotation angle can be

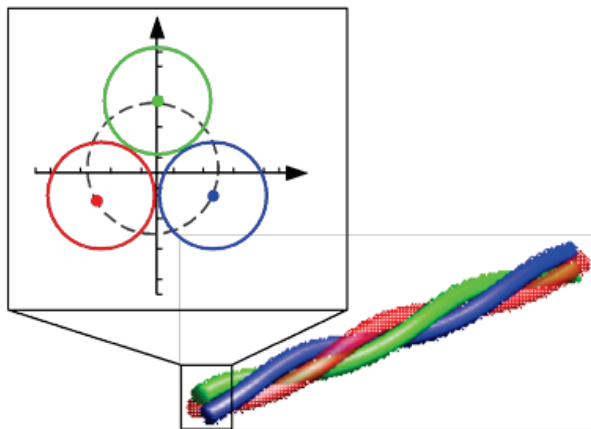


Fig. 2. Three-core twisted wire model.

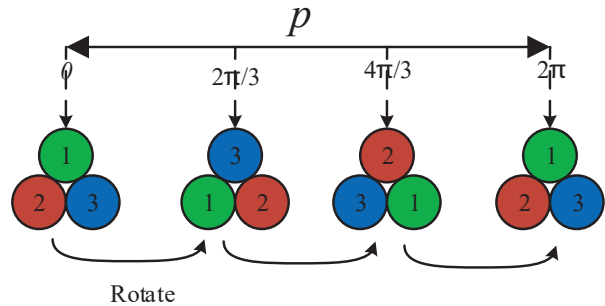


Fig. 3. Three-core twisted single-pitch conversion model.

expressed as:

$$\begin{cases} l = mp/n \\ \theta = 2m\pi/n \end{cases} \quad (8)$$

Where  $m$  is a constant and  $n$  is the number of cores.

With the axial extension of the twisted wire, the cross-sectional shape of the twisted wire is also changing, which corresponds to the change of the parasitic parameters of the twisted wire, that is, there is a nonlinear mapping relationship between the axial coordinate of the twisted wire and the parasitic parameters of the twisted wire. The functional relationship can be expressed as:

$$f(l) = [\mathbf{R}, \mathbf{L}, \mathbf{C}, \mathbf{G}]. \quad (9)$$

Where  $[\mathbf{R}, \mathbf{L}, \mathbf{C}, \mathbf{G}]$  is the parasitic parameter matrix of the twisted wire, and  $l$  represents the horizontal distance between any cross-section of the twisted wire and the initial cross-section.

Through the structural analysis of the twisted wire and the relationship between the axial length of the transposition and its corresponding rotation angle, the coordinates of any point on the twisted wire can be converted into the rotation angle of the twisted wire at that point, expressed as:

$$\begin{cases} \theta = \frac{l}{p}2\pi, 0 \leq l \leq p \\ \theta = \frac{(l-mp)}{p}2\pi + 2m\pi, mp \leq l \leq (m+1)p \leq d \end{cases} \quad (10)$$

Where  $l$  is the axial coordinate of the strand,  $\theta$  is the rotation angle,  $p$  is the pitch, and  $d$  is the total length of the strand.

From formula (10), formula (9) can be transformed into:

$$f(\theta) = [\mathbf{R}, \mathbf{L}, \mathbf{C}, \mathbf{G}]. \quad (11)$$

#### B. BP neural network

The BP neural network is introduced in [12] to approximate the mapping relationship between the independent variable and the dependent variable with high precision, avoiding the difficulty of mathematical formulas to deal with nonlinear problems.

The neural network takes the rotation angle as input, and the output is RLCG parasitic parameters. Selecting

a single hidden layer can determine the topology of the BP neural network as shown in Fig. 4. Among them, the weight from the input layer to the  $t$ -th hidden layer is expressed as  $w_{1,t}$ , the weight from the  $t$ -th hidden layer to the  $m$ -th output layer is expressed as  $w_{t,m}$ . The number of hidden layer neurons  $t$  is an empirical range value, affected by the number of input elements  $n$  and the number of output elements  $m$  can be expressed as:

$$t = (m+n)^{0.5} + a, (a = 1, 2, \dots, 10). \quad (12)$$

The output of the corresponding BP neural network is the RLCG parasitic parameter matrix. However, the matrix cannot exist directly as the output quantity, and the matrix needs to be transformed. Study the problem of twisted wires in the initial pitch, analyze the training data of training the neural network within the line length, and combine the theory of multi-conductor transmission line to know that RLCG is a diagonal matrix. Therefore, the RLCG matrix only needs the upper or lower triangular elements as the research target. The diagonal and upper triangular elements in the  $R'L'C'G'$  matrix are extracted.

$$\begin{cases} \mathbf{R}'' = [r_{11}, \dots, r_{1n}, r_{22}, r_{23}, \dots, r_{2n}, \dots, r_{nn}] \\ \mathbf{L}'' = [l_{11}, \dots, l_{1n}, l_{22}, l_{23}, \dots, l_{2n}, \dots, l_{nn}] \\ \mathbf{G}'' = [g_{11}, \dots, g_{1n}, g_{22}, g_{23}, \dots, g_{2n}, \dots, g_{nn}] \\ \mathbf{C}'' = [c_{11}, \dots, c_{1n}, c_{22}, c_{23}, \dots, c_{2n}, \dots, c_{nn}] \end{cases} \quad (13)$$

Reorganize  $\mathbf{R}''\mathbf{L}''\mathbf{C}''\mathbf{G}''$  into a vector as:

$$\mathbf{Y} = [\mathbf{R}''\mathbf{L}''\mathbf{C}''\mathbf{G}'']^T = [y_1, y_2, \dots, y_m]^T. \quad (14)$$

Where  $y$  represents the value of the sample element of the RLCG parameter matrix, where the total number of elements in  $y$  is  $m=2n(1+n)$  and  $n$  is the number of cores. It can be seen that the output of the BP neural network is a column vector organized by diagonal and upper triangular elements of the twisted RLCG parameter matrix,  $m$  is the number of outputs, and one element of the corresponding column vector corresponds to one element in the twisted RLCG parameter matrix. The BP neural net-

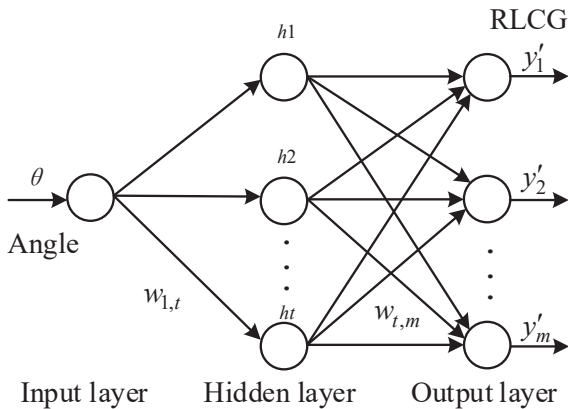


Fig. 4. Topological structure of the multi-core twisted cable neural network.

work prediction model is the twisted wire parasitic parameter extraction model. Through the above analysis, the input of the parasitic parameter extraction network is the axis coordinate of the twisted wire and the output is the column vector of the RLCG parameter matrix.

### C. Genetic algorithm optimizes BP neural network

First, the application effect of the BP neural network is greatly affected by its weight and the initial value of the threshold. Therefore, when the neural network is forwarded, it is easy to fall into a local minimum and affect the prediction effect; secondly, the BP neural network uses the gradient descent method, when optimizing complex objective functions, the required training time is too long, which leads to too many iterations of the algorithm and slower convergence. Based on the above two reasons, this study uses the genetic (GA) algorithm [18] to optimize the weights and thresholds of the BP neural network, forming a new GA-BP neural network algorithm, and applying it to the analysis and calculation of the parasitic parameters of the twisted wire.

The genetic algorithm mainly includes three steps (selection, crossover, and mutation), and its modeling process is as follows:

**Selection:** According to individual fitness, select good individuals to pass on to the next generation. The calculation method used in this study is the roulette method.

$$\begin{cases} f_i = k/F_i \\ p_i = f_i / \sum_{i=1}^N f_i \end{cases} \quad (15)$$

Where  $f_i$  is the fitness of individual  $i$ ;  $F_i$  is the fitness function of individual  $i$ ;  $k$  is the selection coefficient;  $p_i$  is the selection probability of individual  $i$ .

**Crossover:** The GA algorithm uses entity coding in the calculation process. This study uses the real number crossover method.

$$\begin{cases} a_{xi} = a_{xi}(1-b) + a_{yi}b \\ a_{yi} = a_{yi}(1-b) + a_{xi}b \end{cases} \quad (16)$$

Where  $a_{xi}$  is the  $i$  position of the  $x$ th chromosome,  $a_{yi}$  is the  $i$  position of the  $y$ th chromosome, and  $b$  is a random number,  $0 \leq b \leq 1$ .

**Mutation:** After selecting an individual, convert certain genes into other genes with a certain probability.

$$a_{ij} = \begin{cases} a_{ij} + (a_{ij} - a_{\max}) * f(g), r > 0.5 \\ a_{ij} + (a_{\min} - a_{ij}) * f(g), r \leq 0.5 \end{cases} \quad (17)$$

$$f(g) = r_2 \left( 1 - \frac{g}{G_{\max}} \right)^2 \quad (18)$$

Where  $a_{\max}$  is the upper bound of gene  $a_{ij}$ ,  $a_{\min}$  is the lower bound of gene  $a_{ij}$ ,  $r_2$  is a random number,  $g$  is the number of iterations,  $G_{\max}$  is the maximum number of iterations,  $r$  is a random number,  $0 \leq r \leq 1$ .

The steps for GA to optimize BP are as follows:

- (1) The training samples are normalized. Use maximum and minimum normalization to compress the training samples to speed up the training speed while preserving the characteristics of the data.
- (2) Initialize the BP neural network algorithm. Determine the topology of the BP neural network, determine the number of hidden layer units, learning rate and activation function and other network parameters based on the training samples, and generate the corresponding network topology.
- (3) Initialize the genetic algorithm. Generate the initial population, randomly generate the initial values of the weights and thresholds, and use them as individuals in the population to perform real number coding. Define the chromosome code length  $l$ , then for the BP neural network of 1- $M$ - $N$  topology:

$$l = 1 * M + M * N + M + N. \quad (19)$$

- (4) Determine the fitness function. The root mean square error MSE of the test data is used as the fitness evaluation function to evaluate the chromosomes.

$$\text{fitness} = \text{MSE} = \frac{1}{N} \sum_{i=1}^N (t_{sim}(i) - y_i)^2. \quad (20)$$

Where  $N$  is the number of samples in the training set;  $t_{sim}(i)$  is the predicted value of the  $i$ th sample;  $y_i$  is the actual value of the  $i$ th sample. Therefore, the minimum fitness function value when the algorithm iteration stops is the optimal solution.

- (5) Choose the parent. Sort the individuals according to their fitness, and use the roulette algorithm to screen out 2 individuals as parents. Calculate the best-fitness of the individual, and record the chromosome code of the best individual.
- (6) Random crossover. The parent uses the weight and threshold of each layer of the network as genes and uses a random crossover algorithm to combine genes with a certain crossover probability  $p_1$  to generate new offspring.
- (7) Mutation operation. In the generation of offspring, there is a certain probability that some individuals in  $p_2$  will mutate, and the weights and thresholds of the mutated individuals will be re-assigned to generate new genes.
- (8) Iteratively update to solve the optimal individual. If the fitness of the best individual of the next generation is better than that of the previous generation, update the best fitness and the best individual; otherwise, keep the same and eliminate the worst individual.
- (9) Iteration stop condition. When the stop condition is not met, select some individuals with high fitness

from the original population and the newly generated offspring to form a new population, and repeat steps (5) to (8) to continue solving the weights and thresholds of the satisfied conditions. When the stopping condition is satisfied, that is, the maximum number of iterations or the accuracy condition is satisfied, the chromosome encoding information in bestchrom is the optimal weight and threshold, and the optimal solution is generated.

## IV. VERIFICATION AND ANALYSIS

### A. Comparison between BPNN and GA-BPNN

This article takes three-core twisted wire as an example to verify and analyze the method proposed. Strand parameters are shown in Table 1. The specific distribution graph on the ground is shown in Fig. 5.

Taking the cross-section of the wire harness with a rotation degree of  $0^\circ$  in Fig. 5. as the reference cross-section, the RLCG parameter matrix within a single pitch is extracted using Ansys Q3D simulation software. At high frequencies, the resistance per unit length of the conductor increases with the square root of the frequency due to the skin effect [19], and the conductance of the homogeneous medium surrounding the conductor is also frequency dependent. The RLCG parameter in the model in this article uses the value extracted at 500 MHz

In summary, the neural network takes the upper triangular element of the RLCG parameter as the output

Table 1: Three-core twisted cable

Parameters	Values
Single wire radius	0.6 mm
Single wire conductivity	58000000 S/m
Single wire insulation thickness	0.6 mm
Insulation layer relative permittivity	2.7
Pitch	1000 mm
Height	3.5 mm

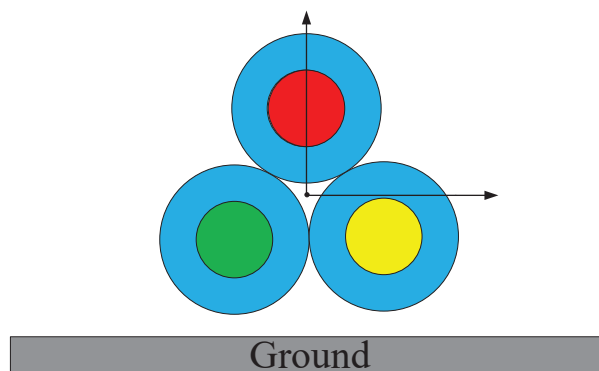


Fig. 5. Reference cross-section of three-core twisted wire model.

and the cross-section rotation angle  $\theta$  as the output. According to the hidden layer neuron empirical formula (12), the value range of hidden layer neurons is [5–15]. The MSE value under the number of neurons in each hidden layer is compared in turn, and the optimal  $t$  value is selected, that is, the hidden layer. The number of layered neurons is 12. Therefore, for the three-core twisted wire, set the BP neural network topology to 1-12-24, and the chromosome code length is 336. At the same time, the error accuracy is set to  $1e-6$ , the learning rate is 0.05, the population size is 50, the number of iterations is 100, the crossover probability  $p_1$  is 0.4, and the mutation probability  $p_2$  is 0.2.

Bring the corresponding angles of the last ten sets of samples into the parameter prediction model to obtain the corresponding prediction output value. The relative error results before and after the algorithm optimization are shown in Fig. 6. The average relative errors of BPNN

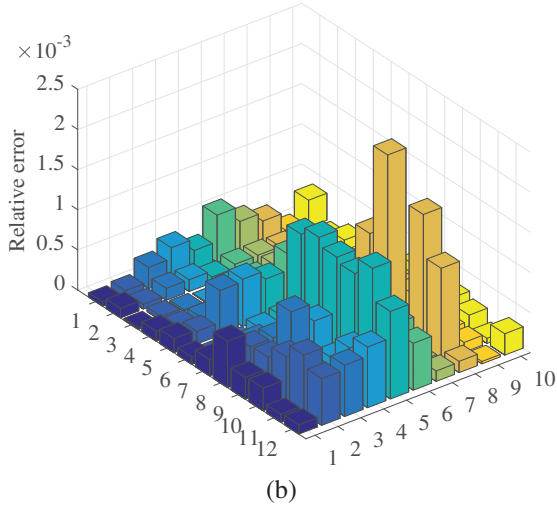
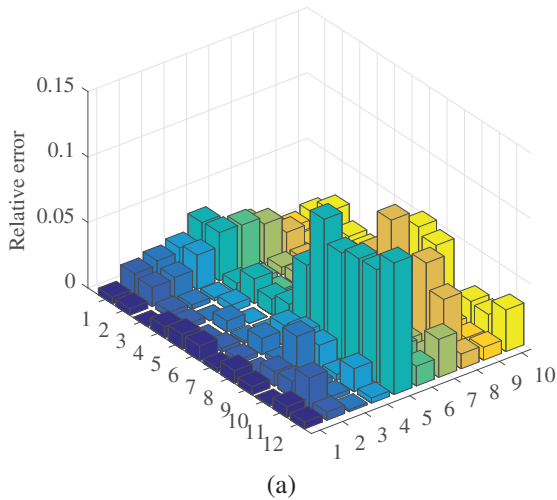


Fig. 6. Neural network relative error: (a) BP-NN and (b) GA-BPNN.

and GA-BPNN are 1.66% and 0.03%, respectively, and the GA algorithm significantly improves the prediction accuracy of the neural network.

**B. Comparison between BPNN and GA-BPNN**

The transmission line matrix method (TLM) is the core algorithm of the electromagnetic simulation software CST Cable Studio. A three-core twisted wire circuit model is established in CST shown in Fig. 7. For the three-core twisted wire, any wire is used as the excitation wire, which is defined as line 1. The other two lines are used as disturbed lines, which are defined as line 2 and line 3, respectively.

The crosstalk obtained by using two methods in 0.1MHz-1GHz are shown in Fig. 8. Due to the symmetry of the twisted wire structure, at the initial frequency of 0.1MHz, the NEXT performance of this simulation on lines 2 and 3 is  $-61.17\text{dB}$ , and the GA-BPNN algorithm performance is  $-61.47\text{dB}$ ; GA-BPNN algorithm and simulation tend to be consistent, and fluctuate around  $-18\text{dB}$  at high frequencies after a steady increase. At the initial frequency of 0.1MHz, the FEXT performance of the simulation on lines 2 and 3 is  $-66.32\text{dB}$ , and the GA-BPNN algorithm performance is  $-66.73\text{dB}$ ; the GA-BPNN algorithm and simulation tend to be consistent and fluctuate around  $-14\text{dB}$  at high frequencies after a steady increase.

The average values of the crosstalk values obtained by the proposed algorithm and simulation in different frequency bands are shown in Tables 2 and 3. The results show that the algorithm proposed in this paper is consistent with the simulation results.

Through the analysis of the crosstalk results, it can be seen that the NEXT and FEXT solved by the proposed algorithm are basically the same as the CST simulation values. In general, the crosstalk based on the proposed algorithm shows good consistency with the simulation experiment results in the crosstalk variation trend, and also shows good accuracy in the numerical value.

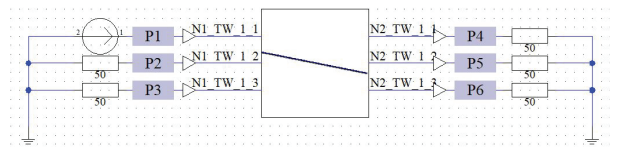


Fig. 7. CST simulation model.

Table 2: The average value of NEXT in different frequency bands of Line 2 (dB)

Frequency/MHz	0.1~100	100~500	500~1000
GA-BP	-19.28	-19.66	-19.92
Simulation	-19.02	-19.27	-17.53

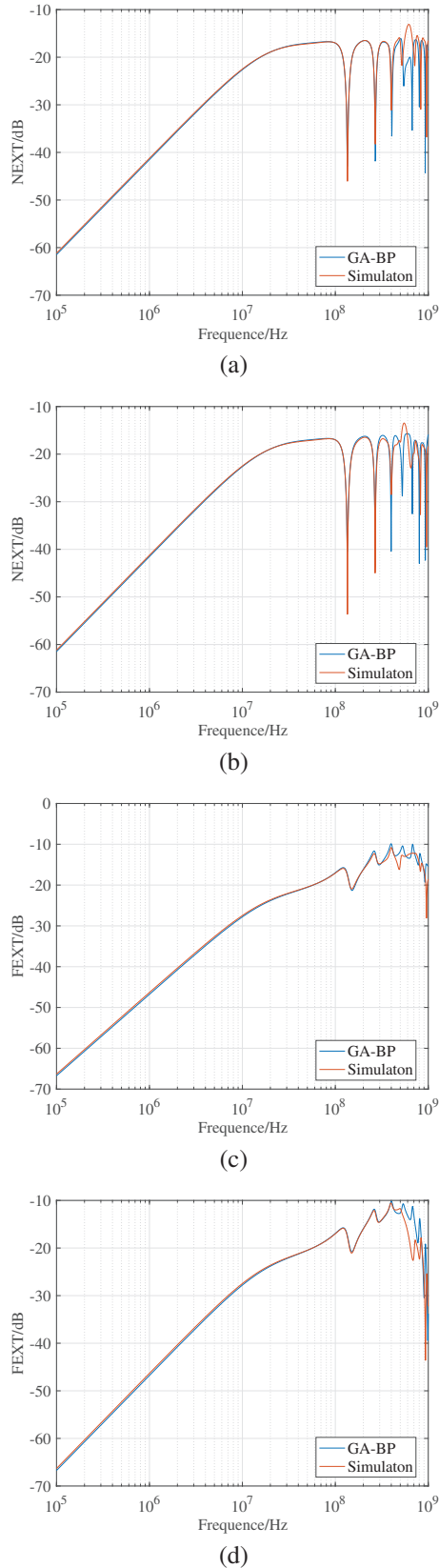


Fig. 8. (a) line 2 NEXT, (b) line 3 NEXT, (c) line 2 FEXT, and (d) line 3 FEXT.

Table 3: The average value of FEXT in different frequency bands of Line 2 (dB)

Frequency/MHz	0.1~100	100~500	500~1000
GA-BP	-22.52	-14.13	-13.61
Simulation	-22.16	-14.80	-14.76

## V. CONCLUSION

This paper proposes a method for extracting the RLCG parameter matrix of twisted wires based on the GA-BP algorithm. In fact, any spatial wiring that satisfies a certain mathematical relationship can extract a high-precision RLCG parameter matrix through this method. In this paper, a multi-conductor transmission line crosstalk model is established, and the second-order differential transmission line equations are decoupled into  $n$  groups of independent two-conductor transmission line equations by the method of similarity transformation, and the crosstalk is finally solved. The effectiveness and applicability of the method in this paper to predict the twisted wire crosstalk are verified by numerical experiments. In engineering applications, the results of NEXT and FEXT predictions can directly provide theoretical reference for the layout, type selection, and parameter adjustment of the line.

## ACKNOWLEDGMENT

The manuscript is funded by the National Institute of Technology National Natural Science Foundation of China, approval number: 52107005.

## REFERENCES

- [1] M. O'Hara and J. Colebrooke, "Automotive EMC test harnesses: standard lengths and their effect on conducted emissions," *IEEE International Symposium on Electromagnetic Compatibility*, vol. 1, pp. 233-236, May 2003.
- [2] K. Armstrong, "EMC for the functional safety of automobiles why EMC testing is insufficient, and what is necessary," *IEEE International Symposium on Electromagnetic Compatibility*, pp. 1-6, Oct. 2008.
- [3] S. Frei, R. G. Jobava, and D. Topchishvili, "Complex approaches for the calculation of EMC problems of large systems," *International Symposium on Electromagnetic Compatibility*, vol. 3, pp. 826-831, Aug. 2004.
- [4] A. Shoory, M. Rubinstein, and A. Rubinstein, "Simulated NEXT and FEXT in twisted wire pair bundles," *10th International Symposium on Electromagnetic Compatibility*, York, UK, pp. 266-271, Sep. 2011.
- [5] P. Manfredi, Daniël De Zutter, and D. V. Ginste, "Analysis of non-uniform transmission lines with an iterative and adaptive perturbation technique,"

- IEEE Transactions on Electromagnetic Compatibility*, vol. 58, no. 3, pp. 859-867, Jun. 2016.
- [6] M. Tang and J. Mao, "A precise time-step integration method for transient analysis of lossy non-uniform transmission lines," *IEEE Transactions on Electromagnetic Compatibility*, vol. 50, no. 1, pp. 166-174, Feb. 2018.
- [7] C. Jullien, P. Besnier, M. Dunand, and I. Junqua, "Advanced modeling of crosstalk between an unshielded twisted pair cable and an unshielded wire above a ground plane," *IEEE Transactions on Electromagnetic Compatibility*, vol. 55, no. 1, pp. 183-194, Feb. 2013.
- [8] K. Afrooz and A. Abdipour, "Efficient method for time-domain analysis of lossy nonuniform multi-conductor transmission line driven by a modulated signal using FDTD technique," *IEEE Transactions on Electromagnetic Compatibility*, vol. 54, no. 2, pp. 482-494, Apr. 2012.
- [9] R.-S. Chen, E. K.-N. Yung, C. H. Chan, D. X. Wang, and D. G. Fang, "Application of the SSOR preconditioned CG algorithm to the vector FEM for 3D full-wave analysis of electromagnetic-field boundary-value problems," *IEEE Transactions on Microwave Theory & Techniques*, vol. 50, no. 4, pp. 1165-1172, Aug. 2002.
- [10] F. M. Tesche, "A simple model for the line parameters of a lossy coaxial cable filled with a nondispersive dielectric," *IEEE Transactions on Electromagnetic Compatibility*, vol. 49, no. 1, pp. 12-17, Feb. 2007.
- [11] C. Yang, W. Yan, Y. Zhao, Y. Chen, C. Zhu, and Z. Zhu, "Analysis on RLCG parameter matrix extraction for multi-core twisted cable based on back propagation neural network algorithm," *IEEE Access*, vol. 2, no. 1, pp. 16-19, Aug. 2019.
- [12] T. Liu, H. Mei, Q. Sun, and H. Zhou, "Application of neural network in fault location of optical transport network," *China Communications*, vol. 16, no. 10, pp. 214-225, Oct. 2019.
- [13] W. Wu, G. Feng, Z. Li, and Y. Xu, "Deterministic convergence of an online gradient method for BP neural networks," *IEEE Transactions on Neural Networks*, vol. 16, no. 3, pp. 533-540, May 2005.
- [14] A. Yang, Y. Zhuansun, C. Liu, J. Li, and C. Zhang, "Design of intrusion detection system for internet of things based on improved BP neural network," *IEEE Access*, vol. 7, pp. 106043-106052, Jul. 2019.
- [15] G. Chen, L. Li, Z. Zhang, and S. Li, "Short-term wind speed forecasting with principle-subordinate predictor based on Conv-LSTM and Improved BPNN," *IEEE Access*, vol. 8, no. 3, pp. 67955-67973, Mar. 2020.
- [16] W. Wang, Q. Zhu, Z. Wang, X. Zhao, and Y. Yang, "Research on indoor positioning algorithm based on SAGA-BP neural network," *IEEE Sensors Journal*, vol. 22, no. 4, pp. 3736-3744, Feb. 2022.
- [17] C. R. Paul, "Decoupling the multiconductor transmission line equations," *IEEE Transactions on Microwave Theory and Techniques*, vol. 44, no. 8, pp. 1429-1440, Aug. 1996.
- [18] G. Oliveri and A. Massa, "Genetic algorithm (GA)-enhanced almost difference set (ADS)-based approach for array thinning," *Microwaves Antennas and Propagation Letters*, vol. 5, no. 3, pp. 305-315, Mar. 2015.
- [19] N. Idir, Y. Weens, and J. Franchaud, "Skin effect and dielectric loss models of power cables," *IEEE Transactions on Dielectrics and Electrical Insulation*, vol. 16, no. 1, pp. 147-154, Feb. 2009.



**Wu Zhang** was born in Anhui Province, China. He received his B.S degree from the School of Electrical Engineering and Automation from Xi'an University of Technology, Xi'an, China, in 2020. He is currently working toward a master's degree in electrical engineering at Nanjing Normal University, Nanjing, China. His main research interests include multi-conductor transmission lines and EMC.



**Yongji Wu** was born in Shanxi Province, China. He received a bachelor's degree from Shanxi Institute of Engineering and Technology in 2018 and is currently studying for a master's degree in electrical engineering at Nanjing Normal University. The main research direction

is the electromagnetic compatibility of the secondary equipment of the substation and the power system.



**Yang Zhao** received his B.E., M.E., and Ph.D. degree all in power electronic technology from Nanjing University of Aeronautics and Astronautics, Nanjing, China, in 1989 and 1992, and 1995, respectively. He is currently the professor with Nanjing Normal University. His research inter-

ests are in the areas of Electromagnetic Compatibility, Power Electronics and Automotive Electronics.



**Jiafei Ding** was born in Nantong City, Jiangsu Province in 1996. He graduated from Nanjing Normal University with a bachelor's degree in 2019 and is currently studying for a master's degree at the School of Electrical and Automation Engineering of Nanjing Normal University.

His main research interests are signal integrity and electromagnetic compatibility of power systems.



**Mingyuan** He was born in Gansu Province, China. He graduated from Hohai University in 2017 with a bachelor's degree. Currently studying for a master's degree in electrical engineering at Nanjing Normal University. The main research direc-

tions are new energy station control, power system optimization operation and stability control.

# Enhancement of Multifrequency Microwave Tomography Breast Imaging System using Flexible Preconditioner Based Krylov Subspace Methods

N. Nithya and M. S. K. Manikandan

Department of Electronics and Communication Engineering  
Thiagarajar College of Engineering, Madurai 625015, India  
nithyan@student.tce.edu, manimsk@tce.edu.

**Abstract** – Microwave Tomography Imaging System (MwTIS) is an emerging tool for medical diagnosis in the non-invasive screening process. This paper addresses the ill-condition problem by proposing two new schemes incorporated into the DBIM image reconstructed algorithm for high frequencies in MwTIS. The first scheme is to propose an optimal step frequency using the degree of ill-posedness value for reducing the frequency diversity problem. The second scheme is to propose Krylov Subspace-based regularization method called Flexible Preconditioned Conjugate Gradient Least Square (FP-CGLS) method to resolve the ill-condition problem. The iteratively updated preconditioner matrix in the proposed FP-CGLS method reduces the number of iterations and it is stable in high-level Gaussian noise. The efficiency of the proposed FP-CGLS method is validated by imposing Gaussian noise up to 30% in scattered breast phantom in the multifrequency range of 2 GHz -3 GHz. It achieves an enhanced reconstructed image at 12 iterations with a relative error of 0.1802 for 20% of Gaussian noise and for the same scheme the existing CGLS method has a 0.4480 relative error at the 77 iterations. Further, the FP-CGLS along with the DBIM method produces a reconstructed image with the accuracy of 0.8760 in four DBIM iterations.

**Index Terms** – CGLS, ill-posedness, Krylov subspace method, microwave tomography, regularization.

## I. INTRODUCTION

Microwave Tomography Imaging System (MwTIS) is a promising diagnostic tool in breast cancer detection [1] and monitoring [2, 3] its progress towards widespread clinical application. It inspires several benefits such as usage of nonionizing low power electromagnetic signals, cost-effective antenna-array, low health risk, and portability. MwTIS aims at estimating the dielectric values of internal tissues from processing measured electromagnetic field data is stated to solve the electromagnetic inverse scattering problem [4]. Various inverse scattering

problem resolving algorithms such as the Born iterative method (BIM), Distorted Born iterative method (DBIM), and Gauss Newton (GN) can employ to compute images by a set of underdetermined linear equations. Every iteration of the DBIM algorithm, the linear system of equations is solved by using regularization methods and has found optimal solutions by the inversion process. Thresholding [5, 6], Compressive sensing with Sparsity [7], and Krylov subspace-based methods [8] are explored towards the quality of the resultant image.

Refinement of image resolution and reduction of computation time is currently needed in medical diagnosis applications for microwave imaging. While incorporating prior information [9], reducing the size of resolution grid elements [10], contrast enhancement [11], and high frequency microwaves [12] certainly increased the quality of microwave tomography images. High frequencies in MwTIS have inherently obtained fine internal details of the tissues in a high resolution grid than low frequency. Although high frequency microwave has increased the spatial resolution that may be acquired in high resolution images, unstable convergence is a significant limiting factor in the inversion process. The multifrequency [6, 13] approach has stabilized the inversion process by reducing the imbalance ratio between the number of measurements and the number of pixels in high resolution grid. Hence, this paper has conducted a detailed study and proposed a method to improve significant resolution enhancement with multifrequency in breast imaging systems. Excellent imaging results have been obtained using frequency hopping techniques which is an initial guess pursued by inverting single-frequency data then followed by processing of multifrequency data. This can be extremely time-consuming due to non-linearity raised by the frequency diversity problem (switching from low frequency to high frequency) and ill-posedness in the linear system of equations. A credible work in the literature, DBIM with Thresholding method [6] and wavelet basis with CGLS method [14] resolved the above problem by hybrid frequency hopping technique. It is performed well

in the resolution of 1 mm to 4 mm but they lacked to perform below 1 mm resolution breast images. Because, each frequency range has its unique characteristics like convergence time, stability in solution estimation, and also put in high measurement noise in the received scattered fields. Further, it meets more computational burdens like a greater number of iterations to construct sufficiently high-resolution images. Therefore, this paper gives special attention to the multifrequency techniques and regularization method to handle nonlinearity and ill-posedness problems in the reconstruction algorithm.

This paper proposed two schemes to resolve the above-mentioned problems in DBIM with a multifrequency microwave tomography breast imaging system. The first is reducing the nonlinearity by selecting the optimal step frequency in frequency hopping techniques. The value called degree of ill-posedness helps to select the suitable step frequency which makes the minimum effects of ill-posedness in the linear system of equations. The second scheme is proposing a Preconditioner incorporating the Krylov subspace regularization method to achieve optimal imaging accuracy and reconstruction stability by solving the ill-posedness problem. Conjugate Gradient Least Square (CGLS) is one of the credible Krylov subspace regularization methods that worked well with the DBIM reconstruction algorithm for tumor detection [15] and density estimation [16] in breast imaging applications. This paper proposed a modified version of the CGLS method called the Flexible Preconditioner CGLS (FP-CGLS) method for inverting underdetermined multifrequency linear equations with high measurement error. In this proposed scheme, the Flexible Preconditioner is being updated in every iteration helps to stable and quicken the convergence time in an unstable high-frequency imaging system. In addition, the non-negativity constraint in the estimation of the appropriate dielectric values of unknown breast tissues is increases the truthfulness of the solution. These proposed schemes take less iteration for the DBIM algorithm to find the high accuracy resultant images.

The paper is organized into the following sections. Section 2 explains the measurement matrix formation process. A detailed description of the proposed method is stated in section 3. Section 4 explained the properties of breast phantom, implementation specifications, and the results achieved from the study. The conclusion is explained in section 5.

## II. MEASUREMENT MATRIX FORMULATION

This section explains the formation of a measurement matrix based on the design characteristics of the MWTIS. The circular measurement domain (S) with the transmitter ( $N_t$ ) and receiver ( $N_r$ ) antennas and the object

are present in the D domain. The object is illuminated by the  $N_t$  and the scattered fields are received by the  $N_r$  simultaneously. The integral equation of imaging domain (D) linearized by the first-order Born approximation which governs the entire DBIM algorithm expressed in eqn (1),

$$E_{scat}(r) = k_b^2 \int_d G(r, r') \cdot X_{object}(r') E_{inc}(r') dr' \quad (1)$$

$G(r, r')$  is the Green's function with the wavenumber of the background medium ( $k_b$ ).  $X_{object}(r')$  is relative permittivity ( $\frac{\epsilon_r - \epsilon_b}{\epsilon_b}$ ) of an object to be imaged.  $E_{inci}$  is the plane wave incident fields.  $r', r$  are the spatial positions in S and D domains. To format the measurement matrix of the proposed work, integral (1) of the imaging domain is discretized using Fredholm of the first kind and pixel-based smooth basis function [17]. It leads to an increase the imaging accuracy as well as resolution. Now, the integral equation (1) is converted into a linear system of equations as,

$$A_{M \times N} \cdot X_{N \times 1} = b_{M \times 1} \quad (2)$$

Here  $A_{(M \times N)}$  is the measurement matrix which is the outcomes of the interaction between the incident field and background medium.  $b_{M \times 1}$  is the received scattered field. Here  $M$  is the number of measurement antenna pairs and  $N$  is the row vector representation of the number of pixels in the image grid. In the multifrequency forward process, the size becomes  $(M \times F) \times N$ . Here  $F$  is the number of frequencies in the multifrequency range.

## III. PROPOSED ENHANCEMENT SCHEME FOR MICROWAVE BREAST IMAGING

### A. Proposed optimized step frequency to resolve frequency diversity problem

This section has detailed the behavior of condition number in the system measurement matrix (A) due to variation in the operating frequency value and selection of optimum multifrequency range with minimum condition number. The performance of the reconstruction algorithms is based on the condition number of the system coefficient matrix (A). Small changes in the condition number of A will affect more in the solution more. It takes more iteration to converge the solution and struggle to produce the appropriate solution. This is called an ill-posed condition problem. In this paper, a study has been conducted to analyse the impact of the frequency diversity problem in the existing studies [6, 14]. It depicts, that the condition value increases in the multifrequency range due to the high frequency hopping step from 1 GHz to 3 GHz To meet the high spatial resolution requirement of MWTIS, the paper needs to find the optimum multifrequency scenario with a high frequency range. So, the measurement matrix (A) of the proposed multifrequency needs to estimate the effect of ill-posedness on the frequency diversity problem. The factor called degree of

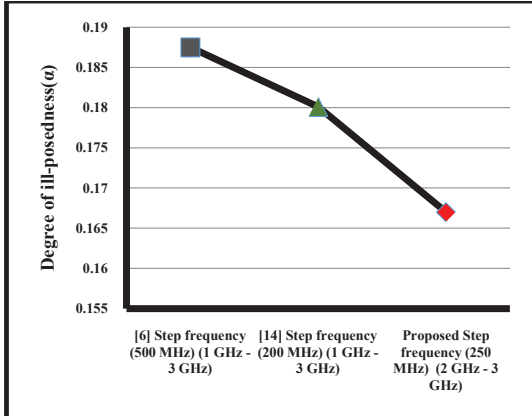


Fig. 1. Analysis of  $\alpha$  value for the proposed multifrequency scenario in high frequency range.

ill-posedness ( $\alpha$ ) value [18] was used to find the proposed multifrequency scenario. It is calculated using,

$$K(A) = \exp(-\alpha.i). \quad (3)$$

Here,  $K(A)$  is the condition number of  $A$  and  $i$  is the number of the singular value spectrum.  $\alpha$  is the positive integer value. The  $\alpha$  is calculated for two different step frequencies such as 500 MHz [6] and 200 MHz [14] in the 1 GHz to 3 GHz frequency range. As well,  $\alpha$  is calculated for the 250 MHz jumping frequency for the proposed multifrequency range from 2 GHz to 3 GHz. These values are plotted in Fig. 1. It has shown that the proposed frequency has a minimum  $\alpha$  value than the existing scenario. Based on the above analysis the suitable frequency range for the desired application can be fixed. Further, this analytical proof has depicted the proposed multifrequency scenario will produce a good quality image in the regularization process. However, the measurement matrix ( $A$ ) in eqn (2) is under-determined and needs to solve by the normal equation in the least square method such as the CGLS method. A detailed explanation of the solving procedure of  $A$  is stated in the next section.

### B. Proposed flexible preconditioned CGLS (FP-CGLS) regularization method

This section has explained the steps and advantages of the proposed Flexible Preconditioned CGLS (FP-CGLS) Krylov subspace regularization method. Especially in medical imaging, Born (BIM, DBIM) type reconstruction algorithms give under-determined ( $(M \times F) \ll N$ ) set of linear equations which means the imbalance between  $(M \times F)$  and  $(N)$ . The cost function is represented as,

$$\min \phi(x) = A^T A x = A^T b. \quad (4)$$

The results from the analytical study in section 3.1 depict the  $A$  having  $\alpha$  as 0.169 and it conveys

the  $A$  is stuck with the ill-posedness problem. Due to the large condition number of  $A$ , the right-hand side  $b$  is contaminated by noise ( $b + \dot{\eta}$ ) in real-time. Eqn (4) solved using CGLS may compute the useless solution and often converge very slowly and cannot stable in the number of iterations in frequency diversity problem in the multifrequency scenario. To resolve the above problem, one needs additional computational matrix called preconditioner ( $P$ ) is added to eqn (4). The linear equations become,

$$\min \phi(x) = P^{-H} A^T A P^{-1} x - P^{-H} A^T b. \quad (5)$$

Here,  $P \in \mathbb{R}^{N \times N}$ . In this paper, the Krylov subspace method called Flexible Preconditioner CGLS method is taken to solve eqn (5). It is an enhanced version of the PCGLS [19] method. It is used to estimate dielectric values of  $x$  by fast convergence in ill-condition  $A$  and appropriate  $x$  in noise is corrupted in the received scattered field. It increases the accuracy and reduces the number of iterations compared to the standard solvers. To compute the meaning solution one additional constraint called non-negativity is added in this method. The appropriate solution  $x_m$  in standard CGLS is determined as follows,

$$x_m = x_{m-1} + \alpha_{m-1}.d_m. \quad (6)$$

In FP-CGLS the parameters such as scalar step length ( $\alpha_m$ ) and the direction vector ( $d_m$ ) enforce non-negativity in every iteration

$$\alpha_{m-1} = \frac{(res_{m-1}, w_{m-1})}{(w_{m-1}, w_{m-1})}. \quad (7)$$

Here  $m$  is the iteration index.  $\alpha_{m-1}$  selected by satisfying the bounded step length  $\overline{\alpha_{m-1}}$  condition  $\overline{\alpha_{m-1}} > 0$ . The bounded step length is computed as follows,

$$\overline{\alpha_{m-1}} = \min(\alpha_{m-1}, \min(\frac{-x_{m-1}(d_{m-1} < 0)}{d_{m-1}(d_{m-1} < 0)})). \quad (8)$$

The scalar  $\overline{\alpha_{m-1}}$  is satisfies the condition of orthogonality which project the  $A^T b$  in the nonnegative orthant, due to  $x_m = 0$  until the  $\overline{\alpha_{m-1}} > 0$ . It gives added truthfulness to the solution in which the imaged object does not contain negative dielectric properties. The iteration depends on the residual norm vector  $res = (b + \dot{\eta}) - A.x_m$  and  $d_m$ . To improve the speed of convergence the left preconditioner ( $P_m$ ) is multiplied to  $res_m$ . It is computed as follows,

$$P_m = P_m A^T res_m. \quad (9)$$

The standard PCGLS method calculated the  $L$  as a  $(N \times N)$  sparse matrix but in the proposed FP-CGLS the  $P^{(m)} = \text{diag}(x_m)$  and it is updated in every iteration. Every iteration step ensures the nonnegativity constraints and proceeds right direction towards the appropriate subspace. So that it is called as Flexible Preconditioner CGLS method. This is the reason the solution  $x$  does not distort by the measurement noise ( $\dot{\eta}$ ). The cost of

computing vector and matrix multiplication with a preconditioner is minimum compared to other Krylov methods like CGLS. The residual norm is set as the stopping criteria. The discrepancy principal inequality condition helps to stop the iteration at right time. The FP-CGLS does not require an explicit regularization parameter instead of that the step length ( $\alpha$ ) and tuning parameter ( $\beta$ ) do the same. In this manner, the proposed FP-CGLS method controls the measurement error and unstable convergence due to the frequency diversity problem by resolving the ill-condition problem with less number of iterations. It improves the quality of high-resolution MWTIS for the breast category.

#### IV. RESULTS AND DISCUSSION

This section has explained the numerical setting of the simulation study and evaluated the results achieved by the proposed FP-CGLS method for desired multifrequency scenario using scattered breast phantoms. The main purposes of the study have mentioned below,

- Analysed the reconstruction performance of the proposed multifrequency range 2 GHz to 3 GHz with 250 MHz step frequency using the proposed FP-CGLS. The relative error and optimal iteration count are used to evaluate the performance.
- The convergence behavior of the proposed FP-CGLS is examined by adding different measurement error levels ( $\dot{\eta}$ ) in the scattered field (b) that are  $\dot{\eta} = 10\%$ ,  $20\%$ , and  $30\%$ . The relative residual norm and iteration count are the parameters used for the convergence analysis.
- The efficiency of the FP-CGLS in the DBIM reconstruction algorithm is analyzed by the Mean Square Error (MSE) and DBIM iteration count.

The simulation study has also been conducted by the standard CGLS method for comparative analysis.

##### A. Simulation specification and dataset

The circular imaging system (domain S) is set with a diameter of 30 cm. The  $N_t=15$  and  $N_r=16$  are placed around the boundary of the S domain. In the real-time scenario, the breast was immersed in a lossless coupling medium, for that the background medium is assigned to  $\epsilon_b=2.6$  in the proposed method. The  $M = 240$  samples of scattered fields are collected by consecutive incidence and reception of these  $N_t$  and  $N_r$ . The five equally spaced ( $F = 5$ ) multifrequency scenarios are in the range of 2 GHz to 3 GHz (proposed in section 3.1). The numerical process and evaluation were done in MATLAB-R2021. The Scattered (ID=070604PA1) breast phantom has been taken from the numerical repository of the Cross-Disciplinary Electromagnetics Laboratory [20] (University of Wisconsin

CEM Laboratory) for the proposed work. The 2D slice No 135 of the phantom is extracted from the 3D breast model.

The breast phantom is shown in Fig. 2. The pixel size is equal to 0.5 mm and other prerequisite data are initialized as mentioned in the instruction manual [20] of the same. The dielectric values of the breast tissues [21] in the phantoms are listed in Table 1. The numerical process and evaluation were done in MATLAB-R2021.

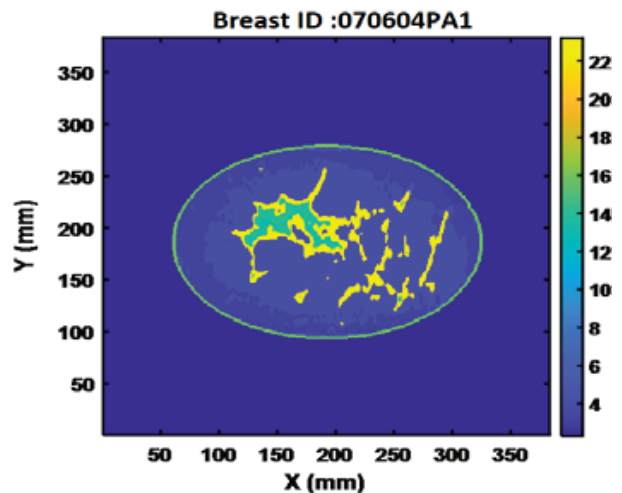


Fig. 2. Reference scattered breast phantom.

Table 1: Debye parameters of the breast tissues: [21]

Material	$\epsilon_\infty$	$\Delta\epsilon$	$\sigma_s$
Adipose	3.987	3.545	0.080
Fibrogland	13.91	40.49	0.824
Background medium	2.6	0.092	0.005
Skin	15.93	23.83	0.831

##### B. Assessment of proposed FP-CGLS in desired multifrequency range

This section has explained the performance of the proposed multifrequency range using the FP-CGLS method in the reconstructed breast phantoms. The below-mentioned results are taken at A matrix of size ( $1280 \times 146689$ ). The reconstruction quality of the proposed FP-CGLS method and the parameters like Relative Error and total iteration (*Iter*), the count is compared with CGLS. In this study, the maximum iteration count is set as 150 and  $\dot{\eta}=0$  to compare the performance of these two methods. The calculation of Relative Error (*RE*) as follows,

$$RE = \frac{\|X(r') - x_m\|_2}{\|X(r')\|_2} \quad (10)$$

Table 2: Comparison of relative error and their optimal stopping iterations for proposed FP-CGLS

Breast phantom	Methods	Iter	RE
Scattered Breast ID:070604PA1	FP-CGLS	18	0.1770
	CGLS	77	0.4480

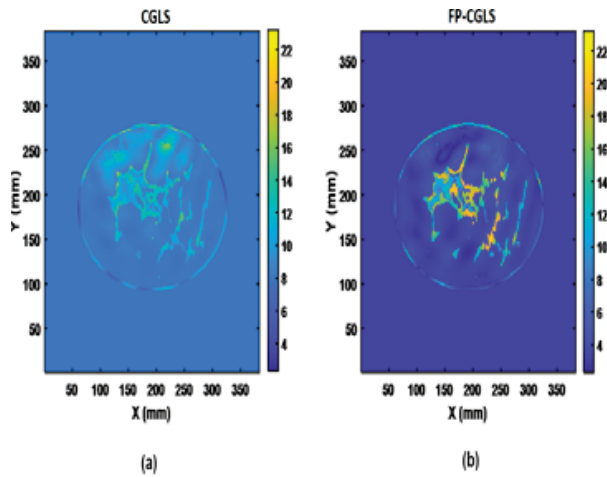


Fig. 3. Reconstructed images of CGLS and proposed FP-CGLS method using multifrequency range 2 GHz to 3 GHz.

The best iteration count is selected by the discrepancy principle and listed in Table 2. This result has been achieved in the single DBIM iteration. The results in Table 2 clearly explained the benefits of the preconditioner ( $\mathbf{P}_m$ ) in the FP-CGLS methods.

The FP-CGLS method has achieved a minimum relative error of 0.1773 within 18 iterations. Further CGLS method has required 77 iterations to reach the minimum relative error value of 0.4480. The reason behind this is the FP-CGLS regularization method effectively quickens the slow convergence of the gradient in the CGLS method. Note that, the proposed FP-CGLS produces a better result with the minimum number of iterations for the proposed high frequency multifrequency range microwave tomography imaging system. The reconstructed image of the final DBIM iterations is shown in Fig. 3. Assessment of Proposed FP-CGLS Convergence on Gaussian Noise This section has explained the convergence behavior of the proposed FP-CGLS regularization method by varying the different Gaussian noise levels.

Computing the differences in Relative Residual Norm ( $RR\_Norm$ ) for newly estimated  $x$  in successive iterations is called convergence analysis. It shows how the algorithms are moved closer to the desired solution. In this study, the Gaussian noise model is used to simu-

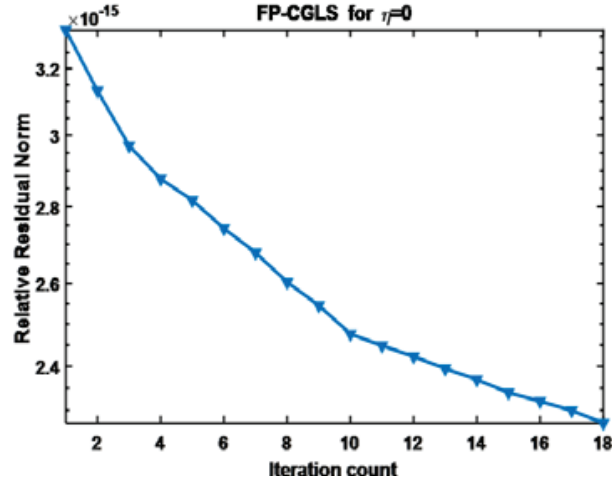


Fig. 4. Convergence plot for the reconstructions of the scattered breast using proposed FP-CGLS method.

late the error vector of three distinct noise levels that are  $\eta = 10, 20, 30\%$ .

It is added to  $b$  in eqn (2). This approach is used to test the stability and robustness of the regularization method against uncertainties like noise and other artifacts in the measurement system. The calculation of relative residual norm is calculated as,

$$RR\_Norm = \frac{\|A^T d_m - x_m\|}{\|A^T b\|_2}. \quad (11)$$

The semi-log plot of Relative Residual Norm ( $RR\_Norm$ ) and iteration count helps to numerically analyze the convergence behavior of the proposed solution based Preconditioner ( $\mathbf{P}_m$ ). Figures 4 and 5 show the semilog plot for the CGLS method and proposed FP-CGLS method. These figures are show the convergence of these two regularization methods without noise distortion. The noticeable value in this plot is the magnitude of  $RR\_Norm$ .

The FP-CGLS method reaches the minimum value ( $10^{-15}$ ) at the beginning of the iteration, But CGLS method reached  $10^{-4}$  only at the end of the iteration.

The product of  $\mathbf{P}_m$  with  $\mathbf{res}_m$  quickly move to the negative descent direction. Figure 6 shows the comparison plot between FP-CGLS and CGLS regularization methods for the different noise levels. The increments in noise level reduce the iteration count in both FP-CGLS and CGLS methods, but the FP-CGLS method is stable in convergence (12 iterations) up to 20% of noise distortion. The CGLS has sudden fall from 77 iterations to 17 iterations in 20% of noise distortion.

The relative error value and the number of iterations are recorded for the FP-CGLS and CGLS methods for the three noise levels are listed in Table 3. It shows that FP-CGLS has a substantially higher measurement

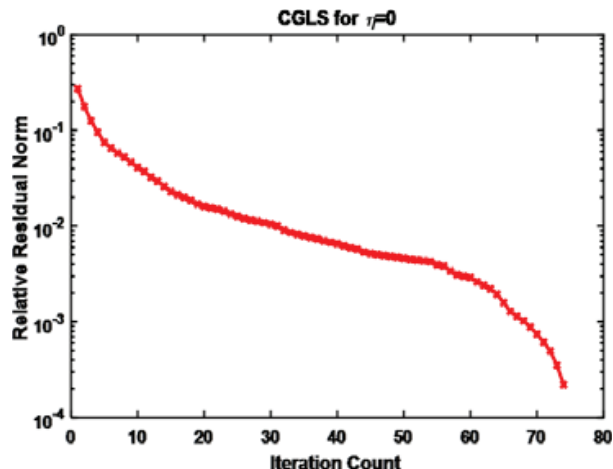


Fig. 5. Convergence plot for the reconstructions of the scattered breast using CGLS method.

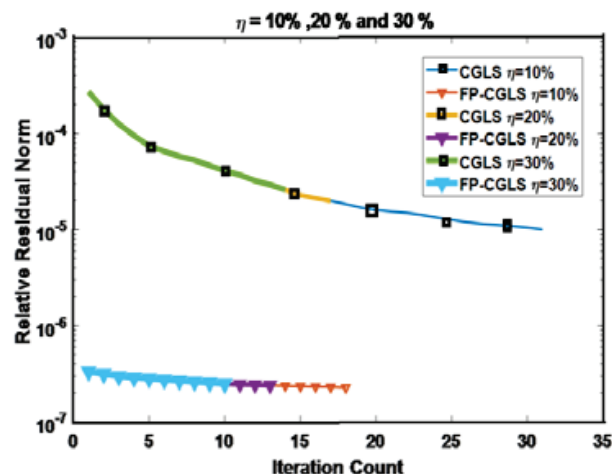


Fig. 6. Comparison of relative residual norm versus iteration count for the  $\eta = 10\%$ ,  $20\%$ , and  $30\%$  for FP-CGLS and CGLS methods.

error handling ability than the CGLS method in  $\eta$  up to  $20\%$  except for the error level  $\eta=30\%$ . There is a minor increment in the relative error value. Another observation is, that the CGLS method stuck into stagnation problem even though in  $\eta=20\%$ . Based on the results, FP-CGLS has stable convergence behavior in higher measurement error.

### C. Assessment of proposed FP-CGLS on DBIM

This section has explained the overall reconstruction performance of the DBIM algorithm combined with the proposed FP-CGLS method for the desired multi-frequency range in a scattered breast phantom. The results are taken at A matrix of size  $(1280 \times 146689)$ . The  $\eta$  is set as 0. The pixel size is assigned as 0.5 mm for high resolution reconstructed image. A cross-

Table 3: Comparison of relative error and their optimal stopping iterations for different Gaussian noise

Methods	$\eta=10\%$		$\eta=20\%$		$\eta=30\%$	
	Iter	RE	Iter	RE	Iter	RE
FP-CGLS	17	0.17	12	0.18	10	0.2215
CGLS	31	0.47	17	0.49	13	0.51865

section plot (Fig. 7) of the reconstructed image illustrates the goodness of the proposed FP-CGLS method. It is plotted between the spatial position on X-axis and its corresponding static relative permittivity values on Y-axis. These types of visualization help to identify the estimated dielectric values of the reconstructed image have met the actual values in the reference breast phantom. Figure 7 shows the reconstructed image in the second and fourth iteration of the iteration of the DBIM algorithm along with the reference profile. It showed the proposed FP-CGLS produces an appropriate result in 4 DBIM iterations. It has achieved accuracy values 0.6030, 0.6936, 0.7665, 0.8760 in DBIM iteration 1, 2, 3 and 4 respectively. According to this analysis, the proposed FP-CGLS method is performed well in the high frequencies in multifrequency microwave tomography breast imaging even though in higher noise levels.

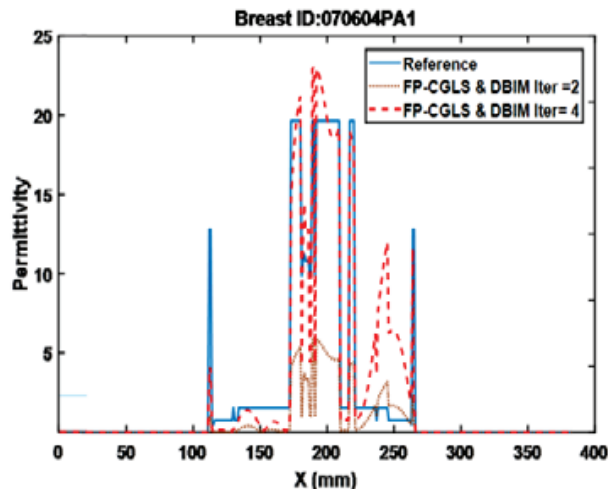


Fig. 7. Cross-sectional view of reconstructed permittivity of scattered breast using proposed FP-CGLS with iteration of DBIM algorithm.

## V. CONCLUSION

This paper presents the high frequencies in multifrequency DBIM with a proposed Krylov subspace based regularization method called FP-CGLS for high-

resolution MWTIS breast imaging. The frequency diversity problem is a major issue in multifrequency microwave tomography imaging. It leads to received scattered fields corrupted by Gaussian noise and unstable convergence in the reconstruction process. This paper addresses these issues modelled as the ill-condition problem. It was resolved by the proposed optimal step frequency (250 MHz) for the high frequency range (2 GHz to 3 GHz) selected based on the degree of ill-posedness value. The unstable convergence and accuracy of the solution are resolved by the iteratively updated preconditioner based FP-CGLS method. A scattered breast phantom has been taken for this study. Stand CGLS method is used to compare the performance of the proposed multifrequency and FP-CGLS method. The iteratively updated preconditioner  $P_m$  in the proposed FP-CGLS method supports reaching the appropriate  $x_m$  at 12 iterations with a relative error of 0.1802 even though in 20% of Gaussian noise. Compare the results with the Standard CGLS method; it achieved a 0.4480 relative error value at the 77 iterations. The FP-CGLS along with the DBIM method produces a reconstructed image with the accuracy of 0.8760 in 4 DBIM iterations.

#### ACKNOWLEDGMENT

This work was supported by the Thiagarajar Research Fellowship (TRF) scheme in Thiagarajar College of Engineering, Madurai.

#### REFERENCES

- [1] N. Abdollahi, I. Jeffrey, and J. LoVetri, "Improved tumor detection via quantitative microwave breast imaging using eigenfunction-based prior," *IEEE Trans. Comput. Imaging*, vol. 6, pp. 1194-1202, 2020.
- [2] B. Oliveira, D. Godinho, M. O'Halloran, M. Glavin, E. Jones, and R. Conceição, "Diagnosing breast cancer with microwave technology: Remaining challenges and potential solutions with machine learning," *Diagnostics*, vol. 8, no. 2, pp. 1-22, 2018.
- [3] G. Boverman, C. E. L. Davis, S. D. Geimer, and P. M. Meaney, "Image registration for microwave tomography of the breast using priors from nonsimultaneous previous magnetic resonance images," *IEEE J. Electromagn. RF Microwaves Med. Biol.*, vol. 2, no. 1, pp. 2-9, Mar. 2018.
- [4] Semenov, "Microwave tomography: Review of the progress towards clinical application," *Philos. Trans. A. Math Phys. Eng. Sci.*, vol. 367, pp. 3021-3042, 2009.
- [5] M. Ambrosiano, P. Kosmas, and V. Pascazio, "A multithreshold iterative DBIM-based algorithm for the imaging of heterogeneous breast tissues," *IEEE Trans. Biomed. Eng.*, vol. 66, no. 2, pp. 509-520, 2019.
- [6] Z. Miao and P. Kosmas, "Multiple-frequency DBIM-TwIST algorithm for microwave breast imaging," *IEEE Trans. Antennas Propag.*, vol. 65, no. 5, pp. 2507-2516, 2017.
- [7] M. Azghani, P. Kosmas, and F. Marvasti, "Fast microwave medical imaging based on iterative smoothed adaptive thresholding," *IEEE Antennas Wirel. Propag. Lett.*, vol. 14, pp. 438-441, 2015.
- [8] H. Harada, D. J. N. Wall, T. Takenaka, and M. Tanaka, "Conjugate gradient method applied to inverse scattering problem," *IEEE Trans. Antennas Propag.*, vol. 43, no. 8, pp. 784-792, 1995.
- [9] L. M. Neira, B. D. Van Veen, and S. C. Hagness, "High-resolution microwave breast imaging using a 3-d inverse scattering algorithm with a variable-strength spatial prior constraint," *IEEE Trans. Antennas Propag.*, vol. 65, no. 11, pp. 6002-6014, Nov. 2017.
- [10] Y. Suzuki and S. Kidera, "Resolution enhanced distorted born iterative method using ROI limiting scheme for microwave breast imaging," *IEEE J. Electromagn. RF Microwaves Med. Biol.*, vol. 5, no. 4, pp. 379-385, 2021.
- [11] M. T. Bevacqua and R. Scapaticci, "A compressive sensing approach for 3D breast cancer microwave imaging with magnetic nanoparticles as contrast agent," *IEEE Trans. Med. Imag.*, vol. 35, no. 2, pp. 665-673, Feb. 2016.
- [12] M. A. Aldhaeebi, K. Alzoubi, T. S. Almoneef, S. M. Bamatraf, H. Attia, and O. M. Ramahi, "Review of microwaves techniques for breast cancer detection," *Sensors*, vol. 20, no. 390, pp. 1-38, 2020.
- [13] C. Kaye, I. Jeffrey, and J. LoVetri, "Improvement of multi-frequency microwave breast imaging through frequency cycling and tissue-dependent mapping," *IEEE Trans. Antennas Propag.*, vol. 67, no. 11, pp. 7087-7096, Nov. 2019.
- [14] R. Scapaticci, P. Kosmas, and L. Crocco, "Wavelet-based regularization for robust microwave imaging in medical applications," *IEEE Trans. Biomed. Eng.*, vol. 62, no. 4, pp. 1195-1202, 2015.
- [15] T. Rubaek, P. M. Meaney, P. Meincke, and K. D. Paulsen, "Nonlinear microwave imaging for breast-cancer screening using Gauss-Newton's method and the CGLS inversion algorithm," *IEEE Trans. Antennas Propag.*, vol. 55, no. 8, pp. 2320-2331, 2007.
- [16] J. D. Shea, P. Kosmas, S. C. Hagness, and B. D. Van Veen. "Three-dimensional microwave imaging of realistic numerical breast phantoms via a multiple-frequency inverse scattering technique," *Medical Phys.*, vol. 37, no. 8, pp. 4210-4226, 2010.
- [17] D. W. Winters, J. D. Shea, P. Kosmas, B. D. Van Veen, and S. C. Hagness, "Three-dimensional

microwave breast imaging: Dispersive dielectric properties estimation using patient-specific basis functions," *IEEE Trans. Med. Imaging*, vol. 28, no. 7, pp. 969-981, 2009.

- [18] Q. Fang, P. M. Meaney, and K. D. Paulsen, "Singular value analysis of the Jacobian matrix in microwave image reconstruction," *IEEE Trans. Antennas Propag.*, vol. 54, no. 8, pp. 2371-2380, Aug. 2006.
- [19] S. Gazzola, "Fast nonnegative least squares through flexible Krylov subspaces," *SIAM J. Sci. Comput.*, vol. 39, pp. A655-A679, 2017.
- [20] Available from <https://uwcem.ece.wisc.edu/phantomRepository.html>
- [21] P. T. Nguyen, A. Abbosh, and S. Crozier, "Microwave hyperthermia for breast cancer treatment using electromagnetic and thermal focusing tested on realistic breast models and antenna arrays," *IEEE Trans. Antennas Propag.*, vol. 63, no. 10, pp. 4426-4434, Oct. 2015.



**N. Nithya** received the B.E. degree in computer science and engineering from Anna University, Tamilnadu, India, in 2009 and the M.E. degree in computer science and engineering from Anna University, Tamilnadu, India, in 2014. She is

currently pursuing the Ph.D. degree in Information and Communication at Anna University, Tamilnadu, India from 2017 to 2020. From 2015 to 2018, she was a Assistant Professor in the Department of computer science and engineering. Her current research interests include microwave tomography imaging, inverse problems techniques, regularization method for the breast cancer detection and brain stroke microwave imaging, ill-posed and ill-condition problems in linear equation.



**M. S. K. Manikandan** received the BE degree in Electronics and communication engineering from NIT-Trichy, Tamilnadu, India, in 1998 and the ME degree in communication systems from Thiagarajar College of Engineering, Tamilnadu, India in 2000. He completed Ph.D in Information and communication at Anna University, Tamilnadu, India in 2010. Since 2001 he has been an faculty with Electronics and communication engineering department, Thiagarajar College of Engineering. He is the author of more the 25 articles in reputed journals and conference. His research interests include wireless communication and medical image analysis.

# Computational Analysis for Miniaturization of Tapered Slot Antenna using Elliptical Conducting Loaded Strips

Bismah Tariq, Muhammad Amjad, and Abdul Aziz

Faculty of Engineering  
The Islamia University of Bahawalpur, Pakistan  
bismah.tariq91@gmail.com, muhammd.amjad@iub.edu.pk, abdul.aziz@iub.edu.pk

**Abstract** – In this paper, the computational analysis for miniaturization of antipodal Vivaldi antenna (AVA) by an additional single elliptical loaded strip (SELS) is presented. The performance of the miniaturized antenna is evaluated by finite difference time domain (FDTD) technique, while its performance is also verified by finite element method (FEM). The computational time and cost of the two techniques are also compared to highlight the significance of the most suitable technique for miniaturization of the wideband antenna. It achieves ultra-wideband performance with lower cutoff frequency at 0.668 GHz and 19.52 % size reduction with suitable gain performance. The proposed compact antenna exhibits good performance in the sub-GHz and ultra-wideband (UWB) frequency ranges, which makes it a suitable candidate for low power energy harvesting systems as well as for ultra-wideband applications.

**Index Terms** – Antipodal Vivaldi antenna (AVA), compact, energy harvesting, sub-GHz, tapered slot antenna (TSA), ultra-wideband (UWB) applications, Vivaldi antenna.

## I. INTRODUCTION

Wireless remote-controlled systems for Internet of Things (IoT) are always appealing to everyone as they add ease to daily mankind's routine and also help in multi-tasking. IoT typically requires a wider frequency range, which can be provided by ultra-wideband antennas with extended ranges to sub-GHz frequency ranges. It has the benefit of extended frequency range and lower power consumption. Thus it is suitable for networking where a small amount of data is to be transmitted periodically such as in IoT networking [1], Chaos-based communication systems [2], RFID tagging, air quality network sensor devices [3], wireless drones and microphones. Therefore, an antenna that can cater to the high-frequency region as well as the sub-GHz band efficiently seems attractive for energy harvesting systems in low energy application systems.

Antipodal Vivaldi antenna (AVA) is one such family of antennas, which has promising potential to meet the need of the hour due its wide bandwidth, high directivity, better radiation efficiency and stable radiation pattern properties. This is the reason why AVA attracts the attention of researchers nowadays for energy harvesting applications [4, 5]. Efforts are being made to improve its performance and reduce the size of conventional Vivaldi antenna [6] and antipodal Vivaldi antenna [7] particularly for the sub-GHz frequency band. However, there is still need to improve its compactness for sub-GHz frequency ranges to make it more suitable candidate for energy harvesting applications.

Different flare shapes and tapering techniques [8, 9] nowadays are being practiced and proposed for the size reduction and performance enhancement of AVA. Printing of meta-material unit cells on either side of the substrate is helpful for improving gain and reducing antenna size and sidelobe levels [10, 11]. The gain performance of the antenna can also be improved by substrate integrated waveguide (SIW) structure [12] and the corrugation technique [13, 14], however, it increases the complexity level of fabrication. The resistance loading and slotting technique can also be helpful for antenna miniaturization and gain enhancement [15, 16]. However, most of these techniques are complex and size reduction of an AVA for sub-GHz applications is still challenging. Moreover, the computational time and cost for analysis of such wideband antennas make the task more difficult.

This paper presents a modified AVA design that uses the simple technique of loading elliptical shaped conducting strips for reducing the antenna size with comparable radiation and gain performance in the sub-GHz range without affecting its performance at higher frequencies. As the proposed technique affects only lower frequencies performance, so parametric analysis computational cost can be reduced significantly by limiting the analysis to lower frequencies only. Section II discusses the antenna configuration and design, section III presents

all the results and discussion and section IV presents conclusions of the study.

## II. ANTENNA DESIGN

A conventional AVA (CAVA) proposed in [8], is selected for its size reduction.

Initial aperture size  $D$  of a CAVA is an important parameter to decide its lower cutoff frequency  $f_L$  through an empirical relation given as [8]:

$$D = \frac{c}{f_L} \frac{1}{1.5\sqrt{\epsilon_r + 1}}. \quad (1)$$

In eqn (1),  $c$  is the velocity of light in free space and  $\epsilon_r$  is the relative permittivity of the dielectric substrate. The significance of the aperture size comes from the fact that, if it is less than the value obtained from eqn (1) then it affects negatively the broadband characteristics of the antenna [16]. The general expression for determination of the shape contour of a Vivaldi antenna is quoted as eqn (2):

$$y = \pm Ae^{px}. \quad (2)$$

While for better impedance characteristics, the slot is typically exponentially tapered [16] as per the eqn (3):

$$x = \begin{cases} w_1 - 0.5w_1e^{\alpha y} & \text{top layer,} \\ -w_1 + 0.5w_1e^{\alpha y} & \text{bottom layer.} \end{cases} \quad (3)$$

In eqn (3),  $w_1$  is the width of the feeding microstrip and  $\alpha$  is the exponential rate of transition and is determined by the eqn (4):

$$\alpha = \frac{1}{l_{eff}} \ln \frac{w_1 + 0.5D}{0.5w_1}, \quad (4)$$

where  $l_{eff}$  is the effective radiation length.

All the design parameters for CAVA are summarized in Table 1. All the dimensions are measured in millimeters.

The CAVA has a lower cutoff frequency of 0.83 GHz. Its size is  $0.446 \lambda_L \times 0.387 \lambda_L$ , where  $\lambda_L$  is the wavelength in free space at the lowest cutoff frequency.

The surface current distribution analysis for CAVA played important role to modify its structure to shift lower cutoff frequency towards left without changing its aperture size. The surface current distributions for CAVA at 0.69 GHz and 2.5 GHz are illustrated in Fig. 1. It can be seen that the surface current density is accumulated at the lower curves of the radiating flares as well as around the slot between the two flares at 0.69 GHz. However, the surface current distribution at 2.5 GHz and higher frequencies is focused only around the slot between the two flares and no significant current can be seen at the lower curves of both the flares. It shows that lower curves of both the flares have a significant role to decide the lower cutoff frequency of CAVA. So, any possible way to increase the electrical path of the current along the lower curve of the flare may help to shift the lower cutoff fre-

Table 1: Antenna design parameters

Parameter	Value	Parameter	Value
<b>CAVA</b>			
$L_{sub}$	161.25	$x_1$	2.975
$W_{sub}$	140	$y_1$	60
$f_{r1}$	32.5	$x_2$	10
$f_{r2}$	42.25	$y_2$	70
$t_{r1}$	43.2	$x_3$	33.5
$t_{r2}$	27	$y_3$	72.75
$D$	132	$x_4$	33.5
$Sep$	67	$y_4$	115
$L_b$	8	$L_2$	10
$W_b$	60	$W_2$	5.95
$L_1$	7.5	$L_3$	42.5
$W_1$	4.65	$L_4$	12.75
<b>SELS-AVA</b>			
$a_{r1}$	15	$x_5$	33.5
$a_{r2}$	37	$y_5$	45

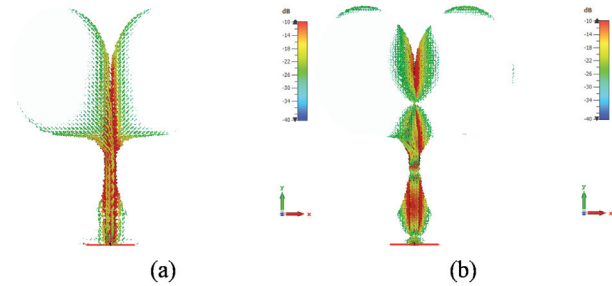


Fig. 1. The surface current distribution of CAVA at (a) 0.69 GHz and (b) 2.5 GHz.

quency of CAVA towards the left without any increase in its aperture size.

### A. Modified CAVA configuration

An elliptical conducting strip is loaded on lower curves of both the flares of CAVA to shift its lower cutoff frequency towards the left. As the strips are loaded to the lower curves of the flares of CAVA at which it has appreciable current density for low frequencies. Therefore, it helps to increase the electrical length of the antenna at low frequencies. The modified CAVA is named SELS-AVA and is presented in Fig. 2.

While loading the CAVA with additional strips, the antenna symmetry is kept intact. The center of the loaded strip is  $(x_5, y_5)$  and its major and minor axes are  $a_{r1}$  and  $a_{r2}$ , respectively. Both the strips are the mirror image of one another, just like the radiating flares of CAVA.

The added strips are chosen to be elliptical rather than rectangular or some other staircase shape to achieve continuous wideband coverage at lower frequencies too. The curved boundaries of elliptical strips are suitable

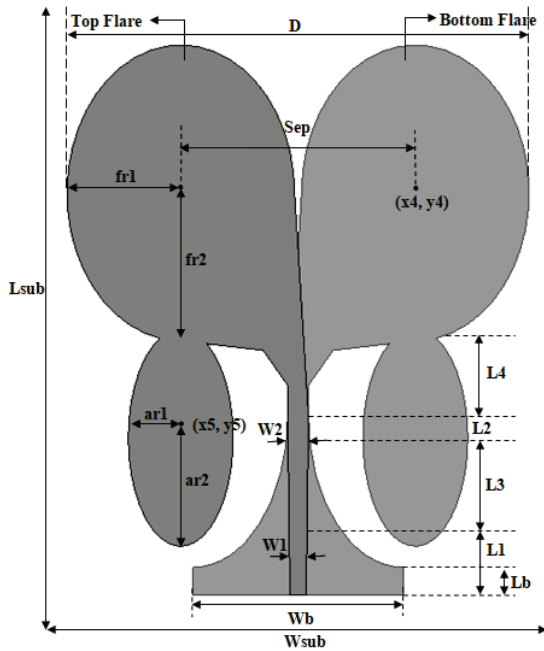


Fig. 2. Schematic of the SELS-AVA design.

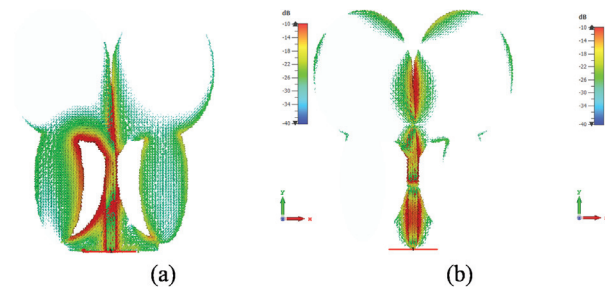


Fig. 3. The surface current distribution of SELS-AVA at (a) 0.69 GHz and (b) 2.5 GHz.

for wideband coverage with consistent impedance bandwidth.

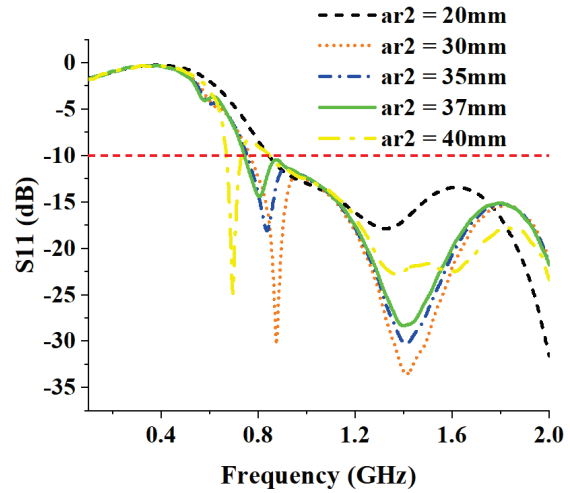
FDTD modeling is adapted to the curved boundaries of the conducting regions by employing perfect boundary approximation (PBA). The PBA works on the fact that the path for integration needed for the numerical solution of Maxwell’s equations within each mesh cell, can be chosen to conform to the geometry of the object inside the cell rather than to its edges or faces.

The surface current distributions for optimized SELS-AVA at the frequencies of 0.69 GHz and 2.5 GHz are revealed in Fig. 3. At lower frequency, it can be seen that the electrical path for the current is significantly increased due to elliptical loaded strips, while the loaded strips have almost no contribution at the higher frequencies. As the frequency increases, the maximum surface current density focuses only on the central region of the

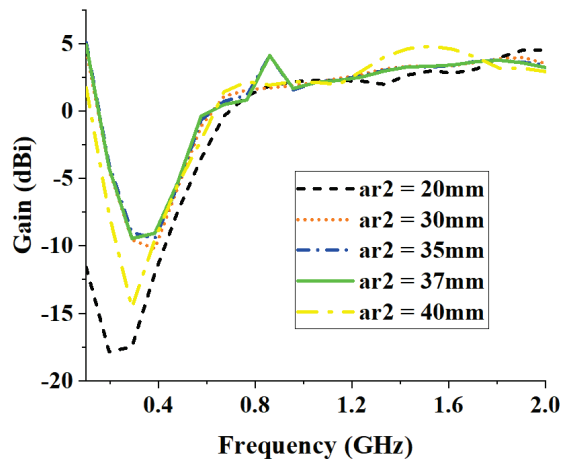
antenna. It shows that the additional strips affect only performance at lower frequencies and causes to shift the lower frequency toward the left and hence contributing to miniaturize the aperture size of the antenna. So, for parametric analysis, the frequency range can be limited to only the sub-2GHz frequency band to reduce its computational cost.

**B. Parametric analysis**

The SELS-AVA design is analyzed for different values of  $a_{r1}$  and  $a_{r2}$  only in the sub-2 GHz frequency band to reduce the computational cost. The sub-2GHz response of SELS-AVA is elaborated in Fig. 4, in terms of its return loss and gain by varying the  $a_{r2}$  parameter while keeping the  $a_{r1}$  constant. It can be seen that the lower cut-off frequency can be shifted towards the left by

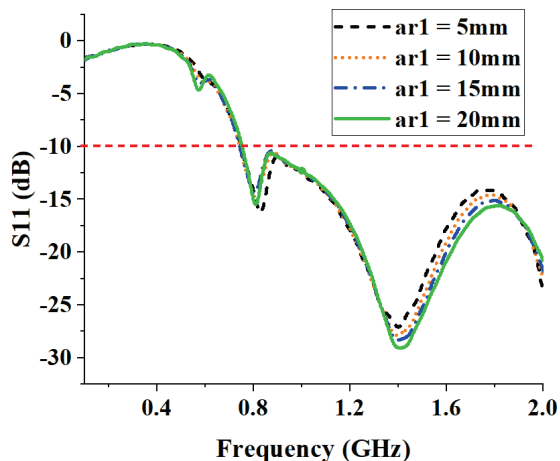


(a)

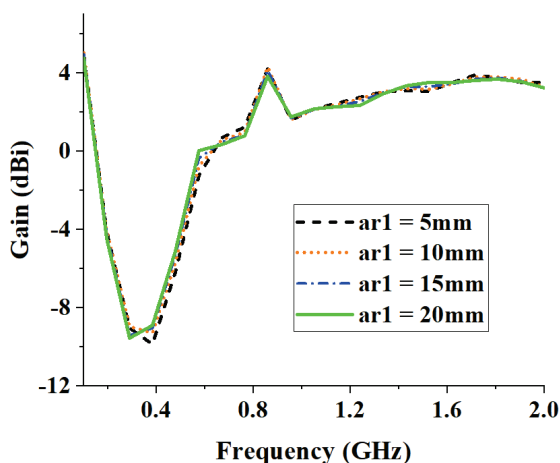


(b)

Fig. 4. SELS-AVA response for varying  $a_{r2}$  and constant  $a_{r1}$ : (a) return loss and (b) gain.



(a)



(b)

Fig. 5. SELS-AVA response for varying  $a_{r1}$  and constant  $a_{r2}$ . (a) Return loss and (b) gain.

increasing  $a_{r2}$ . However, if the value of  $a_{r2}$  is increased by more than 40 mm then a narrow-band notch is started to create at about 800 MHz.

Similarly, the effect of varying  $a_{r1}$  while keeping  $a_{r2}$  constant on the return loss and gain in the sub-2GHz band is explained in Fig. 5. Varying  $a_{r1}$  has a negligible effect on the lower cutoff frequency and gain performance. After the detailed parametric analysis of SELS-AVA parameters, the optimum values of  $a_{r1}$  and  $a_{r2}$  are finalized and listed in Table 1.

### III. COMPUTATIONAL PERFORMANCE AND DISCUSSION

The addition of conducting strips contributes to extend the lower frequency range. The return loss of SELS-AVA is compared with that of CAVA and is plotted in Fig. 6. It can be seen that the lower cut-off frequency for

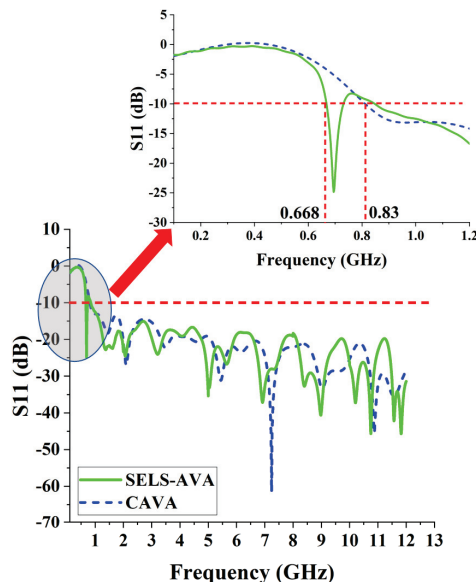


Fig. 6. Simulated return loss of CAVA and SELS-AVA.

SELS-AVA is 0.668 GHz as compared to 0.83 GHz for CAVA. So the size is reduced to  $0.359 \lambda_L \times 0.312 \lambda_L$ , which is a 19.5% size reduction as compared to the size of CAVA.

In this study, the proposed design is simulated and evaluated using two different computational techniques, one is Finite Difference Time-Domain (FDTD) method and the other is the Finite Element Method (FEM). CST Microwave Studio is used to implement both the mentioned computational techniques. These computational techniques are also compared to highlight the significance of the most suitable technique for miniaturization of a wideband antenna (0.668 to more than 14 GHz) with a common PC (2.59 GHz Core i3 processor with 8 GB memory).

Several simulations are carried out using FDTD with an increasing number of mesh cells until convergence is achieved. Table 2, lists the FDTD statistics of the simulations for the proposed SELS-AVA design.

The return loss for various mesh densities is shown in Fig. 7. It can be seen that the return loss is converged for greater than 2,500,911 hexahedral mesh cells and the lowest cutoff frequency is obtained at 0.668 GHz.

Similarly, the proposed design is analyzed using the FEM solver by increasing the number of tetrahedron mesh cells. The FEM computation statistics for various mesh densities are summarized in Table 3 and corresponding results for return loss are plotted in Fig. 8. It can be seen that the FEM takes appreciably long computation duration for wideband simulations as the mesh

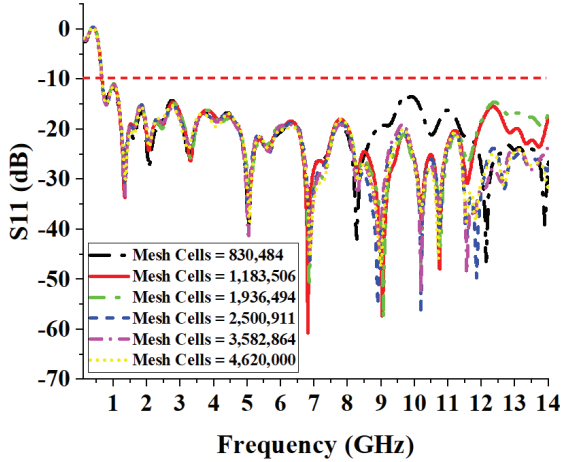


Fig. 7. Return loss of SELS-AVA for varying mesh density using FDTD.

Table 2: FDTD statistics for SELS-AVA in wideband

Cells per wavelength near the model	Smallest cell size (mm)	Largest cell size (mm)	Total hexahedral cells	Run time (M:S)
5	0.524933	3.54365	830,484	3:29
6	0.49375	3.54365	1,183,506	7:53
7	0.3937	2.65773	1,936,494	34:9
8	0.3937	0.265773	2,500,911	40:09
9	0.33333	2.12619	3,582,864	45:06
10	0.31496	2.12619	4,620,000	32:07

density increases and convergence is also really hard to achieve in this case.

As, FEM is considered a more efficient technique for narrow band applications, so, the proposed design is analyzed in narrow-band continuous chunks of the whole wide frequency band as shown in Table 4. This way to analyze a wideband antenna using FEM in small chunks of the wide frequency bands helps a lot to achieve converged results with considerably less computational cost as compared to FEM analysis for the whole frequency band in a single run; however, its computational cost is still higher than that of FDTD analysis. Therefore, FDTD is more computationally efficient than FEM for the analysis of the proposed SELS-AVA. However, the computational cost of FEM can also be reduced significantly by its analysis in small continuous chunks of the whole frequency band instead of analysis for the whole frequency band in a single run.

The comparison of the converged return loss curves for FDTD and FEM analysis for the proposed antenna is shown in Fig. 9. It can be seen that the return loss

Table 3: FEM statistics for SELS-AVA in wideband

Max. no. of passes	Min edge length	Max edge length	Average quality	Total tetrahedrons	Run time (H:M:S)
5	0.0608401	9.67442	0.755319	280,804	00:30:51
6	0.029147	9.49687	0.757769	446,414	00:17:41
7	0.0274142	9.51305	0.759502	611,627	00:15:11
15	0.0153071	9.44517	0.7606	799,307	21:44:42

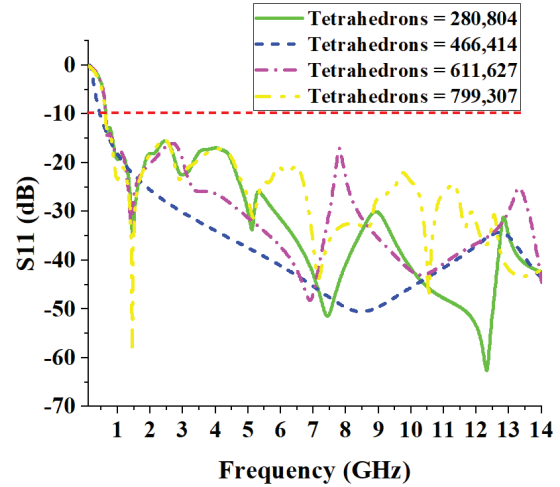


Fig. 8. Return loss for SELS-AVA with varying mesh density using FEM.

curves for both the computational techniques are in close agreement.

The simulated gain of the proposed SELS-AVA is compared with that of CAVA in the Fig. 10. The peak gain offered by CAVA and SELS-AVA is 9.1 dBi and 9.5 dBi respectively. Although the peak gains offered by the two designs are similar, however, the performance of proposed antenna also exhibits suitable gain in sub-GHz frequency ranges.

The proposed SELS-AVA is compared with some other recent AVAs presented in the literature. The comparison is summarized in Table 5. The comparison is in terms of the operational frequency range, dielectric used,

Table 4: FEM statistics for SELS-AVA in small chunks of the frequency band

Frequency bands (GHz)	Max no. of passes	Total tetrahedrons	Run time (M:S)
0.1 – 2	8	26,938	00:03
2 – 5	8	39,993	01:25
5 – 8	8	90,214	16:53
8 – 10	8	123,306	06:35
10 – 12	8	111,993	05:13
12 – 14	8	227,263	06:34

Table 5: Comparison of proposed SELS-AVA with some other AVAs in literature

Ref.	Frequency band (GHz)	Size ( $\lambda_L$ x $\lambda_L$ )	$\epsilon_r$	Gain (dBi)
[8]	0.83 – 9.8	0.446 x 0.39	2.33	9.1
[12]	11.02 – 40	0.84 x 0.367	2.2	2.15 – 5.75
[11]	3 – 10.6	0.45 x 0.486	4.4	8.45
[17]	5.2 – 40	0.66 x 0.68	2.2	0.6 – 13.9
[10]	25 – 33.4	0.67 x 0.4	4.4	5 – 9.53
[9]	1.14 – 2.6	0.6 x 0.5	4.15	8.2
SELS-AVA	0.668 – 20+	0.359 x 0.31	2.65	9.4

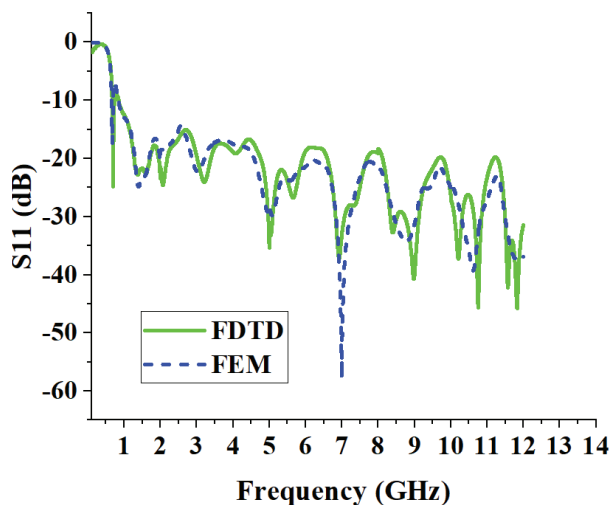


Fig. 9. Comparison of return loss curves for FDTD and FEM.

antenna size, and gain. It can be seen that the proposed technique achieves size reduction in the sub-GHz frequency band with a very simple technique and its performance is also comparable with existing techniques.

#### IV. CONCLUSION

In this work, computational analysis for miniaturization of the conventional AVA using FDTD and FEM is presented. The size of the conventional antenna is reduced intuitively by increasing the electrical path of the current by loading elliptical strips at the point, which has a maximum current density at lower frequencies, only. The size of the proposed SELS-AVA design is  $0.359 \lambda_L$  x  $0.312 \lambda_L$ , which is 19.5 % smaller as compared to the size of CAVA. The gain of the proposed SELS-AVA design is 1.3 – 2.2 dBi in the sub GHz range of 0.668 – 1 GHz and an appreciable gain level over the entire operating range otherwise. The proposed design is simulated

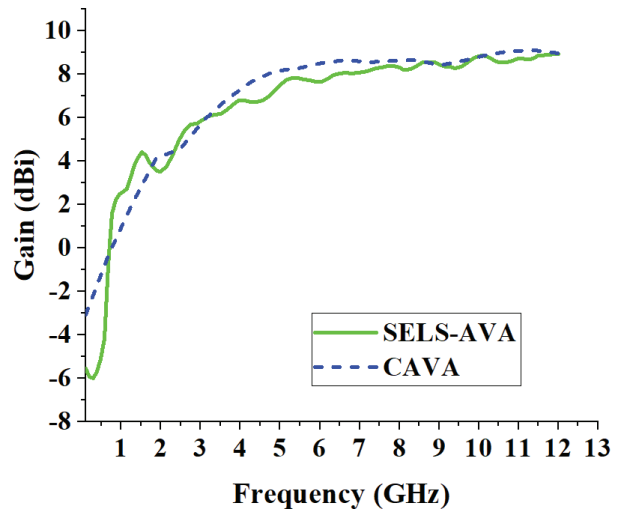


Fig. 10. Simulated gain of SELS-AVA in comparison with CAVA.

in FDTD and FEM solver and the results are counter-verified. The FDTD is a more efficient way to analyze the proposed antenna with less computational and memory resources. However, FEM can also be used efficiently for analysis and verification of the results of such antenna with a common PC if the analysis is carried out in small continuous chunks of the whole frequency band instead of the analysis for the whole frequency band in a single run. The antenna performance, compact size, and non-complexity make it a good addition to the antenna family for ultra-wideband applications and sub-GHz applications.

#### REFERENCES

- [1] S. Raksanta, P. P. Kumar, and P. Saxena, "A sub-1GHz rectangular dielectric resonator antenna for IoT," in *Proc. 2019 IEEE Int. WIE Con. Electr. Comp. Eng. (WIECON-ECE)*, pp. 1-4, IEEE, 2019.
- [2] M. Moundher, B. Hichem, T. Djamel, and S. Said, "Novel four-dimensional chaotic oscillator for sub-1GHz chaos-based communication systems," in *Proc. 2019 6th Int. Conf. Image Signal Process. Appl. (ISPA)*, pp. 1-5, IEEE, 2019.
- [3] A. Sharma, B. Mishra, R. Sutaria, and R. Zele, "Design and development of low-cost wireless sensor device for air quality networks," in *Proc. TENCON 2019-2019 IEEE Region 10 Conf. (TENCON)*, pp. 2345-2350, IEEE, 2019.
- [4] A. Benayad and M. Tellache, "Broad band rectenna based on Antipodal Vivaldi antenna and NULT rectifier," in *Proc. 2020 2nd Int. Workshop Human-Centric Smart Environ. Health Well-being (IHSH)*, pp. 40-43, IEEE, 2021.

- [5] K. N. Salim, M. R. Fairuzi, M. R. Sutoyo, and F. Y. Zulkifli, "Wideband Vivaldi microstrip antenna for rectenna application," in *Proc. 2020 Int. Seminar Intell. Technol. Its Appl. (ISITIA)*, pp. 317-320, IEEE, 2020.
- [6] D. Yang, S. Liu, and D. Geng, "A miniaturized ultra-wideband Vivaldi antenna with low cross polarization," *IEEE Access*, vol. 5, pp. 23352-23357, 2017.
- [7] M.-A. Boujemaa, R. Herzi, F. Choubani, and A. Gharsallah, "UWB Antipodal Vivaldi antenna with higher radiation performances using metamaterials," *Appl. Phys. A*, vol. 124, no. 10, pp. 1-7, 2018.
- [8] J. Y. Siddiqui, Y. Antar, A. Freundorfer, E. Smith, G. Morin, and T. Thayaparan, "Design of an ultra-wideband antipodal tapered slot antenna using elliptical strip conductors," *IEEE Antennas Wireless Propag. Lett.*, vol. 10, pp. 251-254, 2011.
- [9] A. Loutridis, S. Kazıcı, O. V. Stukach, A. B. Mirmanov, and D. Caratelli, "A novel class of super-elliptical Vivaldi antennas for ultra-wideband applications," *Adv. Radio Frequency Antennas Modern Commun. Medical Syst.*, 2020.
- [10] A. S. Dixit and S. Kumar, "The enhanced gain and cost-effective Antipodal Vivaldi antenna for 5G communication applications," *Microw. Opt. Technol. Lett.*, vol. 62, no. 6, pp. 2365-2374, 2020.
- [11] S. Guruswamy, R. Chinniah, and K. Thangavelu, "Design and implementation of compact ultra-wideband Vivaldi antenna with directors for microwave-based imaging of breast cancer," *Analog Integrated Circuits Signal Process.*, vol. 108, no. 1, pp. 45-57, 2021.
- [12] J.-Y. Deng, R. Cao, D. Sun, Y. Zhang, and L.-X. Guo, "Bandwidth enhancement of an Antipodal Vivaldi antenna facilitated by double-ridged substrate-integrated waveguide," *IEEE Trans. Antennas Propag.*, vol. 68, no. 12, pp. 8192-8196, 2020.
- [13] Z.-F. Yin, X.-X. Yang, and T. Lou, "A high gain UWB Vivaldi antenna loaded with elliptical slots," in *Proc. 2018 Int. Appl. Comput. Electromagn. Soc. Symp.-China (ACES)*, pp. 1-2, IEEE, 2018.
- [14] M. A. Ashraf, K. Jamil, A. Sebak, M. Shoaib, Z. Alhekail, M. Alkanhal, and S. Alshebeili, "Modified Antipodal Vivaldi antenna with shaped elliptical corrugation for 1-18 GHz UWB application," *Appl. Comput. Electromagn. Soc. J. (ACES)*, pp. 68-77, 2015.
- [15] Y. Zhu, D. Su, W. Xie, Z. Liu, and K. Zuo, "Design of a novel miniaturized Vivaldi antenna with loading resistance for ultra wideband (UWB) applications," *Appl. Comput. Electromagn. Soc. J. (ACES)*, pp. 895-900, 2017.
- [16] J. Bai, S. Shi, and D. W. Prather, "Modified compact antipodal Vivaldi antenna for 4-50-GHz UWB application," *IEEE Trans. Microw. Theory Techn.*, vol. 59, no. 4, pp. 1051-1057, 2011.
- [17] Z. Yin, X.-X. Yang, F. Yu, and S. Gao, "A novel miniaturized antipodal Vivaldi antenna with high gain," *Microw. Opt. Technol. Lett.*, vol. 62, no. 1, pp. 418-424, 2020.

# Advanced Numerical and Experimental Analysis of Ultra-Miniature Surface Resonators

Yakir Ishay, Yaron Artzi, Nir Dayan, David Cristea, and Aharon Blank

Schulich Faculty of Chemistry  
Technion - Israel Institute of Technology, Haifa, 3200003, Israel  
yakir387@gmail.com, yaron160@gmail.com, nirdayan11@gmail.com, cristea.david@gmail.com,  
ab359@technion.ac.il

**Abstract** – Many scientific and technological applications make use of strong microwave fields. These are often realized in conjunction with microwave resonators that have small geometric features in which such fields are generated. For example, in magnetic resonance, large microwave and RF magnetic fields make it possible to achieve fast control over the measured electron or nuclear spins in the sample and to detect them with high sensitivity. The numerical analysis of resonators with small geometric features can pose a significant challenge. This paper describes a general method of analysis and characterization of surface microresonators in the context of electron spin resonance (ESR) spectroscopy and spin-based quantum technology. Our analysis is based on the Electric Field Integral Equation (EFIE) and the Poggio-Miller-Chang-Harrington-Wu-Tsai (PMCHWT) formulation. In particular, we focus on a class of resonator configurations that possesses extremely small subwavelength features, which normally would require an ultra-fine mesh. We present several efficient techniques to numerically model, solve, and analyze these types of configurations for both normal and superconducting structures. The validation of these techniques is established both numerically and experimentally by the  $S_{11}$  parameters as well as the provision of direct mapping of the resonator's microwave magnetic field component using a unique electron spin resonance micro-imaging method.

**Index Terms** – electric field integral equation, electron spin resonance, surface resonators.

## I. INTRODUCTION

Surface microresonators belong to a subclass of planar printed resonators [1]. They constitute a key component in many scientific and technological applications ranging from filters [2] and oscillators [3] for analog and digital communications to building blocks for metamaterials [4] and including quantum technology [1, 6]. Essentially, this is a result of the richness of resonator

topologies, which can be generated and rendered optimal for various uses. Indeed, recent advances in fabrication techniques [7] and lower manufacturing costs allow designing such surface resonator configurations to obtain the desired microwave (MW) field distribution in a certain bandwidth (BW).

One of the emerging fields of application of surface resonators is magnetic resonance and specifically electron spin resonance (ESR) [8]. This method makes use of such resonators to focus the microwave magnetic field component on a small region in space [9], thereby increasing the effectiveness, and especially the sensitivity, of ESR [10, 11]. The capability to generate specific MW magnetic field patterns can be useful in a variety of ESR applications such as the detection and imaging of defects on the surface and subsurface of semiconductors [12], measurements of paramagnetic monolayers [13], and the inspection of small biological systems [14]. Many types of ESR surface resonators are often comprised of a mixed structure of metallic and dielectric parts and characterized by areas with small geometric features that can range from  $0.01 \lambda$  to even  $10^{-6} \lambda$ , where  $\lambda$  is the operating wavelength. In terms of full Electromagnetic (EM) simulation, this results in an ultra-fine mesh in and around these areas. Therefore, achieving an accurate numerical solution presents a difficulty that in many applications, and especially in ESR, may be critical. Primarily, this is because the system's ultimate performance is determined by the resonator's properties such as its filling factor [15]:

$$\eta_f = \frac{\int_{Sample} |\mathbf{H}_t|^2 dv}{\int_{Resonator} |\mathbf{H}|^2 dv},$$

where  $\mathbf{H}_t$  is the component of the MW magnetic field that is tangential to  $\mathbf{B}_0$ , the direction of the static field, and  $|\mathbf{H}|$  is the modulo of the MW magnetic field. This means that finding  $\eta_f$  requires an accurate solution of the resonant MW fields all over the resonator, both near and far from its core.

Another difficulty originates in the inclusion of a long (several wavelengths) excitation device (typically a microstrip line), which further amplifies the need to address the challenge of having objects with dimensions spanning many orders of magnitude with respect to  $\lambda$ . Our experience has shown that for these types of EM problems, leading commercial EM solvers such as CST or HFSS, which are based on the Finite Difference Time Domain (FDTD) [16], or Finite Element Method (FEM) [17], frequently fail to achieve a numerical solution with the desired degree of accuracy within a reasonable time frame. Essentially, this is because such a solution requires a very fine mesh across most of the volume defined by the boundary box. Numerical solvers based on Method of Moments (MoM) [18] and Surface Integral Equation (SIE) [19] methods can solve this obstacle given that once the surface currents are known, it is possible to have accurate data throughout the entire space. Yet, naively employing MoM solvers is not sufficient, in particular for configurations of surface resonators with an overall size of  $\sim 0.1 \lambda$  that have  $10^{-5} \lambda$  features whose numerical solution involves solving a matrix system with an extremely high condition number ( $10^{11}-10^{15}$ ).

Here, we present a numerical MoM-SIE solver based on the Electric Field Integral Equation (EFIE) [20] and the Poggio-Miller-Chang-Harrington-Wu-Tsai (PMCHWT) [21, 22] formulation for general composite structures that have been optimized for EM problems involving the complex geometries common in the field of ESR surface resonators. This paper aims to present our advanced techniques for obtaining an accurate and efficient numerical solution to these challenging types of EM problems while providing experimental validation of the theoretical results. The increased efficiency with respect to calculation time and memory usage is revealed when comparing our algorithm to the industry standard CST frequency domain and integral equation solvers. This efficiency is attributed to three main features of this work: (i) the achievement of reasonable condition numbers by applying proper model discretization, even for very fine physical features; (ii) the application of unique procedures for matrix system preconditioning; and (iii) the implementation of Impedance Boundary Conditions (IBC) to represent thin conductors as a surface impedance to exclude ultra-small elements that significantly increase the impedance matrix condition number and to account for lossy realistic structures.

## II. 2 EFIE-PMCHWT SURFACE INTEGRAL EQUATIONS

### A. Formulation

The EFIE-PMCHWT formulation applies the EFIE to open/closed metallic surfaces and the PMCHWT to dielectric domains [23]. Closed metallic surfaces can

also be treated with the Combined Field Integral Equation (CFIE) [24] to remove interior resonances. However, thin conductors are required to be modeled as open surfaces, either to make use of Impedance Boundary Conditions (IBC) [25] or because they practically cannot be modeled as closed surfaces, as explained in Section 3.2. Here, the EFIE-PMCHWT equations are reviewed with respect to the following EM scattering problem, illustrated in Fig. 1. Consider a time-harmonic regime with a time factor  $e^{j\omega t}$  and a primary or incident field ( $\mathbf{E}^{Inc}, \mathbf{H}^{Inc}$ ) illuminating domains  $D_c, D_1$  immersed in an unbounded background medium  $D_0$  whose impedance is  $\eta_0$ . Here,  $D_c$  represents a thin conductor modeled as an open surface  $S_c$  with surface impedance  $Z_s$ .  $S_c$  is assumed to have a radius of curvature that is large compared to the operating wavelength  $\lambda$ .  $D_1$  denotes a dielectric domain enclosed by a surface  $S_1$  with material properties  $\epsilon_1$  and  $\mu_1$ . Let  $\mathbf{E}^s$  and  $\mathbf{H}^s$  be the secondary microwave fields generated by  $\mathbf{J}$  and  $\mathbf{M}$  representing electric and magnetic surface currents, respectively. We define integral operators  $\mathbf{T}_i$  and  $\mathbf{K}_i$  associated with region  $i \in [0, 1]$ , acting on vector field  $\mathbf{F}$  across a surface  $S$ , by [20, 24]

$$\mathbf{T}_i(\mathbf{F}) = jk_i \hat{\mathbf{n}} \times \int_S \left( \mathbf{I} + \frac{\nabla \nabla}{k_i^2} \right) G_i(\mathbf{r}, \mathbf{r}') \mathbf{F}(\mathbf{r}') d\mathbf{r}', \quad (1)$$

$$\mathbf{K}_i(\mathbf{F}) = \hat{\mathbf{n}} \times \int_S \nabla G_i(\mathbf{r}, \mathbf{r}') \times \mathbf{F}(\mathbf{r}') d\mathbf{r}'. \quad (2)$$

Here,  $\hat{\mathbf{n}}_i$  is the surface normal of  $S$ ,  $G(\mathbf{r}, \mathbf{r}')$  is the Green's function of an infinite homogeneous medium with wavenumber  $k_i$  given by:

$$G_i(\mathbf{r}, \mathbf{r}') = \frac{e^{-jk_i |\mathbf{r} - \mathbf{r}'|}}{4\pi |\mathbf{r} - \mathbf{r}'|}, \quad (3)$$

and  $\mathbf{I}$  represents the identity operator.

For conductors with  $|Z_s| \ll \eta_0$ , the boundary condition on  $S_c$  can be approximated as [25]:

$$\mathbf{T}_0(\eta_0 \mathbf{J}) + Z_s \mathbf{J} \times \hat{\mathbf{n}} - \mathbf{K}_0(\mathbf{M}) = -\hat{\mathbf{n}} \times \mathbf{E}^{Inc}, \quad (4)$$

and on the surface  $S_1$  the boundary conditions read [21]:

$$\sum_{i=0}^1 \frac{\eta_i}{\eta_0} \mathbf{T}_i(\eta_i \mathbf{J}) - \sum_{i=0}^1 \mathbf{K}_i(\mathbf{M}) = -\hat{\mathbf{n}} \times \mathbf{E}^{Inc}, \quad (5)$$

$$\sum_{i=0}^1 \frac{\eta_0}{\eta_i} \mathbf{T}_i(\mathbf{M}) + \sum_{i=0}^1 \mathbf{K}_i(\eta_0 \mathbf{M}) = -\eta_0 \hat{\mathbf{n}} \times \mathbf{H}^{Inc}, \quad (6)$$

with  $\eta_i$  being the impedance of region  $i$ . Equation (4) represents the EFIE and (5) and (6) represent the PMCHWT.

### B. Discretization

The numerical solution is obtained by transforming the EFIE-PMCHWT equations (4), (5), and (6) into a matrix system. First,  $\mathbf{J}$  and  $\mathbf{M}$  are approximated in terms of vector basis functions:

$$\mathbf{J} = \sum_{n=1}^{N_c} a_n \mathbf{f}_n, \quad \mathbf{M} = \sum_{n=1}^{N_m} b_n \mathbf{f}_n, \quad (7)$$

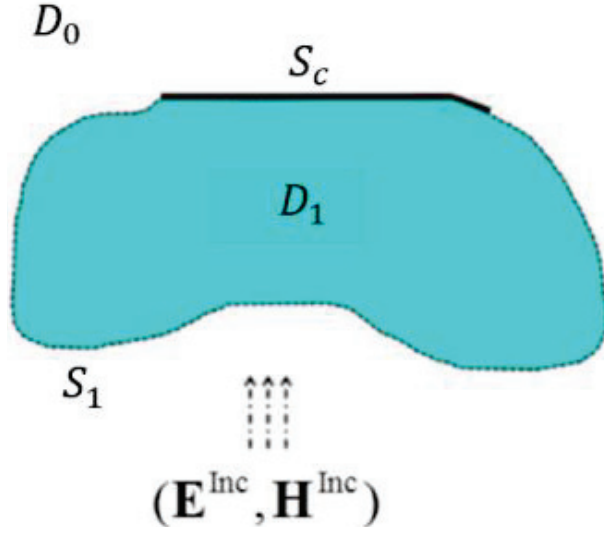


Fig. 1. Scattering by composite conductor and dielectric structures. The solid black line corresponds to an open surface  $S_c$  modeling a thin conductor associated with a domain  $D_c$ . The dashed line corresponds to a surface  $S_1$  enclosing a dielectric domain  $D_1$ .

where  $\mathbf{f}_n$  is the Rao-Wilton-Glisson (RWG) basis function [20] assigned to the edge  $e_n$  defined as (Fig. 2).

$$\mathbf{f}_n(\mathbf{r}) = \begin{cases} \frac{L_n}{2A_n^+} (\mathbf{r} - \mathbf{v}_n^+), & \mathbf{r} \in T_n^+ \\ \frac{L_n}{2A_n^-} (\mathbf{v}_n^- - \mathbf{r}), & \mathbf{r} \in T_n^- \\ 0, & \text{otherwise.} \end{cases} \quad (8)$$

Here,  $A_n^\pm$  is the area of the triangular patch  $T_n^\pm$ ,  $L_n$  is the length of the common edge  $e_n$ , and  $\mathbf{v}_n^\pm$  is the vertex of  $T_n^\pm$ . An RWG function domain is displayed in Fig. 2. The  $a_n$  and  $b_n$  parameters are associated with  $N_e$  unknown electric and  $N_m$  magnetic current amplitudes, respectively. The values of  $N_e$  and  $N_m$  are determined by the number of edges associated with each surface so that  $N_e$  corresponds to both conductor and dielectric surfaces  $S_c \cup S_1$ , whereas  $N_m$  applies only to  $S_d = S_1 \setminus S_c$ . The latter condition applies only for conductors with  $|Z_s| \ll \eta_0$ , where the magnetic edges lying in  $S_c$  are removed (note that for their correct removal, the meshes applied to opposite sides of the interface must be identical). To discretize the EFIE-PMCHWT equations, the Galerkin method is applied so that (4), (5), and (6) are tested using  $\{\mathbf{f}_{m1}, e_{m1} \in S_c\}$ ,  $\{\mathbf{f}_{m2}, e_{m2} \in S_1\}$ , and  $\{\mathbf{f}_{m3}, e_{m3} \in S_d\}$ , respectively. This procedure results in the following matrix equation:

$$\sum_{n=1}^{N_e} (ik_0\eta_0\mathbf{A}_{m1,0} + \mathbf{C}_{m1n})a_n + \sum_{n=1}^{N_m} \mathbf{B}_{m1n,0}b_n = V_{m2}^E, \quad (9)$$

$$\sum_{n=1}^{N_e} \sum_{i=0}^1 jk_i\eta_i\mathbf{A}_{m2n,i}a_n + \sum_{n=1}^{N_m} \sum_{i=0}^1 \mathbf{B}_{m2n,i}b_n = V_{m2}^E, \quad (10)$$

$$\sum_{n=1}^{N_m} \sum_{i=0}^1 jk_i\eta_i\mathbf{A}_{m3n,i}b_n - \sum_{n=1}^{N_e} \sum_{i=0}^1 \mathbf{B}_{m3n,i}a_n = V_{m3}^H, \quad (11)$$

Here we define:

$$\mathbf{A}_{mn,i} = \int_S \mathbf{f}_m(\mathbf{r}) \cdot \int_S \mathbf{f}_n(\mathbf{r}') G_i(\mathbf{r}, \mathbf{r}') d\mathbf{r}' d\mathbf{r} - \quad (12)$$

$$k_i^{-2} \int_S \nabla_S \cdot \mathbf{f}_m(\mathbf{r}) \int_S \nabla' S \cdot \mathbf{f}_n(\mathbf{r}') G_i(\mathbf{r}, \mathbf{r}') d\mathbf{r}' d\mathbf{r},$$

$$\mathbf{B}_{mn,i} = \int_S \mathbf{f}_m(\mathbf{r}) \cdot \int_S \mathbf{f}_n(\mathbf{r}') \times \nabla' G_i(\mathbf{r}, \mathbf{r}') d\mathbf{r}' d\mathbf{r}, \quad (13)$$

$$\mathbf{C}_{mn} = Z_s \int_S \mathbf{f}_m(\mathbf{r}) \cdot \mathbf{f}_n(\mathbf{r}) d\mathbf{r}, \quad (14)$$

$$V_m^E = \int_S \mathbf{f}_m(\mathbf{r}) \cdot \mathbf{E}^{\text{Inc}}(\mathbf{r}) d\mathbf{r}, \quad (15)$$

$$V_m^H = \int_S \mathbf{f}_m(\mathbf{r}) \cdot \mathbf{H}^{\text{Inc}}(\mathbf{r}) d\mathbf{r}. \quad (16)$$

Hence, the impedance matrix  $Z$  is of the form:

$$Z = \begin{bmatrix} Z_c^{EJ} & Z_c^{EM} \\ Z_d^{EJ} & Z_d^{EM} \\ Z_d^{HJ} & Z_d^{HM} \end{bmatrix}, \quad (17)$$

where the elements of the block matrices are:

$$\{Z_c^{EJ}\}_{m \in m_1, n=1 \dots N_e} = jk_0\eta_0\mathbf{A}_{m1,0} + \mathbf{C}_{m1n,0}, \quad (18)$$

$$\{Z_c^{EM}\}_{m \in m_1, n=1 \dots N_m} = \mathbf{B}_{m1n,0}, \quad (19)$$

$$\{Z_d^{EJ}\}_{m \in m_2, n=1 \dots N_e} = \sum_{i=0}^1 jk_i\eta_i\mathbf{A}_{m2n,i}, \quad (20)$$

$$\{Z_d^{EM}\}_{m \in m_2, n=1 \dots N_m} = \sum_{i=0}^1 \mathbf{B}_{m2n,i}, \quad (21)$$

$$\{Z_d^{HJ}\}_{m \in m_3, n=1 \dots N_e} = \sum_{i=0}^1 -\mathbf{B}_{m3n,i}, \quad (22)$$

$$\{Z_d^{HM}\}_{m \in m_3, n=1 \dots N_m} = \sum_{i=0}^1 \frac{jk_i}{\eta_i} \mathbf{A}_{m3n,i}. \quad (23)$$

The evaluation of the double integrals (12) to (16) is performed using the singularity subtraction technique with closed-form integral representations [26].

### III. SIMULATION OF ESR RESONATOR CONFIGURATIONS

#### A. Model

ESR surface resonators typically operate in the range of 1–100 GHz where their size is, in most cases, much smaller than the resonant wavelength. Figure 3 shows a typical layout of the “ParPar” (“butterfly” in Hebrew) surface resonators we have recently developed [27]. It consists of a thin (50–500 nm) butterfly-shaped conductor (either normal or superconductor) printed on a thick (100–500  $\mu\text{m}$ ) dielectric substrate whose width/length is typically 1.2 – 1.6 mm. The bridge (at the center of Fig. 3 (a)) is chosen so that it maximizes the magnetic field in a particular region of thin ( $\leq 200 \mu\text{m}$ ) samples that cover the resonator plane

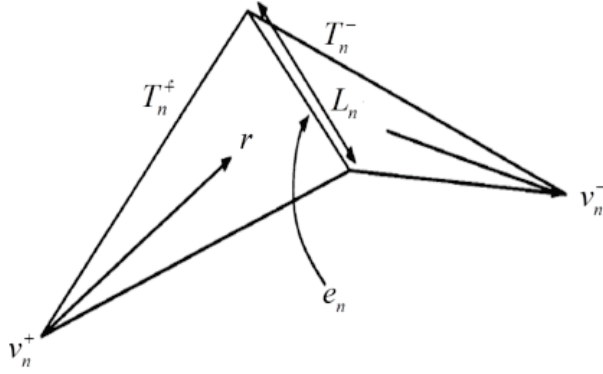


Fig. 2. An RWG function  $\mathbf{f}_n$  composed of a pair of triangular patches  $T_n^{+}$  and  $T_n^{-}$  common to the  $n^{\text{th}}$  edge  $e_n$ .

(i.e., the substrate's upper plane). The resonators are inductively coupled by a microstrip line placed 10 – 300  $\mu\text{m}$  below the substrate's bottom plane, where critical (optimal) coupling [28] can be achieved by moving the resonator in the x-y plane (Fig. 3 (b)). The microwave configuration composed of a surface resonator and a microstrip transmission line can be represented by the equivalent circuit shown in Fig. 4.

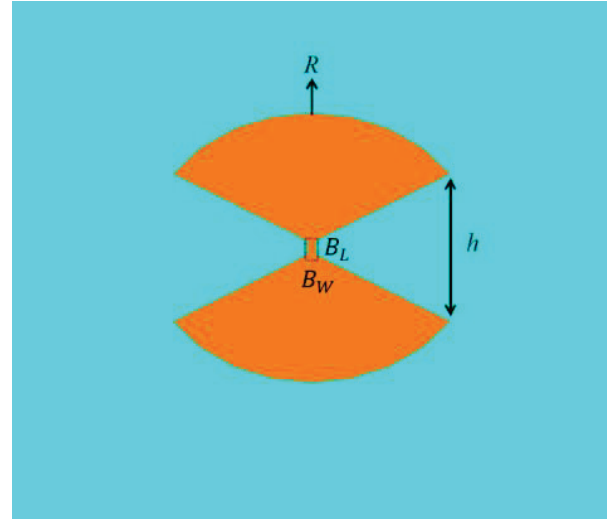
## B. Boundary conditions

Common ESR surface resonators consist of extremely thin conductors (including those associated with the microstrip) whose thickness  $t_s$  can be smaller than the penetration depth  $\Delta$  for normal conductors (e.g., copper, silver, etc.) and the London penetration depth  $\Delta$  [29] for superconductors<sup>1</sup>. As a result, the use of Impedance Boundary Conditions (IBC) is critical because modeling the conductors as closed surfaces might result in ill-conditioned matrix systems, as explained in detail in the following subsection. The implementation of IBC is performed using the single sheet model [30], in which the conductor is modeled as a single sheet with the appropriate surface impedance  $Z_s$ . The value of  $Z_s$  depends on the type of conductor (normal or superconductor) used. In the case of normal conductors, the surface impedance is given by [30]:

$$Z_s = \frac{\kappa e^{\kappa t_s} + \frac{\sigma\eta - \kappa}{\sigma\eta + \kappa} e^{-\kappa t_s}}{\sigma e^{\kappa t_s} - \frac{\sigma\eta - \kappa}{\sigma\eta + \kappa} e^{-\kappa t_s}}, \quad (24)$$

where  $\eta$  is the medium impedance,  $\sigma$  is the complex conductivity, and  $\kappa = (1+j)\sqrt{(\omega\mu\sigma)/\sqrt{2}}$ .

<sup>1</sup> The term "superconductors" refers here to materials that exhibit zero DC conductivity at low temperatures and have finite RF surface resistance, such as YBCO or Nb, and not to PEC. Moreover, even if the metals are considered to be PEC at DC, from the physical point of view, conductors whose thickness is smaller than the corresponding penetration depth can no longer be treated as perfect electric/magnetic conductors.



(a)



(b)

Fig. 3. ESR microwave configuration. (a) General layout of the ParPar surface resonator. The dashed rectangular line indicates the bridge whose length and width are  $B_L$  and  $B_W$ , respectively. The arcs' radii  $R$  and  $h$  denote the complementary physical characteristics of the ParPar resonator. (b) Excitation of ParPar by a microstrip line.

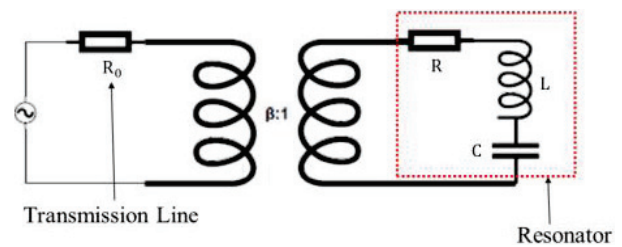


Fig. 4. Equivalent circuit for ESR microwave configuration. The microstrip line and surface resonator are represented by the elements  $R_0$  and  $R$ ,  $L$ , and  $C$ , respectively.  $\beta$  denotes the inductive coupling coefficient.

For superconductors, the surface impedance is [30]:

$$Z_s = j\omega\mu\lambda_L \frac{e^{t_s/\lambda_L} + \frac{\eta - j\omega\mu\lambda_L}{\eta + j\omega\mu\lambda_L} e^{-t_s/\lambda_L}}{e^{t_s/\lambda_L} - \frac{\eta - j\omega\mu\lambda_L}{\eta + j\omega\mu\lambda_L} e^{-t_s/\lambda_L}}. \quad (25)$$

The single sheet model can also be applied to either planar or non-planar surfaces whose radii are much greater than the operating wavelength.

Note that regardless of the type of conductor used, the underlying assumption of the boundary impedance model is that the corresponding penetration depth is not much greater than the conductor's thickness [30]. In this paper, we focus on structures fabricated out of planar normal conductors, while our latest paper [31] deals with resonators made of a superconducting material.

### C. Impedance matrix preconditioning and inversion

As mentioned in the previous subsection, the use of IBC alleviates the need for solving ultra-small elements (compared to the operating wavelength) resulting from the inclusion of thin finite conductors. Mathematically, the presence of small elements gives rise to an impedance matrix whose condition number grows as  $(k\delta_a)^{-2}$  [32]. Here  $\delta_a$  is the weighted average edge length of the mesh so that smaller edges are given more weight. The increase in the condition number results mainly from the EFIE matrix system becoming severely ill-conditioned with increasing mesh density and decreasing element size. In cases where direct solvers cannot be applied (e.g., for large matrix systems), this eventually leads to slowly- or non-converging iterative solvers, namely a dense discretization breakdown [33]. In fact, the mesh applied to a specific model is of importance, and this is especially true for MoM-based integral equations solvers [34–36]. However, numerically solving a microwave configuration composed of an electrically large microstrip line and a small surface resonator possessing fine and localized geometric features still requires solving a large impedance matrix whose condition number is considerably high (e.g.,  $10^8$ – $10^{14}$  when solving typical ParPar layouts, as described above). Furthermore, the resulting MW fields are required to be very accurate within the sample volume and at least 1  $\mu\text{m}$  spatial resolution is necessary for resolving ultra-small samples (i.e., with volume  $\leq 1$  nL). Therefore, the impedance matrix must be preconditioned properly to improve its condition number and enable an accurate solution to the problem.

Theoretically, preconditioning can be based either on simple algebraic techniques, such as incomplete LU (ILU) factorization [37, 38] or approximate inverse preconditioners [39] or on a more physical class of preconditioners, such as the Calderon Multiplicative Preconditioner (CMP) [40]. On the one hand, under quasi-uniform discretization, Calderon identity-based preconditioners might result in a condition number whose upper bound can be independent of  $\delta_a$  [41], while algebraic preconditioners still exhibit a growing condition number as  $\delta_a$  decreases. On the other hand, CMP

might not be applicable to these types of problems for the following reasons: first, improving the condition number in the presence of a non-uniform mesh is not guaranteed, given that the CMP-EFIE method still suffers from an inaccuracy problem at low frequencies associated with quasi-static regions [42, 43], and imposing a uniform mesh is not practical, especially in complex ESR resonators geometries. Second, employing CMP for open surfaces is less effective because the condition number might grow similarly to the EFIE matrix system [44]. Third, for a matrix system that can be preconditioned algebraically, applying CMP can be a time-consuming procedure due to an excess in matrix-matrix and matrix-vector products. Fourth, CMP might not be trivially extended for EFIE-PMCHWT formulations, whereas an extra challenge is added by the inclusion of IBC. The latter also applies to other formulations, such as multiple-traces PMCHWT [45], that can lead to a well-conditioned impedance matrix in configurations comprising perfectly conducting objects.

As shown in Section IV.C below, a matrix preconditioned via an incomplete LU factorization can significantly improve its condition number. In particular, compared to the left ILU preconditioner, which multiplies the impedance matrix on the left, the right ILU preconditioner is much more efficient and provides exceptional iterative solver convergence speed: up to 30 GMRES iterations to achieve relative residuals  $< \min(10^{-6}, \text{condition number}^{-1})$  with respect to the unpreconditioned matrix system. Calculating the residual in this manner excludes either delayed or premature convergence associated with left preconditioners [46]. Typically, for condition numbers  $> 10^{11}$ , the left ILU becomes less practical due to slow convergence and an inaccurate numerical solution compared to the right ILU. Moreover, the standard diagonal preconditioner (DP) cannot resolve condition numbers  $\geq 10^8$  and results in non-convergence. Mathematically, solving configurations near resonance requires a substantial decrease in the matrix's high condition number, which cannot be achieved by decreasing the dominance of its diagonal alone. However, the DP can lower the condition number by 2–3 orders of magnitude; therefore, it can be applied prior to the left ILU preconditioner to enhance convergence.

As for the particular iterative solver to be used, there are several methods to choose from, including the generalized minimum residual (GMRES) method proposed by Saad and Schultz [47], the biconjugate gradient (BiCG) developed by Fletcher [48], the conjugate gradient squared (CGS) method proposed by Sonneveld [49], the transpose-free quasiminimal residual method (TFQMR) by Freund and Nachtigal [50], and van der Vorst's gradient stabilized (BiCGSTAB) [51] method. While they are applicable to our problems, GMRES

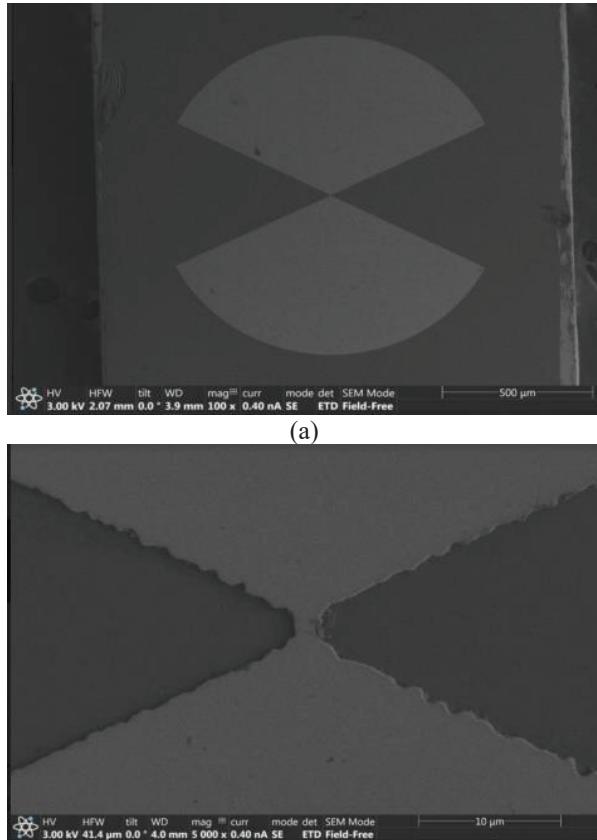


Fig. 5. SEM photos of ParPar2 surface resonators. (a) Low magnification. (b) High magnification.

with right ILU preconditioning has provided the fastest convergence. Accordingly, in this work, we employed GMRES with residue tolerance of  $\min(10^{-6}, \text{condition number}^{-1})$  following ILU factorization performed with pivoting (ILUP [47]) and drop tolerance of  $10^{-6}$ .

## IV. NUMERICAL & EXPERIMENTAL RESULTS

### A. ParPar topology

This section presents numerical and experimental results that demonstrate the time efficiency and the accuracy of our method to resolve complex ESR microwave resonator configurations. In particular, we show accurate near-field solutions that were validated via a sensitive and unique ESR microimaging setup. Three types of ParPar surface resonators were tested: ParPar50, ParPar20, and ParPar2, whose bridge sizes ( $B_W, B_L$  – see Fig. 3 (a)) are  $(25 \mu\text{m}, 50 \mu\text{m})$ ,  $(10 \mu\text{m}, 20 \mu\text{m})$ , and  $(1 \mu\text{m}, 2 \mu\text{m})$ , respectively. Each of these resonators consisted of a  $0.5 \mu\text{m}$ -thin copper metallization printed on  $\text{LaAlO}_3$  or silicon dielectric substrates ( $1.6 \text{ mm} \times 1.6 \text{ mm} \times 0.2 \text{ mm}$ ) with permittivity of  $\sim 24$  and  $\sim 11.5$ , respectively. The arcs' radii  $R$  (Fig. 3 (a)) were  $380 \mu\text{m}$  for the  $\text{LaAlO}_3$  substrate, and  $560 \mu\text{m}$  for the sil-

icon substrate. Figures 5 (a) and 5 (b) show the scanning electron microscope (SEM) photos of the ParPar2 resonator for illustration purposes. Coupling to the resonators was achieved via a  $0.46 \text{ mm}$ -wide microstrip line (RO4003 LoPro Series, Rogers Corp., thickness of  $0.22 \text{ mm}$ ) whose end was placed  $10 \mu\text{m}$ ,  $12 \mu\text{m}$ , and  $190 \mu\text{m}$  below the substrate's bottom plane for ParPar50, ParPar20, and ParPar2, respectively. Note that an inductive coupling to ParPar2 is much more challenging, considering the magnetic flux generated by the millimeter-scale microstrip line. The comparison between measured and calculated reflection coefficients  $S_{11}$  is presented in Figs. 6 and 7; in all cases (Figs. 6 (a) to 6 (c) and 7 (a) to 7 (c)), the resulting maximal relative error between the measured and calculated  $S_{11}$  is  $< 2\%$  in the resonance and  $< 5\%$  in the 3 dB BW. This fine agreement is definitely not trivial, in particular for the ParPar2 resonator whose structure was discretized with an average element  $\lambda/50$  in size (minimum edge length  $\delta_m$  of  $3 \times 10^{-5} \lambda$ ), resulting in a MoM matrix condition number of  $\sim 10^{13}$ . The calculated resonant magnetic field distributions for ParPar50, ParPar20, and ParPar2 geometries are presented in Figs. 8 (a) to 8 (c), respectively. Evidently, in all cases, the magnetic field is mostly localized in and around the bridge. The pattern of this mode can be verified via 2D ESR microimaging [52], considered to be a very sensitive method to reveal the intensity of the actual microwave magnetic field. Additional details about the ESR imaging procedure used in this work are provided in the Appendix. For example, results of the imaging experiments carried out with ParPar50 and ParPar2 (Fig. 9) showed that the desired mode is indeed excited in both cases.

### B. Impedance matrix preconditioning

In this section, we demonstrate our method's capability to solve the high condition number matrices resulting from the discretization of ParPar2 and ParPar20 surface resonators ( $\text{LaAlO}_3$  substrate). On both structures, the simulations were repeated for 11 non-uniform discretizations with an average edge length  $\delta_a$  that varied from  $0.02 \lambda_r$  to  $0.05 \lambda_r$ , corresponding to 4016 RWG functions for the largest  $\delta_a$  and 16248 for the smallest. Here,  $\lambda_r$  is the resonant wavelength at 36.3 GHz. For all discretizations, the minimum edge lengths were kept the same— $3 \times 10^{-5} \lambda_r$  and  $3 \times 10^{-4} \lambda_r$  for ParPar2 and ParPar20, respectively. Figure 10 (a) presents the resulting condition numbers of the EFIE-PMCHWT matrices for simulated ParPar2 and ParPar20. Regarding Fig. 10 (a), the minimum condition number ( $10^{12}$ ) of the ParPar2 impedance matrix is 2 orders of magnitude larger than the maximum condition number of the ParPar20 matrix. These results clearly suggest that discretizations having a lower  $\delta_m$ -to- $\delta_a$  ratio

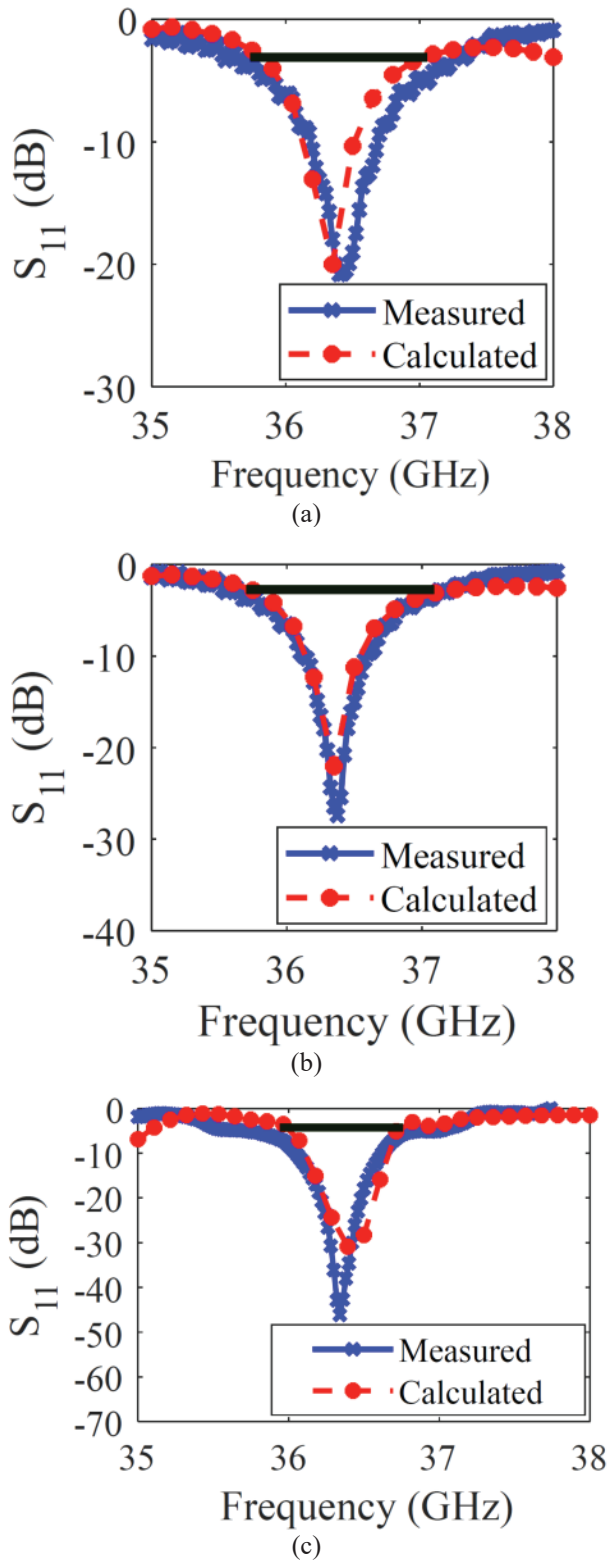


Fig. 6. Measured and calculated reflection coefficient  $S_{11}$  for  $\text{LaAlO}_3$  resonators. (a) ParPar50, (b) ParPar20, and (c) ParPar2.

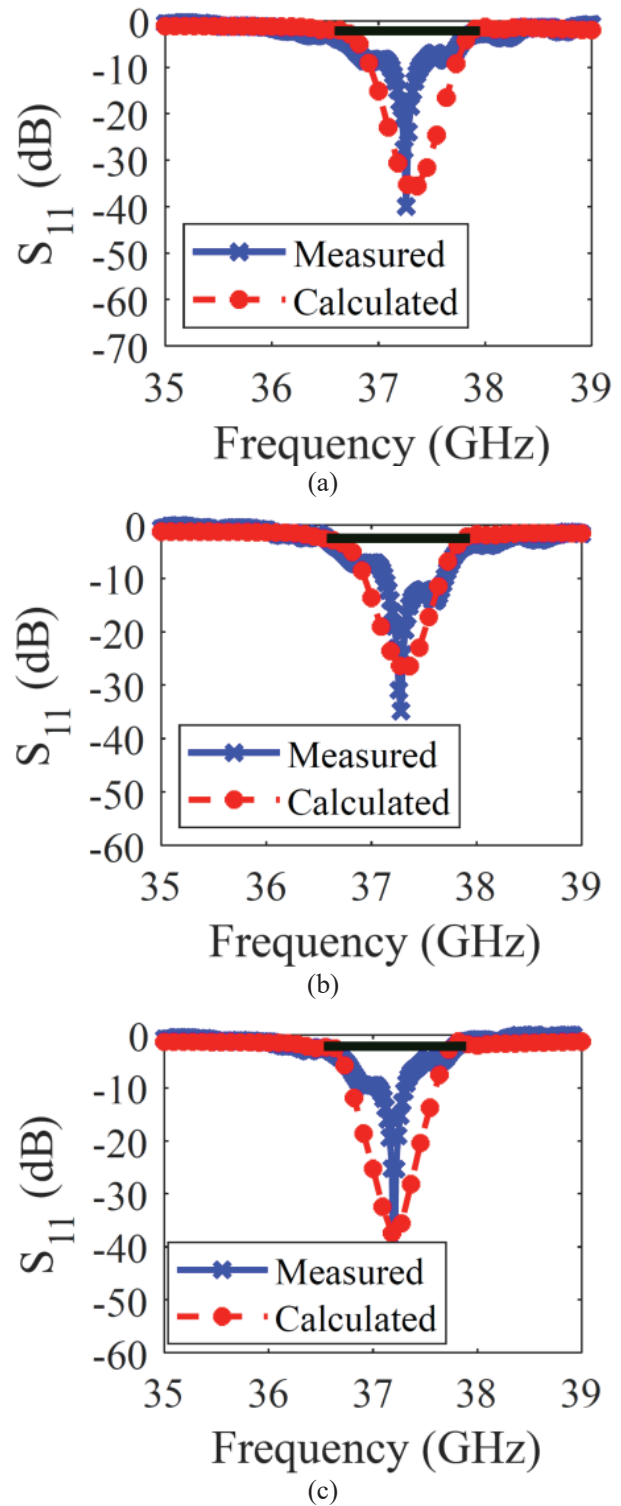


Fig. 7. Measured and calculated reflection coefficient  $S_{11}$  for silicon resonators. (a) ParPar50, (b) ParPar20, and (c) ParPar2.

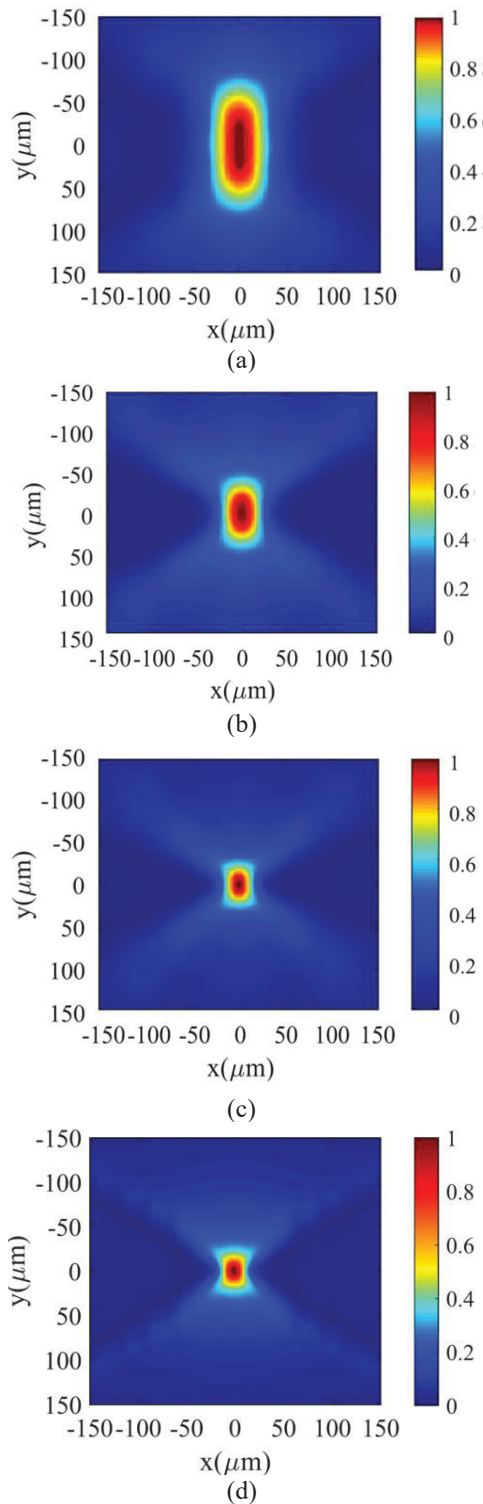


Fig. 8. Calculated normalized magnitude of resonant magnetic field distributions  $16 \mu\text{m}$ ,  $8 \mu\text{m}$ , and  $4 \mu\text{m}$  above the substrate's upper plane for (a) silicon-ParPar50, (b)  $\text{LaAlO}_3$ -ParPar20, and (c)  $\text{LaAlO}_3$ -ParPar2, respectively. (d) The corresponding CST results for  $\text{LaAlO}_3$ -ParPar2.

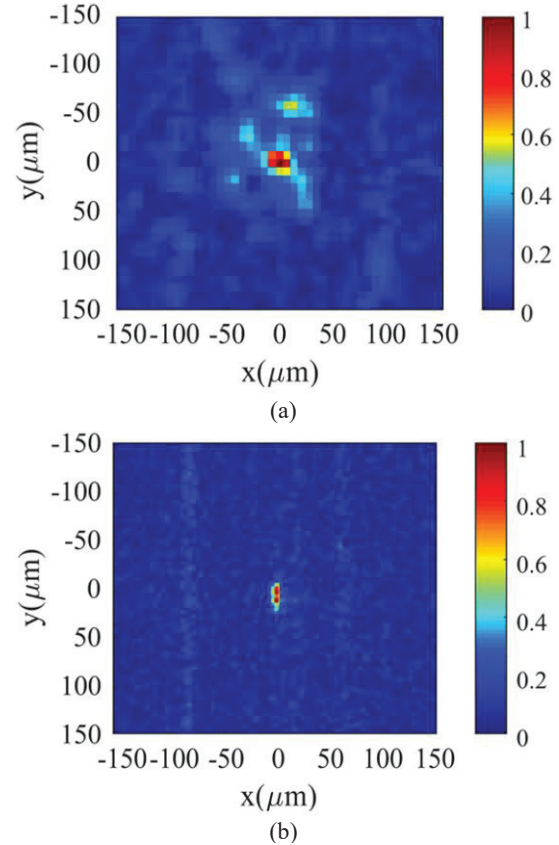


Fig. 9. Results of ESR microimaging carried out with (a) ParPar50 using a silicon substrate and (b) ParPar2 using  $\text{LaAlO}_3$ . Both resonators were covered completely by a sample consisting of paramagnetic microcrystals, which resulted in a non-uniform (grainy) mode image. A detailed description of the experiments can be found in the Appendix.

are significantly more susceptible to higher condition numbers than more uniform discretizations with smaller  $\delta_a$  values. In practical terms, this means that extra mesh refinements of subwavelength regions, which correspond to an excessive presence of smaller elements, can greatly impair the quality of the numerical solution. Figure 10 (b) presents the performance of the diagonal preconditioner (DP) with left and right ILU ILU applied to resolve the high condition numbers of the impedance matrix for the aforementioned discretizations of ParPar2. Applying the right ILU allows for the convergence of GMRES (relative residual  $< \text{condition number}^{-1}$ ) on every discretization, while the left ILU preconditioner becomes less effective for dense discretizations so that the GMRES residual gradually increases and surpasses  $10^{-6}$ . Thus, while memory usage for the left and right ILU were quite similar, the right ILU typically required  $< 15$  iterations to converge, for all

examined discretizations, whereas the left ILU resulted in  $\geq 30$  iterations and non-convergence (a stagnation of the GMRES) for condition numbers  $< 10^{12}$ , and  $\geq 10^{12}$ , respectively. Note that using DP alone could not resolve these high condition numbers, even for the coarsest discretization. Namely, the iterative solver did not converge when attempting to solve the diagonally preconditioned impedance matrix. In practice, we found the tolerance of  $10^{-6}$  to be unachievable by GMRES, which stagnated after 300 iterations

Lastly, to illustrate the importance of the right ILU preconditioner, we attempted to solve the ParPar2 structure for extremely fine discretization—32450 RWG functions at a resonance of 36.3 GHz. While the GMRES stagnated following 800 iterations using the left ILU, for the right ILU-preconditioned impedance matrix we achieved GMRES convergence following 101 iterations. Therefore, we conclude that the left ILU preconditioner can be ineffective to solve complex structures near resonance, in particular for very fine discretizations and large matrices.

### C. Comparison with CST

In the last section, our MoM-based solver is compared with the CST Frequency Domain Solver (Fsolver) via simulation of the configuration composed of the LaAlO<sub>3</sub>-ParPar2 resonator and a microstrip line described in previous sections. Both solvers were compared regarding simulation time per frequency point (STFP) and the number of unknowns (NoU) resolved for near-field and S<sub>11</sub> convergence (i.e.,  $< 0.2\%$  norm variation), where near-field convergence was tested using  $10^8$  grid points within a  $1.6 \text{ mm} \times 1.6 \text{ mm} \times 100 \text{ }\mu\text{m}$  sample volume situated above the resonator's surface. Figure 8 (d) shows the corresponding CST results depicting the resonant magnetic field distribution (respective to Fig. 8 (c)). All simulations were carried out on a 3.2 GHz Intel Xeon 1660 processor. The results are summarized in Table 1.

It is evident from Table 1 that while our MoM solver required the same NoU for both S<sub>11</sub> and near-field convergence, the CST Fsolver required almost double NoU to converge in the near-field region. Moreover, for CST, an additional manual mesh refinement was required at the center of the resonator, as it was not refined properly during the adaptive mesh refinement process. 650774757Note that being an FEM-based method, the CST

Fsolver divided the geometric model into a large number of tetrahedra within a predefined bounding box—a property that results in a very large matrix system to solve. In terms of simulation time, both solvers were comparable regarding STFP ( $\sim 210\text{--}270$  s) to achieve S<sub>11</sub> convergence. However, the STFP of the

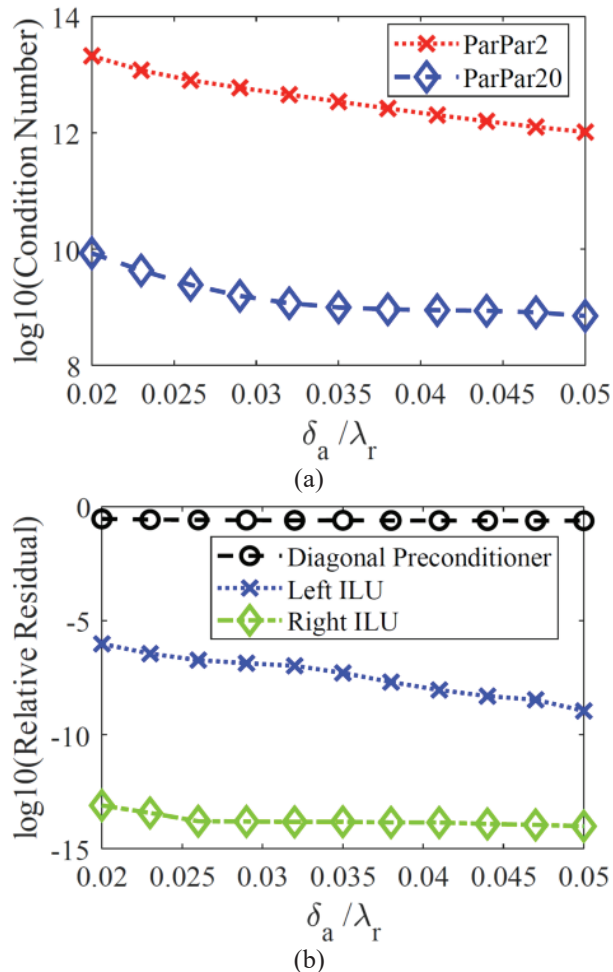


Fig. 10. Performance of the DP with left and right ILU to precondition the EFIE-PMCHWT impedance matrix of ParPar20 and ParPar2. (a) Condition number of ParPar20 and ParPar2 impedance matrices. (b) GMRES residual following  $\leq 30$  iterations.

CST Fsolver for nearfield convergence was  $\sim 430$  s, due to the need for a much finer mesh in the sample region. Furthermore, the total simulation time per frequency point plus the duration required for the adaptive mesh refinement process for the Fsolver was typically  $> 1$  hour due to the time-consuming adaptive mesh refinement process. Contrastingly, in the case of EFIE-PMCHWT, the total simulation time and STFP were equivalent. We also note that the MoM solver greatly outperformed the CST Fsolver when applying the right ILU as a preconditioner, whereas a left ILU-preconditioned impedance matrix resulted in very slow convergence of the iterative solver—the STFP was  $\sim 4$  times larger than the corresponding right ILU preconditioner. The total simulation times calculated for 21 frequency steps in a range of 34–39 GHz were approximately 210 minutes (including

Table 1: Comparative typical simulation times for the ParPar2 configuration. The STPFP does not include the initial calculation required for mesh refinement

EM Solver	S <sub>11</sub> convergence		Near-field convergence	
	NoU	STPFP [s]	NoU	STPFP [s]
CST Fsolver	~270,000	270	>600,000	431
EFIE-PMCHWT	4828	210	4828	210

the adaptive mesh process) in CST and 37 minutes in the EFIE-PMCHWT solver employing the right ILU as a preconditioner. The relatively short simulation time of the EFIE-PMCHWT solver is due to the computation of the singularity extraction, which was executed once for any given frequency band [26].

Lastly, we also attempted to use CST with the Integral Equation Solver (Isolver) to solve the ParPar2. Unfortunately, the results were not correct for the near-field region. Note that to make a fair comparison, the Isolver results were obtained with approximately the same NoU as our MOM solver. However, as explained in Section 3.3, performing a simulation with a finer mesh would probably not provide better results because it would lead to higher condition numbers, which were already very high owing to the complex geometry and near-resonance state.

## V. CONCLUSION

In this work, we developed an efficient methodology using a modified EFIE-PMCHWT formulation with impedance boundary conditions to solve surface MW resonators with dimensions and features that span several orders of magnitude with respect to the operating wavelength. The new methodology was used to solve three complex, realistic resonator configurations. The complexity of these configurations arises from a combination of electrically large structures, such as microstrip lines, and small surface resonators that have subwavelength localized geometric features. These types of configurations require dense and non-uniform discretizations, resulting in an impedance matrix whose condition number is in the range of  $10^8$ – $10^{14}$ . On the one hand, we showed that applying right incomplete LU (ILU) preconditioners can improve dramatically the condition number and thus allow for a fast iterative solver convergence. On the other hand, applying left ILU preconditioners resulted in very slow GMRES convergence, suggesting that left ILU preconditioning is considerably less effective than right ILU for this type of problem. We also showed that the standard diagonal preconditioner (DP) might be impractical for these types of resonator con-

figurations, leading to a non-converging iterative solver. We validated our solution via network analyzer measurements and ESR microimaging experiments. Finally, we showed that for the geometries we tested, the preconditioned EFIE-PMCHWT impedance matrix outperformed the CST frequency domain solver (Fsolver) in terms of simulation time because of the ultra-fine mesh required to achieve near-field convergence in the latter. Moreover, the CST integral equation solver could not provide accurate results in the near field for the configurations we tested.

## ACKNOWLEDGMENT

This work was partially supported by Grant #1357/21 from the Israel Science Foundation (ISF), Grant No. AZ 98010 from Forschungskooperation Niedersachsen-Israel, and by a grant from the Technion-Waterloo joint program. This project was also supported by the generosity of Eric and Wendy Schmidt by recommendation of the Schmidt Futures program. A. B. acknowledges the Russell Berrie Nanotechnology Institute (RBNI) at the Technion for supporting the clean room activities. The resonator was fabricated at Technion’s Micro-Nano Fabrication & Printing Unit (MNF&PU). The numerical data of the calculations are available from the authors upon reasonable request.

## REFERENCES

- [1] T. Ōkoshi, *Planar Circuits for Microwaves and Lightwaves*, Springer-Verlag, Berlin, New York, 1985.
- [2] J.-S. Hong, *Microstrip Filters for RF/microwave Applications*, 2nd ed., Wiley, Hoboken, NJ, 2011.
- [3] L. Young-Taek, L. Jong-Sik, K. Chul-Soo, A. Dal, and N. Sangwook, “A compact-size microstrip spiral resonator and its application to microwave oscillator,” *IEEE Microwave and Wireless Components Letters*, vol. 12, pp. 375-377, 2002.
- [4] J. Garcia-Garcia, J. Bonache, I. Gil, F. Martin, M. C. Velazquez-Ahumada, and J. Martel, “Miniaturized microstrip and CPW filters using coupled metamaterial resonators,” *IEEE Transactions on Microwave Theory and Techniques*, vol. 54, pp. 2628-2635, 2006.
- [5] R. Vrijen, E. Yablonovitch, K. Wang, H. W. Jiang, A. Balandin, V. Roychowdhury, T. Mor, and D. DiVincenzo, “Electron-spin-resonance transistors for quantum computing in silicon-germanium heterostructures,” *Phys. Rev. A*, vol. 62, pp. 012-306, 2000.
- [6] V. Ranjan, S. Probst, B. Albanese, A. Doll, O. Jacquot, E. Flurin, R. Heeres, D. Vion, D. Esteve, J. J. L. Morton, and P. Bertet, “Pulsed electron spin resonance spectroscopy in the Purcell regime,” *J. Magn. Reson.*, vol. 310, pp. 106-662, 2020.

- [7] V.-C. Su, C. H. Chu, G. Sun, and D. P. Tsai, "Advances in optical metasurfaces: fabrication and applications [Invited]," *Opt Express*, vol. 26, pp. 13148-13182, 2018.
- [8] J. A. Weil and J. R. Bolton, *Electron Paramagnetic Resonance: Elementary Theory and Practical Applications*, 2nd ed., Wiley-Interscience, Hoboken, NJ, 2007.
- [9] Y. Twig, E. Suhovoy, and A. Blank, "Sensitive surface loop-gap microresonators for electron spin resonance," *Rev. Sci. Instrum.*, vol. 81, pp. 104-703, 2010.
- [10] Y. Artzi, Y. Twig, and A. Blank, "Induction-detection electron spin resonance with spin sensitivity of a few tens of spins," *Appl. Phys. Lett.*, vol. 106, pp. 84-104, 2015.
- [11] S. Probst, A. Bienfait, P. Campagne-Ibarcq, J. J. Pla, B. Albanese, J. F. D. Barbosa, T. Schenkel, D. Vion, D. Esteve, K. Molmer, J. J. L. Morton, R. Heeres, and P. Bertet, "Inductive-detection electron-spin resonance spectroscopy with 65 spins/root Hz sensitivity," *Appl. Phys. Lett.*, vol. 111, 2017.
- [12] K. Lips, P. Kanschä, and W. Fuhs, "Defects and recombination in microcrystalline silicon," *Sol. Energy Mater.*, vol. 78, pp. 513-541, 2003.
- [13] M. Mannini, D. Rovai, L. Sorace, A. Perl, B. J. Ravoo, D. N. Reinhoudt, and A. Caneschi, "Patterned monolayers of nitronyl nitroxide radicals," *Inorg. Chim. Acta*, vol. 361, pp. 3525-3528, 2008.
- [14] P. P. Borbat, A. J. Costa-Filho, K. A. Earle, J. K. Moscicki, and J. H. Freed, "Electron spin resonance in studies of membranes and proteins," *Science*, vol. 291, pp. 266-269, 2001.
- [15] A. Blank, Y. Twig, and Y. Ishay, "Recent trends in high spin sensitivity magnetic resonance," *J. Magn. Reson.*, vol. 280, pp. 20-29, 2017.
- [16] D. M. Sullivan, *Electromagnetic Simulation using the FDTD Method*, 2nd ed., IEEE Press, John Wiley & Sons, Inc., Hoboken, New Jersey, 2013.
- [17] G. Meunier, *The Finite Element Method for Electromagnetic Modeling*, ISTE, Wiley, London, Hoboken, NJ, 2008.
- [18] R. F. Harrington, "The method of moments in electromagnetics," *Journal of Electromagnetic Waves and Applications*, vol. 1, pp. 181-200, 1987.
- [19] A. W. Glisson, D. Kajfez, and J. James, "Evaluation of modes in dielectric resonators using a surface integral equation formulation," *IEEE Transactions on Microwave Theory and Techniques*, vol. 31, pp. 1023-1029, 1983.
- [20] S. Rao, D. Wilton, and A. Glisson, "Electromagnetic scattering by surfaces of arbitrary shape," *IEEE Transactions on Antennas and Propagation*, vol. 30, pp. 409-418, 1982.
- [21] V. Jandhyala, B. Shanker, E. Michielssen, and W. C. Chew, "Fast algorithm for the analysis of scattering by dielectric rough surfaces," *Journal of the Optical Society of America A*, vol. 15, pp. 1877-1885, 1998.
- [22] A. J. Poggio and E. K. Miller, "Chapter 4 - Integral equation solutions of three-dimensional scattering problems," in R. Mittra (Ed.), *Computer Techniques for Electromagnetics*, Pergamon, pp. 159-264, 1973.
- [23] P. Yla-Oijala, M. Taskinen, and J. Sarvas, "Surface integral equation method for general composite metallic and dielectric structures with junctions," *Progress in Electromagnetics Research*, vol. 52, pp. 81-108, 2005.
- [24] J. R. Mautz and R. F. Harrington, "H-Field, E-Field, and combined field solutions for bodies of revolution," in Defence technical information center, 1977.
- [25] A. W. Glisson, "Electromagnetic scattering by arbitrarily shaped surfaces with impedance boundary conditions," *Radio Science*, vol. 27, pp. 935-943, 1992.
- [26] R. D. Graglia, "On the numerical integration of the linear shape functions times the 3-D Green's function or its gradient on a plane triangle," *IEEE Transactions on Antennas and Propagation*, vol. 41, pp. 1448-1455, 1993.
- [27] N. Dayan, Y. Ishay, Y. Artzi, D. Cristea, E. Reijerse, P. Kuppusamy, and A. Blank, "Advanced surface resonators for electron spin resonance of single microcrystals," *Rev. Sci. Instrum.*, vol. 89, pp. 124-707, 2018.
- [28] A. Okaya and L. F. Barash, "The dielectric microwave resonator," *Proceedings of the IRE*, vol. 50, pp. 2081-2092, 1962.
- [29] R. Prozorov and V. G. Kogan, "London penetration depth in iron-based superconductors," *Rep Prog Phys*, vol. 74, pp. 124-505, 2011.
- [30] A. R. Kerr, "Surface impedance of superconductors and normal conductors in EM simulators," in Electronics Division Internal Report, National Radio Astronomy Observatory, Green Bank, West Virginia, 1996.
- [31] Y. Artzi, Y. Yishay, M. Fanciulli, M. Jbara, and A. Blank, "Superconducting micro-resonators for electron spin resonance - the good, the bad, and the future," *J. Magn. Reson.*, vol. 334, pp. 107-102, 2022.
- [32] F. P. Andriulli, K. Cools, I. Bogaert, and E. Michielssen, "On a well-conditioned electric field integral operator for multiply connected

- geometries," *IEEE Transactions on Antennas and Propagation*, vol. 61, pp. 2077-2087, 2013.
- [33] F. P. Andriulli, A. Tabacco, and G. Vecchi, "Solving the EFIE at low frequencies with a conditioning that grows only logarithmically with the number of unknowns," *IEEE Transactions on Antennas and Propagation*, vol. 58, pp. 1614-1624, 2010.
- [34] C. Lu, X. Cao, and A. Frotanpour, "Method of moments for partially structured mesh," *31st International Review of Progress in Applied Computational Electromagnetics (ACES)*, pp. 1-2, 2015.
- [35] M. F. Catedra, O. Gutierrez, I. Gonzalez, and F. S. De Adana, "Electric and magnetic dual meshes to improve moment method formulations," *Appl Comput Electrom*, vol. 22, pp. 363-372, 2007.
- [36] K. Hill and T. Van, "Fast converging graded mesh for bodies of revolution with tip singularities," *Appl Comput Electrom*, vol. 19, pp. 93-99, 2004.
- [37] K. Sertel and J. L. Volakis, "Incomplete LU preconditioner for FMM implementation," *Microwave and Optical Technology Letters*, vol. 26, pp. 265-267, 2000.
- [38] B. Carpentieri and M. Bollhöfer, "Symmetric inverse-based multilevel ILU preconditioning for solving dense complex non-hermitian systems in electromagnetics," *Progress in Electromagnetics Research-pier*, vol. 128, pp. 55-74, 2012.
- [39] B. Carpentieri, I. S. Duff, L. Giraud, and G. Sylvand, "Combining fast multipole techniques and an approximate inverse preconditioner for large electromagnetism calculations," *SIAM Journal on Scientific Computing*, vol. 27, pp. 774-792, 2005.
- [40] F. P. Andriulli, K. Cools, H. Bagci, F. Olyslager, A. Buffa, S. Christiansen, and E. Michielssen, "A multiplicative calderon preconditioner for the electric field integral equation," *IEEE Transactions on Antennas and Propagation*, vol. 56, pp. 2398-2412, 2008.
- [41] H. C. Snorre and J.-C. Nédélec, "A preconditioner for the electric field integral equation based on calderon formulas," *SIAM Journal on Numerical Analysis*, vol. 40, pp. 1100-1135, 2003.
- [42] S. Sun, Y. G. Liu, W. C. Chew, and Z. Ma, "Calderón multiplicative preconditioned EFIE with perturbation method," *IEEE Transactions on Antennas and Propagation*, vol. 61, pp. 247-255, 2013.
- [43] Q. S. Liu, S. Sun, and W. C. Chew, "Low-frequency CMP-EFIE with perturbation method for open capacitive problems," *Proceedings of the 2012 IEEE International Symposium on Antennas and Propagation*, pp. 1-2, 2012.
- [44] J. Peeters, K. Cools, I. Bogaert, F. Olyslager, and D. D. Zutter, "Embedding calderón multiplicative preconditioners in multilevel fast multipole algorithms," *IEEE Transactions on Antennas and Propagation*, vol. 58, pp. 1236-1250, 2010.
- [45] R. Zhao, Z. Huang, W. Huang, J. Hu, and X. Wu, "Multiple-traces surface integral equations for electromagnetic scattering from complex microstrip structures," *IEEE Transactions on Antennas and Propagation*, vol. 66, pp. 3804-3809, 2018.
- [46] A. Ghai, C. Lu, and X. Jiao, "A comparison of preconditioned Krylov subspace methods for large-scale nonsymmetric linear systems," *Numerical Linear Algebra with Applications*, vol. 26, e2215, 2019.
- [47] Y. Saad and M. Schultz, "GMRES: a generalized minimal residual algorithm for solving nonsymmetric linear systems," *SIAM Journal on Scientific and Statistical Computing*, vol. 7, pp. 856-869, 1986.
- [48] R. Fletcher, "Conjugate gradient methods for indefinite systems," in Springer Berlin Heidelberg, Berlin, Heidelberg, pp. 73-89, 1976.
- [49] P. Sonneveld, "CGS, A fast Lanczos-type solver for nonsymmetric linear systems," *SIAM Journal on Scientific and Statistical Computing*, vol. 10, pp. 36-52, 1989.
- [50] R. W. Freund, "A transpose-free quasi-minimal residual algorithm for non-hermitian linear systems," *SIAM Journal on Scientific Computing*, vol. 14, pp. 470-482, 1993.
- [51] H. A. v. d. Vorst, "Bi-CGSTAB: a fast and smoothly converging variant of Bi-CG for the solution of nonsymmetric linear systems," *SIAM Journal on Scientific and Statistical Computing*, vol. 13, pp. 631-644, 1992.
- [52] A. Blank, E. Suhovoy, R. Halevy, L. Shtirberg, and W. Harneit, "ESR imaging in solid phase down to sub-micron resolution: methodology and applications," *Phys. Chem. Chem. Phys.*, vol. 11, pp. 6689-6699, 2009.



**Yakir Ishay** received BSc, MSc, and Ph.D. degrees in electrical engineering and physical chemistry from the Technion - Israel Institute of Technology in 2011, 2014, and 2020, respectively. He is currently working as an algorithm researcher and developer for Israel's defense industry. His research interests include numerical methods in electromagnetics, design of microwave resonators for magnetic resonance imaging (MRI), and image processing and machine learning algorithms.



**Yaron Artzi** is a Ph.D. student of physical chemistry at the Technion – Israel Institute of Technology’s Department of Chemistry. He obtained his BSc and MSc degrees in physics at that same institution. His research interests include the development of advanced methodologies in the field of electron spin resonance (ESR) for quantum technology applications.



**Nir Dayan** obtained his BSc in chemistry and biology and his MSc in chemistry from Tel Aviv University. Currently, he is a Ph.D. candidate at the Schulich Faculty of Chemistry at the Technion – Israel Institute of Technology. His projects in the Blank group are focused on the development of advanced techniques in electron spin resonance (ESR) for structural biology.



**David Cristea** is a senior researcher at the Schulich Faculty of Chemistry, Technion - Israel Institute of Technology. He holds a BSc in electronics and MSc and Ph.D. degrees in electrical engineering from the Politehnica University of Timisoara, Romania. His research interests include R&D of new resonators in the field of nuclear magnetic resonance (NMR) and electron spin resonance (ESR).



**Aharon Blank** is a full professor at the Schulich Faculty of Chemistry, Technion - Israel Institute of Technology. He holds BSc degrees in mathematics, physics, and chemistry from the Hebrew University of Jerusalem, an MSc in electrical engineering from Tel Aviv University, and a Ph.D. in physical chemistry from the Hebrew University. His research interests include the development and application of new methodologies in the field of nuclear magnetic resonance (NMR) and electron spin resonance (ESR).

# A Robust Algorithm for DOA Estimation of Coherent Sources with UCA

Ye Tian<sup>1,2</sup>, Yonghui Huang<sup>1</sup>, Xiaoxu Zhang<sup>1,2</sup>, and Meiyan Lin<sup>1,2</sup>

<sup>1</sup>National Space Science Center  
Chinese Academy of Sciences, Beijing, 100190, China  
tianyey171@mails.ucas.ac.cn, yonghui@nssc.ac.cn, zhangxiaoxu19@mails.ucas.ac.cn,  
linmeiyan18@mails.ucas.ac.cn

<sup>2</sup>University of Chinese Academy of Sciences, Beijing, 100049, China

**Abstract** – Direction of arrival (DOA) estimation of coherent sources with a uniform circular array (UCA) is an intractable problem. The method-of-direction-estimation (MODE) algorithm has strong superiority in handling coherent sources compared with the classical MUSIC, and ESPRIT algorithms. However, MODE is sensitive to source numbers and does not work well in the UCA scenario. In order to improve the performance of MODE, a robust DOA estimation method named UCA-PUMA (principal-eigenvector-utilization-for-modal-analysis) is proposed. The complicated non-Vandermonde structured steering vector of UCA is transformed into a virtual Vandermonde structured steering vector in mode space. The proposed method gives a closed-form solution compared with the original UCA-MODE algorithm. The performance of the UCA-PUMA method is evaluated by simulations. Simulation results demonstrate that the UCA-PUMA is more robust to source numbers than the UCA-MODE, and coherent sources can be handled without spatial smoothing. In addition, the UCA-PUMA fully takes advantage of the UCA, which is able to discriminate sources coming from a 360° azimuthal field of view.

**Index Terms** – PUMA, coherent, DOA estimation, UCA, MODE.

## I. INTRODUCTION

Direction-of-Arrival (DOA) estimation is attracting considerable critical attention from the array signal processing community. Several classical algorithms have been developed such as MUSIC [1], ESPRIT [2, 3], and Maximum Likelihood (ML) estimation [4, 5] in the past decades. Meanwhile, various array geometries have been considered, such as the uniform linear array (ULA), uniform circular array (UCA), and uniform rectangular array (URA), etc. Among many array configurations, the UCA has attracted much attention due to its advantages such as offering a 360° azimuthal field of view,

being easy to set up, etc. However, the widespread multipath effect of electromagnetic waves leads to coherent sources impinging on the array [6]. Some efforts have been tried in [7, 8] to deal with the problem of DOA estimation of coherent sources. Unfortunately, this problem becomes even trickier in the context of UCA [9], because of the non-Vandermonde structure of its steering vector.

Thanks to the mode space transformation method [10], the UCA can be treated as a virtual ULA and the azimuthal isotropy of UCA are retained. The mode space transformation, also known as beam space transformation, is widely used to solve DOA estimation problems in UCA. In [11, 12], the mode space transformation method has been adopted to improve the accuracy of DOA estimation in the UCA. Also in [13], the authors have proposed a low complexity sparse beamspace DOA estimation method for UCA. The above two works focus on the one-dimensional DOA estimation of uncorrelated sources in the UCA, and the mode space transformation technique is used to improve the estimation performance.

Furthermore, the mode space transformation technique can also play a great role in the context of DOA estimation of coherent sources in UCA. Since the covariance matrix is rank deficient in the scenarios of coherent sources, spatial smoothing techniques have been developed to address this problem [14]. Notably, the spatial smoothing technique requires the covariance matrix to be equipped with a Toeplitz structure, which is achieved by the ULA [15] or the URA [16]. Obviously, the mode space transformation technique provides the opportunity to convert the UCA into a virtual ULA, hence a similar method is also applied in the UCA scenario [17, 18]. However, in the process of implementing the spatial smoothing technique, the whole ULA or virtual ULA is divided into multiple sub-arrays, which reduces the effective array aperture and leads to severe performance degradation [19].

Particularly, the authors in [20] have proposed a ML-based approach to deal with the DOA estimation of coherent sources. Furthermore, with sophisticated mathematical proofs, this paper has shown that the proposed method does not require spatial smoothing in dealing with coherent sources. The MODE [21] is an ML type algorithm which is only required moderate computation. The MODE takes advantage of the autoregressive moving average model (ARMA) of the snapshot vector when the array steering vector has a Vandermonde structure realized by the ULA. In [22], the MODE algorithm has been extended to the UCA scenario by making full use of the mode space transformation. Nevertheless, the UCA-MODE algorithm is not robust to source number. The UCA-MODE performs well in the even source number scenario, but its performance is severely degraded in the odd case. Moreover, it performs even worse in the regime where coherent sources are hybrid with uncorrelated ones.

In this letter, we focus on the robust realization of the MODE algorithm for DOA estimation in UCA based on the recently proposed principal-eigenvector-utilization-for-modal-analysis (PUMA) method [23] combined with the mode space transformation of UCA. In this scheme, the problem of sensitivity to source number is overcome, and coherent sources can be directly handled without spatial averaging. The proposed method is named UCA-PUMA. It is worth noting that the UCA-PUMA can also deal with the scenario of complicated hybrid sources. Computer simulation is performed, and the results demonstrate that UCA-PUMA has a strong superiority over UCA-MODE [22], UCA-Smoothing [18], UCA-ESPRIT [10, 24] and UCA-Root-MUSIC [25]. The main contributions of this work are summarized as follows:

1. A robust DOA estimation algorithm, named UCA-PUMA, is proposed for coherent or hybrid sources impinging the UCA. Meanwhile, the UCA-PUMA does not require standard spatial smoothing steps that lead to loss of effective aperture.
2. The proposed UCA-PUMA algorithm takes advantage of the mode space transformation technique of UCA, and DOAs are obtained by finding the roots of a polynomial.
3. Computer simulations in various scenarios are carried out to demonstrate the superior performance of the proposed UCA-PUMA.

The remainder of this paper is organized as follows. Section II describes the UCA signal model and mode space transformation. In Section III, the proposed UCA-PUMA algorithm is introduced. The simulation results and related discussions are included in Section IV. Finally, Section V concludes the paper.

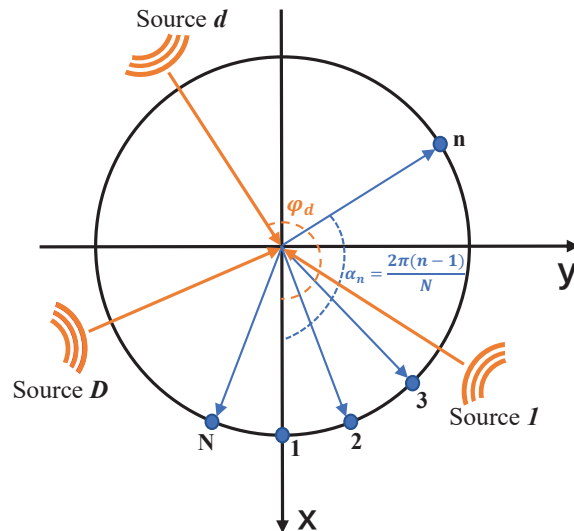


Fig. 1. System model of UCA.

**Notations:** In this letter, superscripts  $(\cdot)^{-1}$ ,  $(\cdot)^*$ ,  $(\cdot)^T$ , and  $(\cdot)^H$  denote the inverse operation, complex conjugate, transpose, and conjugate transpose, respectively.  $\text{diag}\{\cdot\}$  and  $\text{tr}\{\cdot\}$  are diagonal matrix and trace operators, respectively. Boldface lowercase letters such as  $\mathbf{a}$ ,  $\mathbf{b}$  denote vectors, and boldface uppercase letters such as  $\mathbf{A}$ ,  $\mathbf{B}$  denote matrices.  $\mathbf{I}_N$  is the  $N \times N$  identity matrix.  $\otimes$  is the Kronecker product operator of matrices.  $\angle z$  means taking the argument of the complex number  $z$ .

## II. SYSTEM MODEL

As shown in Fig. 1 and 2, consider  $D$  far-field narrowband sources from directions  $\boldsymbol{\varphi} = [\varphi_1, \varphi_2, \dots, \varphi_D]^T$  impinging on a UCA, which consists of  $N$  identical antenna elements uniformly distributed over a circle with radius  $R$ . The angle coordinate of the  $n$ -th antenna element is given by

$$\alpha_n = \frac{2\pi(n-1)}{N}. \quad (1)$$

The manifold matrix  $\mathbf{A}$  of the UCA is expressed as

$$\mathbf{A} = [\mathbf{a}(\varphi_1), \mathbf{a}(\varphi_2), \dots, \mathbf{a}(\varphi_D)] \in \mathbb{C}^{N \times D}, \quad (2)$$

where

$$\mathbf{a}(\varphi_d) = \begin{bmatrix} \exp[j2\pi\tilde{R}\cos(\varphi_d - \alpha_1)] \\ \exp[j2\pi\tilde{R}\cos(\varphi_d - \alpha_2)] \\ \vdots \\ \exp[j2\pi\tilde{R}\cos(\varphi_d - \alpha_N)] \end{bmatrix}, \quad (3)$$

is the  $d$ -th steering vector in  $\mathbf{A}$ , and  $\tilde{R} = R/\lambda$  is the radius normalized by wavelength. The  $k$ -th snapshot of the received signal is expressed as

$$\mathbf{x}(k) = \mathbf{A}\mathbf{s}(k) + \mathbf{n}(k), \quad k = 1, 2, \dots, K, \quad (4)$$

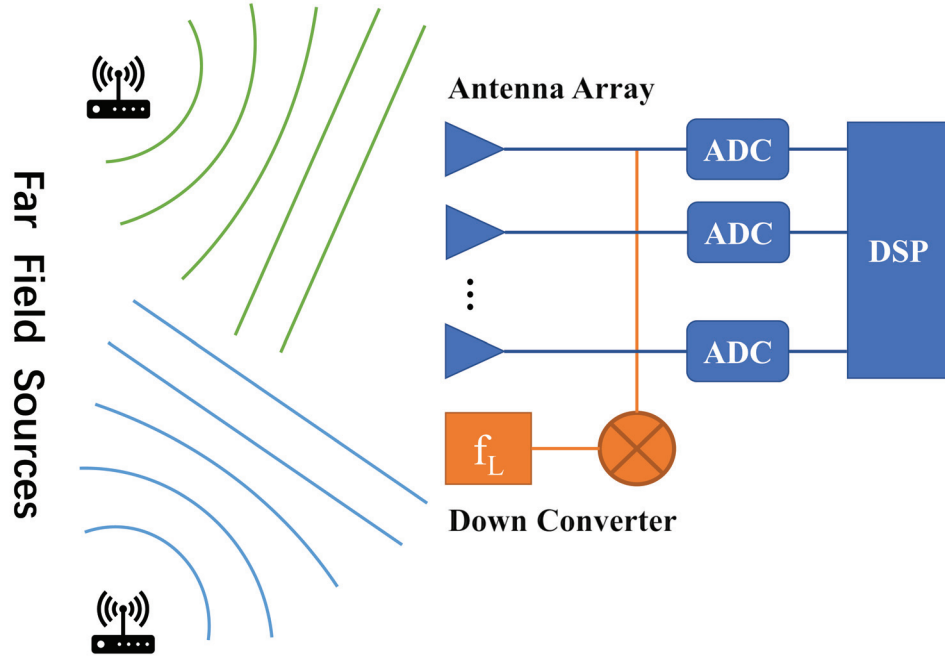


Fig. 2. Block diagram of the DOA estimation system.

where  $\mathbf{s}(k)$  is the source signal vector, and

$$\mathbf{n}(k) \sim \mathcal{C}\mathcal{N}(0, \sigma_n^2 \mathbf{I}_N), \quad (5)$$

is the additive white Gaussian noise vector, which is independent of the source signals.

When electromagnetic waves have multipath in space, coherent sources will appear at the receiving system. Without loss of generality, assume that there are  $D_p$  uncorrelated sources, and there are  $D_c$  sources that are coherent with previous  $D_p$  sources. The total number of sources is  $D = D_p + D_c$ . Then the covariance matrix of the  $D$  incoming sources is given by

$$\mathbf{R}_{\text{ss}} = \mathbb{E}[\mathbf{ss}^H] \in \mathbb{C}^{D \times D}. \quad (6)$$

The above assumption implies that  $\mathbf{R}_{\text{ss}}$  is rank deficient, i.e. its rank is  $D_p < D$ . Moreover, the covariance matrix of the array signal which is given by

$$\mathbf{R}_{\text{xx}} = \mathbb{E}[\mathbf{xx}^H] = \mathbf{A}\mathbf{R}_{\text{ss}}\mathbf{A}^H + \sigma_n^2 \mathbf{I}_N \in \mathbb{C}^{N \times N}. \quad (7)$$

By means of Cholesky factorization, the covariance matrix of the incoming sources is written as

$$\mathbf{R}_{\text{ss}} = \mathbf{T}\mathbf{T}^H, \quad (8)$$

with  $\mathbf{P} \in \mathbb{C}^{D_p \times D_p}$ . Then the following relation can be immediately obtained from 8, which is

$$\mathbf{T} = \begin{bmatrix} \mathbf{I}_{D_p} \\ \mathbf{C} \end{bmatrix} \mathbf{L} = \mathbf{P}\mathbf{L}, \quad (9)$$

where  $\mathbf{L}\mathbf{L}^H = \mathbf{Q} \in \mathbb{C}^{D_p \times D_p}$  and  $\mathbf{C} \in \mathbb{C}^{D_c \times D_p}$ . Based on the above notations,  $\mathbf{R}_{\text{xx}}$  can be rewritten as

$$\begin{aligned} \mathbf{R}_{\text{xx}} &= \mathbf{A}\mathbf{T}\mathbf{T}^H\mathbf{A}^H + \sigma_n^2 \mathbf{I}_N, \\ &= (\mathbf{A}\mathbf{P})\mathbf{Q}(\mathbf{P}^H\mathbf{A}^H) + \sigma_n^2 \mathbf{I}_N, \\ &= \mathbf{A}_p\mathbf{Q}\mathbf{A}_p^H + \sigma_n^2 \mathbf{I}_N. \end{aligned} \quad (10)$$

By taking the eigenvalue decomposition of  $\mathbf{R}_{\text{xx}}$ , we have

$$\mathbf{R}_{\text{xx}} = \mathbf{E}_{D_p}\mathbf{\Lambda}_{D_p}\mathbf{E}_{D_p}^H + \mathbf{E}_n\mathbf{\Lambda}_n\mathbf{E}_n^H, \quad (11)$$

where  $\mathbf{E}_{D_p} = [\mathbf{e}_1, \dots, \mathbf{e}_{D_p}]$  denotes the signal subspace formed by  $D_p$  eigenvectors corresponding to the  $D_p$  principal largest eigenvalues.

The maximum likelihood method [4, 5] maximizes the following loss function

$$f(\varphi) = \text{tr}\{\mathbf{A}_p[\mathbf{A}_p^H\mathbf{A}_p]^{-1}\mathbf{A}_p^H\mathbf{W}\}, \quad (12)$$

where

$$\mathbf{W} = \mathbf{E}_{D_p}\mathbf{\Gamma}_{D_p}\mathbf{E}_{D_p}^H, \quad (13a)$$

$$\mathbf{\Gamma}_{D_p} = \text{diag}\{\gamma_1, \dots, \gamma_{D_p}\} \quad (13b)$$

$$\gamma_d = \frac{(\lambda_d - \sigma_n^2)^2}{\lambda_d}. \quad (13c)$$

The above cost function (12) can be casted as

$$\begin{aligned} f(\varphi) &= \text{tr}\{\mathbf{A}\mathbf{P}[\mathbf{P}^H\mathbf{A}^H\mathbf{A}\mathbf{P}]^{-1}\mathbf{P}^H\mathbf{A}^H\mathbf{W}\}, \\ &= \text{tr}\{\mathbf{P}^H(\mathbf{A}^H\mathbf{A})\mathbf{P}\}^{-1}\mathbf{P}^H(\mathbf{A}^H\mathbf{W}\mathbf{A})\mathbf{P}\}, \end{aligned} \quad (14)$$

According to the extended Rayleigh quotient theorem, we obtain the following inequality

$$f(\varphi) \leq \sum_{p=1}^{D_p} \xi_p, \quad (15)$$

and when

$$\mathbf{P}\mathbf{S} = \mathbf{K} = [\mathbf{k}_1, \dots, \mathbf{k}_{D_p}], \quad (16)$$

is satisfied, the equal sign is obtained. Notably,  $\mathbf{S}$  is an arbitrary nonsingular matrix, moreover,  $\{\xi_p\}_{p=1}^{D_p}$  and  $\{\mathbf{k}_p\}_{p=1}^{D_p}$  denote the  $D_p$  principal eigenvalues

and their associated eigenvectors of the matrix  $(\mathbf{A}^H \mathbf{A})^{-1} (\mathbf{A}^H \mathbf{W} \mathbf{A})$ .

Since  $\mathbf{E}_{D_p}$  and  $\mathbf{A}$  span the same subspace, which implies  $\mathbf{E}_{D_p} = \mathbf{A} \mathbf{G}$  with the help of some matrix  $\mathbf{G} \in \mathbb{C}^{N \times D_p}$ . Note that

$$\mathbf{E}_{D_p}^H \mathbf{E}_{D_p} = (\mathbf{E}_{D_p}^H \mathbf{A}) \mathbf{G} = \mathbf{I}_{D_p}, \quad (17)$$

implies that

$$\text{rank}[\mathbf{E}_{D_p}^H \mathbf{A}] = D_p. \quad (18)$$

Notably, observe that

$$\text{rank}[(\mathbf{A}^H \mathbf{A})^{-1} (\mathbf{A}^H \mathbf{W} \mathbf{A})] = \text{rank}(\mathbf{E}_{D_p}^H \mathbf{A}) = D_p. \quad (19)$$

In other words, the  $D_p$  principal eigenvalues  $\{\xi_p\}_{p=1}^{D_p}$  is also all eigenvalues of  $(\mathbf{A}^H \mathbf{A})^{-1} (\mathbf{A}^H \mathbf{W} \mathbf{A})$ . Therefore we obtain that

$$\sum_{p=1}^{D_p} \xi_p = \text{tr}\{(\mathbf{A}^H \mathbf{A})^{-1} (\mathbf{A}^H \mathbf{W} \mathbf{A})\}. \quad (20)$$

To sum up, maximizing the cost function (12) is equivalent to minimizing the following function:

$$g(\varphi) = \text{tr}\{[\mathbf{I}_N - \mathbf{A}(\mathbf{A}^H \mathbf{A})^{-1} (\mathbf{A}^H)] \mathbf{W}\}. \quad (21)$$

### A. UCA mode space transformation

DOA estimation in UCA based on the mode space transformation method is first proposed in [10]. Let  $M$  denote the highest order mode that can be excited on a circle of radius  $R$  at a reasonable strength which is given as

$$M = \lfloor 2\pi\tilde{R} \rfloor, \quad (22)$$

where  $\lfloor \cdot \rfloor$  is the round-down operator. The  $m$ -th, ( $|m| \leq M$ ) phase mode is excited by the normalized beamforming vector in terms of

$$\mathbf{b}_m^H = \frac{1}{N} [e^{jm\alpha_1}, e^{jm\alpha_2}, \dots, e^{jm\alpha_N}]. \quad (23)$$

The resulting far field beam pattern of the UCA for mode  $m$  is

$$\begin{aligned} f_m(\varphi) &= \mathbf{b}_m^H \mathbf{a}(\varphi) \\ &= \frac{1}{N} \sum_{n=1}^N e^{jm\alpha_n} e^{j2\pi\tilde{R}\cos(\varphi_d - \alpha_n)} \\ &= j^m J_m(2\pi\tilde{R}) e^{jm\varphi} \\ &\quad + \sum_{c=1}^{\infty} \left[ j^p J_p(2\pi\tilde{R}) e^{-jp\varphi} + j^q J_q(2\pi\tilde{R}) e^{-jq\varphi} \right], \end{aligned} \quad (24)$$

where  $p = cN - m$  and  $q = cN + m$ . In order to make the item  $j^m J_m(2\pi\tilde{R}) e^{jm\varphi}$  of (24) be the dominant one, the number of antenna  $N$  should meet the following condition

$$N > 2M. \quad (25)$$

The property  $J_{-m}(2\pi\tilde{R}) = (-1)^m J_m(2\pi\tilde{R})$  of Bessel functions is used, and the residual items are omitted [10], then the far field beam pattern UCA for mode  $m$  can be expressed as

$$f_m(\varphi) \approx j^{|m|} J_{|m|}(2\pi\tilde{R}) e^{jm\varphi} \quad |m| \leq M. \quad (26)$$

The phase mode excitation matrix is defined as

$$\mathbf{W}_B^H = \mathbf{C}_J \mathbf{B}^H, \quad (27)$$

where

$$\mathbf{C}_J = \text{diag}\{j^{-M}, \dots, j^{-1}, j^0, j^{-1}, \dots, j^{-M}\} \quad (28a)$$

$$\mathbf{B} = \sqrt{N} [\mathbf{b}_{-M}, \dots, \mathbf{b}_0, \dots, \mathbf{b}_M]. \quad (28b)$$

Then the resulting beamspace steering vector synthesized by  $\mathbf{W}_B$  is given as

$$\mathbf{a}_B(\varphi) = \mathbf{W}_B^H \mathbf{a}(\varphi) = \begin{bmatrix} J_M(2\pi\tilde{R}) e^{-jM\varphi} \\ \vdots \\ J_1(2\pi\tilde{R}) e^{-j\varphi} \\ J_0(2\pi\tilde{R}) \\ J_1(2\pi\tilde{R}) e^{j\varphi} \\ \vdots \\ J_M(2\pi\tilde{R}) e^{jM\varphi} \end{bmatrix}. \quad (29)$$

The above relation can be rewritten as

$$\mathbf{a}_B(\varphi) = \mathbf{J} \mathbf{a}_v(\varphi), \quad (30)$$

where

$$\mathbf{J} = \text{diag}\{J_M(2\pi\tilde{R}), \dots, J_1(2\pi\tilde{R}), J_0(2\pi\tilde{R}), J_1(2\pi\tilde{R}), \dots, J_M(2\pi\tilde{R})\}, \quad (31)$$

is the diagonal matrix of Bessel functions, and

$$\mathbf{a}_v(\varphi) = [e^{-jM\varphi}, \dots, e^{-j\varphi}, 1, e^{j\varphi}, \dots, e^{jM\varphi}]^T \quad (32)$$

is the Vandermonde structured steering vector of the virtual linear array.

To sum up, the total transforming matrix is defined as

$$\mathbf{T}_B = \mathbf{J}^{-1} \mathbf{W}_B^H, \quad (33)$$

and the transformed  $k$ -th snapshot vector is

$$\begin{aligned} \mathbf{y}_v(k) &= \mathbf{T}_B \mathbf{x}(k) \\ &= \mathbf{A}_v \mathbf{s}(k) + \mathbf{n}_v(k), \end{aligned} \quad (34)$$

where  $\mathbf{A}_v = [\mathbf{a}_v(\varphi_1), \mathbf{a}_v(\varphi_2), \dots, \mathbf{a}_v(\varphi_D)]$  is the virtual manifold matrix with Vandermonde structure, and  $\mathbf{n}_v(k) = \mathbf{T}_B \mathbf{n}(k)$  is the transformed noise vector. The  $K$  transformed snapshots can be packed into a matrix with the following form

$$\mathbf{Y}_v = [\mathbf{y}_v(1), \mathbf{y}_v(2), \dots, \mathbf{y}_v(K)] \in \mathbb{C}^{N_v \times K}, \quad (35)$$

where  $N_v = 2M + 1$  is the number of elements in the virtual linear array.

The sample covariance matrix  $\hat{\mathbf{R}}_v$  is calculated as

$$\hat{\mathbf{R}}_v = \frac{1}{K} \mathbf{Y}_v \mathbf{Y}_v^H. \quad (36)$$

However, the transformed noise vector  $\mathbf{n}_v(k)$  is no longer a white noise vector; in this case, the signal and noise subspace can be solved based on the following **Generalized Eigenvalue Decomposition** (GEVD) problem:

$$\hat{\mathbf{R}}_v \mathbf{u} = \lambda (\mathbf{T}_B \mathbf{T}_B^H) \mathbf{u}. \quad (37)$$

Afterward, sort the  $N_v$  generalized eigenvalues in descending order; the signal subspace is formed by the generalized eigenvectors corresponding to the first

$D_p = D - D_c + 1$  ( $D_c$  is the number of coherent sources.) large eigenvalues. The signal subspace  $\mathbf{U}_s$ , noise subspace  $\mathbf{U}_n$  and corresponding generalized eigenvalues  $\mathbf{\Lambda}_s$ ,  $\mathbf{\Lambda}_n$  have the following forms

$$\mathbf{U}_s = [\mathbf{u}_1, \dots, \mathbf{u}_{D_p}], \quad (38a)$$

$$\mathbf{U}_n = [\mathbf{u}_{D_p+1}, \dots, \mathbf{u}_{N_v}], \quad (38b)$$

$$\mathbf{\Lambda}_s = \text{diag}\{\lambda_1, \dots, \lambda_{D_p}\}, \quad (38c)$$

$$\mathbf{\Lambda}_n = \text{diag}\{\lambda_{D_p+1}, \dots, \lambda_{N_v}\}. \quad (38d)$$

### B. MODE algorithm

In this subsection, we briefly introduced the core idea of the MODE algorithm [5, 21, 22]. The MODE algorithm is an efficient implementation of ML type algorithm which explores the ARMA structure of the observed snapshot vector. The ML algorithm estimates DOA by minimizing the following cost function:

$$f(\mathbf{A}_v) = \text{tr}\{\mathbf{\Pi}_{\mathbf{A}_v}^\perp \hat{\mathbf{R}}_v\}, \quad (39)$$

where

$$\begin{aligned} \mathbf{\Pi}_{\mathbf{A}_v}^\perp &= \mathbf{I}_{N_v} - \mathbf{\Pi}_{\mathbf{A}_v} \\ &= \mathbf{I}_{N_v} - \mathbf{A}_v(\mathbf{A}_v^H \mathbf{A}_v)^{-1} \mathbf{A}_v^H, \end{aligned} \quad (40)$$

is the orthogonal projection of  $\mathbf{A}_v$ . Moreover, the cost function in (39) can be replaced with a parameter vector

$$\mathbf{g} = [g_1, g_2, \dots, g_D]^T \in \mathbb{C}^D, \quad (41)$$

and the connection between  $\mathbf{g}$  and DOAs  $\{\varphi_d\}_{d=1}^D$  in terms of the following polynomial

$$F(z) = g_0 z^D + g_1 z^{D-1} + \dots + g_D \quad (42a)$$

$$= g_0 \prod_{d=1}^D (z - e^{j\varphi_d}) = 0. \quad (42b)$$

Then a matrix  $\mathbf{G} \in \mathbb{C}^{N_v \times (N_v - D)}$  is defined as

$$\mathbf{G} = \begin{bmatrix} g_D^* & 0 & \dots & 0 \\ \vdots & g_D^* & \ddots & \vdots \\ g_0^* & \vdots & \ddots & 0 \\ 0 & g_0^* & \vdots & g_D^* \\ \vdots & \ddots & \ddots & \vdots \\ 0 & \dots & 0 & g_0^* \end{bmatrix}, \quad (43)$$

and a link between  $\mathbf{G}$  and  $\mathbf{A}_v$  is established as follows

$$\mathbf{\Pi}_{\mathbf{A}_v}^\perp = \mathbf{\Pi}_{\mathbf{G}} = \mathbf{G}(\mathbf{G}^H \mathbf{G})^{-1} \mathbf{G}^H. \quad (44)$$

By substituting (44) into (39), a reparameterized cost function is cast as

$$f(\mathbf{g}) = \text{tr}\{\mathbf{\Pi}_{\mathbf{G}} \mathbf{U}_s \hat{\mathbf{\Gamma}} \mathbf{U}_s^H\}, \quad (45)$$

where

$$\hat{\mathbf{\Gamma}} = \text{diag}\{\hat{\gamma}_1, \dots, \hat{\gamma}_{D_p}\}, \quad (46a)$$

$$\hat{\gamma}_d = \frac{(\lambda_d - \hat{\sigma}_n^2)^2}{\lambda_d}, \quad (46b)$$

$$\hat{\sigma}_n^2 = \frac{1}{N_v - D_p} \text{tr}(\mathbf{\Lambda}_n). \quad (46c)$$

### III. PROPOSED ALGORITHM

Comparing the cost function (39) and (45), a complicated searching  $\mathbf{A}_v$  problem is reduced to an efficient searching  $\mathbf{g}$  problem based on the MODE method. However, additional assumptions on  $\mathbf{g}$  such as conjugate symmetry is requested by the original MODE algorithm. This additional assumption causes the MODE algorithm less robust to the number of sources. Fortunately, in literatures [26, 27], it has been proved that the solution of cost function (45) is equivalent to the solution of the following weighted least square (WLS) problem:

$$\mathbf{g} = \arg \min_{\mathbf{g}} (\mathbf{F}\mathbf{g} - \mathbf{h})^H \hat{\mathbf{W}} (\mathbf{F}\mathbf{g} - \mathbf{h}), \quad (47)$$

where  $\mathbf{F}$ ,  $\mathbf{h}$  and the weighting matrix  $\hat{\mathbf{W}}$  are given as

$$\mathbf{F} = \begin{bmatrix} \mathbf{F}_1 \\ \vdots \\ \mathbf{F}_d \\ \vdots \\ \mathbf{F}_{D_p} \end{bmatrix}, \quad \mathbf{h} = \begin{bmatrix} \mathbf{h}_1 \\ \vdots \\ \mathbf{h}_d \\ \vdots \\ \mathbf{h}_{D_p} \end{bmatrix}, \quad (48)$$

and  $\mathbf{F}_d \in \mathbb{C}^{(N_v - D) \times D}$  is the  $d$ -th submatrix in  $\mathbf{F}$ :

$$\mathbf{F}_d = \begin{bmatrix} (\mathbf{u}_d)_D & (\mathbf{u}_d)_{D-1} & \dots & (\mathbf{u}_d)_1 \\ (\mathbf{u}_d)_{D+1} & (\mathbf{u}_d)_D & \dots & (\mathbf{u}_d)_2 \\ \vdots & \vdots & \ddots & \vdots \\ (\mathbf{u}_d)_{N_v-1} & (\mathbf{u}_d)_{N_v-2} & \dots & (\mathbf{u}_d)_{N_v-D} \end{bmatrix}, \quad (49)$$

$$\mathbf{h}_d = -[(\mathbf{u}_d)_{D+1}, \dots, (\mathbf{u}_d)_{N_v}]^T \in \mathbb{C}^{N_v - D}, \quad (50)$$

$$\hat{\mathbf{W}} = \hat{\mathbf{\Gamma}} \otimes (\mathbf{G}^H \mathbf{G})^{-1}. \quad (51)$$

Moreover, the solution to (47) is given by

$$\hat{\mathbf{g}} = (\mathbf{F}^H \hat{\mathbf{W}} \mathbf{F})^{-1} \mathbf{F}^H \hat{\mathbf{W}} \mathbf{h}. \quad (52)$$

As we can see, there are no additional requirements in (52), and it is easy to update  $\hat{\mathbf{W}}$  and  $\hat{\mathbf{g}}$  iteratively. The DOAs can be calculated by

$$\hat{\varphi}_d = \angle \hat{z}_d, \quad (53)$$

where  $\hat{z}_d$  is the  $d$ -th root of the polynomial (42). The detailed steps of the proposed algorithm are summarized in Algorithm 1.

---

**Algorithm 1 UCA-PUMA Based DOA Estimation**


---

**Require:**

Transformed Snapshots  $\mathbf{Y}_v$ ,  
 Source Number  $D$ ,  
 Coherent Source Number  $D_c$ ,  
 Maximum Number of Iterations  $N_{\text{Iter}}$ ,  
 Tolerance  $\varepsilon$ ;

**Ensure:**

Estimated DOAs  $\{\hat{\phi}_1, \hat{\phi}_2, \dots, \hat{\phi}_D\}$

- 1: Calculate  $\hat{\mathbf{R}}_v$  and its GEVD via (36) and (37);
  - 2: Calculate  $\mathbf{F}$  and  $\mathbf{h}$  via (48)-(50);
  - 3: Initialize  $\hat{\mathbf{g}}$  as  $\hat{\mathbf{g}}_0 = (\mathbf{F}\mathbf{F}^H)^{-1}\mathbf{F}^H\mathbf{h}$ ;
  - 4: **for**  $i = 1, 2, \dots, N_{\text{Iter}}$  **do**
  - 5:    $\hat{\mathbf{W}}_{i+1} = \hat{\mathbf{\Gamma}} \otimes (\mathbf{G}_i^H \mathbf{G}_i)^{-1}$ ;
  - 6:    $\hat{\mathbf{g}}_{i+1} = (\mathbf{F}^H \hat{\mathbf{W}}_{i+1} \mathbf{F})^{-1} \mathbf{F}^H \hat{\mathbf{W}}_{i+1} \mathbf{h}$ ;
  - 7:    $\mathbf{G}_{i+1}$  is formed via (43);
  - 8:   **if**  $\|\hat{\mathbf{g}}_{i+1} - \hat{\mathbf{g}}_i\|_2 / \|\hat{\mathbf{g}}_i\|_2 < \varepsilon$  **then**
  - 9:     **break**
  - 10:   **end if**
  - 11: **end for**
  - 12: Calculate DOAs with  $\hat{\mathbf{g}}_{i+1}$  based on (53).
- 

#### IV. SIMULATION RESULTS

In this section, we evaluate the performance of the proposed **UCA-PUMA** algorithm in different scenarios by numerical simulations. The root-mean-square error (RMSE) is adopted to evaluate the estimated DOAs, which is defined as

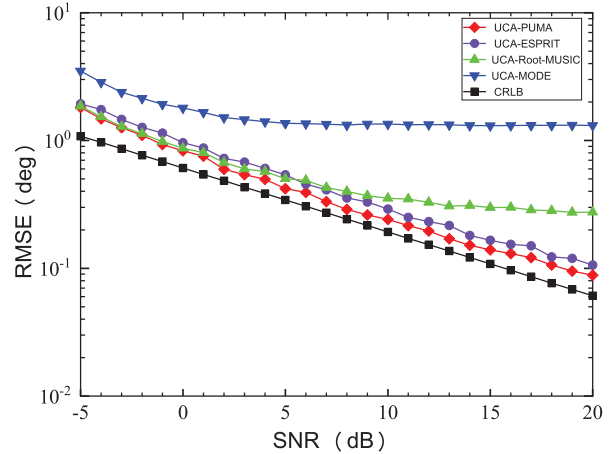
$$\text{RMSE} = \sqrt{\frac{1}{PD} \sum_{p=1}^P \sum_{d=1}^D (\hat{\phi}_d(p) - \phi_d(p))^2}, \quad (54)$$

where  $P = 500$  is the number of Monte-Carlo trials.

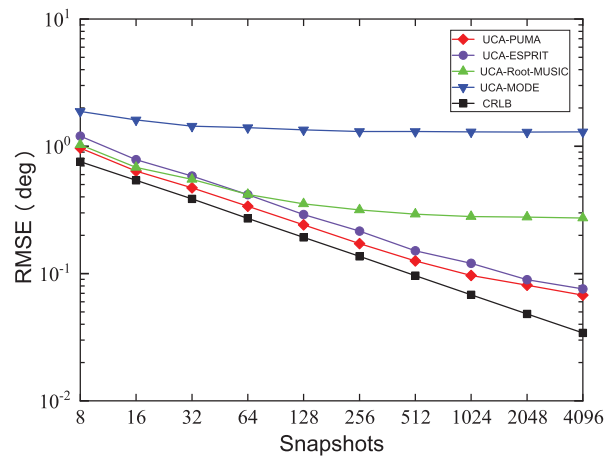
##### A. Single source

In this simulation, we evaluate the performance of the UCA-PUMA algorithm with respect to different SNRs and numbers of snapshots  $K$  in the single source ( $D = 1$ ) scenario. The DOA of the single source is randomly selected from  $\varphi \in [0^\circ, 360^\circ)$  in each Monte-Carlo trial. The array parameters are  $N = 7$ ,  $R/\lambda = 0.5$ , and  $M = 3$ . The UCA-MODE, UCA-Root-MUSIC, UCA-ESPRIT algorithms, and Cramér-Rao Lower Bound (CRLB) are compared with the UCA-PUMA algorithm.

The RMSE performance versus SNR (Snapshots  $K=128$ ) and snapshots (SNR=10 dB) are plotted in Fig. 3 (a) and Fig. 3 (b), respectively. As shown in Fig.3, the proposed UCA-PUMA algorithm performs better than the UCA-Root-MUSIC, the UCA-ESPRIT, and the UCA-MODE. Moreover, the RMSE curve of the proposed UCA-PUMA is closest to CRLB for all SNRs and snapshots being simulated, which proves the superiority of our method in the case of a single source.



(a) RMSE versus SNR, Snapshots  $K=128$

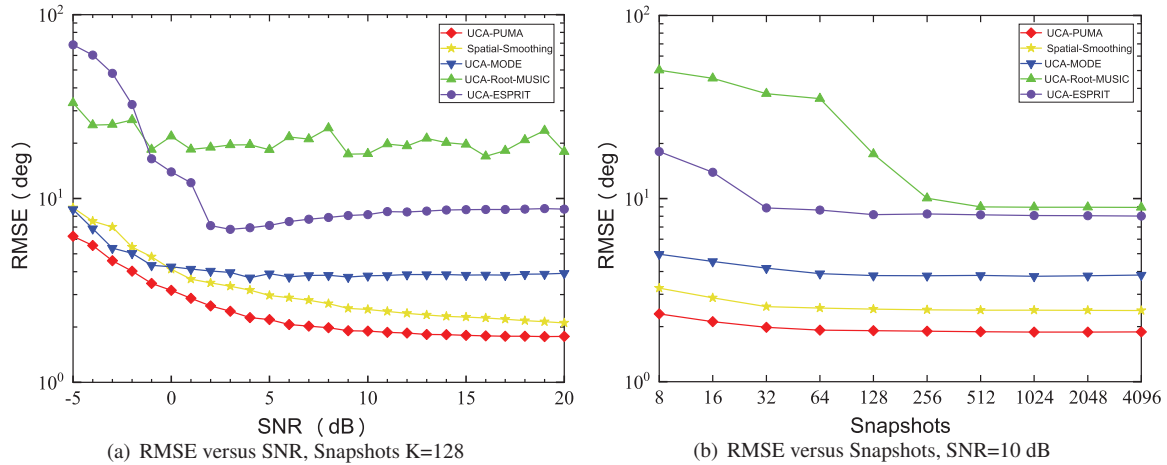
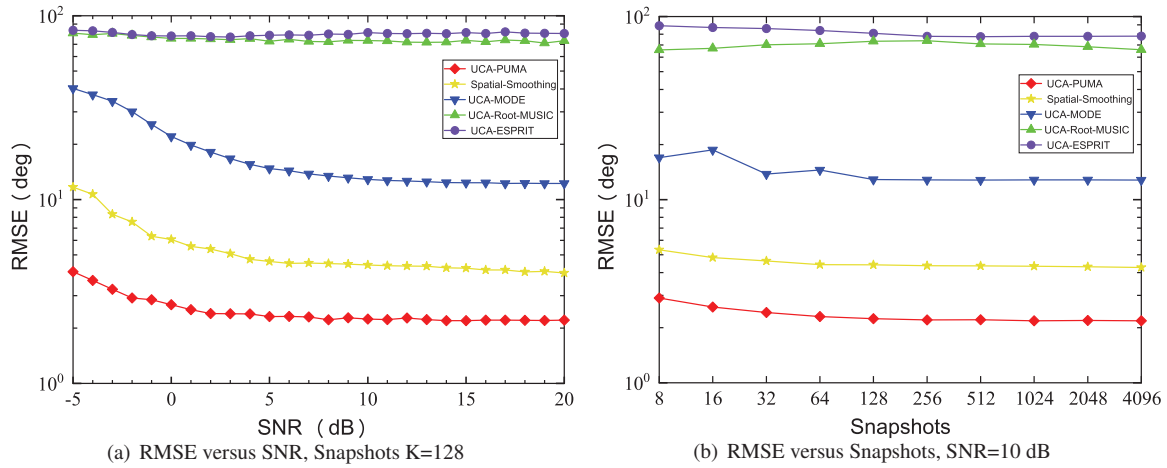


(b) RMSE versus Snapshots, SNR=10 dB

Fig. 3. Source number  $D=1$ .

##### B. Coherent sources

In this simulation, we focus on the complicated scenarios of multiple coherent sources. Moreover, the aforementioned classical method of processing coherent signals, namely spatial smoothing [18], is also used as a comparison. In the first example, two coherent sources whose DOAs ( $\varphi_1, \varphi_2$ ) are randomly selected from  $[0^\circ, 360^\circ)$ , and the separation between  $\varphi_1$  and  $\varphi_2$  is  $\Delta\varphi = |\varphi_1 - \varphi_2| \geq 5^\circ$ . As shown in Fig. 4 (a) and Fig. 4 (b), the RMSE of the UCA-PUMA, the Spatial-Smoothing, and the UCA-MODE are lower than  $10^\circ$ , and the RMSE of the UCA-MODE is slightly lower than the Spatial-Smoothing when the SNR is lower than 0 dB. The proposed UCA-PUMA algorithm has the best performance among these methods, and converges to a tolerable value ( $1.6^\circ$ ) when SNR is greater than 5 dB. Furthermore, we fix the SNR to a moderate value (10 dB), the UCA-PUMA still performs the best under various numbers of snapshots. The UCA-MODE and the Spatial-Smoothing

Fig. 4. Source number  $D=2$  (coherent sources).Fig. 5. Source number  $D=3$  (coherent sources).

behave similarly to the UCA-PUMA in this scenario, yet both the Spatial-Smoothing and the UCA-MODE algorithms show larger RMSEs over the UCA-PUMA. Meanwhile, the performance of the classical subspace-type algorithms (UCA-ESPRIT and UCA-Root-MUSIC) fail significantly.

In the second example, three fully coherent sources with DOAs being  $\varphi_1, \varphi_2$  and  $\varphi_3$  are simulated; meanwhile the three DOAs are randomly selected from  $[0^\circ, 360^\circ)$  and the angular separation between two DOAs is  $\Delta\varphi = |\varphi_i - \varphi_j| \geq 5^\circ$  ( $i, j \in \{1, 2, 3\}, i \neq j$ ). The simulation results are shown in Fig. 5 (a) and Fig. 5 (b), respectively. In this scenario with the odd number of sources, the UCA-MODE gives RMSE more than  $10^\circ$  which is severely degraded compared with the even source number scenario. There is also a decrease in the performance of the Spatial-Smoothing compared to

the scenario of two sources. However, the UCA-PUMA algorithm still works well. Moreover, the RMSE of the Spatial-Smoothing converges to  $4^\circ$  while the UCA-PUMA converges to  $2.2^\circ$ , and the reason is that the effective aperture of the UCA is reduced in the process of spatial smoothing.

Furthermore, the results depicted in Fig. 6 (a) and Fig. 6 (b) are in the regime where coherent sources are hybrid with uncorrelated ones (Hybrid Sources Scenario). Concretely, the first two sources are coherent, and the third one is uncorrelated from the previous. The DOAs of these three sources are selected in the same way as above. In this hybrid sources scenario, the RMSE of the UCA-MODE is roughly equivalent to  $20^\circ$ , and the RMSE of the Spatial-Smoothing converges to  $5^\circ$  which is slightly higher than the result in the scenario of three coherent sources. Furthermore, the UCA-ESPRIT along

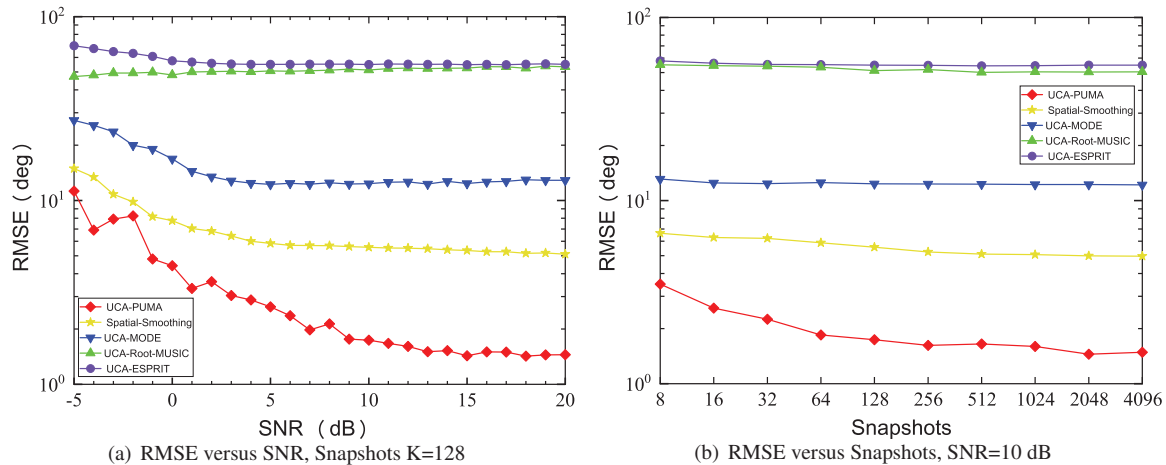


Fig. 6. Source number  $D=3$  (hybrid sources).

with the UCA-Root-MUSIC is completely failed ( $\text{RMSE} \approx 100^\circ$ ). However, the UCA-PUMA gives considerable RMSE ( $1.5^\circ$ ) and performs best among the above algorithms whether in scenarios of fully coherent sources or hybrid sources. This also verifies that the UCA-PUMA algorithm is robust to source numbers and performs better than the UCA-MODE or the Spatial-Smoothing.

## V. CONCLUSION

In this paper, a robust algorithm named UCA-PUMA for DOA estimation of coherent sources in UCA has been proposed. In order to take advantage of the ARMA model of the snapshot vectors, the non-Vandermonde structured steering vector of UCA is transformed into a virtual Vandermonde structured steering vector in mode space. After that, the recently developed PUMA algorithm performs well in UCA without spatial smoothing. Simulation results demonstrate that the proposed UCA-PUMA algorithm is robust to various numbers of sources. Moreover, the proposed UCA-PUMA exhibits significantly better performance than the algorithms including the UCA-MODE, the Spatial-Smoothing, the UCA-ESPRIT, and the UCA-Root-MUSIC.

## REFERENCES

- [1] R. Schmidt, "Multiple emitter location and signal parameter estimation," *IEEE Trans. Antennas Propag.*, vol. 34, no. 3, pp. 276-280, 1986.
- [2] R. Roy and T. Kailath, "ESPRIT-estimation of signal parameters via rotational invariance techniques," *IEEE Trans. Acoust., Speech, Signal Process.*, vol. 37, no. 7, pp. 984-995, 1989.
- [3] F.-M. Han and X.-D. Zhang, "An ESPRIT-like algorithm for coherent DOA estimation," *IEEE Antennas and Wireless Propagation Letters*, vol. 4, pp. 443-446, 2005.
- [4] P. Stoica, R. L. Moses, B. Friedlander, and T. Soderstrom, "Maximum likelihood estimation of the parameters of multiple sinusoids from noisy measurements," *IEEE Transactions on Acoustics, Speech, and Signal Processing*, vol. 37, no. 3, pp. 378-392, 1989.
- [5] P. Stoica and K. Sharman, "Maximum likelihood methods for direction-of-arrival estimation," *IEEE Trans. Acoust., Speech, Signal Process.*, vol. 38, no. 7, pp. 1132-1143, 1990.
- [6] W. Xie, F. Wen, J. Liu, and Q. Wan, "Source association, DOA, and fading coefficients estimation for multipath signals," *IEEE Transactions on Signal Processing*, vol. 65, no. 11, pp. 2773-2786, 2017.
- [7] W. Du and R. L. Kirlin, "Improved spatial smoothing techniques for DOA estimation of coherent signals," *IEEE Transactions on signal processing*, vol. 39, no. 5, pp. 1208-1210, 1991.
- [8] C. Qi, Y. Wang, Y. Zhang, and Y. Han, "Spatial difference smoothing for DOA estimation of coherent signals," *IEEE Signal Processing Letters*, vol. 12, no. 11, pp. 800-802, 2005.
- [9] L. Ni, J. Zhang, and H. Chen, "Sparse construction decorrelation algorithm of uniform circular array," in *Proceedings of the 2020 4th International Conference on Digital Signal Processing*, pp. 263-267, 2020.
- [10] C. Mathews and M. Zoltowski, "Eigenstructure techniques for 2-D angle estimation with uniform circular arrays," *IEEE Trans. Signal Process.*, vol. 42, no. 9, pp. 2395-2407, 1994.
- [11] Z. Xu, S. Wu, Z. Yu, and X. Guang, "A robust direction of arrival estimation method for uniform

- circular array,” *Sensors*, vol. 19, no. 20, p. 4427, 2019.
- [12] Y. Ma, X. Wang, and X. Cao, “Coarray beamspace transformation based DOA estimation for uniform circular arrays,” in *2018 IEEE Radar Conference (RadarConf18)*, pp. 0792-0797, IEEE, 2018.
- [13] D. Zhao, W. Tan, Z. Deng, and G. Li, “Low complexity sparse beamspace DOA estimation via single measurement vectors for uniform circular array,” *EURASIP Journal on Advances in Signal Processing*, vol. 2021, no. 1, pp. 1-20, 2021.
- [14] T.-J. Shan, M. Wax, and T. Kailath, “On spatial smoothing for direction-of-arrival estimation of coherent signals,” *IEEE Transactions on Acoustics, Speech, and Signal Processing*, vol. 33, no. 4, pp. 806-811, 1985.
- [15] J. Pan, M. Sun, Y. Wang, and X. Zhang, “An enhanced spatial smoothing technique with ESPRIT algorithm for direction of arrival estimation in coherent scenarios,” *IEEE Transactions on Signal Processing*, vol. 68, pp. 3635-3643, 2020.
- [16] Y.-M. Chen, “On spatial smoothing for two-dimensional direction-of-arrival estimation of coherent signals,” *IEEE Transactions on Signal Processing*, vol. 45, no. 7, pp. 1689-1696, 1997.
- [17] M. Wax and J. Sheinvald, “Direction finding of coherent signals via spatial smoothing for uniform circular arrays,” *IEEE Transactions on Antennas and Propagation*, vol. 42, no. 5, pp. 613-620, 1994.
- [18] Z. Ye, L. Xiang, and X. Xu, “DOA estimation with circular array via spatial averaging algorithm,” *IEEE Antennas and Wireless Propagation Letters*, vol. 6, pp. 74-76, 2007.
- [19] K. M. Reddy and V. Reddy, “Analysis of spatial smoothing with uniform circular arrays,” *IEEE Transactions on Signal Processing*, vol. 47, no. 6, pp. 1726-1730, 1999.
- [20] P. Stoica, B. Ottersten, M. Viberg, and R. L. Moses, “Maximum likelihood array processing for stochastic coherent sources,” *IEEE Transactions on Signal Processing*, vol. 44, no. 1, pp. 96-105, 1996.
- [21] A. B. Gershman and P. Stoica, “New MODE-based techniques for direction finding with an improved threshold performance,” *Signal Processing*, vol. 76, no. 3, pp. 221-235, 1999.
- [22] C. Ma, Y. Peng, and L. Tian, “An improved MODE algorithm for DOA estimation based on UCA,” in *TENCON '97 Brisbane - Australia. Proceedings of IEEE TENCON '97. IEEE Region 10 Annual Conference. Speech and Image Technologies for Computing and Telecommunications (Cat. No. 97CH36162)*, vol. 2, pp. 811-814 vol. 2, 1997.
- [23] H. C. So, F. K. W. Chan, W. H. Lau, and C.-F. Chan, “An efficient approach for two-dimensional parameter estimation of a single-tone,” *IEEE Trans. Signal Process.*, vol. 58, no. 4, pp. 1999-2009, 2010.
- [24] H. Minghao, Y. Yixin, and Z. Xianda, “UCA-ESPRIT algorithm for 2-D angle estimation,” in *WCC 2000 - ICSP 2000. 2000 5th International Conference on Signal Processing Proceedings. 16th World Computer Congress 2000*, vol. 1, pp. 437-440, 2000.
- [25] R. Goossens, H. Rogier, and S. Werbrouck, “UCA Root-MUSIC with sparse uniform circular arrays,” *IEEE Trans. Signal Process.*, vol. 56, no. 8, pp. 4095-4099, 2008.
- [26] C. Qian, L. Huang, M. Cao, J. Xie, and H. C. So, “PUMA: An improved realization of MODE for DOA estimation,” *IEEE Trans. Aerosp. Electron. Syst.*, vol. 53, no. 5, pp. 2128-2139, 2017.
- [27] C. Qian, L. Huang, N. D. Sidiropoulos, and H. C. So, “Enhanced PUMA for Direction-of-Arrival estimation and its performance analysis,” *IEEE Trans. Signal Process.*, vol. 64, no. 16, pp. 4127-4137, 2016.



**Ye Tian** was born in Liaoning Province, China, in 1996. He received the B.S. degree in Nanjing University of Aeronautics and Astronautics, Nanjing, Jiangsu, China, in 2017. He is currently pursuing the Ph.D. degree in electromagnetic field and microwave

technology with National Space Science Center (Beijing, China) of Chinese Academy of Sciences. His current research interests include array signal processing, DOA estimation and RF signal geolocation.



**Yonghui Huang** was born in Anshan, China. He received the B.Sc. degree in electronics engineering from Tsinghua University of Beijing, China in 1998. In 2001, he obtained the M.S. degree in aero-spacecraft design from University Chinese Academy of Sciences,

China. He achieved the Ph.D. degree in wireless communication from Aalborg University of Aalborg, Denmark in 2008. He is currently a professor with National Space Science Center of Chinese Academy of Science in Beijing, China. From 2002 to 2011,

He worked as a Postdoc. and research assistant in Aalborg University of Aalborg, Denmark. He is currently a researcher at the National Space Science Center of the Chinese Academy of Sciences. His current research interests include radio frequency machine learning, phased array antenna and transmitter linearization. He is the TPC member of IEEE CCET and IEEE WiSEE.



**Xiaoxu Zhang** was born in Fujian Province, China, in 1997. She received the B.S. degree in Nanjing University of Aeronautics and Astronautics, Nanjing, Jiangsu, China, in 2019. She is currently pursuing the Ph.D. degree in Computer Science and Technology with the

National Space Science Center at the Chinese Academy of Sciences, Beijing, China. Her current research interests include signal sorting, RF fingerprint recognition, and deep learning.



**Meiyang Lin** was born in Fujian Province, China, in 1995. She received the B.S. degree in School of Electronic and Information Engineering from Beijing Jiaotong University, Beijing, China, in 2018. She is currently pursuing the Ph.D. degree in National Space Science Center at Chinese Academy of Sciences, Beijing, China. Her main research interests include statistical signal processing and emitter localization.

# Design of Compact Multiband MIMO Antenna Based on Ground Neutralization Line Decoupling

Zhonggen Wang<sup>1</sup>, Weidong Mu<sup>1\*</sup>, Ming Yang<sup>2</sup>, and Chenlu Li<sup>3</sup>

<sup>1</sup>School of Electrical and Information Engineering  
Anhui University of Science and Technology, Huainan, 232001, China  
zgwang@ahu.edu.cn, mwd18755802702@163.com

<sup>2</sup>Department of Electrical and Communications Engineering  
West Anhui University, Lu'an, 237012, China  
myang@ahu.edu.cn

<sup>3</sup>School Electrical and Information Engineering  
Hefei Normal University, Hefei, 230061, China  
chenluli@hfnu.edu.cn

\*Corresponding author: Weidong Mu

**Abstract** – A compact, multiband two-port MIMO antenna is proposed in this paper for various wireless transmission networks, where the overall size of the antenna is only  $30 \times 20 \times 1.6 \text{ mm}^3$ . The proposed MIMO antenna consists of two radiating patches, each of which comprises a semicircle and a semi-regular hexagon, as well as the surface-etched C-slot and U-slot to tailor the antenna's return loss characteristics. In proposed antenna, a parasitic branch forms when the ground plane's meandering branches are symmetrically distributed. On one hand, it can increase the ground plane's effective area and enhance the antenna's return loss characteristics. A neutralization line, on the other hand, is generated, thereby limiting the current transmission on the ground plane. A cross-shaped slit in the ground's center is also employed to further promote isolation between the radiation elements. According to obtained results, the antenna can cover the frequency bands 0.67-7.29 GHz, 8.07-12.11 GHz, 14.07-15.41 GHz, and 16.04-22 GHz ( $S_{11} < -10 \text{ dB}$ ). Moreover, an RF isolation larger than 18 dB exists between the two ports. Lastly, in terms of ECC, DG, TARC, CCL, and MEG, the diversity performances are all satisfactory.

**Index Terms** – Decoupling, diversity performance, MIMO antenna system, multiband.

## I. INTRODUCTION

Multiple-input multiple-output (MIMO) technology is becoming increasingly popular in wireless transmission terminals and systems, owing to its high speed and scalability [1]. The MIMO antenna system is used in the

wireless transmission systems to meet the demands of increased system capacity, reduced latency, improved resilience, and restricted area [2]. Furthermore, miniaturized MIMO antenna systems are now being developed to reduce the size and cost, and improve portability. In view of this, the realization of appropriate and well-specified MIMO antenna designs is a major challenge for current wireless systems [3]. If the MIMO antenna functions only in a single restricted frequency band, the MIMO antenna in that frequency band will not be able to fully utilize the antenna's inherent benefits and will squander the frequency band resources. Therefore, designing an antenna for wireless applications that can encompass dual-band or multi-band while maintaining a sufficient amount of performance is one of the key technical issues encountered by current wireless terminals and systems.

Due to a demand for multiple frequency bands, various strategies have been utilized in literature to design dual-band or multi-band antennas. A novel metamaterial based antenna etched with a spiral-shaped structure to behave as a complimentary split ring resonator (CSRR) antenna is presented in [4]. The optimized antenna can cover three bands: 1.9 GHz (1.78-1.91 GHz), 2.45 GHz (2.23-2.52 GHz), and 3.2GHz (2.9-3.25 GHz). In [5], a 4-shaped, two-element MIMO antenna system that can cover the bands 0.803-0.823 GHz and 2.44-2.9 GHz of LTE wireless standard were designed. Likewise, in [6], a compact monopole antenna with a pentagon-shaped patch, symmetrical hook-shaped resonators, and one vertical slot was reported, which was claimed to operate at three frequencies: 3.5 GHz, 5.4 GHz, and 8 GHz. In addition, a defected ground plane-based planar antenna

operating at frequencies of 2.47 GHz, 3.55 GHz, and 5.55 GHz for Wi-Fi/WiMAX/WLAN applications was presented in [7]. Utilizing a new coplanar waveguide (CPW) with two slots reported in [8], the lower band operating at 2.453-2.821 GHz, and the higher band running at 5.876-6.892 GHz, might be created. To minimize the size of MIMO antennas while maintaining electrical performance, [9] employed a unique iterative approach based on Koch curves and Sierpinski square-slot fractals for rectangular patches. By combining fractal structure and CPW feed technology, the hybrid MIMO antenna provides dual-band coverage (1.81-3.17 GHz). Furthermore, a unique and compact planar MIMO antenna composed of a collapsed monopole and an inclined rectangular metal patch was reported in [10] for several frequencies such as GSM 900 MHz, DCS 1800 MHz, LTE-E 2300 MHz, and LTE-D 2600 MHz. The WLAN MIMO antenna system, operating in the frequency ranges of 2.4–2.48 GHz and 5.15-5.825 GHz and consisting of a dual frequency monopole structure and a curved decoupling resonator coupled to the ground, was first described in [11]. Similarly, the monopole structure was also utilized in [12], where each antenna covered the 2.45 GHz and 5.25-5.775 GHz frequency bands using double-folded monopoles for wireless communication. Progressively, for WLAN/WiMAX/Wi-Fi/4G-LTE and 5G bands, a four-element dual-band MIMO design containing inverted-L monopole antenna modules loaded by a split-ring resonator (SRR) was developed in [13]. In [14], a CPW-fed MIMO antenna was reported with an inverted U-shape and meandering line slots that increased the bandwidth performance. The antenna was observed to be advantageous for Bluetooth, WLAN, and WiMAX applications. A microstrip patch antenna in the form of a hexagon that can operate in three frequency bands was shown in [15]. By applying two inclined strips and cutting modified slots on the radiating patch, the antenna's multiband functionality was improved, allowing it to be tailored for WLAN, TV satellite broadcasting, WiMAX (5.25-5.85 GHz), IEEE 802.11a (5.47-5.725 GHz), 5G Unlicensed band (5.2-5.7 GHz), weather monitoring, and radar applications, where the antenna operated at three frequencies of 5.40 GHz, 6.76 GHz, and 8.82 GHz. In addition, as shown in [16], the characteristic mode theory (TCM) was used to create multifrequency antennas. When one of three identical square monopoles was excited using TCM, the other two monopoles were viewed as parasitic elements, lowering the monopole's Q factor and increasing the antenna's bandwidth. The high-order loops of the metal were activated and new resonance spots were created by adding metal patches to parasitic components, and then metal strips were added to the metal ring for low-frequency bandwidth. However, the MIMO antenna systems mentioned above have

drawbacks such as a limited frequency range, large size, or complicated structure, and there is still potential for improvement in antenna operating frequency, size, and structure.

However, on the other hand, mutual coupling between the antenna elements is severe in compact MIMO systems, due to a small distance between the radiation patches, thus affecting the diversity performance. Hence, the key to maintaining the MIMO system's performance is to reduce the mutual coupling between the radiating elements. The electromagnetic coupling effects have been addressed using a variety of methods in an integrated antenna system. Various decoupling measures have been investigated and applied in the literature including defected ground structure (DGS) [17–19], orthogonal polarization [20], electromagnetic band gap (EBG) [21, 22], neutralization line [23, 24], meander lines [25], and artificial resonators [26–29]. These decoupling techniques provide valuable guidance in the design of MIMO antenna systems.

Above all, the goal of this work is to develop a unique multiband two-port MIMO antenna with a simple structure for wireless communication, which can achieve multi-frequency coverage (0.67-7.29 GHz, 8.07-12.11 GHz, 14.07-15.41 GHz, and 16.04-22 GHz). The proposed antenna is  $30 \times 20 \times 1.6 \text{ mm}^3$  in size, and the isolation between its radiating elements is improved by the proposed ground branch and cross-shaped slot. The proposed antenna has four operational bands that may essentially be used to support various communication networks. In addition, diversity characteristics are also good. It should be stated here that this work aims to develop an antenna template for a new generation of ground early warning radar for a research institute in East China. Its basic requirements are small size, can cover 5G, X, and Ku bands, and can achieve linear polarization.

## II. ANTENNA DESIGN

### A. Geometry of the proposed antenna

The structure of the proposed compact and multiband two-port MIMO antenna with a defected ground plane is presented in Fig. 1. The proposed antenna has an overall size of  $30 \times 20 \times 1.6 \text{ mm}^3$  and was designed on FR4 substrate with 1.6mm thickness ( $\tan\delta = 0.02$  and  $\epsilon_r = 4.4$ ). It contains two identical modified radiating elements and a defected ground plane. A single radiating element excited by a microstrip line is composed of a semicircle and a semi-regular hexagon, where C-shaped and U-shaped slots are etched perpendicularly on its surface to ameliorate the impedance matching performance and the bandwidth. By introducing meandering ground branch and etching two symmetrical rectangular slots and a cross-shaped slot, the ground structure of this article is presented. In this design, the purpose of

meandering ground branch is two-fold. On one hand, it acts as a part of the antenna element to change and improve the return loss characteristics. While on the other hand, it is used as a neutralization line to improve the isolation between two ports. An additional etched cross-shaped slot is put in the center of ground plane to minimize the mutual coupling based on neutralization line even further, without affecting the elements' reflection coefficient performances. Table 1 lists the optimum parameter dimensions of the proposed two-port MIMO antenna.

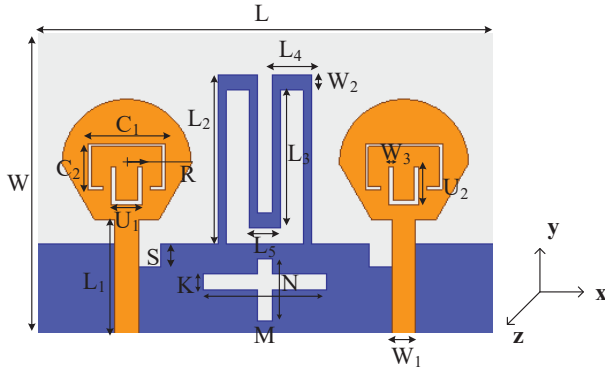


Fig. 1. Geometrical structure of the proposed two-port MIMO antenna.

Table 1: Optimized parametric dimensions of proposed MIMO antenna (unit: mm)

L	W	L <sub>1</sub>	L <sub>2</sub>	L <sub>3</sub>	L <sub>4</sub>
30	20	7.56	11	10	2.5
L <sub>5</sub>	C <sub>1</sub>	C <sub>2</sub>	C <sub>3</sub>	R	W <sub>2</sub>
2	5	3	1.15	4.2	1
U <sub>1</sub>	U <sub>2</sub>	M	N	K	S
2	2.5	8	4	1	1.5

## B. Design evolution stages of the single antenna

Initially, a planar monopole antenna with a wide frequency range was used in the design of a single radiating element, to ensure a wideband design. Fundamentally, the circular or regular hexagonal radiating patch has greater wideband properties, as highlighted in literature [30, 31]. Accordingly, this design combines a semicircle and a semi-regular hexagon to construct the fundamental radiation element based on the above. The radius has been calculated by following Equation (1) and (2) [32].

$$F = \frac{8.791 \times 10^9}{f_r \sqrt{\epsilon_\gamma}}, \quad (1)$$

$$R = \frac{F}{\left\{ 1 + \frac{2h}{\pi F \epsilon_\gamma} \left[ \ln \left( \frac{\pi F}{2\pi} \right) + 1.7726 \right] \right\}^{\frac{1}{2}}}. \quad (2)$$

Since the fundamental radiating element can only exhibit broadband characteristics within a specific frequency range and cannot provide multi-frequency coverage, the shape of antenna patch must be altered. To target several frequencies and improve the antenna's impedance matching qualities, it is beneficial to etch a C-shaped slot on its surface. The slit acts as a quarter-wavelength resonator, the length of C-shaped slot and resonant frequency can be calculated as

$$Ls_1 = C_1 + 2C_2 + 2C_3, \quad (3)$$

$$fs_1 = \frac{c}{4Ls_1 \sqrt{\epsilon_{\gamma\text{eff}}}}, \quad (4)$$

where  $Ls_1$  is the total length of the C-shaped slot,  $fs_1$  is the first resonant frequency,  $\epsilon_{\gamma\text{eff}}$  is half of the dielectric constant of the FR4, due to the lack of ground,  $c$  is the speed of light. The length of  $Ls_1$  is 13.3 mm and the resonant frequency  $fs_1$  is at 3.8 GHz by calculating.

Next, the 50  $\Omega$  transmission line feed is in conjunction with the fractional ground plane to investigate the effects of alternative single antenna structures. The steps in the design of a single antenna element of the proposed MIMO antenna system are depicted in Fig. 2, whereas the operating principle of the antenna element is explained using its reflection coefficient characteristics in Fig. 3.

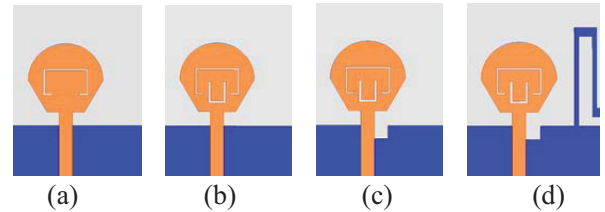


Fig. 2. Evolution of the design process of single element: (a) Step-1, (b) Step-2, (c) Step-3, (d) Step-4 (proposed single element).

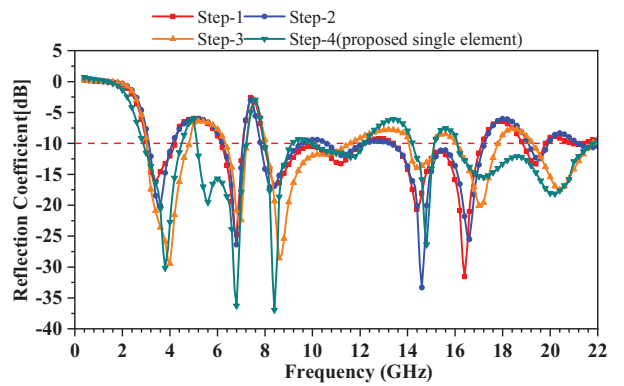


Fig. 3. Comparison of reflection coefficient of 4 designs of a single element of the proposed antenna.

It can be observed from Fig. 3 that the antenna designed in Step-1 (including a C-shaped slit and a complete ground) exhibits seven resonating frequency points i.e., 3.5, 6.9, 8.5, 11.3, 14.5, 16.5 and 19.5 GHz with impedance available bandwidths of 1.1 GHz, 1.0 GHz, 4.0 GHz, 3.6 GHz and 0.8 GHz, respectively. And after comparison, when the C-shaped slit is only etched, the first resonance frequency generated is close to the result calculated by Equation (4).

Furthermore, as illustrated in Step-2 of Fig. 2, introducing a U-shaped slot under the C-shaped slit in the single antenna patch allows the antenna to resonate at eight different frequencies. The length of U-shaped slot and resonant frequency can also be calculated as

$$Ls_2 = U_1 + 2U_2, \quad (5)$$

$$fs_2 = \frac{c}{4Ls_2\sqrt{\epsilon_{\gamma\text{eff}}}}. \quad (6)$$

From the result of Fig. 3, the second resonant frequency is around 6.8 GHz, which is similar to the calculation value of 7.1 GHz, indicating etched U-shaped slot acting as a quarter-wavelength resonator in step-2. In particular, 21.8 GHz is added to the resonance points compared to the design in Step-1, where the common resonance points are just slightly changed. It is worth noticing that the antenna's reflection coefficient decreases at low frequencies, indicating an improvement in impedance matching performance. Essentially, the reflection coefficient is reduced by 3.85 dB at 3.6 GHz, and 5.05 dB at 8.2 GHz. However, since the reflection coefficient data from Step-1 and 2 show that just changing the antenna shape (etching C and U-shaped slots) does not provide enough bandwidth at low frequencies (particularly at 3-5 GHz), the next step in the design process is to investigate the modification of ground plane geometry.

A defective monopole ground plane with a rectangular slit is proposed in the following design, as highlighted in Fig. 2. In comparison to the design of Step-2, this geometry possesses two less frequency bands and resonates at six different frequencies (4.0, 7.0, 8.6, 14.4, 17.0, and 20.4 GHz). In addition, the antenna element's impedance bandwidth in the low-frequency band is increased compared Step-1 to Step 2, reaching 1.80 GHz (3.1-4.9 GHz) and 3.4 GHz (8.1-11.5 GHz), thereby covering additional 5G bands and X-band. Certainly, alterations to the ground plane structure have caused these changes. Based on the foregoing explanation, it is reasonable to expect that any further advancements in the ground plane structure will allow the antenna components to have lower frequency bands with enhanced bandwidths.

Correspondingly, a new antenna design (Step-4) was created to improve the performance by applying a meandering ground branch in the fractional ground plane as shown in Fig. 2 (d). The branch functions as a resonator

to obtain an extra resonance mode. The resonant frequency can be calculated as:

$$L = L_2 + L_3 + L_4 + L_5/2, \quad (7)$$

$$f = \frac{c}{L\sqrt{\epsilon_{\gamma}}}. \quad (8)$$

The calculated length of L is 24.5 mm and the resonant frequency is at 5.8 GHz. The corresponding reflection coefficient curve can be seen in Fig. 3. From Fig. 3, the antenna developed in Step-4 indeed aids in the addition of a 5.6 GHz (closed to calculated value) frequency band (5.15-7.22 GHz) to the existing six frequency bands. When compared to the design of Step-3, the lower frequency in this design is moved to the left, where the equivalent impedance bandwidth is 1.63 GHz (2.87-4.50 GHz). Essentially, the meandering branch increases the ground's effective area, improves the antenna's impedance matching performance, and effectively saves space, thereby allowing the integration of multiple similar antennas in a small space to create an innate condition and allowing the antenna design to progress towards miniaturization. Owing to improved parameters in terms of impedance characteristics i.e., increased number of resonating frequencies and enhanced impedance bandwidths, it is noticeable from the findings that the antenna structure created in Step 4 can be used as the final geometry of a single element of the proposed two-port MIMO antenna.

### C. Influences of ground plane on two-port MIMO antenna

A single antenna element is transformed into a MIMO system to achieve effective diversity characteristics and high isolation, thereby allowing the proposed wireless device to boost data throughput. The distance, relative location, and other parameters between multiple elements are addressed during the design of the overall MIMO system. Finally, the meandering ground branches are joined to form the original ground geometry structure using a two-port antenna system. The goal here is to minimize the antenna size, and the linked stubs in the MIMO system create a neutralization line that may be utilized to increase the isolation. Besides, the geometry of the ground plane has been adjusted based on the structure of the neutralization line to improve the antenna's impedance matching performance and the isolation between the antenna components. Fig. 4 demonstrates the evolution phases of the ground plane for the proposed MIMO antenna system. Likewise, Fig. 5 and 6 plot the reflection coefficient (S11) and transmission coefficient (S12) determined from the simulations.

Evidently, the integrated MIMO system exhibits enhanced impedance bandwidth as compared to a single antenna. At sub-7 GHz, the single antenna has two bands (2.86-4.49 GHz and 5.12-6.88 GHz), whereas

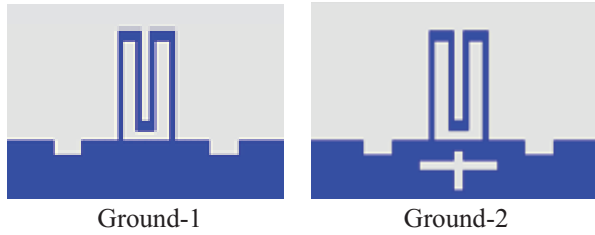


Fig. 4. Evolution stages of the ground plane.

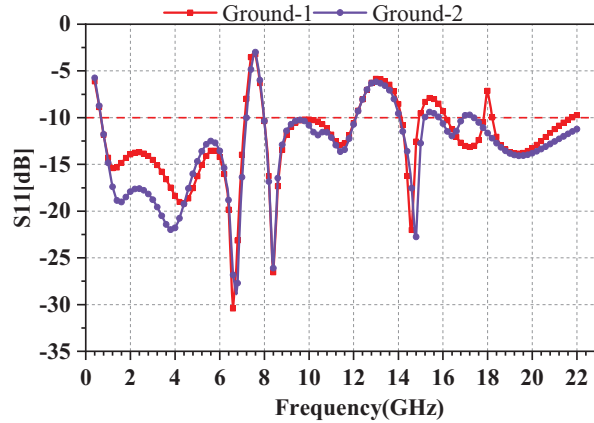


Fig. 5. S11 parameter of MIMO antenna for different structure of ground plane.

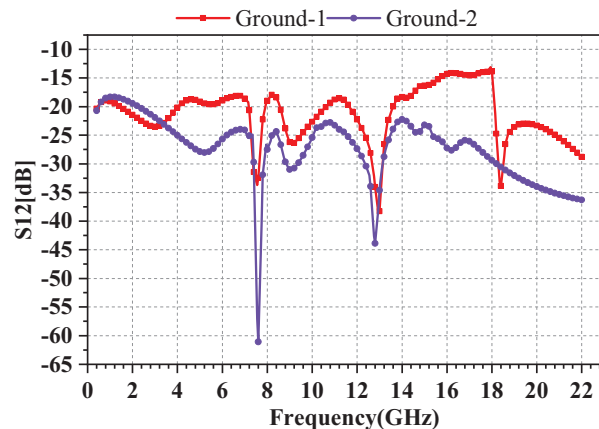


Fig. 6. S12 parameter of MIMO antenna for different structure of ground plane.

the MIMO antenna combines the two bands into one wider band (0.68-7.13 GHz). Similarly, in the X-band, MIMO antenna has a broader bandwidth of 7.98-12.09 GHz, although there is no significant difference at higher frequencies. The frequencies covered by the MIMO antenna with Ground-1 are 0.68-7.13 GHz, 7.98-12.09 GHz, 14.13-14.97 GHz, 16.14-17.83 GHz, and 18.20-21.79 GHz (for  $S_{11} < -10$  dB). In the frequency ranges of 0.68-7.13 GHz and 7.98-12.09 GHz, the

mutual coupling ( $S_{12}$ ) is less than  $-18$  dB. Similarly,  $S_{12}$  is less than  $-16$  dB,  $-13$  dB, and  $-23$  dB in the frequency range of 14.13-14.97 GHz, 16.14-17.83 GHz, and 18.20-21.79 GHz, respectively. That is to say, MIMO antenna has remarkable decoupling properties.

Next, a cross-shaped slot is inserted in the middle of the ground plane structure of Ground-1 to realize the geometry of Ground-2. To further minimize the mutual coupling between the two antennas, as shown in Fig. 4. The reflection coefficient at lower frequencies is noticeably lowered after using Ground-2, showing a further improvement in the impedance matching ability. Particularly, the  $S_{11}$  is  $-19.1$  dB at 1.52 GHz and  $-22.4$  dB at 3.80 GHz, which is significantly better than the characteristics of Ground-1. Meanwhile, the higher frequency of 17.22 GHz is moved to the left to 16.38 GHz, without having a significant impact on the high-frequency coverage. Aside from that, the reflection coefficient for 8-12 GHz frequency band is scarcely changed in any situation. To put it another way, the addition of a cross-shaped slot has little impact on the original frequency range. The mutual coupling, on the other hand, has improved substantially. That is to say, the proposed MIMO antenna has eight resonant frequency points at 1.52, 3.80, 6.80, 8.40, 11.37, 15.00, 16.38, and 19.40 GHz, with mutual coupling ( $S_{12}$ ) values of  $-18.6$ ,  $-24.3$ ,  $-23.9$ ,  $-24$ ,  $-23.2$ ,  $-27.1$ , and  $-32.8$  dB. The  $S_{12}$  achieves the lowest value of  $-60.1$  dB at 7.60 GHz. The cross-shaped slot effectively removes the coupling effect without changing the frequency band, as illustrated in Fig. 6. It is reasonable to assume that the ground plane plays a critical role in enhancing the proposed MIMO antenna's performance characteristics in terms of impedance matching and isolation. Ground-2 has a simpler structure and great practicability as compared to other reported decoupling structures, making the antenna structure more compact.

#### D. Current distribution

The surface current distribution in the prominent resonance modes is shown in Fig. 7, to visually highlight the decoupling impact of the adopted ground plane geometry. Port-1 is excited in the MIMO system, whereas port-2 is terminated with a matching load of  $50\Omega$ . When just port-1 is excited, the majority of the current is dispersed on the radiating element-1, and there is almost no current distribution on the surface of radiating element-2. The current distribution characteristics of the ground when the two ports are excited simultaneously are simulated, and the vector current distribution of the ground plane in the resonance modes is shown in Fig. 8, to further demonstrate the working mechanism of the ground decoupling structure. From Fig. 8, near-identical currents in opposite directions cancel out

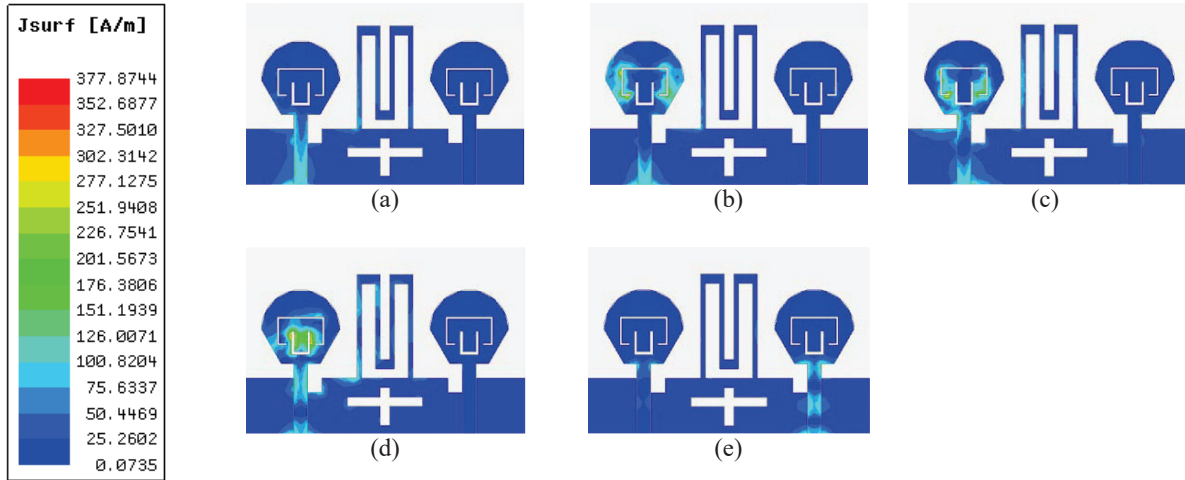


Fig. 7. Surface current distribution only when port1 is excited at (a) 3.8 GHz, (b) 6.8 GHz, (c) 8.4 GHz, (d) 15 GHz, (e) 19.4 GHz.

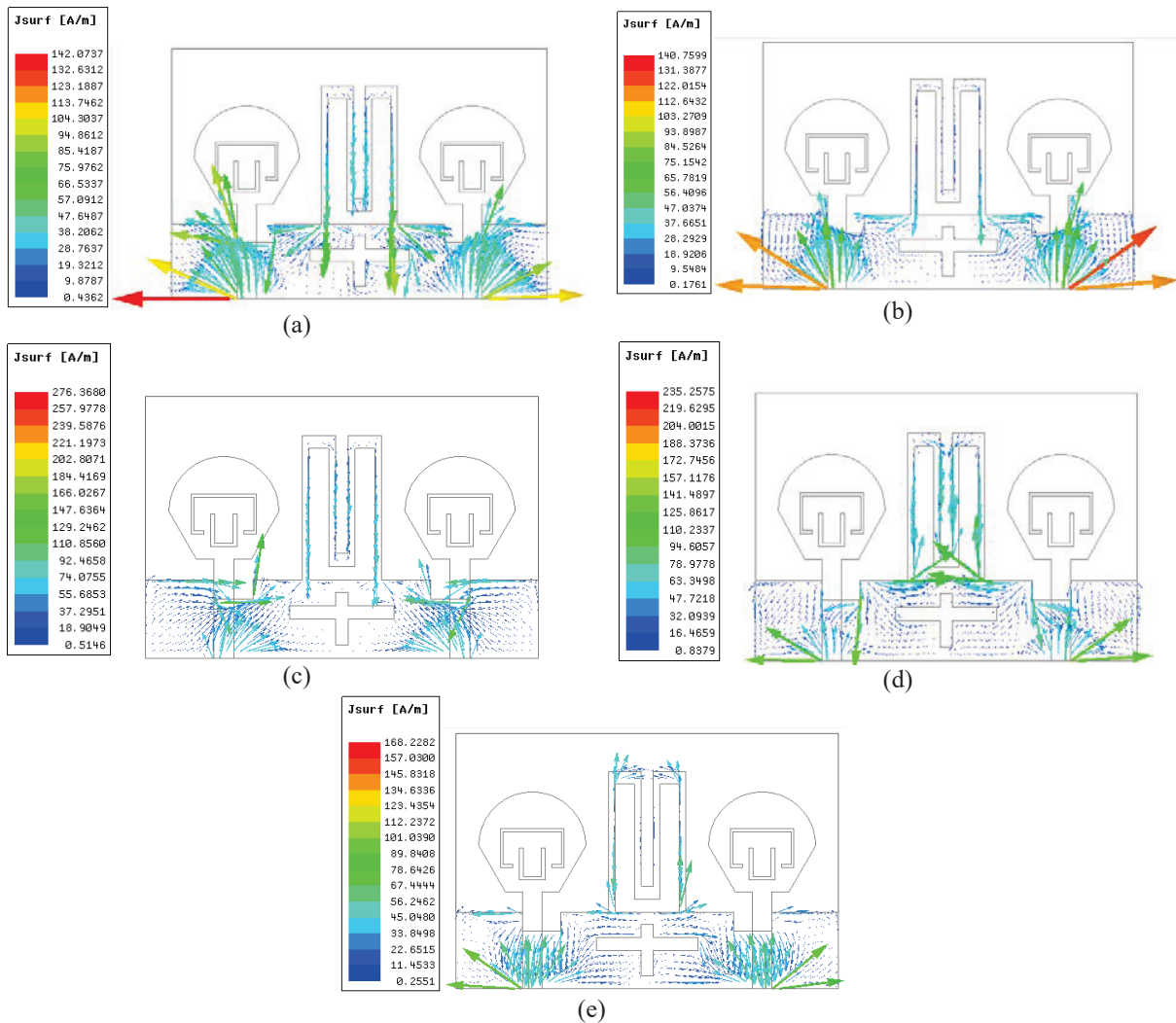


Fig. 8. Vector current distribution of ground plane at (a) 3.8 GHz, (b) 6.8 GHz, (c) 8.4 GHz, (d) 15 GHz, (e) 19.4 GHz.

at the meandering ground branch in major resonance modes, reducing part of the current interference provided by the ground. The meandering ground branch offsets the current to some degree and acts as a neutralization line in this operation. Moreover, the etched cross-shaped slot, on the other hand, efficiently limits or prolongs the ground's current transmission, enhancing the decoupling effect even more. According to the findings, the meandering ground branch-based double decoupling structure would effectively improve isolation.

### III. RESULTS AND DISCUSSIONS

Figure 9 shows the fabricated prototype of the proposed antenna, which is excited by a  $50\ \Omega$  coaxial cable. An Agilent N5247A vector network analyzer was used for testing the S-parameters. During the measurement process, the selected sweep frequency range for the measurement method is 0.4-22 GHz, the intermediate frequency bandwidth (IFBW) is 100 kHz, and the number of frequency points is 201. The results are presented and explained in the sections that follow.

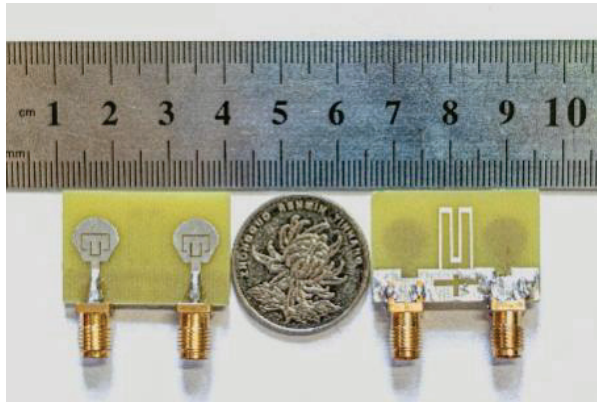
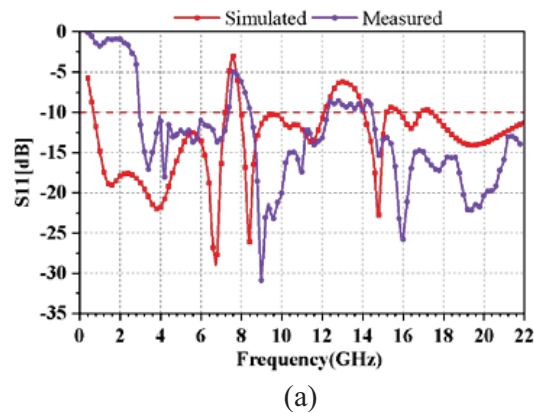


Fig. 9. Fabricated prototype of proposed two-port MIMO antenna.



#### A. S-parameter

The results of simulated and measured S-parameters are compared in Fig. 10. It can be observed from Fig. 10 (a) that the operative bands of the measured reflection coefficients ( $S_{11} < -10$  dB) encompass 2.9-7.3 GHz, 8.48-12.3 GHz, 14.5-22 GHz. It is worth emphasizing that the discrepancy between the measured and the simulated result mainly exists below 5 GHz, which may be due to fabrication flaws such as changes in physical dimensions of the fabricated prototype, soldering process, environmental conditions, and so on, but it has hardly affected on its operating bandwidth characteristics. In terms of isolation, as evident from Fig. 10 (b), the measured isolation of the proposed MIMO antenna has a minimum value of 44 dB. Moreover, the transmission coefficient is below  $-12$  dB at the operative bands, indicating a good decoupling effect.

#### B. Radiation characteristics

The measurements of the radiation patterns were carried out in an anechoic chamber and the selected IF bandwidth of the NSI antenna system for measuring radiation patterns was 1 kHz. The simulated and measured radiation patterns at five resonance frequencies demonstrating the antenna's  $xoz$  and  $yoz$ -plane are delineated in Fig. 11. The radiation patterns of both radiating elements are almost similar since the two antennas are symmetrically placed and virtually indistinguishable. Therefore, only the radiation patterns at port-2 are analyzed. As seen in Fig. 11, the radiation pattern is skewed at lower frequencies and practically omnidirectional at higher frequencies. The highest radiation at low frequencies (3.8, 6.8, and 8.4 GHz) is largely spread at roughly  $90^\circ$  in both  $xoz$ - and  $yoz$ -planes, thereby showing that the antenna is linearly polarized. The direction of the major lobe of the  $xoz$ -plane is  $90^\circ$  and  $270^\circ$  at

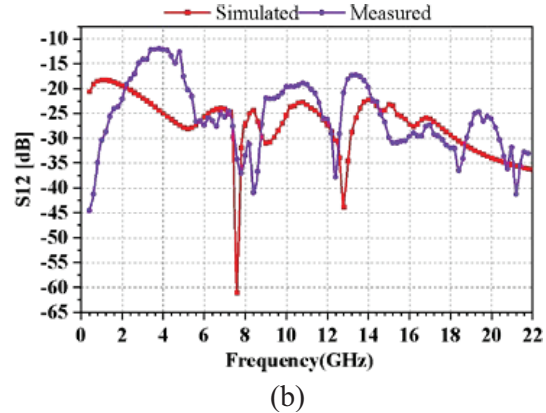


Fig. 10. The results of simulated and measured S-parameters of (a)  $S_{11}$ , (b)  $S_{12}$ .

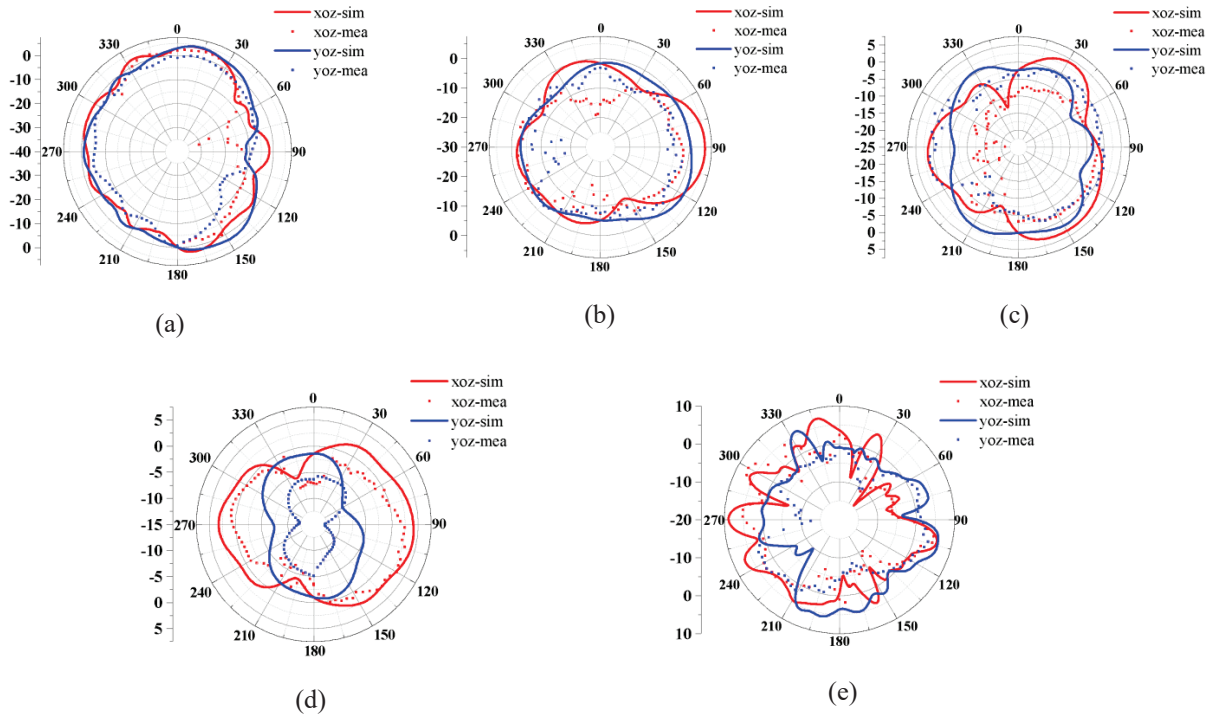


Fig. 11. The simulated and measured radiation patterns of port-2 at (a) 3.8 GHz, (b) 6.8 GHz, (c) 8.4 GHz, (d) 15 GHz, (e) 19.4 GHz.

15 GHz, while that of the yoz-plane is  $0^\circ$  and  $180^\circ$ , implying that the electromagnetic wave propagates vertically on these two surfaces. At 19.4 GHz, the radiation pattern improves and spreads more widely. Essentially, it can be assumed that the antenna possesses a strong radiation performance, and can transmit and receive signals well in various wireless networks.

Figures 12 and 13 demonstrate the radiation efficiency and peak gain of the proposed two-port MIMO antenna. The numbers for just one radiator are pro-

vided here since the proposed MIMO antenna's radiators are symmetrical in design. Radiation efficiency ranges between 70 and 93 percent, indicating that the bulk of the energy is radiated away. At 7.6 GHz, the single antenna achieves a maximum gain of 6.2 dBi. The proposed MIMO antenna has a positive gain value ranging from 3.37 to 6.2 dBi over the whole operating frequency range. Based on the foregoing findings, the proposed two-port MIMO antenna system has good radiation characteristics.

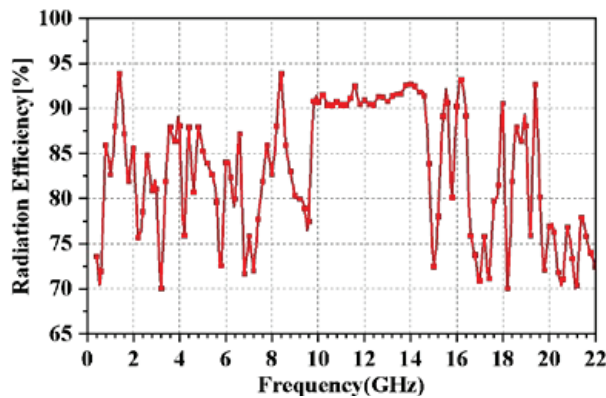


Fig. 12. The radiation efficiency of the proposed two-port MIMO antenna.

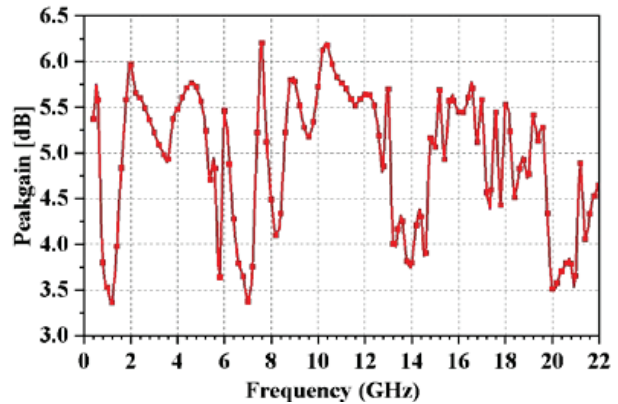


Fig. 13. The peakgain of the proposed two-port MIMO antenna.

### IV. DIVERSITY PERFORMANCE

The MIMO antenna's excellent diversity features provide an improved anti-fading and anti-interference performance, allowing each antenna to operate independently. This section will detail and examine the proposed MIMO antenna's diversity performance in terms of envelope correlation coefficient (ECC), diversity gain (DG), total active reflection coefficient (TARC), channel capacity loss (CCL), and mean effective gain (MEG).

#### A. Envelope correlation coefficient (ECC)

The ECC value is a key metric for assessing the radiation pattern's performance, among MIMO radiators. Fundamentally, the ECC is zero if the polarization orientations of the two antennas are perpendicular to each other. When acting alone, the smaller the value of ECC, the less the antennas are impacted by each other. The specified ECC value of a MIMO system in wireless communication networks is normally less than 0.5, to ensure the effective operation of each antenna [33]. The formula

for calculating the ECC is given as [34]:

$$ECC = \frac{|S_{11}^* S_{12} + S_{21}^* S_{22}|^2}{(1 - |S_{11}|^2 - |S_{21}|^2)(1 - |S_{22}|^2 - |S_{12}|^2)}. \quad (9)$$

Accordingly, the ECC values computed for the proposed MIMO antenna are displayed in Fig. 14 (a). From Fig. 14 (a), the ECC values are less than 0.008, thereby indicating a satisfactory degree of diversity performance.

#### B. Diversity gain (DG)

The Diversity Gain (DG) is a metric that measures how beneficial diversity is. In the working frequency range, the optimal value of DG for achieving an acceptable wireless communication system dependability is approximately 10 dB [35]. Using the ECC value, DG can be determined from Equation (10) [36]. Likewise, Fig. 14 (b) depicts the calculated DGs for the proposed antenna, where it can be observed that the DGs of the MIMO antenna are roughly 10 dB within the operation bands.

$$DG = 10 \times \sqrt{1 - |ECC|}. \quad (10)$$

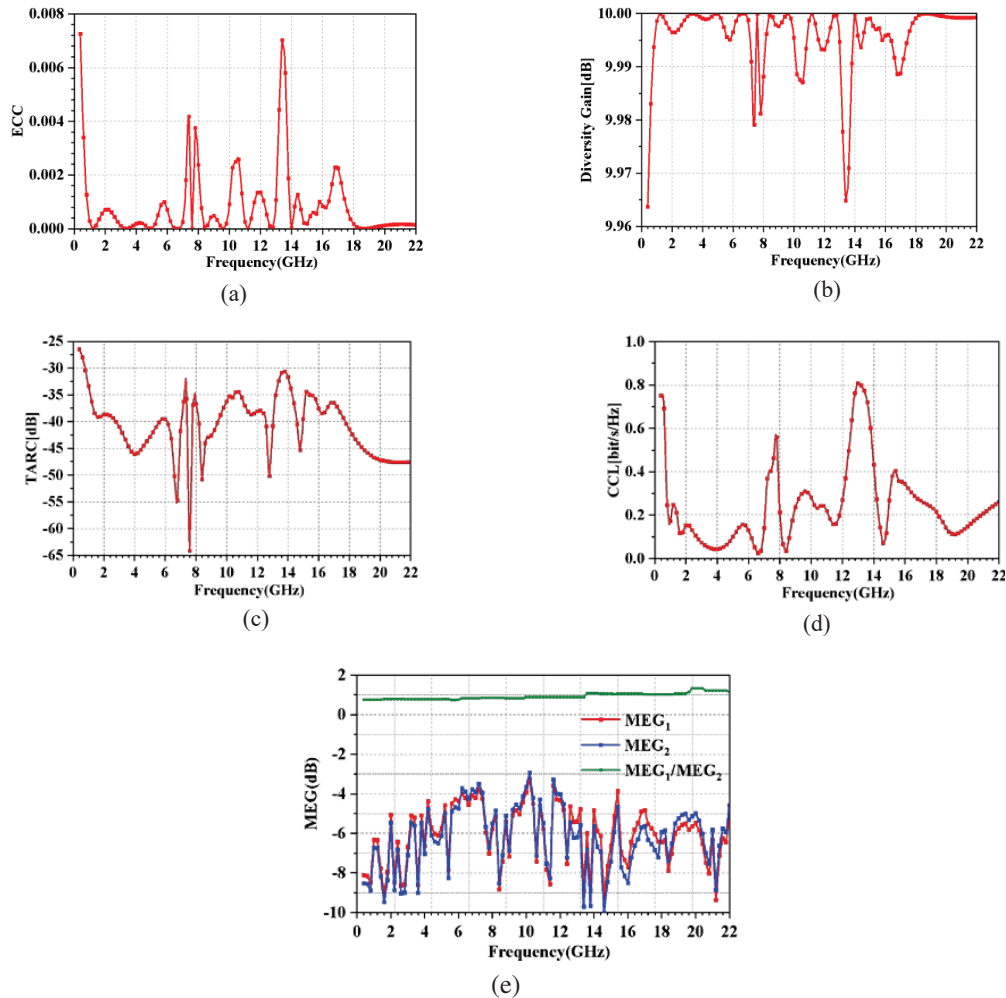


Fig. 14. The calculated diversity performance parameters of (a) ECC, (b) DG, (c) TARC, (d) CCL, (e) MEG.

### C. Total active reflection coefficient (TARC)

In a MIMO system, the metric TARC is related to the total reflected power and total incident power. Ideally, the TARC should be zero, which implies that the antenna receives all of the incident power [37]. The TARC measurement is critical since it can determine the efficacy of the MIMO system. For a two-port system, TARC can be calculated by Equation (11) [38]. The calculated TARC of the proposed MIMO antenna is presented in Fig. 14 (c) which shows that the calculated TARC is below  $-30$  dB at the operative frequency bands.

$$\text{TARC} = -\sqrt{\frac{(S_{11} + S_{12})^2 + (S_{21} + S_{22})^2}{2}}. \quad (11)$$

### D. Channel capacity loss (CCL)

CCL denotes the transmission rate's greatest range without loss, and for a well-designed MIMO system, 0.4 bits/s/Hz is an acceptable value [39]. The CCL can be computed using Equation (12), and the CCL of the proposed MIMO system is shown in Fig. 14 (d). It can be seen that the CCL for the proposed antenna is below 0.4 bits/s/Hz at the operative frequencies.

$$\text{CCL} = -\log_2 |\beta^R|, \quad (12)$$

$$\beta^R = \begin{bmatrix} \beta_{11} & \beta_{12} \\ \beta_{21} & \beta_{22} \end{bmatrix}, \quad (13)$$

where,

$$\beta_{22} = 1 - (|S_{22}|^2 + |S_{21}|^2)$$

$$\beta_{12} = -(S_{11} * S_{12} + S_{21} * S_{22})$$

$$\beta_{21} = -(S_{22} * S_{21} + S_{12} * S_{11}),$$

and  $\beta^R$  indicates the correlation matrix of receiving antenna.

### E. Mean effective gain (MEG)

MEG is another important parameter to characterize the multiparty function, which is the ratio of the average received power to the average incident power and the ideal value is around  $\pm 3$  dB. If the value of  $|MEG_1/MEG_2| < \pm 3$  dB, it represents that the MIMO system will obtain good diversity performance [40]. The MEG is calculated by the Equation (14) and (15), and the results are displayed in Fig. 14 (e). It can be clearly seen that these results are still satisfactory.

$$\text{MEG}_1 = 0.5 [1 - |S_{11}|^2 - |S_{12}|^2], \quad (14)$$

$$\text{MEG}_2 = 0.5 [1 - |S_{12}|^2 - |S_{22}|^2]. \quad (15)$$

## V. PERFORMANCE COMPARISON AND DISCUSSION

Table 2 compares the proposed compact and multiple-band antenna with various previously reported antennas, where a comprehensive comparison is provided in terms of size, isolation, frequency band coverage, and diversity performance. The proposed antenna has more and wider frequency bands compared to other mentioned literature. The proposed decoupled structure is more advantageous compared to [5], [14], [28], [38], [39], [41], [43] and [45]. Of course, the proposed MIMO system also has good diversity and gain characteristics. Evidently, the proposed antenna system has higher performance in the considered indices, as shown in the table, and is a good fit for the mobile terminals used in various wireless communication networks.

Table 2: Performance comparison of proposed two-port MIMO antenna with other works

Reference	Size (mm <sup>2</sup> )	Bandwidth (GHz)	Isolation (dB)	ECC	TARC (dB)	CCL (bits/s/Hz)	Peakgain (dBi)
[5]	100×50	0.803-0.823 2.44-2.9	>17	<0.21			
[8]	120×100	2.453-2.821 5.876-6.892	>20	<0.048	-	-	4-8.6
[10]	60×80	0.89-0.96 1.71-1.88 2.32-2.37 2.575-2.635	>30	-	-	-	3-4
[11]	60×60	2.4-2.48 5.15-5.825	>20	<0.08	-	-	-
[12]	25.5×18	2.4-2.48 5.15-5.825	>20	<0.0043	<-10	-	
[13]	40×40	2.2-3.5 5.2-5.8	>15	<0.05	<-10	<0.5	4
[14]	42×62	2.38-2.52 3.19-6.44	>15	<0.02	-	-	2.9
[24]	35×33	3.1-5.0	>22	<0.1	-	-	-

Table 2: (continued)

Reference	Size (mm <sup>2</sup> )	Bandwidth (GHz)	Isolation (dB)	ECC	TARC (dB)	CCL (bits/s/Hz)	Peakgain (dBi)
[28]	40×40	2.2-2.7 4.9-5.9	>15	<0.1	-	-	2.9-4.5
[37]	52×30	1-4 5.47-8.41 9.36-9.79 10.8-11.38 11.86-13.56 14.54-16.27	20-40	<0.024	-9.96	<0.23	8.86
[39]	60×60	0.85-0.9 1.725-1.77 2.41-2.466	>17	<0.024	-	<0.4	-
[41]	100×65	0.89-0.92 1.78-1.83 2.4-2.68	>16	<0.4	-	-	-
[42]	150×75	3.3-3.84 4.61-5.91	>15	<0.02	-	-	>4.2
[43]	38×37	2.1-2.7 3.29-3.67 4.9-5.35	>20	<0.05			-
[44]	45×25	2.37-2.64 3.39-3.58 4.86-6.98	>15	<0.012	-	<0.4	-
[45]	70×50	2.4-2.48 2.91-3.49 3.27-3.97 3.4-3.8 5.15-5.85	>30	<0.028	-8	<0.3	3-4
[46]	56×30	2.38-2.52 3.28-3.63 5.05-6.77	>16	>0.005	<-10	<0.4	1.5-4.5
[47]	32×20	3.3-7.8 8.0-12.0	>20	<0.05	<-10	<0.35	4
This work	30×20	0.67-7.29 8.07-12.11 14.07-15.41 16.04-22	>18	<0.008	<-30	<0.38	3.37-6.2

## VI. CONCLUSION

This work proposes a compact two-port MIMO antenna for transmission networks, which utilizes a ground plane meandering branch for decoupling. Two ground planes with distinct geometries (Ground-1 and Ground-2) are proposed and discussed in this paper, and it is concluded that the Ground-2, which is based on Ground-1 (with a meandering ground branch, acting as a neutralization line), adds a cross-shaped slot to offer greater benefits in enhancing the antenna port isolation while avoiding any impact on the antenna frequency bands. The proposed MIMO antenna has a relative bandwidth of

166.3%, 40%, 9.1%, and 31.4% and can cover four frequency bands: 0.67-7.29 GHz, 8.07-12.11 GHz, 14.07-15.41 GHz, and 16.04-22 GHz. Moreover, the proposed MIMO antenna has been fabricated and tested, and the obtained results well match the simulations. ECC, DG, TARC, CCL, and MEG, among the diversity performance indicators, are computed and determined to be at adequate levels. The antenna reported in this article has several advantages over other antenna designs in terms of size, frequency band coverage, diversity characteristics, and so on. The designed antenna has also reached the expected requirements put forward by the cooperative unit

in the required size, frequency bands, and polarization mode, and it will also definitely be useful in wireless communication networks.

### ACKNOWLEDGMENT

This research was funded in part by the Anhui Provincial Natural Science Foundation under grant no. 2108085MF200, the Natural Science Foundation of Anhui Provincial Education Department under grant no. KJ2020A0307 and no. KJ2020A0768, the Academic Funding Project for Distinguished Top Talents of Colleges and Universities in Anhui Province under grant no. gxbjZD2021088, and the Graduate Innovation Fund of Anhui University of Science and Technology under grant no. 2021CX2070.

### REFERENCES

- [1] X.-T. Yuan, Z. Chen, T. Gu, and T. Yuan, "A wide-band PIFA-pair-based mimo antenna for 5G smartphones," *IEEE Antennas and Wireless Propagation Letters*, vol. 20, no. 3, pp. 371-375, 2021.
- [2] M. A. Jensen and J. W. Wallace, "A review of antennas and propagation for MIMO wireless communications," *IEEE Transactions on Antennas and Propagation*, vol. 52, no. 11, pp. 2810-2824, 2004.
- [3] K. V. Babu, S. Das, S. Lakrit, S. K. Patel, B. T. P. Madhav, and H. Medkour, "Compact dual-band printed MIMO antenna with very low mutual coupling for WLAN, Wi-MAX, Sub-6 GHz 5G and X-band satellite communication applications," *Progress in Electromagnetics Research C*, vol. 117, pp. 99-114, 2021.
- [4] N. Rajesh Kumar, P. D. Sathya, S. K. A. Rahim, M. Z. M. Nor, A. Alomainy, and A. A. Eteng, "Compact tri-band microstrip patch antenna using complementary split ring resonator structure," *Applied Computational Electromagnetics Society (ACES) Journal*, vol. 36, no. 3, pp. 346-353, 2021.
- [5] M. S. Sharawi, A. B. Numan, M. U. Khan, and D. N. Aloï, "A dual-element dual-band MIMO antenna system with enhanced isolation for mobile terminals," *IEEE Antennas and Wireless Propagation Letters*, vol. 11, pp. 1006-1009, 2012.
- [6] N. K. Mallat and A. Iqbal, "Multi-band printed antenna for portable wireless communication applications," *Progress in Electromagnetics Research Letters*, vol. 84, pp. 39-46, 2019.
- [7] A. Pandya, T. Upadhyaya, and K. Pandya, "Tri-band defected ground plane based planar monopole antenna for Wi-Fi/WiMAX/WLAN applications," *Progress in Electromagnetics Research C*, vol. 108, pp. 127-136, 2021.
- [8] X. Liu, Y. Wu, Z. Zhuang, W. Wang, and Y. Liu, "A dual-band patch antenna for pattern diversity application," *IEEE Access*, vol. 6, pp. 51986-51993, 2018.
- [9] P. Prabhu and S. Malarvizhi, "Compact dual-band hybrid-fractal MIMO system for UMTS and LTE mobile applications," *Applied Computational Electromagnetics Society (ACES) Journal*, vol. 34, no. 1, 2019.
- [10] Y. Yang, Q. Chu, and C. Mao, "Multiband MIMO antenna for GSM, DCS and LTE indoor applications," *IEEE Antennas and Wireless Propagation Letters*, vol. 15, pp. 1573-1576, 2016.
- [11] J. Deng, Z. Wang, J. Li, and L. Guo, "A dual-band MIMO antenna decoupled by a meandering line resonator for WLAN applications," *Microwave and Optical Technology Letters*, vol. 60, pp. 759-765, 2018.
- [12] L. S. Yahya, L. S. Yahya, and K. H. Sayidmarie, "Dual-Band folded monopole mimo antennas with enhanced isolation," *Applied Computational Electromagnetics Society (ACES) Journal*, vol. 36, no. 12, pp. 1569-1578, 2021.
- [13] D. Sarkar and K. V. Srivastava, "Compact four-element SRR-loaded dual-band MIMO antenna for WLAN/WiMAX/WiFi/4G-LTE and 5G applications," *Electronics Letters*, vol. 53 pp. 1623-1624, 2017.
- [14] I. Desde, G. Bozdog, and A. Kustepeli, "Multi-band cpw fed mimo antenna for bluetooth, WLAN, and WIMAX applications," *Microwave and Optical Technology Letters*, vol. 58, no. 9, pp. 2182-2186, 2016.
- [15] P. P. Singh and S. K. Sharma, "Design and fabrication of a triple band microstrip antenna for WLAN, satellite TV and radar app," *Progress in Electromagnetics Research C*, vol. 117, pp. 277-289, 2021.
- [16] Y. Deng, X.-F. Li, and J.-S. Hong, "A compact tri-band miniaturized antenna with parasitic elements loading," *Applied Computational Electromagnetics Society (ACES) Journal*, vol. 35, no. 7, pp. 829-836, 2020.
- [17] J. Deng, J. Li, L. Zhao, and L. Guo, "A dual-band inverted-F MIMO antenna with enhanced isolation for WLAN applications," *IEEE Antennas and Wireless Propagation Letters*, vol. 16, pp. 2270-2273, 2017.
- [18] J. Dong, X. Yu, and L. Deng, "A decoupled multi-band dual-antenna system for WWAN/LTE smartphone applications," *IEEE Antennas and Wireless Propagation Letters*, vol. 16, pp. 1528-1532, 2017.
- [19] F. Zhu, J. Xu, and Q. Xu, "Reduction of mutual coupling between closely packed antenna elements using defected ground structure," *Electronics Letters*, vol. 45, no. 12, pp. 601-602, 2009.

- [20] M. Li, Z. Xu, Y. Ban, Q. Yang, and Q. Zhou, "Eight-port dual-polarized MIMO antenna for 5G smartphone applications," *IEEE 5th Asia-Pacific Conference on Antennas and Propagation (AP-CAP)*, pp. 195-196, 2016.
- [21] H. S. Farahani, M. Veysi, M. Kamyab, and A. Tadjalli, "Mutual coupling reduction in patch antenna arrays using a UC-EBG superstrate," *IEEE Antennas and Wireless Propagation Letters*, vol. 9, pp. 57-59, 2010.
- [22] E. Rajo-Iglesias, Ó. Quevedo-Teruel, and L. Inclán-Sánchez, "Mutual coupling reduction in patch antenna arrays by using a planar EBG structure and a multilayer dielectric substrate," *IEEE Transactions on Antennas and Propagation*, vol. 56, no. 6, pp. 1648-1655, 2008.
- [23] Y. Wang and Z. Du, "A wideband printed dual-antenna with three neutralization lines for mobile terminals," *IEEE Transactions on Antennas and Propagation*, vol. 62, no. 3, pp. 1495-1500, 2014.
- [24] S. Zhang and G. F. Pedersen, "Mutual coupling reduction for UWB MIMO antennas with a wideband neutralization line," *IEEE Antennas and Wireless Propagation Letters*, vol. 15, pp. 166-175, 2015.
- [25] M. G. N. Alsath, M. Kanagasabai, and B. Balasubramanian, "Implementation of slotted meander line resonators for isolation enhancement in microstrip patch antenna arrays," *IEEE Antennas and Wireless Propagation Letters*, vol. 12, pp. 15-18, 2013.
- [26] M. M. Bait-Suwailam, O. Siddiqui, and O. Ramahi, "Mutual coupling reduction between microstrip patch antennas using slotted-complementary split-ring resonators," *IEEE Antennas and Wireless Propagation Letters*, vol. 9, pp. 876-878, 2010.
- [27] M. Leeladhar, M. V. Kartikeyan, and R. K. Pani-grahi, "Offset planar MIMO antenna for omnidirectional radiation patterns," *International Journal of RF and Microwave Computer Aided Engineering*, vol. 28, no. 6, pp. e21274, 2018.
- [28] Y. Liu, L. Yang, Y. Liu, J. Ren, J. Wang, and X. Li, "Dual-band planar MIMO antenna for WLAN application," *Microwave and Optical Technology Letters*, vol. 57, no. 10, pp. 2257-2262, 2015.
- [29] C. Luo, J. Hong, and M. Amin, "Mutual coupling reduction for dual-band MIMO antenna with simple structure," *Radioengineering*, vol. 26, pp. 51-56, 2017.
- [30] N. Moradi, F. Nazari, H. Aliakbarian, and F. A. Namin, "Compact ultrawideband monopole antenna with continuously tunable notch band characteristics," *Progress in Electromagnetics Research C*, vol. 118, pp. 71-81, 2022.
- [31] V. Saritha and C. Chandrasekhar, "A compact wide band MIMO antenna with quadruple notches in UWB," *Progress in Electromagnetics Research M*, vol. 108, pp. 237-247, 2022.
- [32] N. Sharma and S. S. Bhatia, "Metamaterial inspired fidget spinner-shaped antenna based on parasitic split ring resonator for multi-standard wireless applications," *Journal of Electromagnetic Waves and Applications*, vol. 34, no. 10, pp. 1471-1490, 2019.
- [33] Y. Li, C.-Y.-D. Sim, Y. Luo, and G. Yang, "High-isolation 3.5 GHz eight-antenna mimo array using balanced open-slot antenna element for 5G smartphones," *IEEE Transactions on Antennas and Propagation*, vol. 67, no. 6, pp. 3820-3830, 2019.
- [34] M. S. Sharawi, "Printed multi-band MIMO antenna systems and their performance metrics [wireless corner]," *IEEE Antennas and Propagation Magazine*, vol. 55, no. 5, pp. 218-232, 2013.
- [35] R. Gurjar, D. K. Upadhyay, B. K. Kanaujia, and A. Kumar, "A compact modified sierpinski carpet fractal UWB MIMO antenna with square-shaped funnel-like ground stub," *AEU- International Journal of Electronics and Communications*, vol. 117, pp. 153-126, 2020.
- [36] R. Chandel, A. K. Gautam, and K. Rambabu, "Tapered fed compact UWB MIMO-diversity antenna with dual band-notched characteristics," *IEEE Transactions on Antennas and Propagation*, vol. 66, no. 4, pp. 1677-1684, 2018.
- [37] S. S. Bhatia and N. Sharma, "Modified spokes wheel shaped mimo antenna system for multiband and future 5G applications: design and measurement," *Progress in Electromagnetics Research C*, vol. 117, pp. 261-276, 2021.
- [38] S. I. Jafri, R. Saleem, M. F. Shafique, and A. K. Brown, "Compact reconfigurable multiple-inputmultiple-output antenna for ultra wideband applications," *IET Microwaves, Antennas & Propagation*, vol. 10, pp. 413-419, 2015.
- [39] A. Kumar, A. Q. Ansari, B. K. Kanaujia, and J. Kishor, "High isolation compact four-port MIMO antenna loaded with CSRR for multi-band applications," *Frequenz*, vol. 72, pp. 415-427, 2018.
- [40] R. Gurjar, D. K. Upadhyay, B. Kanaujia, and A. Kumar, "A compact U-shaped UWB-MIMO antenna with novel complementary modified minkowski fractal for isolation enhancement," *Progress in Electromagnetics Research C*, vol. 107, pp. 81-96, 2021.
- [41] J.-S. Sun, H.-S. Fang, P.-Y. Lin, and C.-S. Chuang, "Triple-band MIMO antenna for mobile wireless applications," *IEEE Antennas and Wireless Propagation Letters*, vol. 15, pp. 500-503, 2016.

- [42] J. Huang, G. Dong, Q. Cai, Z. Chen, L. Li, and G. Liu, "Dual-band MIMO antenna for 5G/WLAN mobile terminals," *Micromachines*, vol. 12, no. 489, pp. 1-12, 2021.
- [43] A. A. Chaudhari and R. K. Gupta, "A simple tri-band MIMO antenna using a single ground stub," *Progress in Electromagnetics Research C*, vol. 86, pp. 191-201, 2018.
- [44] S. Nand and A. Mohan, "CRLH unit cell loaded tri-band compact MIMO antenna for WLAN/WiMAX applications," *IEEE Antennas and Wireless Propagation Letters*, vol. 16, pp. 1816-1819, 2017.
- [45] R. Saleem, M. Bilal, H. T. Chattha, S. Ur Rehman, A. Mushtaq, and M. F. Shafique, "An FSS based multiband mimo system incorporating 3D antennas for WLAN/WiMAX/5G cellular and 5G Wi-Fi applications," *IEEE Access*, vol. 7, pp. 144732-144740, 2019.
- [46] C. Du, Z. Zhao, X. Wang, and F. Yang, "A compact CPW-fed triple-band mimo antenna with neutralization line decoupling for WLAN/WiMAX/5G applications," *Progress in Electromagnetics Research M*, vol. 103, pp. 129-140, 2021.
- [47] A. G. Alharbi, J. Kulkarni, A. Desai, C.-Y.-D. Sim, and A. Poddar, "A multi-slot two-antenna MIMO with high isolation for sub-6 GHz 5G/IEEE802.11ac/ax/C-band/X-band wireless and satellite applications," *Electronics*, vol. 11, no. 3, pp. 473, 2022.



**Zhonggen Wang** received the Ph.D. degree in electromagnetic field and microwave technique from the Anhui University of China (AHU), Hefei, P. R. China, in 2014. Since 2014, he has been with the School of Electrical and Information Engineering, Anhui University of Science

and Technology. His research interests include computational electromagnetics, array antennas, and reflect arrays.



**Weidong Mu** received the B.E degree from Anhui University of Science and Technology in 2020. He is currently pursuing the M.S degree in Anhui University of Science and Technology. His current research interest includes the theory and design of MIMO antenna.



**Ming Yang** received the Ph.D degree in electromagnetic field and microwave technology from Anhui University (Hefei, P. R. China) in 2019. He used to be the deputy director of the Department of Electronic and Information Engineering of Bozhou University. He is currently a professor at the School of Electronic and Information Engineering, West Anhui University. His research interests include MIMO antennas, SIW antennas, base station antennas and millimeter wave antennas.



**Chenlu Li** received the Ph.D. degree in electromagnetic field and microwave technique from the Anhui University of China (AHU), Hefei, P. R. China, in 2017. Since 2018, she has been with the School Electrical and Information Engineering, Hefei Normal University. Her research interests include computational electromagnetics, array antennas, and reflect arrays.

# Compact Dual-band (28/38 GHz) Patch for MIMO Antenna System of Polarization Diversity

Mai Abo. El-Hassan, Khalid F. A. Hussein, and Asmaa E. Farahat

Microwave Engineering Department  
Electronics Research Institute, Cairo, El-Nozha, 11843, Egypt  
mayaboelhassan@yahoo.com, fkalid@eri.sci.eg, asmaa@eri.sci.eg

**Abstract** – In this work a novel design of a compact-size patch antenna is introduced for dual-band operation at 28/38 GHz. The antenna is constructed as a perforated resonant patch on a defected ground structure (DGS). The development stages of the design are described in detail. The patch is inset-fed through a microstrip line. A four-port MIMO antenna system is constructed using the proposed patch antenna. The antennas are arranged at the corners of a mobile handset in orthogonal orientations which results in polarizations and spatial diversities as well as low mutual coupling. The single antenna as well as the MIMO antenna system performance is assessed through numerical simulations and experimental measurements. The scattering parameters including the reflection and coupling coefficients are calculated using the commercially available CST<sup>®</sup> package and measured experimentally showing good agreement. The proposed antenna has a bandwidth of 0.6 GHz at 28 GHz and 1.17 GHz at 38 GHz. To evaluate the performance of the proposed MIMO antenna system, key performance parameters such as the radiation efficiency, envelope correlation coefficient (ECC), and diversity gain (DG) are investigated. The proposed four-port MIMO antenna system configuration is shown to be suitable for polarization and spatial diversity schemes as illustrated from the resulting radiation patterns. The proposed antenna has high radiation efficiency and the MIMO system has very good values for the ECC and DG over the operating frequency bands. The MIMO system possesses good polarization and spatial diversities with good isolation between the antennas without the use of any isolation enhancement techniques.

**Index Terms** – Fifth Generation, Patch Antenna, MIMO.

## I. INTRODUCTION

Large bandwidth, high data rate and reliability are the main objectives for 5G mobile communications. The multiple channels through multiple-input-multiple-output (MIMO) technology result in high throughput in non-line-of-sight (NLOS) communications. The

International Telecommunications Union (ITU) has allocated some bands for the 5G communications including the 28, 38, 60, and 73 GHz bands [1], [2]. Short range communications and high speed wireless communication have been assigned the unlicensed frequency band 59-64 GHz by the FCC [3], [4].

The polarization diversity in MIMO antenna systems is a diversity scheme that employs several antennas placed in orthogonal orientations [5]. It can be equally incorporated with similar/dissimilar or mixed radiating structures. The orthogonal orientation of the antennas limits the coupling between the different ports [6–8]. In [9], a compact 2×2 dual-band MIMO antenna is proposed with polarization diversity technique for wireless applications in the frequency bands 38/41. A 2×2 circular disc array antenna with conical beam radiation pattern for all polarization senses and polarization diversity at 2.4 GHz is introduced in [10]. In [11], an 8-port planar UWB MIMO antenna is proposed for 5G micro wireless access point applications formed by integrating three monopole strips with different structures and resonant modes. In [12], a dual-band MIMO antenna consisting of two printed dual-band PIFAs with a slotted strip using polarization diversity is proposed for 4G mobile handset application. A compact MIMO antenna for polarization and spatial diversity applications consisting of two planar-monopole antenna elements printed on one side of FR-4 substrate is proposed in [13]. In [14], a planar low-profile wideband circularly polarized MIMO antenna operating in the X-band, with pattern and polarization diversity is introduced where a grounded stub between two linearly polarized monopole antennas is used to realize wideband circular polarization, pattern diversity, and high isolation between the antennas.

This work uses the CST Studio Suite<sup>®</sup> for 3D modeling, designing, analyzing and optimizing the proposed antenna design. The time domain solver is selected for calculating the numerical results including the reflection and transmission coefficients, radiation patterns, and the MIMO performance assessment parameters as the envelope correlation coefficients and the diversity gain.

The hexahedral meshing is applied on the metallic and dielectric parts with. The simulation frequency is set to 20–45 GHz with discretization cell size of 15 cells per wavelength. Also, the simulation accuracy is set to  $-40$  dB. Finally free space boundary conditions are selected to ensure accurate results.

In this paper a diamond patch antenna operates in its principal mode at 28 GHz is modified to have another higher order resonant frequency at 38 GHz. A new design method is proposed to achieve the dual-band operation and a suitable radiation pattern at both operating frequencies and high radiation efficiency with accepted values for maximum gain. The basic idea of the design method is to reduce the size of the diamond patch by eliminating parts of its conducting surface that has negligible surface current density at higher order resonant mode at 38 GHz. This will prevent the higher order surface current density pattern to form on the patch surface and thus nulls will be avoided in the resulting radiation pattern with no effect on the antenna performance at 28 GHz. To get a higher order resonance located at 38 GHz frequency band, a cross-shaped slot is cut in the ground plane of the reduced size 28-GHz patch. The cross-shaped slot disturbs the current distribution in the ground plane resulting in a field configuration between the patch and the ground that is appropriate for radiation at 38 GHz. The dimensions of the patch and the ground slots are set such that the first-order resonance of the structure occurs at 28 GHz and the second resonance occurs at 38 GHz.

The present work introduces a MIMO antenna system with four ports and polarization diversity for operation in the dual-band 28/38 GHz. The reflection and coupling coefficients, and the radiation patterns at each port, are calculated using the commercially available CST<sup>®</sup> package showing the suitability of the proposed MIMO system with polarization diversity scheme for 5G mobile communications. The envelope correlation coefficient (ECC) and diversity gain (DG) are also calculated proving a good performance of the proposed MIMO system.

In section II, the design steps and the operation mechanisms of the 28/38 GHz modified diamond patch antenna on defected ground structure (DGS) are investigated in detail. In Section III, a four port MIMO system configuration that employs polarization diversity in 5G mobile handset is described. The simulation results and the experimental verifications concerning the performance assessment of the proposed diamond patch with detailed discussions are presented in section IV. Comparisons of the antenna size and performance with other published works are presented in section V. At the end of the paper in Section VI, the important conclusions of the present work are discussed.

## II. PROPOSED DUAL-BAND PATCH ANTENNA

In this section, the design of the proposed diamond patch antenna is explained in detail showing the steps of the design starting from a regular diamond patch which resonates at 28 GHz till we reach a compact size dual-band patch antenna resonates at 28 and 38 GHz.

### A. Diamond patch antenna design at 28 GHz

A curved-corners diamond patch antenna with solid ground plane is designed to operate at 28 GHz with the dimensions shown in Fig. 1 (a). The patch is inset fed through a microstrip line. The inset length is 1.35 mm. The used substrate material is Rogers RO3003<sup>TM</sup> with dielectric constant  $\epsilon_r = 3$  and height  $h = 0.25$  mm. The surface current distribution, the reflection coefficient  $|S_{11}|$ , and the radiation pattern in the two principal planes  $\phi = 0^\circ$  and  $\phi = 90^\circ$  of the diamond patch antenna are shown in Figs. 1 (a), (b), and (c), respectively. The maximum antenna gain is 5.98 dBi.

At higher frequencies greater than 28 GHz, the designed patch is considered electrically large. This allows the formation of higher order resonant modes with sidelobes and nulls in the radiation pattern and this is not suitable for a mobile handset antenna. The shape of the

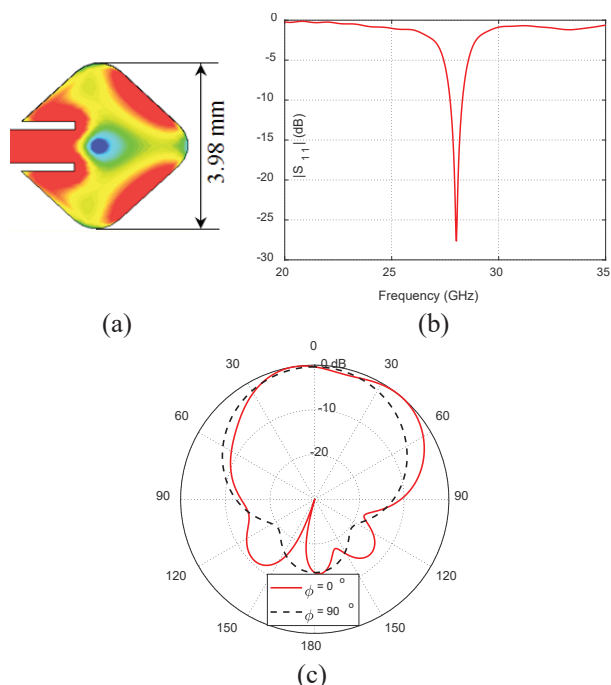


Fig. 1. Resonant diamond patch antenna operating at 28 GHz. (a) Surface current distribution and patch dimensions, (b) reflection coefficient  $|S_{11}|$ , (c) radiation patterns in the two principal  $\phi = 0^\circ$  and  $\phi = 90^\circ$  planes at 28 GHz.

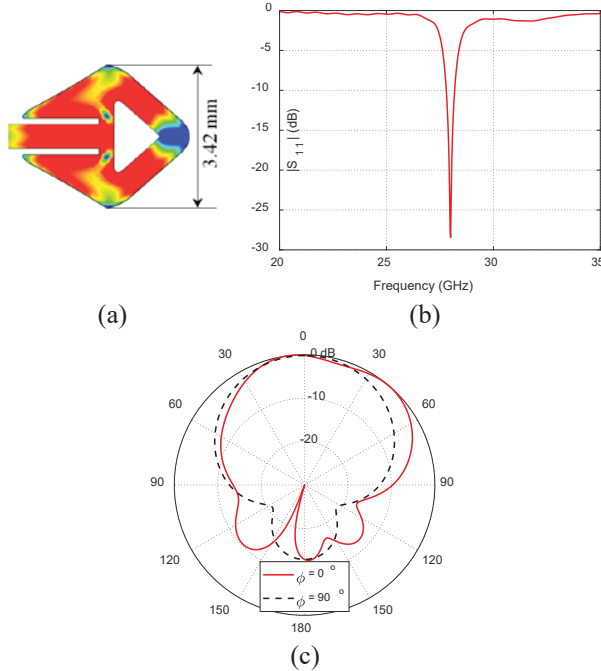


Fig. 2. Modified diamond patch antenna with triangular cut at 28 GHz. (a) Surface current distribution and dimensions, (b) reflection coefficient  $|S_{11}|$ , (c) radiation patterns at 28 GHz.

diamond patch can be modified by removing the conducting surface parts with insignificant current density without affecting the patch performance at 28 GHz. This has the effect of reducing the patch size which in turn allows the formed surface current pattern at higher frequencies to have appropriate distribution for a radiation pattern with accepted shape without nulls.

### B. Diamond patch size reduction

By looking at the surface current distribution in Fig. 1 (a), it can be seen that the center of the patch has very low current density. Thus, the metal at the center of the patch can be removed without significantly affecting the patch performance at 28 GHz. A triangular cut is made at the center of the patch as shown in Fig. 2 (a). The patch dimensions are modified to let it resonate at 28 GHz and also the inset length is changed to 1.64 mm. The new modified patch has a 13% reduction in size from the original diamond patch in Fig. 1 (a). The surface current distribution, reflection coefficient, and the radiation pattern of the modified diamond patch are shown in Figs. 2 (a), 2 (b), and 2 (c), respectively. The maximum antenna gain is 5.57 dBi.

### C. Compact patch design on a defected ground

To further reduce the diamond patch size and in order to get a higher-order resonance at 38 GHz, a crossed-slot defect is made in the ground plane as shown

in Fig. 3 (a). The dimensions of the compact patch together with the dimensions of the crossed-slot defect of the ground plane are set to get the higher-order resonance exactly at 38 GHz. Extensive parametric studies have been done through electromagnetic simulation to arrive at the optimal dimensions of the patch and the ground slots to let the structure resonate at 28 and 38 GHz. By comparing the dimension of the original diamond patch and the patch designed on a defected ground, it can be deduced that the patch dimension has been reduced by about 45%. The surface current distribution of the modified diamond patch antenna with DGS is shown in Fig. 3 (a). The reflection coefficient  $|S_{11}|$  and the elevation radiation patterns at 28 GHz is presented in Figs. 3 (b) and 3 (c), respectively. The maximum antenna gain is 4.39 dBi at 28 GHz. The design of the proposed patch, with its final dimensional parameters, is shown in Fig. 4.

## III. MIMO ANTENNA SYSTEM WITH SPATIAL AND POLARIZATION DIVERSITIES

A MIMO antenna system with four ports is constructed from four elements of the proposed dual-band 28/38 GHz diamond patch antenna for the future 5G mobile handsets. It is proposed that the four antennas of the MIMO system are arranged at the corners of the mobile handset with progressive rotational orientations such that the successive elements have

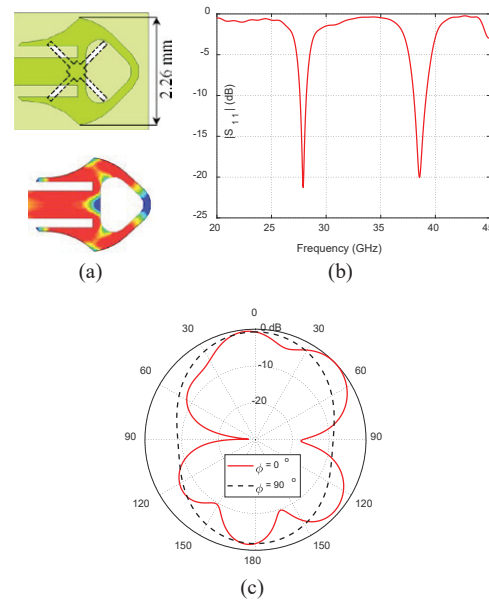


Fig. 3. Design of diamond patch antenna with curved corners and triangular cut on DGS. (a) Patch dimensions and surface current distribution, (b) reflection coefficient  $|S_{11}|$ , (c) elevation radiation patterns at 28 GHz.

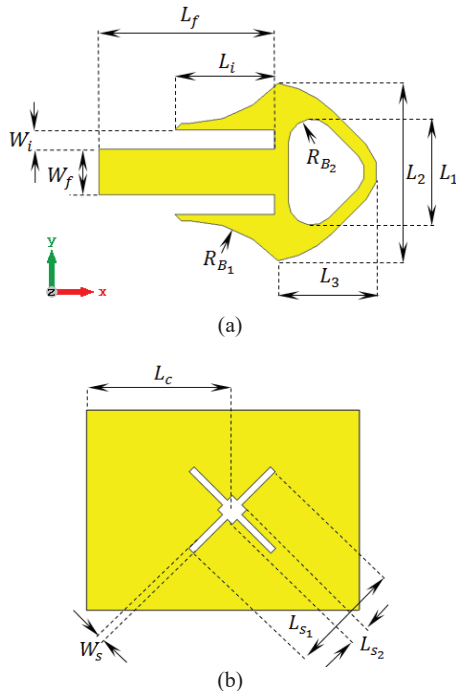


Fig. 4. Design and dimensional parameters of the proposed dual-band diamond patch antenna, (a) patch dimensions, (b) DGS dimensions.

orthogonal orientations as shown in Fig. 5. Two antennas are horizontally oriented ( $x$ -directed) whereas the other two antennas are vertically oriented ( $y$ -directed). This arrangement including the orthogonal orientation and the wide separation among the antennas result in both polarization and spatial diversities which are recommended to enhance the communication system performance for the target 5G applications.

Moreover, this MIMO antenna system can produce circular polarization. If the MIMO antenna elements are fed with progressive rotational phase such that the phase shift between the successive elements is  $90^\circ$  degrees, this will produce circular polarization [15, 16].

The reflection and coupling coefficients at the proposed MIMO antenna system ports are investigated

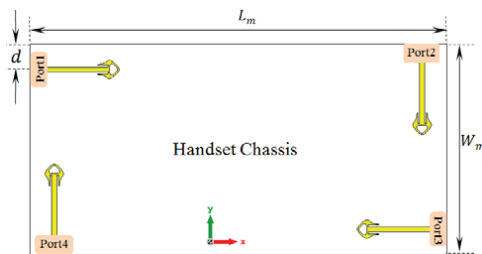


Fig. 5. Four-port MIMO antenna system proposed for 5G mobile phones arranged for polarization diversity.

together with the resulting radiation patterns in the elevation planes through numerical simulation and experimental measurements.

## IV. RESULTS AND DISCUSSIONS

The single element diamond patch antenna as well as the proposed MIMO system performance is studied by numerical simulations and experimental measurements.

### A. Dual-band diamond patch antenna simulations and experimental measurements

In this section, the dual-band patch antenna is subjected to performance assessment through electromagnetic simulation as well as experimental measurements of the impedance matching bandwidth and the radiation patterns.

#### A.1. Operating bands and return loss

The substrate material used in constructing the printed diamond patch antenna is Rogers RO3003C<sup>TM</sup> with dielectric constant  $\epsilon_r = 3$ , dielectric loss tangent  $\tan \delta = 0.0021$ , and height  $h = 0.25$  mm. The conducting metal of the upper and lower surfaces of the substrate is made of high conducting copper. The dimensions of the microstrip line that feeds the modified diamond patch is  $W_f \times L_f$  and have a characteristic impedance of  $50\Omega$ . The antenna is fed through an inset to match the source impedance to  $50\Omega$ . The final values of the design parameters shown in Fig. 4 are given in Table 1. The fabricated prototype is shown in Fig. 6 (a) compared in size to a one-inch metal coin. A long feeding microstrip line is employed for the ease of measurements. It is clear in the figure that the designed patch is very compact in size. The fabricated antenna prototype is fed using an end-launcher connector from Southwest Microwave Co. as shown in Fig. 6 (b). The fabricated prototype is connected to the vector network analyzer (VNA) from Rhode and Schwartz model ZVA67 as shown in Fig. 6 (c) to measure the dependence of the reflection coefficient,  $|S_{11}|$ , over a wide frequency band 20-45 GHz. As shown in Fig. 7, the reflection coefficients at 28 and 38 GHz are  $-21.5$  and  $-20$  dB, respectively. The numerical simulations are verified by experimental measurements showing good agreement. The slight difference between the experimental and simulated results is due to the accuracy of the fabrication process. At 28 GHz, the bandwidth is about 0.6 GHz (27.6 – 28.2 GHz), whereas at 38 GHz, the bandwidth is about 1.17GHz (37.5 – 38.67 GHz). The radiation efficiencies are 87% and 89.5% at 28 and 38 GHz, respectively.

#### A.2. Radiation patterns of the modified diamond printed antenna

The radiation pattern in the principle elevation planes  $\phi = 0^\circ$  and  $\phi = 90^\circ$  is measured experimentally using the setup shown in Fig. 8. A reference antenna

Table 1: Modified diamond patch final dimensions

Dimension	$L_1$	$L_2$	$L_3$	$R_{B_1}$	$R_{B_2}$	$W_i$	$L_c$
Value(mm)	1.34	2.26	1.44	1.5	0.3	0.25	10.58
Dimension	$L_{s_1}$	$L_{s_2}$	$L_i$	$W_f$	$L_f$	$W_s$	
Value(mm)	0.62	3.46	1.27	0.58	11.15	0.2	

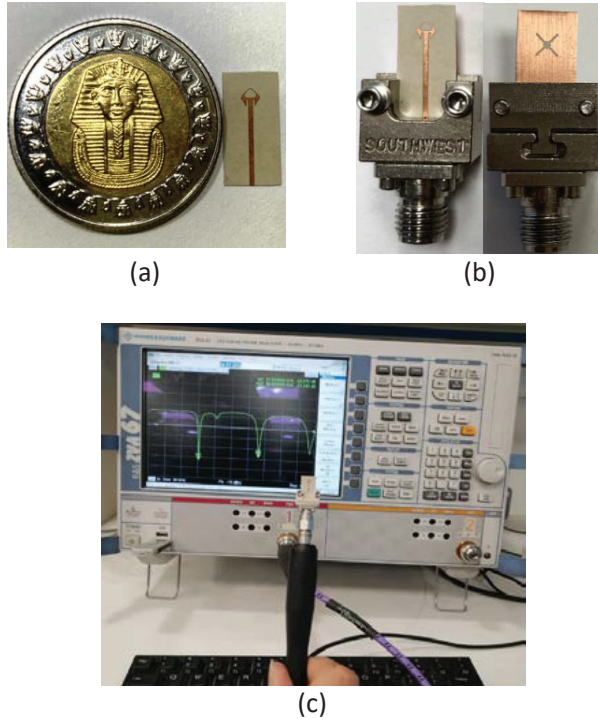


Fig. 6. (a) Fabricated prototype compared to a one-inch metal coin, (b) the top and bottom of the fabricated antenna connected to the end-launch connector, (c) the antenna connected to the VNA model ZVA67.

model LB-018400 is connected to one port of the VNA ZVA67 and the antenna under test (the modified diamond patch) is connected to the second port. The transmission coefficient  $|S_{21}|$  between the two ports is measured. The elevation radiation patterns at 28 GHz are shown in Fig. 9. Also, the E-plane and H-plane radiation patterns corresponding to  $\phi = 0^\circ$  and  $\phi = 90^\circ$ , respectively, at 38 GHz are presented in Fig. 10. The measured radiation patterns show good agreement with the corresponding radiation patterns obtained through numerical simulations using the commercially available CST<sup>TM</sup> package.

## B. MIMO antenna system for polarization and spatial diversity

The MIMO antenna system with four ports shown in Fig. 5 is designed to achieve spatial and polarization diversities. It is subjected to performance assessment through electromagnetic simulation as well as experimental measurements. The results are concerned with the

mutual coupling among the four ports, ECC, DG, and the radiation patterns.

The four antennas are mounted on a handset antenna mockup as shown in Fig. 11 with  $d = 3$  mm,  $L_m = 150$  mm, and  $W_m = 75$  mm. Each antenna has the dimensions listed in Table 1. The handset antenna mockup is shaped like a solid rectangle of overall dimensions  $75 \times 150$  mm<sup>2</sup>. In order to measure the mutual coupling between each two antenna ports in the MIMO system, a 2.4 mm end launch connector is used. The VNA ZVA67 is then employed to measure the transmission coefficient  $|S_{21}|$  between the two ports. The antenna ports which are not tested are terminated with 50 $\Omega$  matched load to prevent any reflections at their ports.

### B.1. MIMO antenna system performance measurements

The dependence of the scattering parameters  $S_{21}$ ,  $S_{43}$ ,  $S_{31}$ ,  $S_{42}$ ,  $S_{41}$ , and  $S_{32}$  on frequency for the proposed MIMO antenna system are obtained through numerical simulations and compared to those obtained experimentally and the results shown in Fig. 12. The experimental results appear to be in agreement with the simulation showing very weak coupling between the MIMO ports.

The ECC and the DG are calculated over a wide frequency range 25-45 GHz for the MIMO antenna system ports and the results are illustrated in Fig. 13. The ECC is near zero at the both of the resonant frequency bands 28/38 GHz and the value of the DG is nearly 10. These values are perfect for a MIMO system. The radiation efficiencies of the MIMO antenna system are about 87 % and 90% at 28 and 38 GHz, respectively.

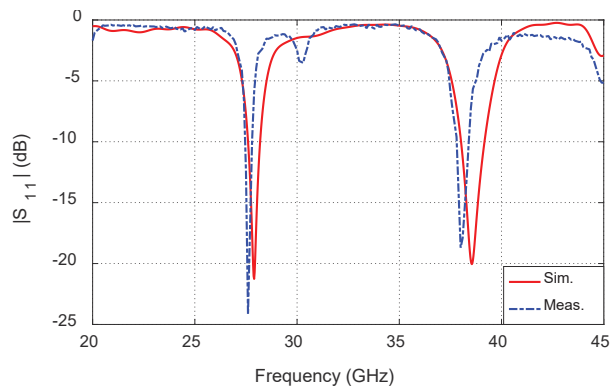


Fig. 7. The reflection coefficient  $|S_{11}|$  dependence on frequency of the proposed diamond patch antenna with the dimensional parameters given in Table 1.

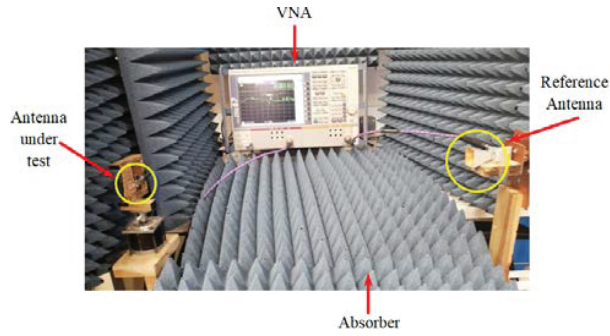


Fig. 8. Measurement setup for measuring the radiation patterns experimentally for the proposed modified diamond patch antenna.

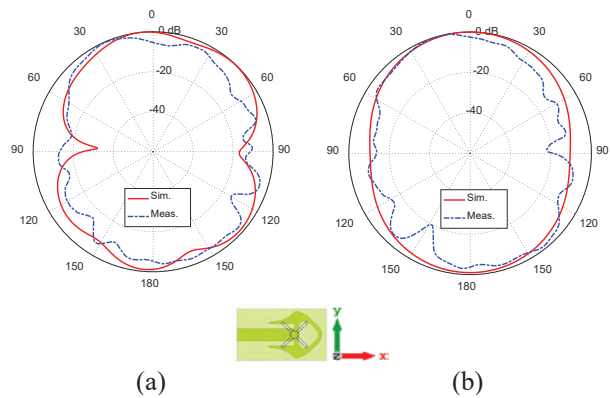


Fig. 9. Modified diamond patch radiation patterns at 28 GHz in the principal planes, (a)  $\phi = 0^\circ$  and, (b)  $\phi = 90^\circ$ .

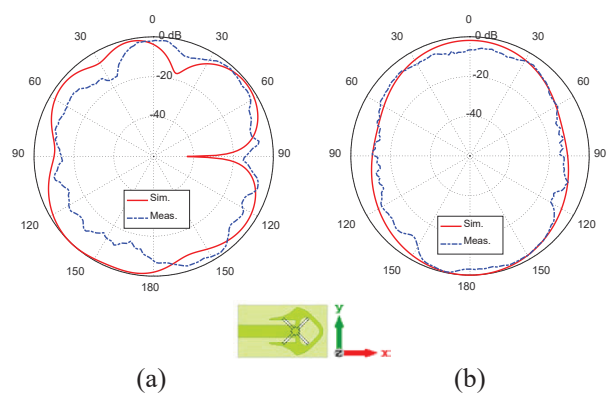


Fig. 10. Modified diamond patch radiation patterns at 38 GHz in the principal planes, (a)  $\phi = 0^\circ$  and, (b)  $\phi = 90^\circ$ .

**B.2. Radiation patterns of the four-port MIMO antenna system**

It should be noted that the term “horizontal polarization” is used to indicate that the electric field is parallel

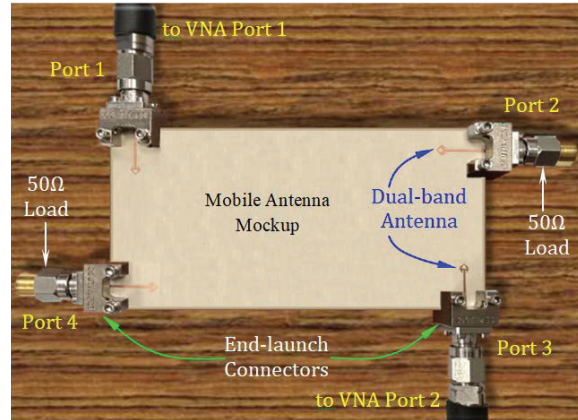


Fig. 11. Mobile phone mockup with the proposed modified diamond patches MIMO system.

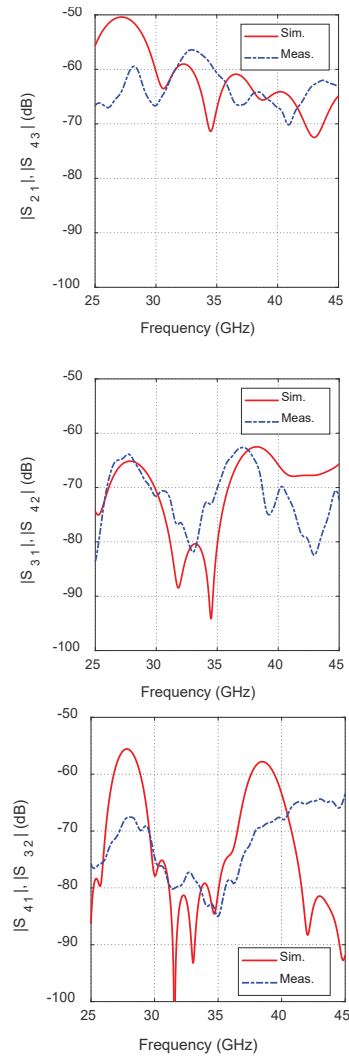


Fig. 12. Scattering parameters  $S_{21}$ ,  $S_{43}$ ,  $S_{31}$ ,  $S_{42}$ ,  $S_{41}$ , and  $S_{32}$  of the MIMO antenna system constructed from four elements of the proposed modified diamond patch antenna.

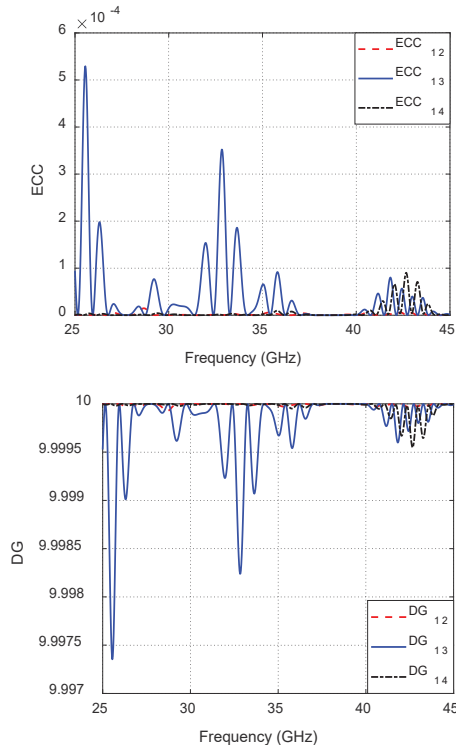


Fig. 13. ECC and DG are calculated over a wide frequency band for the proposed MIMO system constructed from four elements of the modified diamond patch antenna.

to the (horizontal)  $xy$  – plane whereas the term “vertical polarization” indicates that the electric field is parallel to the (vertical)  $zx$  – plane.

The radiation patterns of the vertically and horizontally polarized fields produced at 28 and 38 GHz by the proposed MIMO antenna system in the planes  $\phi = 0^\circ$  and  $\phi = 90^\circ$ , shown in Fig. 3, are presented in Figs. 14–17 when the MIMO antenna system is excited at the different ports. As antenna 1 produces the same polarization as 3, and antenna 2 produces the same polarization as 4, the radiation patterns are demonstrated for antenna 1 and 2 only. It should be noted that the  $x$ -direction is designated for the horizontally polarized electric field and the  $y$ -direction for the vertically polarized electric field.

For each antenna, the cross-polarization ratio is defined as the ratio between the electric field component in the direction normal to the feeding transmission line and that in the direction parallel to it. For example, at antenna 1, the cross polarization ratio is the ratio between the  $y$ -component to the  $x$ -component of the electric field. It is shown in Fig. 14 that the radiated field at 28 GHz is mainly horizontally polarized ( $x$ -directed) where the cross polarization ratio is about  $-35$  dB in the plane  $\phi = 0^\circ$ , and about  $-15$  dB in the plane  $\phi = 90^\circ$ . It is

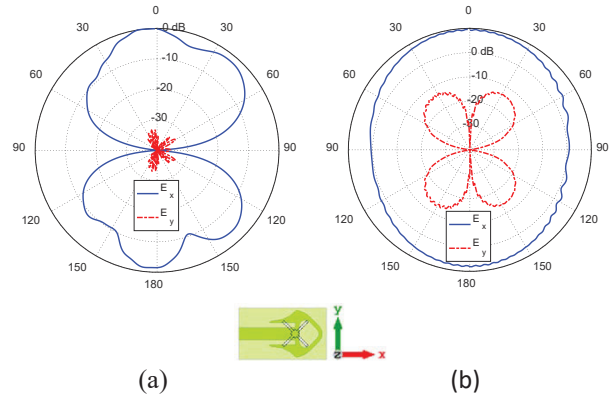


Fig. 14. Radiation patterns for the horizontally ( $x$ -directed) and vertically ( $y$ -directed) polarized fields at 28 GHz in the planes (a)  $\phi = 0^\circ$ , and (b)  $\phi = 90^\circ$  when the MIMO antenna system is fed at port 1.

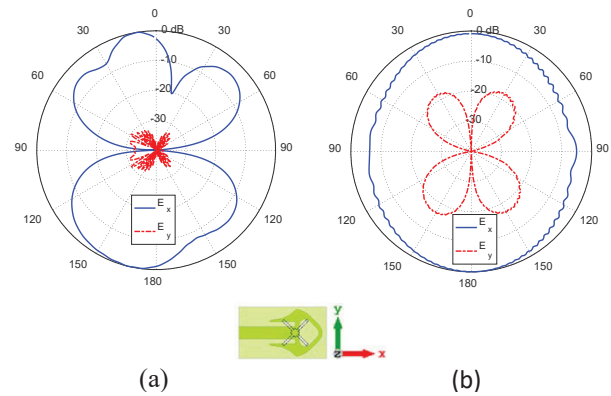


Fig. 15. Radiation patterns for the horizontally ( $x$ -directed) and vertically ( $y$ -directed) polarized fields at 38 GHz in the planes (a)  $\phi = 0^\circ$ , and (b)  $\phi = 90^\circ$  when the MIMO antenna system is fed at port 1.

shown in Fig. 15 that the radiated field is horizontally polarized with cross polarization ratio at 38 GHz of about  $-30$  dB in the plane  $\phi = 0^\circ$ , and  $-12$  dB in the plane  $\phi = 90^\circ$ . It is shown in Figs. 16 and 17 that the radiated field is mainly vertically polarized. Thus, the above results indicate that the proposed MIMO system has satisfactory performance regarding polarization diversity.

## V. PERFORMANCE COMPARISON WITH PUBLISHED WORK

Comparisons among the dual-band patch antenna proposed in the present work and some other published designs are presented in Table 2. The comparison criteria are the size of the antenna, port isolation, efficiency, and gain.

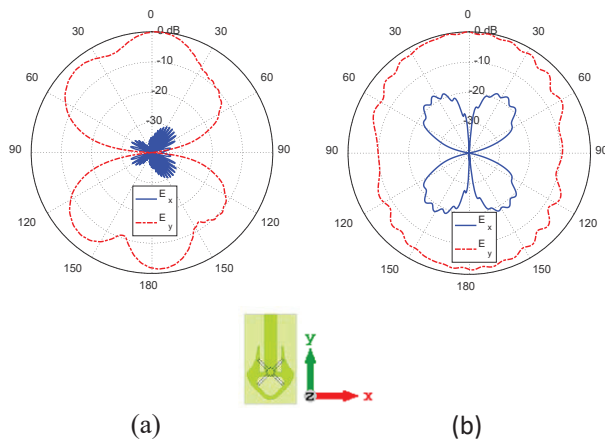


Fig. 16. Radiation patterns for the horizontally ( $x$ -directed) and vertically ( $y$ -directed) polarized fields at 28 GHz in the planes (a)  $\phi = 0^\circ$ , and (b)  $\phi = 90^\circ$  when the MIMO antenna system is fed at port 2.

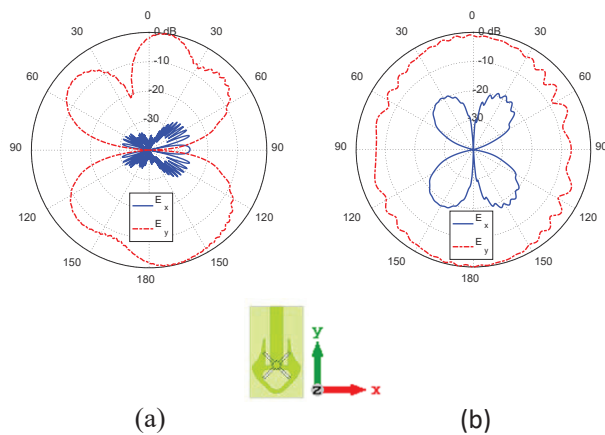


Fig. 17. Radiation patterns for the horizontally ( $x$ -directed) and vertically ( $y$ -directed) polarized fields at 38 GHz in the planes (a)  $\phi = 0^\circ$ , and (b)  $\phi = 90^\circ$  when the MIMO antenna system is fed at port 2.

## VI. CONCLUSIONS

A novel design of a compact-size modified diamond-shape patch antenna is introduced for dual-band operation at 28/38 GHz. The antenna is constructed as a perforated resonant patch on a defected ground structure (DGS). The evolution stages of the design are described in detail. The patch is inset-fed through a microstrip line. A four-port MIMO antenna system is constructed using the proposed patch antenna. The antennas are arranged at the corners of a mobile handset in orthogonal orientations which results in polarizations and spatial diversities as well as low mutual coupling. The single antenna as well as the MIMO antenna system performance is assessed through numerical simulations

Table 2: The proposed modified diamond patch compared to published mm-wave antennas

Work	Center Frequencies (GHz)	Gain (dBi)	Radiation Efficiency (%)	Port Isolation (dB)	Patch Dimensions (mm)
[17]	28/38	7/7.3	96/95	-36	$26.4 \times 20.4$
[18]	28/38	3.7/ 5.1	83/88	-25	$3.7 \times 5.1$
[19]	28/38	9.1/9	98.3/96.5	-40	$8.25 \times 9.45$
[Present]	28/38	4.7/3.75	88/90	-50	$2.26 \times 2.71$

and experimental measurements. The scattering parameters including the reflection and coupling coefficients are calculated using the commercially available CST<sup>TM</sup> package and measured experimentally showing good agreement. The proposed antenna has a bandwidth of 0.6 GHz at 28 GHz and 1.17 GHz at 38 GHz. To evaluate the performance of the proposed MIMO antenna system, key performance parameters such as the radiation efficiency, envelope correlation coefficient (ECC), and diversity gain (DG) are investigated. The proposed four-port MIMO antenna system configuration is shown to be suitable for polarization and spatial diversity schemes as illustrated from the resulting radiation patterns. The proposed antenna has high radiation efficiency and the MIMO system has very good values for the ECC and DG over the operating frequency bands. The MIMO system possesses good polarization and spatial diversities with good isolation between the antennas without the use of any isolation enhancement techniques.

## REFERENCES

- [1] A. Mousazadeh and G. H. Dadashzadeh, "A novel compact UWB monopole antenna with triple band-notched characteristics with EBG structure and two folded V-slot for MIMO/diversity applications," *Applied Computational Electromagnetics Society (ACES) Journal*, vol. 31, no. 1, pp. 1-7, 2016.
- [2] A. E. Farahat and K. F. A. Hussein, "Dual-band (28/38 GHz) MIMO antenna system for 5G mobile communications with efficient DoA estimation algorithm in noisy channels," *Applied Computational Electromagnetics Society (ACES) Journal*, vol. 36, no. 3, 2021.
- [3] S. Jyoti and S. K. Agarwal, "Design a single band microstrip patch antenna at 60 GHz millimeter wave for 5G application," *In 2017 international conference on Computer, Communications and Electronics (Comptelix)*, pp. 227-230, IEEE, 2017.
- [4] H. Wonbin, K. Baek, and S. Ko, "Millimeter-wave 5G antennas for smartphones: Overview and

- experimental demonstration," *IEEE Transactions on Antennas and Propagation*, vol. 65, no. 12, pp. 6250-6261, 2017.
- [5] L. Malviya, R. K. Panigrahi, and M. V. Kartikeyan, "MIMO antennas with diversity and mutual coupling reduction techniques: a review," *International Journal of Microwave and Wireless Technologies*, vol. 9, no. 8, pp. 1763-1780, 2017.
- [6] T. Jiang, T. Jiao, and Y. Li "A low mutual coupling MIMO antenna using periodic multilayered electromagnetic band gap structures," *Applied Computational Electromagnetics Society (ACES) Journal*, vol. 33, no. 3, pp. 305-311, 2018.
- [7] K. Yu, Y. Li, and X. Liu, "Mutual coupling reduction of a MIMO antenna array using 3-D novel meta-material structures," *Applied Computational Electromagnetics Society (ACES) Journal*, vol. 33, no. 7, pp. 758-763, 2018.
- [8] M. Abo El-Hassan, A. E. Farahat, and K. F. A. Hussein, "Compact-size Quad-band patch and MIMO antenna system for 5G mobile handsets," *Progress in Electromagnetics Research C*, vol. 112, pp. 221-238, 2021.
- [9] L. Malviya, R. K. Panigrahi, and M. V. Kartikeyan, "A  $2 \times 2$  dualband MIMO antenna with polarization diversity for wireless applications," *Progress in Electromagnetics Research C*, vol. 61, pp. 91-103, 2016.
- [10] C. Y. D. Sim, "Conical beam array antenna with polarization diversity," *IEEE Transactions on Antennas and Propagation*, vol. 60, no. 10, pp. 4568-4572, 2012.
- [11] X. Li, B. Yu, H. Shen, L. Zhu, and G. Yang, "An 8-port planar UWB MIMO antenna for future 5G micro wireless access point applications," *In 2017 International Applied Computational Electromagnetics Society Symposium (ACES)*, pp. 1-2, IEEE, 2017.
- [12] M. Han and J. Choi, "Dual-band MIMO antenna using polarization diversity for 4G mobile handset application," *Microwave and Optical Technology Letters*, vol. 53, no. 9, pp. 2075-2078, 2011.
- [13] A. Mchbal, N. A. Touhami, H. Elftouh, M. Moubadir, and A. Dkiouak, "Spatial and polarization diversity performance analysis of a compact MIMO antenna," *The 12th International Conference Interdisciplinarity in Engineering*, pp. 647-652, 2019.
- [14] P. Chaudhary, A. Kumar, and B. K. Kanaujia, "A low-profile wideband circularly polarized MIMO antenna with pattern and polarization diversity," *International Journal of Microwave and Wireless Technologies*, vol. 12, no. 4, pp. 316-322, 2019.
- [15] U. H. Khan, B. Aslam, J. Khan, M. Nadeem, H. Shahid, M. A. Azam, Y. Amin, and H. Tenhunen, "A novel asterisk-shaped circularly polarized RFID tag for on-metal applications," *Applied Computational Electromagnetics Society Journal (ACES)*, vol. 31, no. 9, pp. 1035-1042, 2016.
- [16] M. Abo El-Hassan, K. H. Awadalla, and K. F. A. Hussein, "Shaped-beam circularly polarized antenna array of linear elements for satellite and SAR applications," *Wireless Personal Communications*, vol. 110, no. 2, pp. 605-619, 2020.
- [17] F. Alnemr, M. F. Ahmed, and A. A. Shaalan, "A compact 28/38 GHz MIMO circularly polarized antenna for 5 G applications," *Journal of Infrared, Millimeter, and Terahertz Waves*, vol. 42, pp. 338-355, 2021.
- [18] W. Ahmad and W. T. Khan, "Small form factor dual band (28/38 GHz) PIFA antenna for 5G applications," *2017 IEEE MTT-S International Conference on Microwaves for Intelligent Mobility (ICMIM)*, pp. 21-24, IEEE, Mar. 2017.
- [19] A. E. Farahat and K. F. A. Hussein, "28/38 GHz Dual-Band Yagi-Uda antenna with corrugated radiator and enhanced reflectors for 5G MIMO antenna systems," *Progress in Electromagnetics Research C*, vol. 101, pp. 159-172, 2020.



**Asmaa E. Farahat** received her B.Sc. and M.Sc. in the Department of Biomedical engineering, Faculty of Engineering, Cairo University, 2002 and 2006, respectively. She received the PhD 2012, Ain Shams University. She is currently associate professor at the Department of Microwave Engineering at the Electronics Research Institute. She has work experience in scientific research for about 16 years. She has published more than 30 papers in international, regional and local scientific journals and conferences. She has worked as secondary investigator for three research projects. Her research interests are in the areas of antennas, electromagnetic wave propagation, risk assessment of human exposure to microwave radiation, remote sensing systems, and radar systems.



**Khalid F. A. Hussein** received his B.Sc., M.Sc. and Ph.D. degrees in the Department of Electronics and Electrical Communications, Faculty of Engineering, Cairo University, 1990, 1995 and 2001, respectively. He is currently a professor at the Department of Microwave Engineering

at the Electronics Research Institute. He has work experience in scientific research for more than 29 years. He has teaching experience in engineering colleges in many universities for more than 20 years. He has supervised more than seventy doctoral and master theses. He has published more than 100 papers in international, regional and local scientific journals and conferences. He has served as Head of Microwave Engineering Department at the Electronics Research Institute for up to four years. He has been a member of the Egyptian Space Program (currently the Egyptian Space Agency) for more than eight years. He has worked as Principal Investigator for four research projects and Head of Research Group in four other research projects. He designed and implemented several satellite antennas between prototypes and finished products. He has provided scientific consultations and conducted field measurements related to and conducted field measurements related to the design and distribution of mobile communication base station antennas for good signal coverage in behalf of many Egyptian and international companies. His research interests are in the areas of antennas, electromagnetic wave propagation, risk assessment of human exposure to microwave radiation, optical communications, photonics, quantum computing, radar systems, particularly ground penetrating radar (GPR), synthetic aperture radar (SAR), and remote sensing systems.



**M. Abo El-Hassan** received her B.Sc., M.Sc., in Communications and Electronic Engineering, Communications Engineering from Menoufa University, Egypt, in 2007 and 2014 respectively. She received the PhD 2020. She is currently researcher at the Department of

Microwave Engineering at the Electronics Research Institute. Her current research interests include RFID, areas in Antennas, Chipless tags, SAR, Beam shaping. She has published more than 18 papers in international, regional and local scientific journals and conferences.

# Wideband Printed Antipodal Vivaldi Antenna using Straight Slots for UHF DVB-T/T2 Applications

Na-Rae Kwon, Seong-Hyeop Ahn, and Wang-Sang Lee\*

Department of Electronic Engineering  
Gyeongsang National University (GNU), 501, Jinju-daero, Jinju, Gyeongnam, 52828, Republic of Korea  
wsang@gnu.ac.kr

\*Corresponding author

**Abstract** – This paper presents a wideband printed antipodal Vivaldi antenna using straight slots for UHF DVB-T/T2 applications covering a frequency range of 470–862 MHz. The proposed antenna consists of two radiation flares with straight slots and a feeding line. A wideband impedance matching was achieved by inserting the slots between the flares and the feeding line. For the experimental verification of the proposed antenna, it was fabricated on a flat circular printed circuit board (PCB) substrate with a radius of  $0.25 \lambda_0$ , where  $\lambda_0$  is the wavelength at 0.74 GHz (the center frequency of the operating band). The measured  $-10$  dB impedance bandwidth and maximum gain were approximately 72.1% (0.47–1.00 GHz) and 2.57 dBi, respectively. Due to the addition of the slots, the impedance bandwidth of the proposed antenna was improved by approximately 212% compared with the Vivaldi antenna without slots.

**Index Terms** – antipodal Vivaldi antenna, DVB-T/T2, straight slots, UHF applications, wideband.

## I. INTRODUCTION

With the recent advances in internet-of-things technology, stable wireless communication between various devices has become crucial, with high-performance antennas required. A Vivaldi antenna meets the needs of many wireless devices since it exhibits a wide bandwidth, high gain, stable radiation patterns, and low radiation losses. In addition, it is a so-called tapered slot antenna fed into a tapered balanced slot line with a high input impedance (approximately  $300 \omega$ ). To match the high input impedance of the slot line with the  $50 \omega$  feed line, a balun capable of converting the input impedance of the antenna is required. To this end, coplanar and antipodal feeding methods are mainly adopted for Vivaldi antennas [1]. Here, the coplanar Vivaldi antenna (CVA) adopts the balun feed using a microstrip line and a slot, ensuring that the CVA achieves a high gain and symmetrical radiation patterns [2]. However,

due to the exponential tapered radiation unit, the cross-polarization of the CVA is large, the return loss is reduced, and the beam width is narrow. In addition, the CVA has weak competitiveness about miniaturization because the slot line including the balun, is built on one side of the PCB. To overcome these disadvantages, Gazit [3] devised an antipodal Vivaldi antenna (AVA) where the radiation plates, including the tapered balun feed, are fabricated on both sides of PCB, meaning that the AVA is smaller than the CVA. Furthermore, an AVA can be used in systems sensitive to polarization due to the small cross-polarization, while an AVA has better characteristics than a tapered balun CVA since the tapered ground is laid along the microstrip feed line in the former, meaning that the antenna can perform impedance matching with a broader bandwidth [4].

Parasitic patches [5–7] or metamaterials [8–11] are often placed between the flares to improve the directivity of the AVA [12]. Using these characteristics, an AVA can be used for various applications, including ultra-wideband (UWB), radar, Ka-band, and 5G device applications [13], while the antenna has also recently been developed for applications such as vehicle to everything (V2X) communication and energy harvesting [14–15]. Meanwhile, the adoption of AVAs for medical applications has been described in various recent studies [16–17], with the addition of notches inside and outside of the antenna radiation arms in [17] resulting in miniaturization and constant gain. A previous study [18] studied frequency reconfigurable antennas that construct switching circuits with pin diodes at ring-shaped slots between the Vivaldi antenna arms. Recently, AVA using meander line-shaped slots and frequency selective surface (FSS) to enhance the gain and the impedance bandwidth was researched for IoT/WLAN applications [19].

Meanwhile, researchers have turned their attention to investing in a balanced AVA (BAVA), which is essentially an AVA developed to suit the UWB environment. However, while the BAVA has a wider impedance band-

width than the AVA, it involves the disadvantages of having a complex design and being expensive. While many advances concerning Vivaldi antennas have been made through AVA research, bulky structures remain inevitable due to the nature of the Vivaldi antenna itself. As such, various studies have been conducted about the miniaturization of AVAs. Here lowering the operating frequency by increasing the electrical length of the antenna is a typical method for miniaturizing the antenna, while the most commonly used approach involves adopting a corrugate structure for the AVA [24–25], which can effectively increase the electrical length of the antenna [20–23], with the tapered structure allowing for reducing the overall size while maintaining or improving the basic characteristics (e.g., radiation patterns and gains) of the antenna. In a previous study, miniaturization using imaginary effects has also recently been researched [26], while the antenna's characteristics can be improved through using slots in a planar AVA. Here, antenna miniaturization can be implemented to improve the electrical length by applying various-shaped slots to the feeding and radiating parts of the AVA or the space between them [27–29].

Meanwhile, various studies on antennas for ultra-high frequency (UHF) digital television (DTV) bands have been conducted. In [30], DTV transmitting antennas that achieved a low voltage standing wave ratio (SWR) in the DTV broadcasting system using stepped complex impedance transformers and a broadband matching network were devised, whereas in [31], an antenna for Korea's UHD TV frequency range (470–771 MHz) was investigated. This antenna implements various dipoles and patches on the transparent sheets with optical transparency of  $>70\%$ . However, while the antenna is compact and inconspicuous, it has a bulky ground size.

With all this in mind, in this paper, we propose a miniaturized wideband AVA with a straight slot that meets the digital video broadcasting-terrestrial/version-2 (DVB-T/T2) band range (470–862 MHz) [32], a TV frequency band mainly used in Europe and Asia.

## II. PROPOSED ANTIPODAL VIVALDI ANTENNA CONFIGURATION

In general, the width ( $W$ ) of the Vivaldi antenna for effective radiation can be described as follows:

$$W = \frac{c}{f_L} \frac{1}{1.5\sqrt{\epsilon_r + 1}}, \quad (1)$$

where  $c$  is the velocity of light in free space,  $f_L$  is a lower frequency, and  $\epsilon_r$  is a relative permittivity of the substrate [33]. According to (1), when the width of the antenna decreases, the  $f_L$  increases, and the bandwidth decreases. However, by adding straight slots to the feeding portion of the Vivaldi antenna, miniaturization

Table 1: Geometric design parameters of the proposed antenna (unit: mm)

$L_t$	$W_t$	$R$	$L$	$W_b$
168.1	136.5	100	195	85.2
$W_f$	$L_f$	$L_s$	$W_s$	$H$
2.2	45	20	5	67

and bandwidth improvement can be achieved. This is the most effective and simple-to-manufacture slot technology for maintaining the  $f_L$  even if the width of the antenna is reduced. In addition, the proposed antenna was designed with a round-shaped plate of the radiation portion to reduce the side lobe.

The structure of the proposed AVA is shown in Fig. 1 (a). The substrate presents a circular shape and has a radius of  $R=100$  mm. The optimal parameters of the proposed antenna are shown in Table 1. The proposed antenna is fed by a tapered balun to ensure stable signal input. Meanwhile, Figs. 2 (a) and 2 (b) show the equivalent circuit of the proposed antenna with and without straight slots. As shown in Fig. 2 (a), the AVA can be modeled according to the transmission line with antenna impedance ( $Z_{ANT}$ ) whereas as shown in Fig. 2 (b), the straight slots can be equivalent to a series of short stubs for broad impedance matching.

Meanwhile, using a commercial full-wave electromagnetic tool (CST Microwave Studio 2021), the optimal parameter value was found by observing the change in input impedance according to the length, width, and position of the slot. Figure 3 shows the simulated input impedance variations of the proposed antenna on a Smith chart with respect to different widths ( $W_s$ ), lengths ( $L_s$ ) and positions ( $H$ ). The impedance chart in Fig. 3 (a) shows when there are no slots ( $P_1$ ), the input impedance has capacitive reactance, whereas after adding the slots ( $P_2$ ), the inductive reactance increases, resulting in the

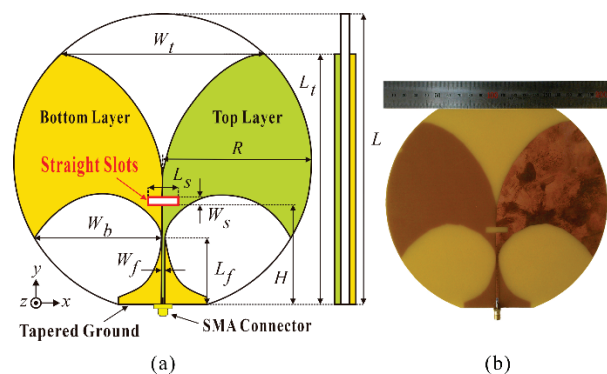


Fig. 1. Proposed antipodal Vivaldi antenna with straight slots: (a) all geometry dimensions with design parameters and (b) a fabricated antenna prototype.

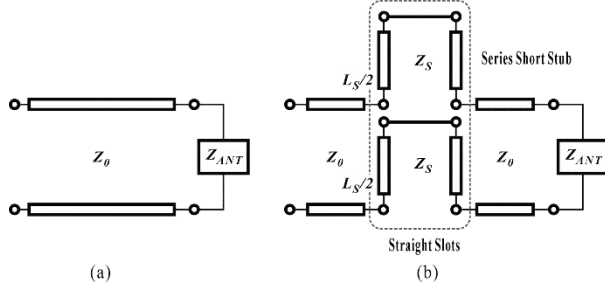


Fig. 2. Equivalent circuit of the proposed antenna (a) without and (b) with straight slots.

total input impedance being a real value. Numerically, the input impedance of the antenna without the slots was  $64.62-j39.79 \omega (P_1)$  at 0.67 GHz, whereas after the addition of the slots, this became  $61.75-j0.09 \omega (P_2)$ . As a result, the impedance trajectory was contained within the SWR 2:1 circle, which improved the impedance bandwidth. As Figs. 3 (b) and 3 (c) show, the input reactance increased significantly compared with the input resistance as the  $L_s$  and  $W_s$  increased, whereas as Fig. 3 (d) shows, the resistance increased when the slot position was closer to the feeding line.

Meanwhile, as shown in Figs. 4 (a) and 4 (b), input

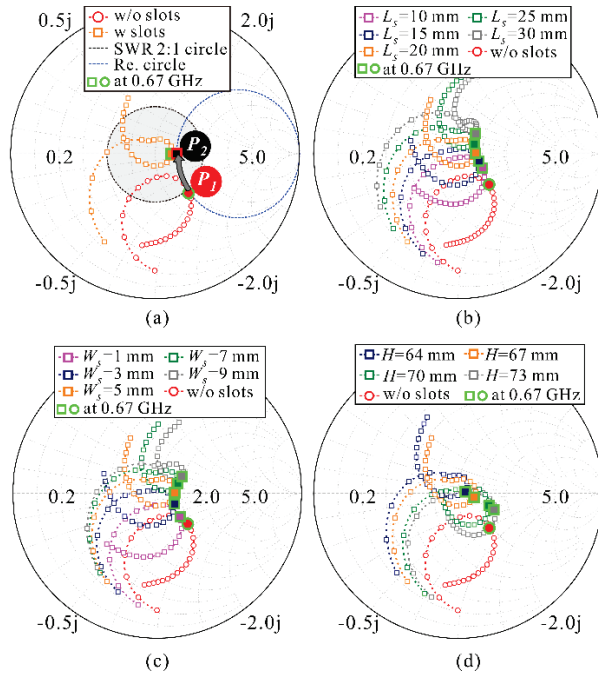


Fig. 3. Simulated input impedance variations on Smith chart: (a) with and without the slots, (b) with respect to various lengths of the slots, (c) with respect to various widths of the slots, and (d) with respect to various positions of the slots.

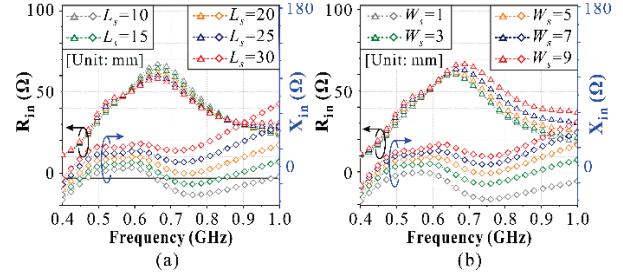


Fig. 4. Real and imaginary parts of the simulated input impedance via the straight slots on the proposed antenna: (a) according to different lengths ( $L_s$ ) and (b) different widths ( $W_s$ ).

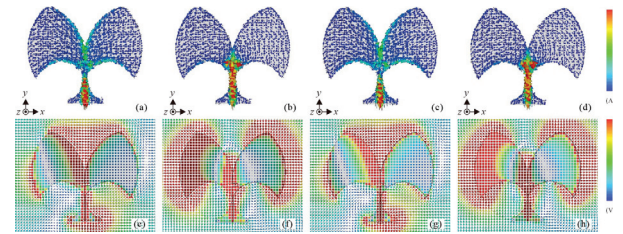


Fig. 5. Simulated surface current and E-field distributions ((a)–(d) and (e)–(f)) of the proposed antenna with respect to the different phases at 670 MHz: (a) and (e)  $0^\circ$ , (b) and (f)  $90^\circ$ , (c) and (g)  $180^\circ$ , and (d) and (h)  $270^\circ$ .

impedance variations depending on the size of the slots were clearly observed. As Fig. 4 (a) shows, the resistance remained almost constant as the  $L_s$  increased, but the reactance increased significantly. Similarly, as shown in Fig. 4 (b), an increase in  $W_s$  resulted in a relatively constant resistance but an increase in reactance. The large slot size increased the inductive reactance of the short serial stub, which verified the equivalent circuit shown in Fig. 2 (b). Meanwhile, the parameter studies allowed us to achieve the impedance bandwidth optimization of the antenna by adjusting the length, width, and position of the slots such that the proposed antenna achieved a wide impedance bandwidth. Here, the frequency band with a reactance close to zero was the widest when the slot size ( $L_s=20$  mm and  $W_s=5$  mm). As a result, The proposed antenna was optimized when the slot size and positions were as follows:  $L_s=20$  mm,  $W_s=5$  mm, and  $H=67$  mm.

Figure 5 shows the simulated surface current and E-field distributions of the proposed antenna for the different phases ( $0^\circ$ ,  $90^\circ$ ,  $180^\circ$ , and  $270^\circ$ ) at 670 MHz.

### III. RESULTS AND DISCUSSIONS

An image of the prototype of the proposed antenna is shown in Fig. 1 (b), with the proposed antenna fabricated on a 1.2 mm thick FR-4 substrate with a relative permittivity ( $\epsilon_r$ ) of 4.3 and a loss tangent ( $\tan$

$\delta$ ) of 0.025. The reference antenna and the proposed antenna were measured in the environment depicted in Fig. 6. The measuring setup for radiation performances utilizing a horn antenna in the anechoic chamber room is shown in Fig. 6 (a). A vector network analyzer was used to measure the reflection coefficient, as shown in Fig. 6 (b). Figure 7 present the simulated and measured results for the reference antenna without slots and the proposed antenna with straight slots. Here, Fig. 7 (a) shows the reflection coefficients to the frequency. The addition of the proposed slots made it possible to match the impedance of the antenna. The measured  $-10$  dB impedance bandwidth of the proposed antenna was 530 MHz, approximately three times higher than the reference antenna (175 MHz). As a result, the proposed antenna achieved an impedance bandwidth of approximately 72.1%. As shown in Fig. 7 (b), the proposed slots improved the gain at the operating frequency. The maximum measured gain of the reference and the proposed antenna was approximately 2.14 and 2.57 dBi, respectively. Furthermore, as shown in Fig. 7 (b), the proposed antenna with added slots has significantly higher measured total efficiency above 0.7 GHz than the reference antenna.

Figure 8 shows the simulated and measured radiation patterns of the proposed antenna at the  $x$ - $y$  and  $x$ - $z$  planes in the operating frequencies of 470, 670,

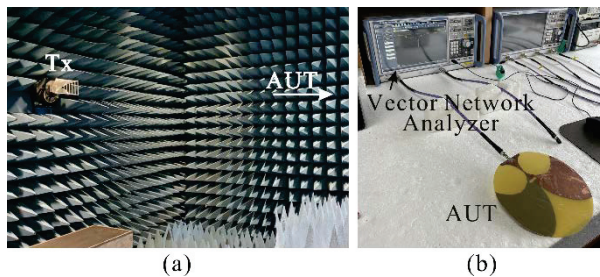


Fig. 6. Measurement setup of the proposed antenna: (a) radiation pattern measurement and (b) reflection coefficient measurement.

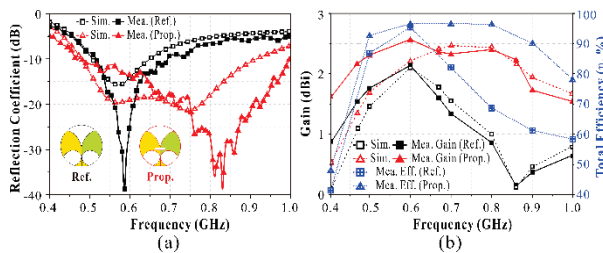


Fig. 7. Simulated and measured results of the proposed antenna in relation to the frequencies: (a) reflection coefficients, (b) peak gains and total efficiency.

Table 2: Comparison between previous works and the proposed antenna

Ref.	$f_c$ (GHz)	BW (%)	Gain (dBi)	Size ( $\lambda_0^3$ )
[5]	17	176.5	12	$6.26 \times 2.95 \times 0.07$
[8]	1.4	100	10.5	$1.11 \times 1.05 \times 0.06$
[14]	4.14	172.9	9.2	$2.07 \times 2.04 \times 2.04$
[15]	6.41	174.7	6.3	$2.16 \times 3.20 \times 0.03$
[26]	1.7	117.7	8.3	$1.16 \times 1.14 \times 0.002$
[29]	0.66	62.4	11.6	$2.66 \times 1.00 \times 0.34$
[30]	0.62	54.5	2.4	$0.60 \times 0.22 \times 0.13$
[34]	2.4	75	6.66	$0.95 \times 0.95 \times 0.01$
<b>Prop.</b>	<b>0.74</b>	<b>77.9</b>	<b>2.57</b>	<b><math>0.48 \times 0.49 \times 0.002</math></b>

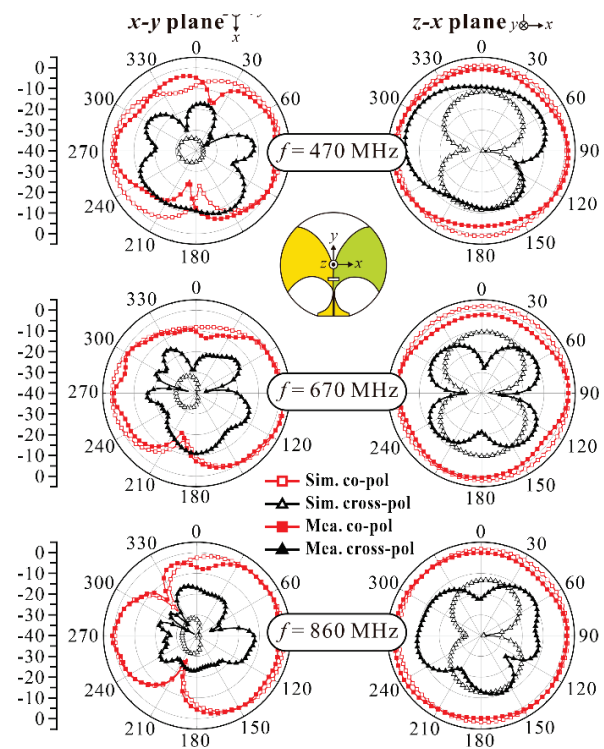


Fig. 8. Simulated and measured radiation patterns of the proposed antenna at the  $x$ - $y$  and  $x$ - $z$  planes in the operating frequencies of 470, 670, and 860 MHz.

and 860 MHz. Here, the proposed antenna presented an omnidirectional radiation pattern in the azimuth plane, whereas in the elevation plane, as the frequency increased, the antenna presented a directional beam in the  $y$ -axis direction.

Table 2 presents a comparison of the proposed antenna with those reported in previous works. Compared with the Vivaldi antennas described in previous studies, the proposed antenna demonstrated an improved impedance bandwidth due to the addition of the straight

slots to the antenna radiator. It was comparatively small in size ( $0.48 \lambda_0 \times 0.49 \lambda_0 \times 0.002 \lambda_0$ ) based on the center frequency wavelength ( $f_c$ ).

#### IV. CONCLUSION

In this paper, a method for miniaturizing a wideband Vivaldi antenna using straight slots was presented. The method can be easily implemented by adding slots to the antenna radiator. Using this method, we devised a wideband printed AVA for UHF DVB-T/T2 applications. Both the proposed antenna and the miniaturization methods will prove useful in designing various directional antennas.

#### ACKNOWLEDGMENT

This work was supported in part by the Korean Government (MSIT) through the National Research Foundation of Korea under Grant 2019R1C1C1008102 and in part by the MSIT (Ministry of Science and ICT), Korea, under the ICAN (ICT Challenge and Advanced Network of HRD) program (IITP-2022-RS-2022-00156409) supervised by the IITP (Institute of Information & Communications Technology Planning & Evaluation).

#### REFERENCES

- [1] Bhattacharjee, A. Bhawal, A. Karmakar, A. Saha, and D. Bhattacharya, "Vivaldi antennas: a historical review and current state of art," *Int. J. Microw. Wirel. Tech.*, vol. 13, no. 8, pp. 833-850, 2021.
- [2] J. Puskely, J. Lacik, Z. Raida, and H. Arthaber, "High gain dielectric loaded Vivaldi antenna for Ka-band application," *IEEE Antennas Wirel. Propag. Lett.*, vol. 15, pp. 2004-2007, 2016.
- [3] Gazit and Ehud, "Improved design of the vivaldi antenna," *IEE Proceedings H-Microw., Antennas Propag.*, vol. 135, no. 2, pp. 89-92, 1988.
- [4] C. J. Hodgkinson, D. E. Anagnostou, and S. K. Podilchak, "Compact UWB antipodal vivaldi array for beam steering applications," *2021 15th European Conf. Antennas Propag.*, pp. 1-5, 2021.
- [5] I. T. Nassar and T. M. Weller, "A novel method for improving antipodal Vivaldi antenna performance," *IEEE Trans. Antennas Propag.*, vol. 63, no. 7, pp. 3321-3324, 2015.
- [6] Z. Li, X. Kang, J. Su, Q. Guo, Y. Yang, and J. Wang, "A wideband endfire conformal Vivaldi antenna array mounted on a dielectric cone," *Int. J. Antennas Propag.*, vol. 2016, 2016.
- [7] X. Zhang, Y. Chen, M. Tian, J. Liu, and H. Liu, "A compact wideband antipodal Vivaldi antenna design," *Int. J. RF Microw. Comput.-Aided Eng.*, vol. 29, no. 4, pp. e21598, 2018.
- [8] H. Cheng, H. Yang, Y. Li, and Y. Chen, "A compact vivaldi antenna with artificial material lens and sidelobe suppressor for GPR applications," *IEEE Access*, vol. 8, pp. 64056-64063, 2020.
- [9] S. Zhu, H. Liu, and P. Wen, "A new method for achieving miniaturization and gain enhancement of vivaldi antenna array based on anisotropic metasurface," *IEEE Trans. Antennas Propag.*, vol. 67, no. 3, pp. 1952-1956, 2019.
- [10] M. Sun, Z. N. Chen, and X. Qing, "Gain enhancement of 60-GHz antipodal tapered slot antenna using zero-index metamaterial," *IEEE Trans. Antennas Propag.*, vol. 61, no. 4, pp. 1741-1746, 2013.
- [11] X. Li, H. Zhou, Z. Gao, H. Wang, and G. Lv, "Metamaterial slabs covered UWB antipodal vivaldi antenna," *IEEE Antennas Wirel. Propag. Lett.*, vol. 16, pp. 2943-2946, 2017.
- [12] A. S. Dixit and S. Kumar, "A survey of performance enhancement techniques of antipodal vivaldi antenna," *IEEE Access*, vol. 8, pp. 45774-45796, 2020.
- [13] S. Kumar, A. S. Dixit, R. R. Malekar, H. D. Raut, and L. K. Shevada, "Fifth generation antennas: A comprehensive review of design and performance enhancement techniques," *IEEE Access*, vol. 8, pp. 163568-163593, 2020.
- [14] P. A. Dzagbletey, J. Shim, and J. Chung, "Quarter-wave balun fed vivaldi antenna pair for V2X communication measurement," *IEEE Trans. Antennas Propag.*, vol. 67, no. 3, pp. 1957-1962, 2019.
- [15] J. Schneider, M. Mrnka, J. Gamec, M. Gamcova, and Z. Raida, "Vivaldi antenna for RF energy harvesting," *Radioengineering*, vol. 25, no. 4, pp. 666-671, 2016.
- [16] A. M. De Oliveira, A. M. de Oliveira Neto, and M. B. Perotoni, "A fern antipodal vivaldi antenna for near-field microwave imaging medical applications," *IEEE Trans. Antennas Propag.*, vol. 69, no. 12, pp. 8816-8829, Dec. 2021.
- [17] A. Alkhaibari, A. F. Sheta, and I. Elshafiey, "Notched antipodal vivaldi antenna for biomedical applications," *2017 7th Int. Conf. Model. Simul. Appl. Optim.*, pp. 1-4, 2017.
- [18] R. Herzi, A. Gharsallah, M. A. Boujemaa, and F. Choubani, "Frequency reconfigurable Vivaldi antenna with switched resonators for wireless applications," *Int. J. Adv. Comput. Sci. Appl.*, vol. 10, no. 5, pp. 414-421, 2019.
- [19] F. Güneş, İ. Ö. Evranos, M. A. Belen, P. Mahouti, and M. Palandöken, "A compact triband antipodal Vivaldi antenna with frequency selective surface inspired director for IoT/WLAN applications," *Wireless Netw.*, vol. 27, pp. 3195-3205, 2021.
- [20] A. M. Abbosh, "Miniaturized microstrip-fed tapered-slot antenna with ultrawideband

- performance,” *IEEE Antennas Wirel. Propag. Lett.*, vol. 8, pp. 690-692, 2009.
- [21] A. S. Dixit and S. Kumar, “A miniaturized antipodal vivaldi antenna for 5G communication applications,” *2020 7th Int. Conf. Signal Process. Integr. Netw.*, pp. 800-803, 2020.
- [22] Moosazadeh and Mahdi, “Sidelobe level reduction using teflon for a microwave and millimetre-wave antipodal vivaldi antenna,” *IET Microw. Antennas Propag.*, vol. 14, no. 6, pp. 474-478, 2020.
- [23] M. Abbak, M. N. Akıncı, M. Ç ayören, and I. Akduman, “Experimental microwave imaging with a novel corrugated vivaldi antenna,” *IEEE Trans. Antennas Propag.*, vol. 65, no. 6, pp. 3320-3307, 2017.
- [24] R. Natarajan, J. V. George, M. Kanagasabai, and A. Kumar Shrivastav, “A compact antipodal vivaldi antenna for UWB applications,” *IEEE Antennas Wirel. Propag. Lett.*, vol. 14, pp. 1557-1560, 2015.
- [25] Dastranj and Aliakbar, “Wideband antipodal vivaldi antenna with enhanced radiation parameters,” *IET Microw. Antennas Propag.*, vol. 9, no. 15, pp. 1755-1760, 2015.
- [26] Z. Yin, G. He, X. Yang, and S. Gao, “Miniaturized ultrawideband half- mode vivaldi antenna based on mirror image theory,” *IEEE Antennas Wirel. Propag. Lett.*, vol. 19, no. 4, pp. 695-699, 2020.
- [27] Y. Dong, J. Choi, and T. Itoh, “Vivaldi antenna with pattern diversity for 0.7 to 2.7 GHz cellular band applications,” *IEEE Antennas Wirel. Propag. Lett.*, vol. 17, no. 2, pp. 247-250, 2018.
- [28] Y. Liu, W. Zhou, S. Yang, W. Li, P. Li, and S. Yang, “A novel miniaturized vivaldi antenna using tapered slot edge with resonant cavity structure for ultrawideband applications,” *IEEE Antennas Wirel. Propag. Lett.*, vol. 15, pp. 1881-1884, 2016.
- [29] P. Ludlow and V. F. Fusco, “Antipodal vivaldi antenna with tuneable band rejection capability,” *IET Microw. Antennas Propag.*, vol. 5, no. 3, pp. 372-378, 2011.
- [30] H. Yu, S. Fang, L. Jiang, and H. Liu, “A full-band digital television transmitting antenna array with dual-layer bowtie dipole unit,” *IEEE Access*, vol. 8, pp. 102138-102145, 2020.
- [31] P. Duy Tung and C. W. Jung, “Optically transparent wideband dipole and patch external antennas using metal mesh for UHD TV applications,” *IEEE Trans. Antennas Propag.*, vol. 68, no. 3, pp. 1907-1917, 2020.
- [32] C. Huang, B. Jeng, and J. Kuo, “Grating monopole antenna for DVB- T applications,” *IEEE Trans. Antennas Propag.*, vol. 56, no. 6, pp. 1775-1776, 2008.
- [33] J. Y. Siddiqui, Y. M. M. Antar, A. P. Freundorfer, E. C. Smith, G. Morin, and T. Thayaparan, “Design of an ultrawideband antipodal tapered slot antenna using elliptical strip conductors,” *IEEE Antennas Wirel. Propag. Lett.*, vol. 10, pp. 251-254, 2011.
- [34] D. Oliveira, M. Alexandre, A. M. de Oliveira Neto, and M. B. Perotoni, “A fern antipodal vivaldi antenna for near-field microwave imaging medical applications,” *IEEE Trans. Antennas Propag.*, vol. 69, no. 12, pp. 8816-8829, 2021.



**Na-Rae Kwon** received the B.S. degree in electronic engineering from Gyeongsang National University (GNU), Jinju, South Korea, in 2017, where she is currently pursuing the M.S. degree.

Her current research interests include wireless power transfer and communication systems, RF/Microwave circuit and system, and RFID/IoT sensors.



**Seong-Hyeop Ahn** received the B.S. and M.S. degrees in electronic engineering from Gyeongsang National University, Jinju, South Korea, in 2018 and 2020, respectively, and is currently working toward the Ph.D. degree.

His research interests are near- and far-field wireless power transfer and data communication system, high-power microwave system with slotted waveguides, and RF/microwave circuit and antenna designs.



**Wang-Sang Lee** received the B.S. degree from Soongsil University, Seoul, South Korea, in 2004, and the M.S. and Ph.D. degrees in electrical engineering from the Korea Advanced Institute of Science and Technology (KAIST), Daejeon, South Korea, in 2006 and 2013,

respectively. From 2006 to 2010, he was with the Electromagnetic Compatibility Technology Center, Digital Industry Division, Korea Testing Laboratory (KTL), Ansan-si, South Korea, where he was involved in the international standardization for radio frequency identification (RFID) and photovoltaic systems as well as electromagnetic interference (EMI)/EMC

analysis, modeling, and measurements for information technology devices. In 2013, he joined the Korea Railroad Research Institute (KRRRI), Uiwang-si, South Korea, as a Senior Researcher, where he was involved in the position detection for high-speed railroad systems and microwave heating for low-vibration rapid tunnel excavation system. Since 2014, he has been an Associate Professor with the Department of Electronic Engineering, Gyeongsang National University (GNU), Jinju, South Korea. From 2018 to 2019, he was a Visiting Scholar with the ATHENA Group, Georgia Institute of Technology, Atlanta, GA, USA. His current research interests include near- and far-field wireless power and

data communications systems, RF/microwave antenna, circuit, and system design, RFID/Internet of Things (IoT) sensors, and EMI/EMC.

Dr. Lee is a member of IEC/ISO JTC1/SC31, KIEES, IEIE, and KSR. He was a recipient of the Best Paper Award at IEEE RFID in 2013, the Kim Choong-Ki Award– Electrical Engineering Top Research Achievement Award at the Department of Electrical Engineering, KAIST, in 2013, the Best Ph.D. Dissertation Award at the Department of Electrical Engineering, KAIST, in 2014, the Young Researcher Award at KIEES in 2017, and the Best Paper Awards at IEIE in 2018 and KICS in 2019.

# Dual-band Dual-polarized Dipole Antenna for Gain and Isolation Enhancements

Peng Chen<sup>1</sup>, Lihua Wang<sup>1</sup>, Yumeng Lin<sup>2</sup>, and Dan Wang<sup>1</sup>

<sup>1</sup>School of Ocean Information Engineering  
Jimei University, Xiamen 361021, China  
chenpeng@jmu.edu.cn, liliya@jmu.edu.cn, wangdan@jmu.edu.cn

<sup>2</sup>College of Navigation  
Jimei University, Xiamen 361021, China  
202012861023@jmu.edu.cn

**Abstract** – A  $\pm 45^\circ$  linear-polarized cross-dipole with enhanced gain and isolation has been designed as an example for 5G applications in this paper. By adding stepped reflector and combined director, the isolation and radiation performance of the antenna can be improved significantly. According to the experimental results, the bandwidths with reflection coefficient lower than 10 dB in the low frequency band and high frequency band are 9.5% (3.2–3.52 GHz) and 17.5% (3.86–4.6 GHz), respectively. The dual band can cover 3.3–3.6 GHz and 4.4–4.5 GHz for 5G bands proposed by China's IMT propulsion group. Therefore, the proposed antenna can be widely used in wireless detection, transmission and communication. The isolation of low frequency band and high frequency band can reach above 26 dB and above 22 dB. The average gain is approximately 10.2 dBi in the low frequency band, but the other band is around 6.37 dBi. Compared with commonly used base station antennas, the proposed antenna has been dramatically improved in terms of size, bandwidth, and other electromagnetic properties.

**Index Terms** – cross-dipole, 5G, dual-band, high gain.

## I. INTRODUCTION

With the development of mobile communication systems, higher requirements are put forward for communication capacity and communication rate [1]. The performance of base station antenna directly affects the whole wireless communication system [2–6]. It is necessary to design an antenna that works in multi frequency band and has excellent performance. However, due to the complex communication environment, the signal received by the client is often affected by the multipath effect, resulting in signal amplitude decline, delay extension and other problems [7]. In order to solve the problem caused by multipath effect, the most effective method is diversity technology.  $\pm 45$ -degree

dual-polarization antennas [8–9] have been widely used to deal with multipath effect, which can not only reduce the installation cost and installation space, but also enhance signal reception quality [10].

Generally, the base station antenna should have the characteristics of stable radiation pattern, high isolation and gain. However, how to improve the multi-port isolation of the antenna is still a great challenge. Gain and bandwidth are also important parts of antenna performance. Many related literatures have been reported on the high isolation of dual polarized antennas. At present, the commonly used methods are mainly based on the application of metamaterials, such as artificial magnetic conductors (AMC) [11], defected ground structure (DGS) [12], electromagnetic band gap (EBG) [13–15] and reflector. High isolation and stable unidirectional radiation patterns have been achieved by using metamaterials in references [16] and [17]. However, the design structure and process implementation are very complex. A reflector with simple structure design can achieve the same effect, and it is easier to realize, as described in References [18] and [19]. However, when the antenna works in multiple frequency bands (at the same height from the reflector) [20–22], it is not conducive to improve the isolation degree of the antenna. Obviously, designing reflectors corresponding to different frequency bands to improve antenna performance is the most effective and easy to manufacture in technology.

On the other hand, high gain has always been an important feature of dual-polarized antenna designs. The common method is to add metal strip director and parasitic elements [23–24]. A director can be placed above or around the dipole (same level), which can improve the gain but has the disadvantage of larger antenna sizes. Compared with the former, the parasitic element can make the structure of the antenna more compact, but the gain improvement is limited. Therefore, a stacked director structure placed vertically over the antenna has been

proposed. As the number of directors increases, the gain increases, according to literature [25–26]. Based on the principle of Yagi antenna [27], the designed director can not only enhance the gain, but also will not increase the overall antenna size.

In this work, a combination of stepped reflector and director has been proposed to improve the low isolation and gain problem in different frequency bands. A reflector with appropriate distance is designed according to different frequency bands to improve the isolation of the low frequency bands and high frequency bands, and reduce the sidelobe. The reflector distances were designed appropriately according to different frequency bands, in order to improve the isolation of both low and high frequency bands and reduce the side lobes at the same time. The director was vertically placed over the main radiator to improve the gain and directivity of the antenna in the working frequency band. The detailed design is described below.

**II. ANTENNA GEOMETRY AND ANALYSIS**

The configuration of the proposed dipole antenna with reflectors and directors loaded is showed in Fig. 1. The proposed antenna comprises a microstrip feed, an integrated balun, a pair of dipole element, an etched ground plane, reflectors and directors. The above-mentioned elements are printed on the upper layer of an FR-4 substrate with a dielectric constant of 4.4, a loss tangent of 0.02, and a thickness of 1 mm. Except for FR-4 substrate with etched ground, which have a thickness of 1.4 mm. All the structure are installed symmetrically with respect to the centre of the reflector.

The main radiator consists of two crossed 45-degree dipoles for dual polarization. To well understand the antenna design, the evolution process of dipoles and related simulation results are given in Fig. 4. Ant.1 denotes the original dipoles. Based on Ant.1, the Ant.2 can be obtained by subtracting the orthogonal rectangular patch of 90-degree. On the basis of the above, the Ant.3, which is the dipole designed in this paper, can be obtained by subtracting the chamfer of the semicircle every 90 degrees from the dipole. Each arm of the dipole can be regarded as a square with chamfers and slots. Compared with the former two, the designed radiation structure can increase the surface current path, excite another frequency point to broaden the bandwidth. The slots between patches can be equivalent to capacitance, and the matching of antenna can be affected by adjusting the slots [28]. When one of the dipoles is excited, the other will operate as a parasitic element, resulting in strong mutual coupling between the two crossed dipoles and thus expand the impedance bandwidth of the dipole.

For dual-band range of operation, an integrated balun is used to feed the proposed antenna. Geometry

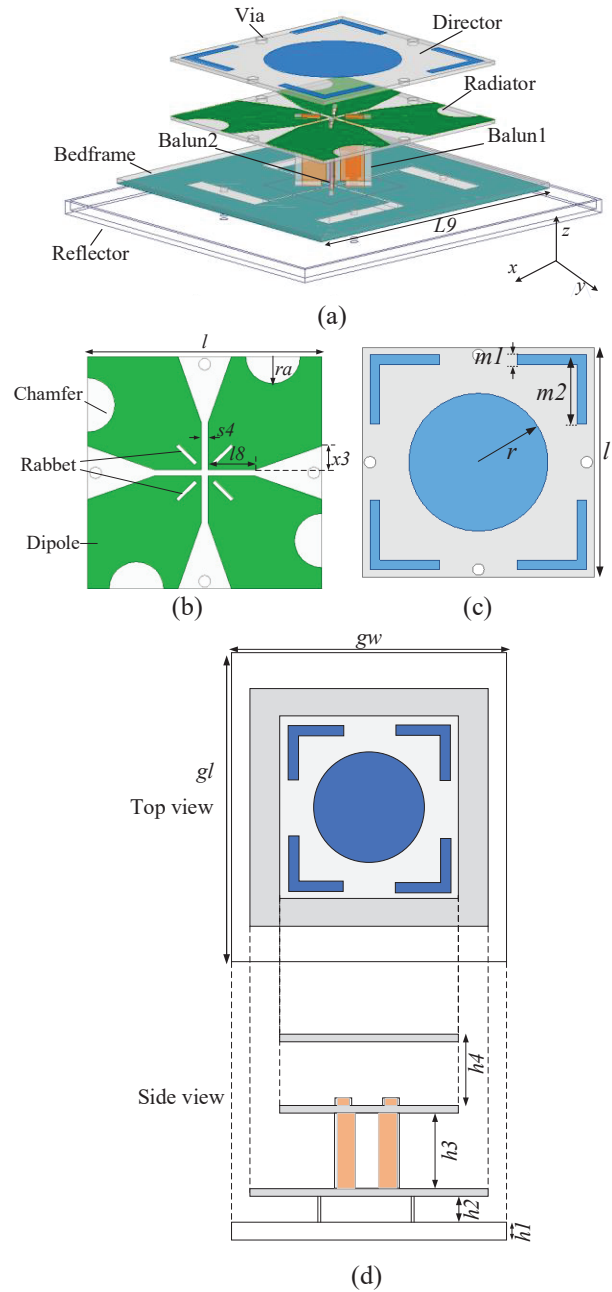


Fig. 1. (a) Three-dimensional view of proposed antenna, (b) patch, (c) director, and (d) top view and side view.

and size parameters of the balun are shown in Fig. 2. One side of the balun is inverted L-shaped feeding, the other side is partially ground. The two sides of the partial ground structure are symmetrical. The structure consists of two rectangles with dimensions of  $20 \times 4.85 \text{ mm}^2$  and  $16 \times 1.45 \text{ mm}^2$ . The partial ground structure can play a role in improving the isolation of the whole design, as shown in Fig. 5. The main reason is that the coupling between the feeding lines can be reduced due to

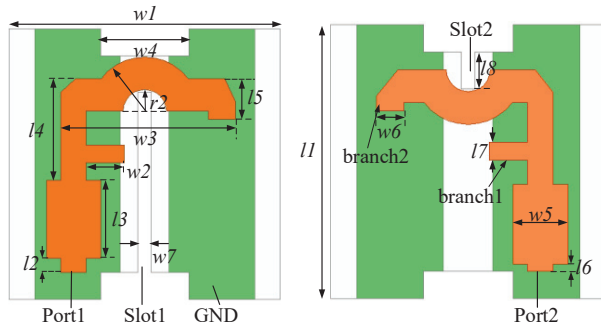


Fig. 2. Feeding structure for port1 and port2.

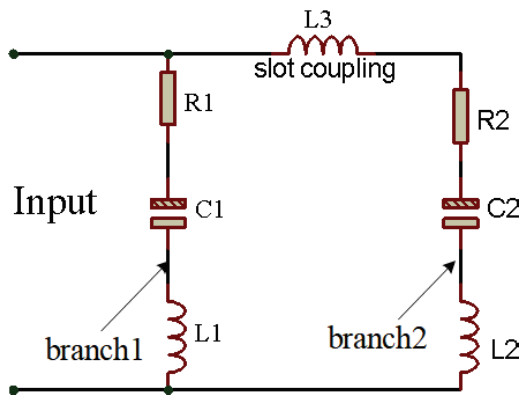


Fig. 3. Equivalent ac circuit diagram of feeding structure.

the partial ground structure. The driven element is fed by a SMA (Sub Miniature A) connector from the bottom of the substrate. The balun structure not only supports the dipoles, but also enables a balanced feeding process. Orthogonal balun's structure is fixed on bed-frame to support radiators. Note that in order to avoid overlap, the  $+45^\circ$  and  $-45^\circ$  polarized microstrip coupling feeding lines are placed orthogonal to each other, slots are notched on the microstrip balun dielectric plate, as shown in Fig. 2.

Beneath the substrate, the reflector is composed of two squares with sizes of  $24 \times 24 \text{ mm}^2$  and  $94 \times 104 \text{ mm}^2$  stacked up and down to improve the isolation and realize a unidirectional radiation. And they are fixed at a distance of 16 mm and 21 mm (about one-quarter-wavelength at the centre frequency of 4.5 GHz and 3.45 GHz) below the antenna, respectively. A cylindrical through-hole with a diameter of 2 mm on the ground and reflector is convenient for connection.

To better understand the working principle of the feeding lines, the equivalent ac circuit diagram of the feeding structure is given in Fig. 3. In the feeding structure, the open branches, branch1 and branch2, can be equivalent to an Inductance-capacitance (LC) resonance circuit.

In addition, the slot coupling can be seen as inductance. Each open branch can be equivalent to LC resonant circuit, in which the resonance points of branch1 and branch2 correspond to low frequency band and high frequency band, respectively. In the low-frequency band, the capacitance is generally regarded as a parallel-plate structure, which is influenced by plate area  $A$ , the distance between plates  $d$ , and the dielectric constant filled by the plates [29]. Inductance is generally related to the structure of the coil, as shown in formulas (1) and (2):

$$C = \epsilon_0 \epsilon_r \frac{A}{d}, \quad (1)$$

$$L = \frac{N\pi r^2 \mu_0}{l}. \quad (2)$$

The value of quality factor  $Q$  and resonance frequency  $f$  can be obtained according to the series equivalent circuit in Fig. 3, as shown in formulas (3) and (4):

$$Q = \frac{\omega_0 L}{R}, \quad (3)$$

$$f = \frac{1}{2\pi\sqrt{LC}}. \quad (4)$$

According to the principle of Yagi antenna, the designed director is composed of a circular patch and four L-shaped metallic strips in Fig. 8. And the director is fixed above the radiator and the location of the convex reflector equal height 16mm. The connection is made by PA66 nylon cylinder, and its relative dielectric constant is about 40. The size of the designed dipole and director are both 60mm. From the literature [25–27], we can get the gain improvement calculation formula of circular director as follows.

$$G \approx 8 \cdot \frac{n_1 \cdot B}{\lambda_0} \left( \frac{\epsilon_2}{n_1 \cdot \epsilon_1 \cdot \mu_2} \right) \cdot f(b_1 \Delta), \quad (5)$$

$$b_1 = 2 \cdot \pi \cdot \frac{n_1 \cdot B}{\lambda_0} \cdot \frac{\epsilon_2}{\epsilon_1} \cdot \frac{n_1}{\mu_2}, \quad (6)$$

$$f(x) = \frac{\frac{1}{1+x^2}}{1 + \left(\frac{2}{\pi}\right) \cdot \tan^{-1}(x)}, \quad (7)$$

$$\Delta = \frac{f}{f_0} - 1, \quad (8)$$

where  $B$ ,  $\epsilon_1$ ,  $\mu_1$  are the thickness, relative permittivity, and permeability of the lower layer, respectively.  $n_1 = \sqrt{\mu_1 \epsilon_1}$ ;  $\Delta$  is the frequency deviation parameter, and  $f$  is near by the centre frequency  $f_0$ .

In this paper, the upper layer of the director can be regarded as air, so the  $\epsilon_2$  and  $\mu_2$  can be equivalent to 1. It can be seen from Fig. 11 (b) that the designed is almost the same as the gain of the circular director. Refer to (5–8), it can be calculated that one layer of director yields an approximate enhancement of 0.78 dB. The experimental result is verified.

The simulations are carried out by full-wave simulation software HFSS 15.0. And the direct solver is used

Table 1: Geometric parameters of the proposed antenna (unit: mm)

Parameter	Value	Parameter	Value	Parameter	Value	Parameter	Value	Parameter	Value
$l9$	80	$h4$	16	$l7$	1.3	$R_a$	7	$m1$	2.5
$h1$	1	$l6$	0.5	$l8$	12	$h3$	21.35	$l4$	8.4
$l5$	3.03	$s4$	1.5	$h2$	3.4	$l2$	1	$w6$	2
$x3$	6	$gl$	104	$w1$	20	$w4$	6.5	$r$	18
$gw$	94	$l1$	20	$w3$	12.875	$r2$	1.6	$l$	60
$w7$	1	$m2$	18	$l8$	2.7	$l3$	5.8	$w5$	4

for simulation design. The optimized geometric parameters of the proposed antenna are shown in Table 1.

### III. RESULTS AND DISCUSSION

Figure 4 shows the evolution process of the dipole and the corresponding S-parameter simulated results. Ant.1 excites a frequency point in the high frequency band above 5G, and Ant. 2 and Ant. 3 are obtained by improving the shape of the radiation patch, which can change the surface current path of the patch. The surface current path becomes longer and the low-frequency points are excited. As can be seen from the Fig. 4, the reflection coefficient of Ant.2 and Ant.3 are obviously better than that of Ant.1, and dual-band has appeared. The improvement of bandwidth and the isolation of high frequency band significantly increases by chamfering and slotting. Considering that Ant.3 can better cover 5G range (3.3-3.6 GHz). So, Ant.3 is the designed dipole in this paper.

Figures 6 and 7 show reflection coefficient and surface current distribution of different  $x3$  values, respectively. As can be seen from the figure, when the value of  $x3$  decreases, dual frequency bands shift toward the low frequency. In addition, when the value of  $x3$  decreases, the current intensity at the slot and chamfer is stronger and the current path is longer, so the frequency point moves to the low frequency. Because the size parameter of the radiation structure has a great influence on the operating frequency of the antenna, the different value of the radiation parameters  $l$  is studied with HFSS 15.0. As shown in Fig. 8, with increasing  $l$ , the two resonant frequency bands move to the low frequency band, and the frequency variation range is large. As shown on Fig. 9, we can achieve better impedance matching of the antenna by adjusting the value of  $R_a$ .

Figure 10 conveys the isolation curves for different reflector shapes. As can be seen from the plot, the isolation of the stepped reflector in the high frequency band and low frequency band is higher than the planar reflector of about 15 dB and 5 dB, respectively.

Because the convex part mainly plays a very great role in the high frequency band. Although the isolation of the stepped reflector is only higher than that without reflector of 5 dB. As can be seen from the Fig. 11 (a),

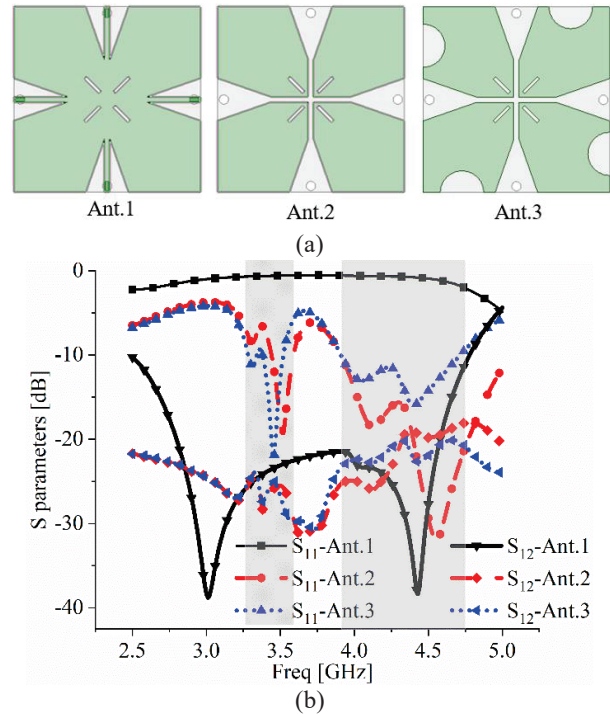


Fig. 4. Dipole structures in evolution processes and simulated results.

the gain of the stepped reflector is increased by nearly 8 dB compared with that without reflector, and the side-lobe is well suppressed. The simulated gain with stepped reflector, planar reflector and without reflector are 10.03, 6.58 and 2.13 dBi, respectively. And the corresponding sidelobe values are  $-6.8$ ,  $-2.69$  and  $1.12$  dBi. According to the experiment, the side lobe of the proposed antenna is not only suppressed to a great extent, but also the simulated gain of the antenna in the  $0^\circ$  direction is greatly enhanced.

In order to analyze the function and mechanism of the directors, the effect of the different shaped directors is studied and fixed at a height of 16 mm (about one quarter wavelength at the centre frequency). To facilitate the comparison, the overall dimensions of the three directors are exactly same. At 3.44 GHz, the radiation-pattern performance is compared with three different structures and without a director, including L-shaped metallic strips

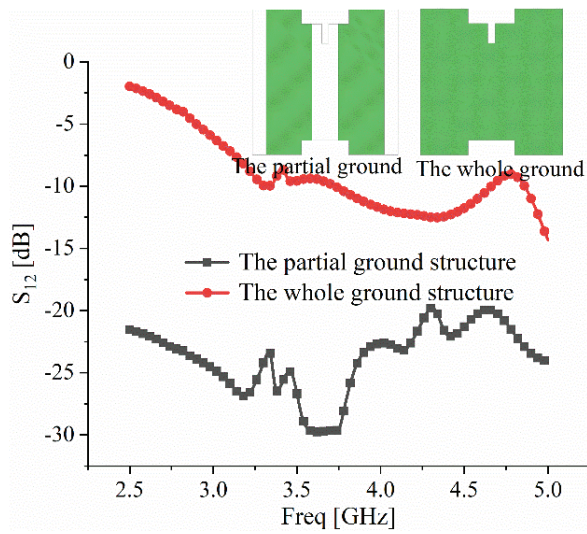


Fig. 5. Effects on the whole antenna isolation with different ground structure.

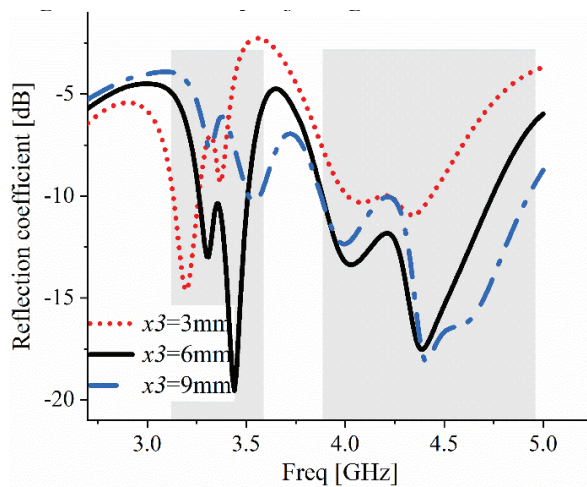


Fig. 6. Effects of dipoles on  $S_{11}$  value with different value of  $x_3$ .

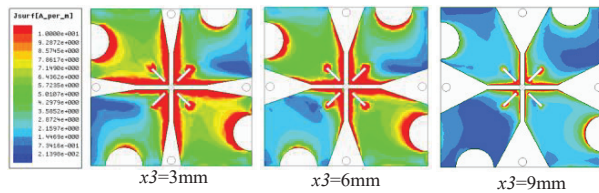


Fig. 7. Patch surface current distribution diagram with different value of  $x_3$ .

(L-shaped), circularly shaped (C-shaped), and a combination of both directors (L+C-shaped), as shown in Fig. 11 (a).

It can be seen from the Fig. 11 (a) that the gain value with the director structure is 0.78 dBi higher than

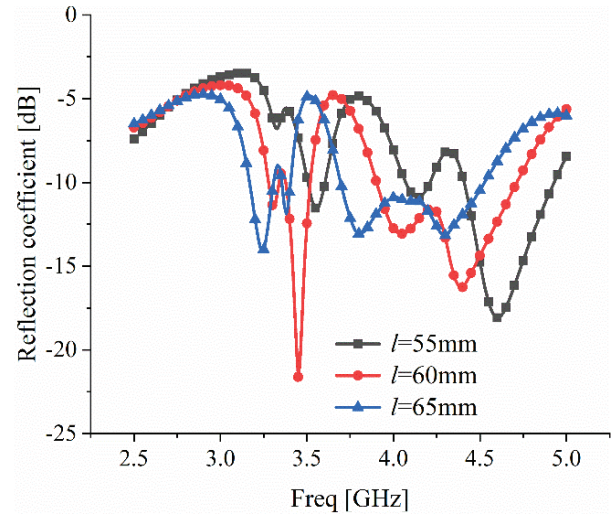


Fig. 8. Effects on reflection coefficient value with different value of  $l$ .

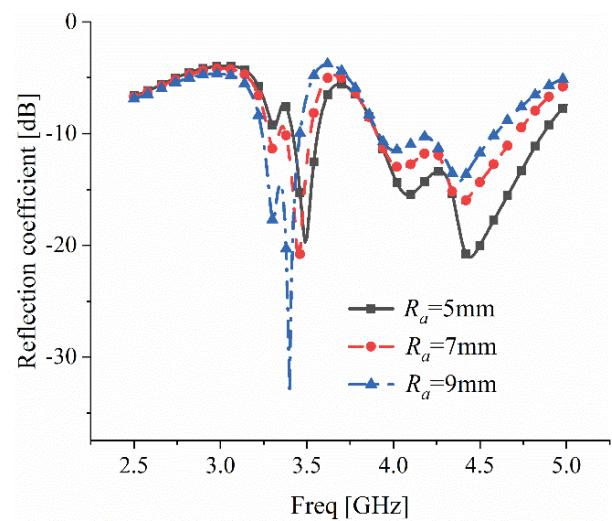


Fig. 9. Effects on reflection coefficient value with different value of  $R_a$ .

that without. It is close to the gain increase calculated by the formula (5) above. Each director has the highest gain which reached 10.4 dBi, while the lowest gain is 8.91 dBi. Compared with the circularly shaped director, a  $90^\circ$  bending strip microstrip line is placed at the diagonal of the patch to increase the gain and reduce the sidelobe value.

Figure 12 depicts the impedance matching of different director structures. The different structure of the director has a great influence on the frequency offset of the low frequency band, while for the high frequency band, the influence of frequency offset is not very large. Especially in the circularly shaped director,

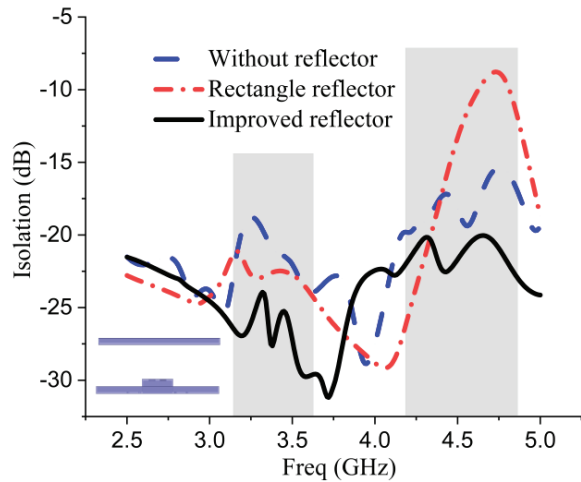


Fig. 10. Comparison of isolation curves: without reflector, planar reflector, and stepped reflector.

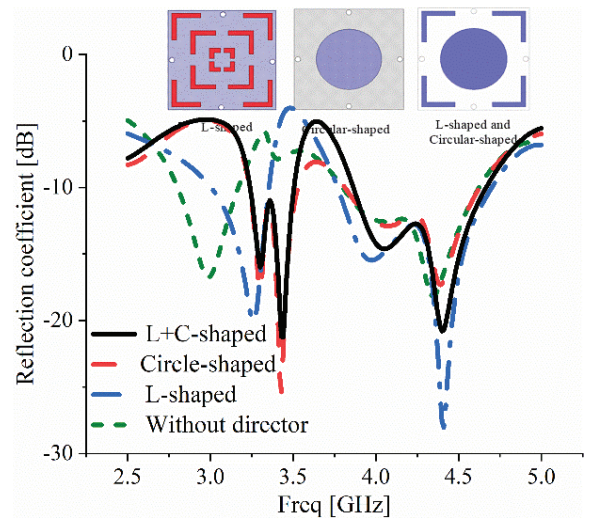


Fig. 12. Comparison of reflection coefficient and radiation pattern between different director structure and without director.

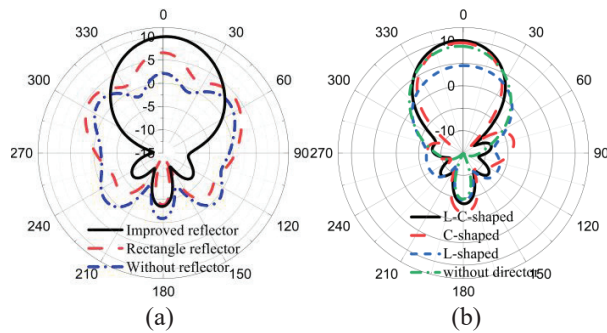


Fig. 11. Radiation pattern: (a) reflector structure, (b) director structure.

the addition of four L-shaped metallic strips makes the value of high frequency reflection coefficient greater. From the Fig. 13, we studied the antenna performance of the director by varying its parameter ‘ $r$ ’, where ‘ $r$ ’ refers to the maximum distance from the centre to the boundary in the circle. It can be clearly from Fig. 13 that the overall gain in the low frequency band of 3.2-3.52 GHz is higher than that in the high frequency band of 3.86-4.6 GHz. Considering the performance of bandwidth and gain, the most appropriate ‘ $r$ ’ value is 18 mm. It can be found that the directors composed of a circle patch and a bending microstrip can achieve the effect of broadening the beamwidth and improving the gain.

Figure 14 illustrates the simulated and measured S parameters characteristics of the two ports. As can be seen from the S-parameter diagram, the simulated bandwidth of low frequency band and high frequency band is 9.5% (3.20–3.52 GHz) and 17.5% (3.86–4.6 GHz),

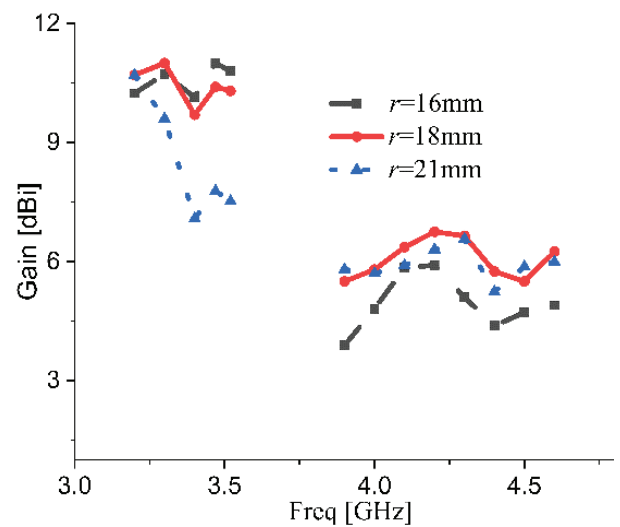


Fig. 13. Gain comparison of the director with different radius.

respectively. The measured bandwidth is 4.47% (3.28–3.43 GHz) and 18.1% (3.97–4.76 GHz), respectively. Compared with the simulated low frequency, the measured low-frequency offset is approximately 0.2 GHz. The low frequency band of the paper can cover the applicable band of 3.3-3.6 GHz of 5G band proposed by China’s IMT propulsion group that is studying the frequency bands including 3.3-3.6 GHz, 4.4-4.5 GHz, 4.8-5 GHz. But the bandwidth of 300 MHz is far from enough, we hope to make more use of the selected frequency band. Therefore, the dual band function realized in this paper can solve the problem of low band utilization, and provide a great reference for the future application of 5G base station antenna.

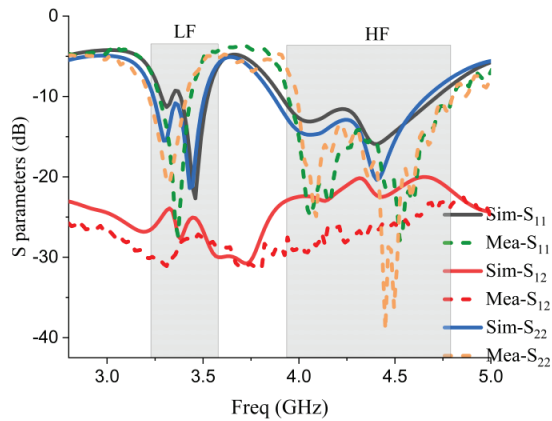


Fig. 14. Simulated and measured S parameters of the antenna.

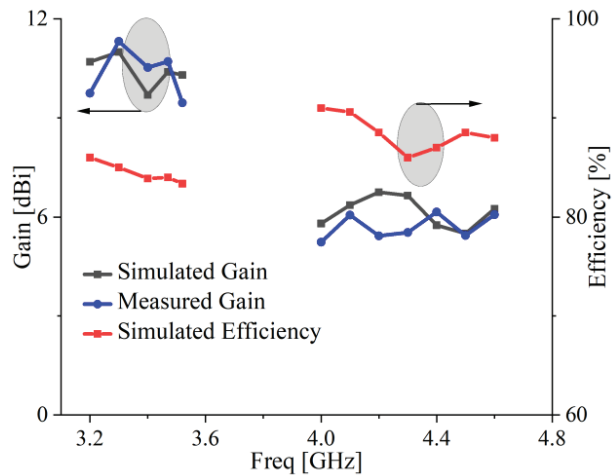


Fig. 15. Simulated and measured gain and efficiency of the antenna.

As described in Fig. 15, the average gain is approximately 10.2 dBi in the low frequency band, and the high frequency band is around 6.37 dBi. Lower antenna gain is mostly due to the fact that the sectional area of the stepped reflector acting on the high-frequency band is much smaller than that of the radiator, which cannot enhance the gain of the whole frequency band of the high frequency band. And the results of simulated and measured gains are in good agreement. Moreover, the efficiency of the antenna reaches an average of 86% in the entire frequency band.

Since the radiation patterns between the  $xoz$ -plane and the  $yoz$ -plane are similar, the radiation pattern of the two ports of the proposed antenna on the  $yoz$ -plane at 3.2 GHz, 3.44 GHz and 4.4 GHz are given in Fig. 16. And when one port is excited to measure the radiation pattern, while other port is terminated to  $50 \Omega$ . when the antenna operates at 3.29 GHz and 3.44 GHz, the

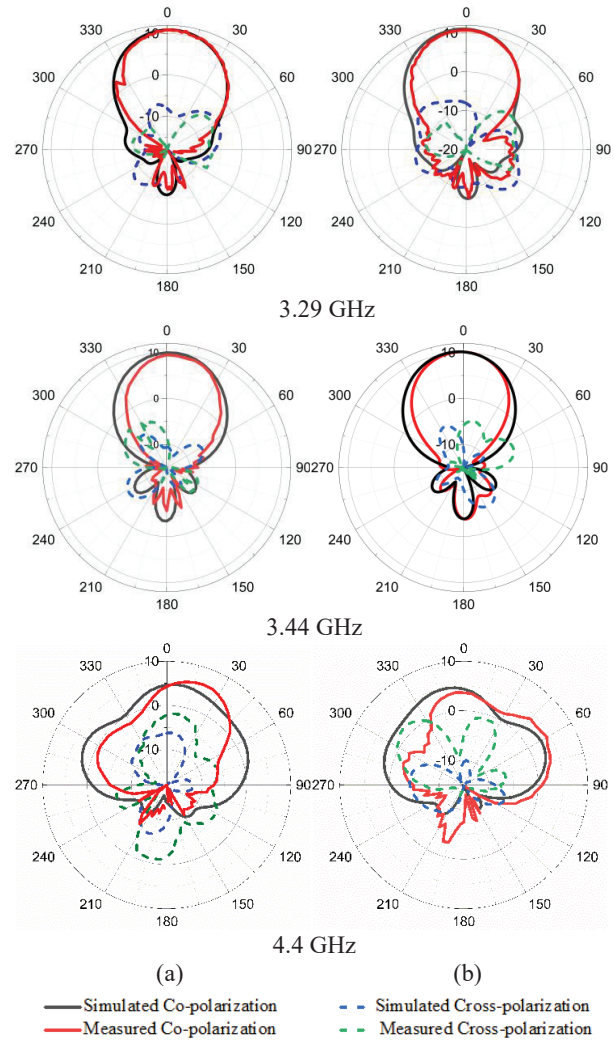


Fig. 16. Radiation patterns at 3.29 and 3.44 GHz in the  $yoz$  plane (a)  $+45^\circ$  polarization, (b)  $-45^\circ$  polarization.

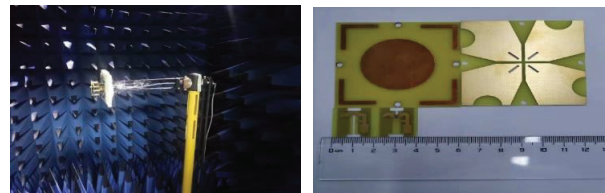


Fig. 17. Antenna undergoing testing and fabricated prototype of antenna.

two ports of the antenna exhibit good directional radiation characteristics in the  $yoz$ -plane. And the directivity of the antenna is largely strong, maximum direction of radiation points to  $\theta = 0^\circ$ , peak gain is 10.52 dBi at 3.29 GHz, that of the corresponding back lobe level is  $-7.05$  dBi. Although the directionality of 4.4 GHz is not as strong as the former, the half power beam

Table 2: Summary of the radiation characteristic of the proposed antenna

Frequency (GHz)	Half-Power Beam-width		Cross-polarization Level(dB)	Back-Lobe Radiation Level(dB)	Peak Gain (dBi)
	Port 1(45°)	Port 2(-45°)			
3.29 GHz	52°	57°	-8.1	-7.05	11.22
3.44 GHz	53°	55°	-10	-3.85	9.43
4.4 GHz	149°	158°	-13	-13.9	6.15

Table 3: Comparison of several antennas

References	Bandwidth (GHz)	Radiator Size (mm <sup>2</sup> )	Gain (dBi)	Isolation (dB)	Type of Director
[9]	1.71-2.69	140	8.5	25	Four rectangles
[20]	1.7-2.69	55	8	22	Square director
[21]	1.61-3.45	78.99	5.87	/	Square director
Proposed	3.2-3.52/3.86-4.6	60	10.52/6.37	26/22	L+C-shaped

width (HPBW) is three times that of the former, and the network coverage is wider, which can be well used in real life. Meanwhile, the zero points of the yoz-plane obtained by simulation and measurement are very consistent at three frequency points. The maximum gain of the antenna at 3.29, 3.44 and 4.4 GHz is 10.52, 11.04 and 6.37 dBi, respectively. The measured HPBW at the frequency points is several degrees smaller than that of the simulation. As can be seen from Fig. 16, the direction coefficient of the measured radiation pattern is much smaller than that of the simulated one, and the gain is reduced by approximately 2.24 dBi. But the radiation patterns are relatively stable at 3.29, 3.44, and 4.4 GHz. Figure 17 shows the fabricated prototype of the antenna and antenna undergoing testing. Overall, the performance consistency between the port 1 and port 2 is a good agreement. Detailed radiation characteristics of the proposed antenna are summarized in Table 2.

Discrepancy between simulation and measurement results is observed at some angles. It is obvious that the simulated and measured results exist in relatively minor differences. The reasons for the difference possibly are caused by the following: First, welding and FR-4 processing and other process errors; second, consistency error of the antenna's dielectric material and transmission line; and, third, reduction degree of the simulation software, and systematic error of the testing instrument. Hence, there is a certain inconsistency between the simulated and the measured results.

Table 3 compares the prototype with the base station antenna published papers in recent years. In [9], four rectangle parasitic elements are placed beside the main radiation to enhance the gain of the dual-polarized antenna; however, this method increases the overall size

of the antenna. But in the design of references [20], [21] and this paper, loading the director above the radiation element can not only enhance the gain, but also reduce the size of the antenna. Compared to these antennas, the proposed antenna has more compact size, higher isolation and gain.

#### IV. CONCLUSION

A wideband dual-polarized dipole with a director and a stepped reflector structure has been proposed herein. The experimental results demonstrate that the proposed designs have two frequency bands with excellent matching, gain and isolation characteristics. The dual band coverage can be applied to the application of 5G frequency band in the future. The good performance of the proposed antenna allows it to be used for a wide range of wireless detection, transmission and communication.

#### ACKNOWLEDGMENTS

This work was supported by the Natural Science Key Foundation of Fujian Province Grant with No. 2020J02042, Research on integration design and industrialization of RF components for 5G wireless communication terminal Grant with No. S22042, and the Natural Science Foundation of Fujian Province of China with Grant No. 2021J05179.

#### REFERENCES

- [1] M. Duarte, C. Dick, and A. Sabharwal, "Experiment-driven characterization of full-duplex wireless systems," *IEEE Trans. on Wireless Communications*, vol. 11, no. 12, pp. 4296-4307, 2012.
- [2] K. Fujimoto and J. R. James, "Mobile antenna systems handbook," Artech House: 2001.

- [3] J. Qi, J. Pan, Y. Li, and G.-L. Huang, "A wideband base station antenna loaded with bow-tie-like parasitic elements," *Applied Computational Electromagnetics Society (ACES) Journal*, 2022.
- [4] X. D. Yang, Y. S. Li, Q. T. Li, and C. Y. Liu, "Analysis and experimental investigation on a novel wideband sleeve dipole array antenna," *AEU- International Journal of Electronics and Communications*, vol. 65, no. 4, pp. 373-376, 2011.
- [5] Y. S. Li, X. D. Yang, C. Y. Liu, and T. Jiang, "A sleeve monopole antenna with wide impedance bandwidth for indoor base station applications," *Progress in Electromagnetics Research C*, vol. 16, pp. 223-232, 2010.
- [6] B. Qiu, S. Luo, and Y. Li, "A broadband dual-polarized antenna for Sub-6GHz based station application," *IEEE 3rd International Conference on Electronic Information and Communication Technology (ICEICT 2020)*, 13-15th, November, Shenzhen, China, 2020.
- [7] D. Z. Zheng and Q. X. Chu, "A wideband dual-polarized antenna for base station applications," *IEEE International Conference on Computational Electromagnetics (ICCEM)*, pp. 268-271, 2016.
- [8] S. Chen and K. M. Luk, "High performance dual-band dual-polarized magneto-electric dipole base station antenna," *Microwave Conference (APMC)*, Sendai, Japan, pp. 321-323, 2015.
- [9] Y. Luo, Q.-X. Chu, and D.-L. Wen, "A plus/minus 45 degree dual-polarized base-station antenna with enhanced cross-polarization discrimination via addition of four parasitic elements placed in a square contour," *IEEE Trans. Antennas Propag.*, vol. 64, no. 4, pp. 1514-1519, 2016.
- [10] E. Yetisir, C. C. Chen, and J. L. Volakis, "Wideband dual-polarized omnidirectional antenna with very high isolation across 1.65-2.7 GHz," *IEEE Antennas and Propagation Society International Symposium (APSURSI)*, pp. 1123-1124, 2014.
- [11] Z. Nie, H. Zhai, L. Liu, J. Li, D. Hu, and J. Shi, "A dual-polarized frequency-reconfigurable low-profile antenna with harmonic suppression for 5g application," *IEEE Antennas Wireless Propag. Lett.*, vol. 18, no. 6, pp. 1228-1232, 2019.
- [12] Y. Chung, S. S. Jeon, D. Ahn, J.-I. Choi, and T. Itoh, "High isolation dual-polarized patch antenna using integrated defected ground structure," *IEEE Microw. Wireless Compon. Lett.*, vol. 14, no. 1, pp. 4-6, 2004.
- [13] L. Peng, C. L. Ruan, and Z. Q. Li, "A novel compact and polarization-dependent mushroom-type ebg using csrr for dual/triple-band applications," *IEEE Microw. Wireless Compon. Lett.*, vol. 20, no. 9, pp. 489-491, 2010.
- [14] K. Yu, Y. Li, X. Liu, "Mutual coupling reduction of a MIMO antenna array using 3-D novel meta-material structures," *Applied Computational Electromagnetics Society (ACES) Journal*, vol. 33, no. 7, pp. 758-763, 2018.
- [15] T. Jiang, T. Jiao, Y. Li, and W. Yu, "A low mutual coupling MIMO antenna using periodic multi-layered electromagnetic band gap structures," *Applied Computational Electromagnetics Society (ACES) Journal*, vol. 33, no. 3, pp. 305-311, 2018.
- [16] H. Zhai, K. Zhang, and S. Yang, "A low-profile dual-band dual-polarized antenna with an amc surface for wlan applications," *IEEE Antennas Wireless Propag. Lett.*, pp. 2692-2695, 2017.
- [17] P. Chen, L. Wang, and T. Ding, "A broadband dual-polarized antenna with CRR-EBG structure for 5G applications," *Applied Computational Electromagnetics Society (ACES) Journal*, vol. 35, no. 12, pp. 1507-1512, 2021.
- [18] Y. Gou, S. Yang, and J. Li, "A compact dual-polarized printed dipole antenna with high isolation for wide band base station applications," *IEEE Trans. Antennas Propag.*, vol. 62, no. 8, pp. 4329-4395, 2014.
- [19] Y. He, Z. Pan, and X. Cheng, "A novel dual-band, dual-polarized, miniaturized and low-profile base station antenna," *IEEE Trans. Antennas Propag.*, vol. 63, no. 12, pp. 5399-5408, 2015.
- [20] Y. Liu, Y. Hao, and F. W. Wang, "A novel miniaturized broadband dual-polarized dipole antenna for base station," *IEEE Antennas Wireless Propag. Lett.*, vol. 12, no. 4, pp. 1335-1338, 2013.
- [21] H. Huang, Y. Liu, and S. Gong, "A broadband dual-polarized base station antenna with sturdy construction," *IEEE Antennas Wireless Propag. Lett.*, vol. 16, pp. 665-668, 2017.
- [22] H. Zhai, L. Xi, and Y. Zang, "A low-profile dual-polarized high-isolation mimo antenna arrays for wideband base-station applications," *IEEE Trans. Antennas Propag.*, vol. 66, no. 1, pp. 191-202, 2018.
- [23] H. Liu, S. Gao, and T.-H. Loh, "Small director array for low profile smart antennas achieving higher gain," *IEEE Trans. Antennas Propag.*, vol. 61, no. 1, pp. 162-168, 2013.
- [24] G. Feng, L. Chen, and X. Wang, "Broadband circularly polarized crossed bowtie dipole antenna loaded with parasitic elements," *IEEE Antennas Wireless Propag. Lett.*, vol. 17, no. 1, pp. 114-117, 2018.
- [25] K. Olivier, D. Tarek, and K. Wu, "Vertically multilayer-stacked yagi antenna with single and

dual polarizations,” *IEEE Trans. Antennas Propag.*, vol. 58, no. 4, pp. 1022-1030, 2010.

- [26] D. R. Jackson and N. G. Alexopoulos, “Gain enhancement methods for printed circuit antennas,” *IEEE Trans. Antennas Propag.*, vol. 33, no. 9, pp. 976-987, 1985.
- [27] H. K. Kan, R. B. Waterhouse, and A. M. Abbosh, “Simple broadband planar cpw-fed quasi-yagi antenna,” *IEEE Antennas Wireless. Propag. Lett.*, vol. 6, pp. 18-20, 2007.
- [28] P. Chen, L. Wang, and Z. Ma, “Reconfigurable planar monopole antenna for fifth-generation mobile communication system,” *Applied Computational Electromagnetics Society (ACES) Journal*, vol. 36, no. 1, pp. 67-74, 2021.
- [29] P. Chen, L. Wang, and T. Ding, “A broadband dual-polarized antenna with CRR-EBG structure for 5G applications,” *Applied Computational Electromagnetics Society (ACES) Journal*, vol. 35, no. 12, pp. 1507-1512, 2020.



**Peng Chen** received the M.S. and Ph.D. degrees in electromagnetic field and microwave technology from the Harbin Engineering University, Harbin, China. Since 2017, he has been an Associate Professor with the College of Information Engineering, Jimei University.

His research interests include antennas, millimeter-wave reconfigurable devices, and radio frequency microwave circuits.



**Lihua Wang** received the B.S. degree from the School of electronic information and electrical engineering, Xiangnan University, Hunan, China. She is now a master student with the College of Information Engineering, Jimei University. Her research interests include base station antennas and liquid crystal antennas.



**Yumeng Lin** received the B.S. degree from the School of Automobile Service engineering, Xi'an Aeronautical University, Shaanxi, China. She is now a master student with the College of Navigation, Jimei University. Her research interests include base station antenna and Planar microstrip antenna.



**Dan Wang** received the B.S. degree from the School of electronic and information electrical engineering, Wuyi University, Fujian, China. She is now a master student with the College of Information Engineering, Jimei University. Her research interests include antenna for body

communication.

# Stacked Metamaterial Patch Antenna Made of Low Permittivity Dielectrics

Bei Zhang<sup>1</sup>, Xiaofei Xu<sup>1,2,\*</sup>, Xiao Deng<sup>1</sup>, Yefang Wang<sup>1</sup>, and Juzheng Wei<sup>1</sup>

<sup>1</sup>School of Communication and Information Engineering  
Shanghai University, Shanghai 200444, China

<sup>2</sup>Key Laboratory of Specialty Fiber Optics and Optical Access Networks  
Shanghai Institute for Advanced Communication and Data Science, Shanghai University, Shanghai 200444, China  
\*xfxu@shu.edu.cn

**Abstract** – A new concept of “*meta-lo*” architecture is contributed to build compact and broadband stacked metamaterial patch antennas (SMPAs). The new antennas are featured with planar mushroom metamaterials that are all made of low permittivity dielectrics. These metamaterials work as good alternatives to conventional high permittivity dielectrics, enabling the new antenna to resonate at a much lower frequency. To examine the antenna performances, one SMPA is experimentally demonstrated. The new antenna is observed to have a broad bandwidth of 27% in a volume of  $0.26\lambda \times 0.26\lambda \times 0.107\lambda$ . The average antenna gain is 7.1 dBi in the operating bandwidth. The compact and broadband SMPA inspired by the *meta-lo* architecture is promising to be used in the high-speed mobile communications.

**Index Terms** – Broadband, compact, metamaterials, stacked patch antenna.

## I. INTRODUCTION

For a long time (over 10 years), it has been deemed necessary to use material combinations of *high* and *low* (*hi-lo*) index dielectrics [1–3] to design a high-performance compact stacked patch antenna, which can be used in the handset high-speed communications. These stacked antennas based on the *hi-lo* architecture [1–3] were demonstrated with smaller parasitic and driven patches than the original stacked antennas made of a low index dielectric and air/foam [4–8]. A main limitation for these *hi-lo* stacked antennas is that high permittivity dielectrics are indispensable [1].

In this effort, a new “*meta-lo*” architecture is contributed to address the problem without utilization of any high permittivity dielectrics. In the *meta-lo* architecture, the lower substrate is now filled with metamaterials [9–12] as good alternatives to the high permittivity dielectrics, while the upper substrate is still a low index dielectric. It is hence named “*meta-lo*” after such ma-

terial combinations of *metamaterials* and *low* index dielectrics. Metamaterials are composed of subwavelength functional structures that are designed included in a host natural material [9–12]. This host natural material itself might be with a low permittivity. However due to the functional inclusions, the metamaterials may exhibit an increasingly higher effective permittivity and/or permeability than the host. This idea provides a new method to make patch antennas smaller [13–20], in which only low permittivity dielectrics are utilized. Inspired by the metamaterial technology, mushroom metamaterials [20] are chosen in this contribution as the lower substrate. A particular advantage for these mushroom metamaterial structures is their planar prototype that can be well integrated into a low profile patch antenna and easily manufactured with the current printed circuit board (PCB) process.

The stacked metamaterial patch antennas (SMPAs) based on the *meta-lo* architecture are numerically studied in the Ansys HFSS solver. One particular SMPA is further experimentally demonstrated. It is observed to have a broad impedance bandwidth (BW) from 3.371 to 4.427 GHz (27.1%). The SMPA occupies a much smaller size than its counterpart built from a low index dielectric and air [4–8]. If we use the free space wavelength  $\lambda$  at the center frequency  $f_c$  (3.899 GHz) in the broad BW to measure the SMPA, we have  $\lambda = 76.9$  mm. The parasitic patch size is 20 mm  $\times$  20 mm ( $0.26\lambda \times 0.26\lambda$ ). The driven square patch is even smaller with side length of  $0.21\lambda$ . The total thickness for the SMPA is 8.2 mm ( $0.107\lambda$ ) in low profile. It is a particularly amazing result that such a compact SMPA is made of dielectrics all with low dielectric constant of 3. In addition, the *meta-lo* architecture does not sacrifice the antenna gain. The measured average antenna gain of the SMPA is 7.1 dBi in the entire BW. The radiation patterns are all observed with suppressed back lobes and cross polarizations, which benefits the directive radiation to the upper half space. We remark that a preliminarily numerical design for the SMPA

was shortly reported in a conference [21]. However, new great advances are made in this work, including the introduction and discussion of new *meta-lo* architecture, numerical optimizations, and particularly, experimental demonstration.

## II. CONCEPT OF THE META-LO ARCHITECTURE

To design a compact stacked patch antenna, the traditional method is to use a *hi-lo* architecture [1–3], which is shown in Fig. 1 (a). It includes a parasitic patch mounted on an upper low index dielectric with dielectric constant  $\epsilon_{ru}$ , and a driven patch on a lower high index dielectric with  $\epsilon_{rl}$ . These two patches are loosely coupled to form an equivalent multi-resonant circuit and make a broad BW. Note that in the *hi-lo* architecture, a high permittivity dielectric is indispensable. To address the problem, an alternative *meta-lo* architecture is proposed in Fig. 1 (b), in which a metamaterial substrate is used to replace the high index substrate in the previous *hi-lo* architecture. The metamaterial substrate is made of low permittivity dielectrics, but exhibit an increased effective permittivity  $\epsilon_{reff}$ .

Following the *meta-lo* architecture, a practical SMPA is designed with planar mushroom metamaterials [20] as the *effective* lower substrate, while the upper substrate is still made of a natural dielectric. The metamaterial substrate is physically built from two PCB layers. As a multilayered antenna, the conceptual SMPA now includes three (top, middle, and bottom) laminate layers shown in Fig. 2 (a). The top layer works as the upper layer in the conventional *hi-lo* architecture. One rectangular parasitic patch with length  $L_u$  and width  $W_u$  is mounted on the top of a low index dielectric substrate with thickness  $h_u$ , dielectric constant  $\epsilon_{ru}$ , and loss tangent  $\tan\delta_u$ . The middle and bottom layers work together as the lower metamaterial substrate. For the middle layer, a driven patch is adhering to another dielectric with  $h_1$ ,  $\epsilon_{r1}$ , and  $\tan\delta_1$ . It has a different patch size of  $L \times W$ . The

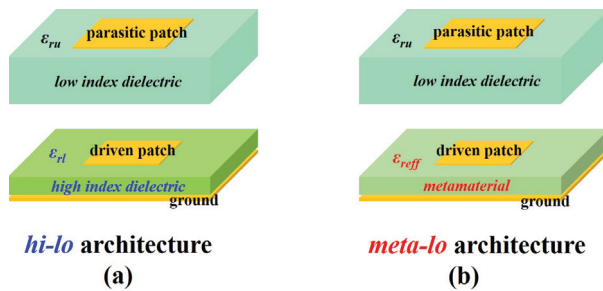


Fig. 1. Comparison of (a) *hi-lo* architecture, and (b) *meta-lo* architecture to build a compact stacked patch antenna.

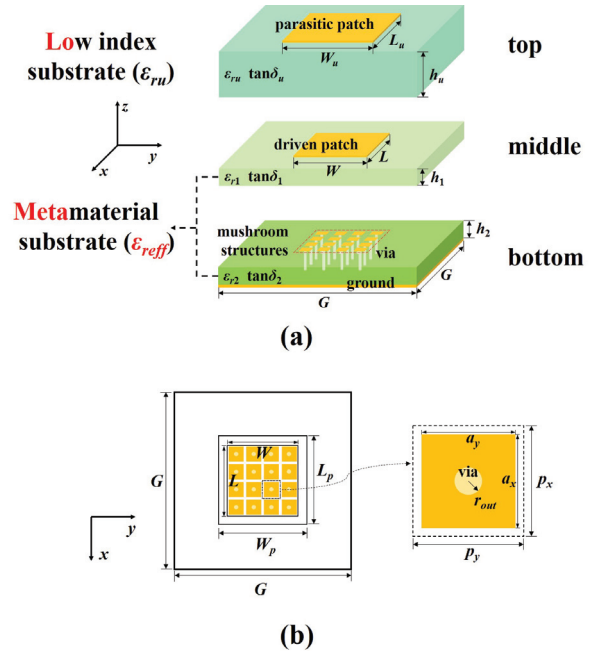


Fig. 2. The configuration of the conceptual SMPA in the (a) overview, and (b) top view.

bottom layer is however more complex. As shown in Fig. 2 (b), it is embedded with numerous composite mushroom structures. These composite structures are periodically distributed beneath the drive patch. The period is  $p_x$  along the  $x$  axis, and  $p_y$  along the  $y$  axis. The total number of these structures is  $m \times n$  ( $L = m \times p_x$  and  $W = n \times p_y$ ). Each mushroom element consists of a rectangular metallic “cap” mounted on the bottom dielectric, and a cylindrical conducting via perforated in the bottom substrate. The cap is connected to the ground plane by via. The mushroom cap is supposed with size of  $a_x \times a_y$ . And the perforated via is with an outer radius of  $r_{out}$ . The ground plane is a square with side length of  $G$ . The bottom dielectric is with  $h_2$ ,  $\epsilon_{r2}$ , and  $\tan\delta_2$ . All of the metal layers are very thin with a small thickness of  $t$ . And all of the substrate layers are made of low permittivity dielectrics.

The SMPA in Fig. 2 can be viewed from two perspectives. The first perspective is that the SMPA is physically made of three layers of low permittivity dielectrics with  $\epsilon_{ru}$ ,  $\epsilon_{r1}$ , and  $\epsilon_{r2}$ , respectively. And the second view is from the equivalent metamaterial perspective. The SMPA is built up from one low permittivity dielectric (equivalent to the top layer) with  $\epsilon_{ru}$ , and another metamaterial substrate (equivalent to the middle and bottom layers) with  $\epsilon_{reff}$ , following the *meta-lo* architecture.

We now discuss the  $\epsilon_{reff}$  of the metamaterial substrate. As seen in Fig. 2, the metamaterial substrate is loaded with periodic mushroom structures in the middle and bottom layers. These composite structures can be

well treated as homogenous metamaterials on condition that  $p_x$  and  $p_y$  are much smaller than wavelength (generally less than  $0.1\lambda$ ). A simple formula can be used to describe the  $\epsilon_{reff}$  as [20]:

$$\epsilon_{reff} \approx \epsilon_{r1} \frac{h_1 + h_2}{h_1}, \quad (1)$$

when  $a_x \approx p_x$ , and  $a_y \approx p_y$ .

Eqn (1) shows how to realize high effective permittivity metamaterials from natural low index dielectrics. The underlying mechanism is attributed to the enhanced capacitive effects in the metamaterial substrate than the original host dielectric [20]. The enhancing ratio is nearly  $(h_1+h_2)/h_1$ . This functionality of mushroom structures is quite different from the previous high impedance surface (HIS) in [22], despite of their similar configurations. Note that the HIS requires the  $p_x$  and  $p_y$  to be close to half wavelength (usually  $0.3$  to  $0.5\lambda$ ). The SMPA can be fed using various methods [4], e.g., a coaxial probe, or coupling from an aperture on the ground plane etc. To validate the concept, a practical probe-fed SMPA is designed in the following section. Its compact and broadband characteristics are demonstrated in both full wave simulations and experiments.

### III. DESIGN AND RESULTS

One SMPA based on the *meta-lo* architecture is considered operating in the Sub-6GHz band for the broadband 5G communications. The parameters are initialized by designing a narrowband metamaterial antenna [20], which is relatively simple. The middle and bottom layers are made of SCGA-500 GF300 by Shengyi Technology Co., Ltd. (SYTECH) with  $\epsilon_{r1} = \epsilon_{r2} = 3$ , and  $\tan\delta_1 = \tan\delta_2 = 0.0023$ . Their thickness values are  $h_1 = h_2 = 1.52$  mm. The driven patch is a square with  $L = W = 16$  mm. The ground length is  $G = 50$  mm. The mushroom structures are with  $p_x = p_y = 4$  mm,  $a_x = a_y = 3.4$  mm, and  $r_{out} = 0.4$  mm. Using the  $L$  and  $\epsilon_{reff}$  in eqn (1), this narrowband antenna is predicted to resonate at nearly 3.83 GHz.

Next, we attempt to broaden the BW by adding a parasitic patch fabricated on an additional top substrate. The top substrate is chosen to be F4BM220 provided by Taizhou Wangling insulating materials factory, with  $\epsilon_{ru} = 2.2$  and  $\tan\delta_u = 0.001$ . Its thickness is  $h_u = 5$  mm, inspired by the recommended ratio of  $h_u$  over  $(h_1+h_2)$  in [23]. After that, we will design the parasitic patch. The parasitic patch is still a square but with length slightly larger than the driven patch. Four typical parasitic patch sizes are chosen as  $L_u = W_u = 18, 19, 20$  and  $21$  mm. In addition, all of the metal layers are made of copper with thickness  $t = 0.035$  mm. The antenna is fed by a  $50\Omega$  coaxial probe between the drive patch and ground plane [4, 23]. The SMPAs are numerically studied in the HFSS solver based on the finite-element method. The full-wave sim-

Table 1: Simulated BW for some stacked antennas

$L_u = W_u$ (mm)	$x_1$ (mm)	-10 dB BW %	Protuberance point
19	7	3.52–4.46 GHz 23.6%	-10.9 dB
20	6	3.36–4.4 GHz 26.8%	-12.4 dB
20	7	3.394–4.4 GHz 25.8%	-13.9 dB
21	6	3.28–4.28 GHz 26.5%	-11.9 dB
21	7	3.32–4.28 GHz 25.3%	-12.9 dB

ulated reflection coefficients ( $S_{11}$ s) for the cases of  $L_u = W_u = 18, 19, 20$ , and  $21$  mm are shown in Figs. 3 (a)–(d), respectively, which are optimized by tuning the feeding position  $x_1$ . The  $x_1$  is measured from the center of driven patch to the probe position, in the range from  $0$  to  $L/2$ .

It is observed in Fig. 3 that the all of these SMPAs have dual resonant frequencies, originated from the couplings between the parasitic and driven patches [1–8]. It makes it possible to broaden the BW. However the “protuberance point” (the locally highest point between the dual resonant frequencies in the  $S_{11}$  curve) levels for some antennas are higher than  $-10$  dB. Therefore, they cannot be regarded as broadband antennas, but work as “dual-band” antennas. By removing these dual-band antennas away, we finally have five potential broadband SMPAs in Table 1. Their  $-10$  dB BWs are all very close at the order of 25%. In theory, all of these five antennas

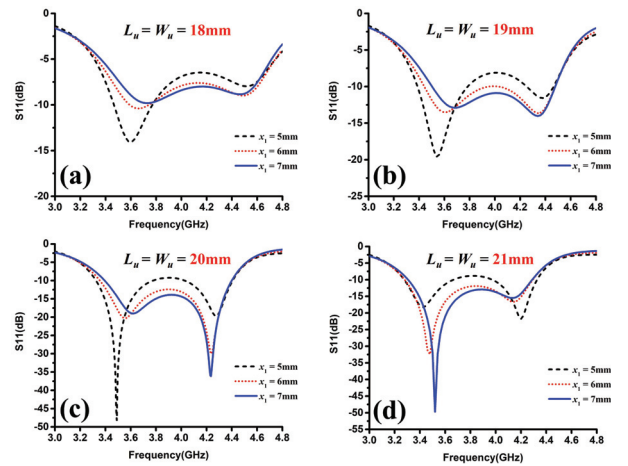


Fig. 3. The full-wave calculated  $S_{11}$ s for the SMPAs with  $L_u = W_u =$  (a) 18 mm, (b) 19 mm, (c) 20 mm, and (d) 21 mm, optimized by tuning the feeding position  $x_1$ .

can work. However, the “protuberance point” levels are different. Considering the practical S11 may get worse than prediction, we conservatively choose the case of  $L_u = W_u = 20$  mm and  $x_1 = 7$  mm, since it is with the lowest “protuberance point” of nearly  $-13.9$  dB.

A particular SMPA is further fabricated following the optimal parameters. The SMPA in the experimental demonstration is assembled from three laminate layers. They are independently fabricated and then manually assembled together. The three different layers are shown in Fig. 4 (a). We remark that in addition to the fabrication precision (e.g., the patch size, radius of vias, dielectric constant of materials, etc.), the accuracy in the assembling work will influence the antenna performances as well. Hence one needs to be very careful when assembling the antenna. To install the coaxial probe, the middle and bottom layers should be tightly compressed with nylon screws, in order to remove the potential air layer between the dielectrics. To allow the inner pin of the feeding probe to pass through the substrates without contacting mushroom caps, some mushroom structures are deliberately designed defected around the feeding point, as shown in Fig. 4 (a). After fixing the probe, the nylon screws which were used before to attach the middle and bottom layers, are temporarily detached. The top thick substrate layer is now added and made together with the lower two layers, still with the help of nylon screws. Fig. 4 (b) shows the finally assembled SMPA.

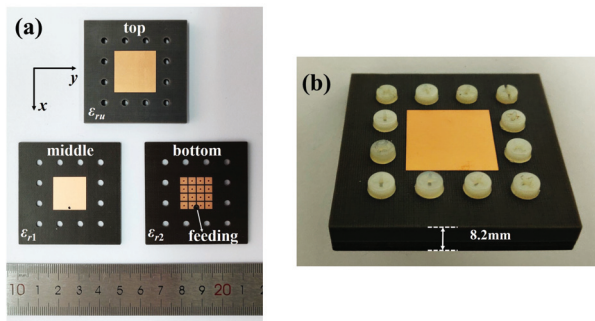


Fig. 4. Photograph of (a) the three different layers, and (b) the assembled SMPA.

The SMPA in the demonstration is made by manually compacting laminate layers. It requires the laminates to be with flat surfaces, even after the PCB fabrication. Therefore, it is not recommended to use those “soft” materials (such as pure Teflon etc.) as the candidate laminates since they are very likely to be wrapped, which is harmful to the antenna assembling. A better fabrication method is to use a multilayer PCB process, without the need of trivially packaging the laminate layers by hand.

The simulated and measured S11s of the SMPA are shown in Fig. 5. Results are in good agreement. It seems

to resonate at dual frequencies of about 3.6 GHz and 4.25 GHz. The simulated BW is 1.006 GHz (25.8%) from 3.394 to 4.4 GHz, while the measured result is slightly wider as 1.056 GHz (27.1%), from 3.371 to 4.427 GHz. The “protuberance point” is  $-13.9$  dB in simulation and deteriorates to  $-13.5$  dB in measurement, both at near 3.9 GHz. Note that the measured “protuberance point” is 3.5 dB lower than the  $-10$  dB line, it is a relatively conservative level. In order to further broaden the BW, the “protuberance point” can be designed higher near the  $-10$  dB line, as shown in some cases in Table 1.

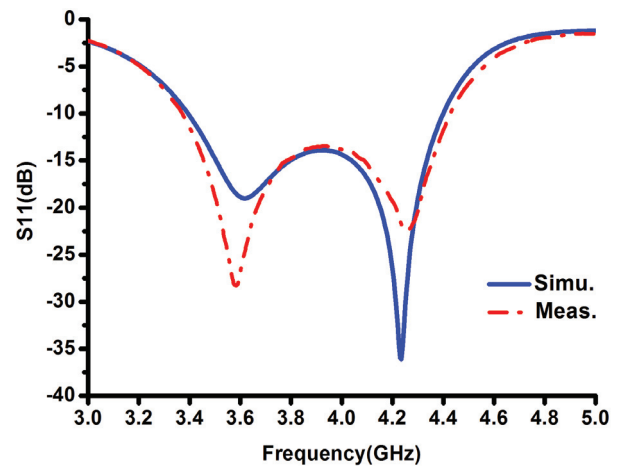


Fig. 5. The simulated and measured S11s of the SMPA.

In Fig. 5, the measured  $f_c$  in the BW is 3.899 GHz that corresponds to  $\lambda = 76.9$  mm. By normalizing the antenna size to  $\lambda$ , the driven patch is featured with an electrically small area of  $0.21\lambda \times 0.21\lambda$ . The parasitic patch is larger that is  $0.26\lambda \times 0.26\lambda$ . The total thickness of the SMPA is 8.2 mm or electrically  $0.107\lambda$ , including all dielectric and metal layers. After these estimations, we conclude that the SMPA in the demonstration occupies a volume of  $0.26\lambda \times 0.26\lambda \times 0.107\lambda$ , which is much more compact than the air-filled stacked patch antennas [7, 8] with a patch length of nearly  $0.5\lambda$  or longer.

The broadband characteristics of the conceptual SMPA are also studied by measuring the antenna gain using a gain-comparison method [24]. Results are given in Fig. 6. The antenna gain curve, either from simulation or measurement, is seen very flat around 7 dBi in the operating BW. However, it descends dramatically when frequencies are out of band, resulted from the reflection loss. The simulated peak gain predicted from HFSS is about 7.6 dBi occurring at near 4.25 GHz and above 6.4 dBi in the entire BW. The measured gain curve seems less smooth. The peak antenna gain is about 8.1 dBi, still at near 4.25 GHz. In the BW, the measured antenna

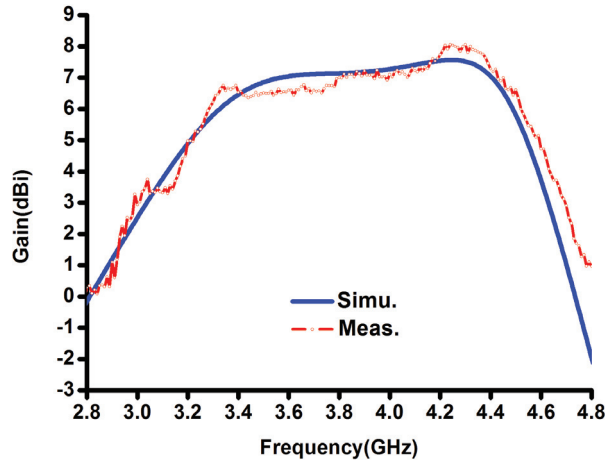


Fig. 6. The antenna gain.

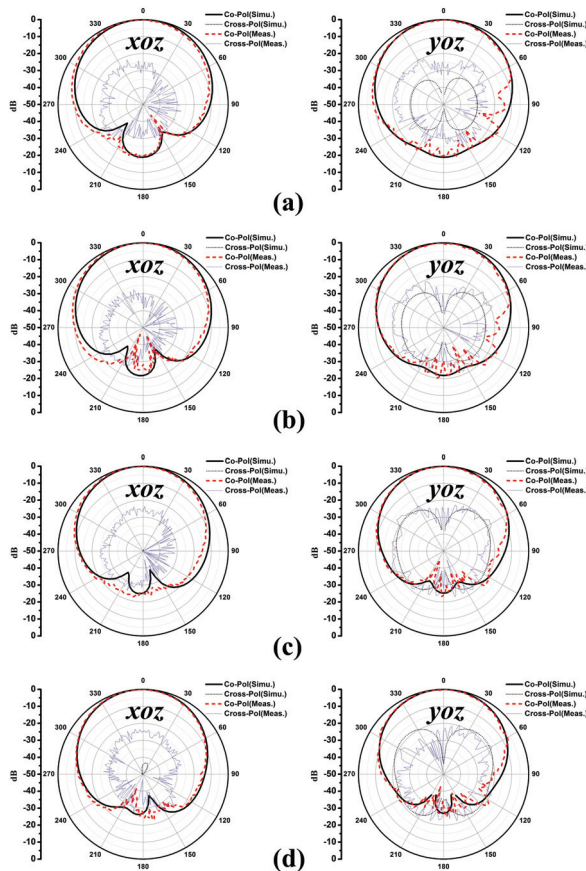


Fig. 7. The radiation patterns at (a) 3.44 GHz, (b) 3.72 GHz, (c) 4.04 GHz, and (d) 4.32 GHz.

gain is all over 6.35 dBi. To better evaluate the broadband characteristics, a more significant statistical phrase “average gain” is used which is defined by algebraically

Table 2: Comparison of different stacked antennas

Design	Small	Broad-band	High per-mittivity dielectrics	Ref.
<i>lo-lo</i>	No	Yes	Not need	[6–8]
<i>hi-lo</i>	Yes	Yes	Need	[1–3]
<i>meta-lo</i>	Yes	Yes	Not need	This

averaging all gain values in the BW. The simulated average gain for the SMPA is about 7.2 dBi, in agreement with the measured 7.1 dBi.

The radiation patterns of the SMPA are numerically calculated and measured at four typical frequencies (3.44, 3.72, 4.04, and 4.32 GHz) so as to cover the BW as possible. Results are given in Figs. 7 (a)–(d) respectively. For each frequency, the left patterns are obtained on the *xoy* plane (E plane) and the right ones are on the *yoZ* plane (H plane). The simulated co-polarized radiation patterns are quite similar with the measured ones. The back lobes are much lower than the main lobes at the backside. An interesting trend is seen that the back lobe is becoming more suppressed when the frequency is higher. It is  $-19$  dB at 3.44 GHz, and reduced to  $-27$  dB at 4.32 GHz in the simulation.

The cross-polarizations are also revealed in Fig. 7. We first discuss the cases on the E plane. From the left column in Fig. 7, it is observed that the calculated cross-polarized fields on the E plane are at the order of or lower than  $-50$  dB. They are too low to be seen. However, the measured cross-polarizations are about  $-23$  dB. The difference might be due to the imperfection of the antenna sample. Another reason might be attributed to the measuring environment that the  $-50$  dB level in simulation is actually too low to be detected in measurement. Now we look at the H plane patterns along the right column of Fig. 7. The simulated cross-polarizations on the H plane are seen much higher than the E plane. They are about  $-30$  dB at 3.44 GHz, and increase to  $-18.3$  dB at 4.32 GHz. The measured cross-polarizations are all at the order of  $-20$  dB in the broadband. They are below  $-19.7$  dB at 3.44 GHz and  $-17.7$  dB at 4.32 GHz. The measured cross-polarization levels on the H plane are in consistency with the simulated levels, especially for high frequency cases. In brief, the cross-polarizations for the SMPA can be all controlled less than  $-17$  dB in the broad band.

The performances for three different stacked patch antenna architectures are summarized in Table 2. In the first design, both of the upper and lower dielectrics are made of low permittivity dielectrics [6–8] that this design is named as the *lo-lo* architecture as proposed in [1]. The upper dielectric is usually the air or foam that  $\epsilon_{ru} \approx 1$ . The *lo-lo* architecture exhibits broadband characteristics

but associated with large antenna patches. For the second *hi-lo* architecture, the antenna sizes can be made smaller. The limitation is that high permittivity dielectrics are necessary. In the third *meta-lo* architecture, the stacked antennas can be designed compact and simultaneously, broadband, which take advantage of all low permittivity dielectrics. The high permittivity dielectrics are not necessary in the new design.

#### IV. CONCLUSION

A new *meta-lo* architecture is proposed to design a compact and broad SMPA. The conceptual SMPA is all made of low dielectric constant materials. One particular probe-fed SMPA is experimentally demonstrated. It is shown with a broad impedance BW of 27%. The lateral patch dimension is  $0.26\lambda \times 0.26\lambda$ . And the vertical profile is  $0.107\lambda$ . The measured average antenna gain is about 7.1 dBi in the broad BW. These characteristics make the SMPA a promising component in applications of portable broadband communications.

#### ACKNOWLEDGMENT

This work is supported by the National Natural Science Foundation of China (No. 11904222) and the Natural Science Foundation of Shanghai (No. 16ZR1446100).

#### REFERENCES

- [1] R. B. Waterhouse, "Stacked patches using high and low dielectric constant material combinations," *IEEE Trans. Antennas Propag.*, vol. 47, pp. 1767-1771, 1999.
- [2] M. A. Saed, "Reconfigurable broadband microstrip antenna fed by a coplanar waveguide," *Prog. Electromagn. Res.*, vol. 55, pp. 227-239, 2005.
- [3] N. Nasimuddin and Z. N. Chen, "Wideband microstrip antennas with sandwich substrate," *IET Microw. Antennas Propag.*, vol. 2, pp. 538-546, 2008.
- [4] R. Garg, P. Bhartia, I. Bahl, and A. Ittipiboon, *Microstrip Antenna Design Handbook*. Norwood, MA: Artech House, 2001.
- [5] L. Shafai, "Wideband microstrip antennas," in *Antenna Engineering Handbook*, J. L. Volakis, Ed. New York, NY: McGraw Hill, Ch. 16, 2007.
- [6] R. Q. Lee, K. F. Lee, and J. Bobinchak, "Characteristics of a two-layer electromagnetically coupled rectangular patch antenna," *Electron. Lett.*, vol. 23, pp. 1070-1072, 1987.
- [7] S. D. Targonski, R. B. Waterhouse, and D. M. Pozar, "Design of wideband aperture-stacked patch microstrip antennas," *IEEE Trans. Antennas Propag.*, vol. 46, pp. 1245-1251, 1998.
- [8] M. A. Matin, B. S. Sharif, and C. C. Tsimenidis, "Probe fed stacked patch antenna for wideband applications," *IEEE Trans. Antennas Propag.*, vol. 55, pp. 2385-2388, 2007.
- [9] J. B. Pendry, A. J. Holden, D. J. Robbins, and W. J. Stewart, "Magnetism from conductors and enhanced nonlinear phenomena," *IEEE Trans. Microw. Theory Tech.*, vol. 47, pp. 2075-2084, 1999.
- [10] Y. Liu and X. Zhang, "Metamaterials: A new frontier of science and technology," *Chem. Soc. Rev.*, vol. 40, pp. 2494-2507, 2011.
- [11] C. L. Holloway, E. F. Kuester, J. A. Gordon, J. O'Hara, J. Booth, and D. R. Smith, "An overview of the theory and applications of metasurfaces: The two-dimensional equivalents of metamaterials," *IEEE Antennas Propag. Mag.*, vol. 54, pp. 10-35, 2012.
- [12] N. I. Zheludev and Y. S. Kivshar, "From metamaterials to metadevices," *Nat. Mater.*, vol. 11, pp. 917-924, 2012.
- [13] R. C. Hansen and M. Burke, "Antenna with magneto-dielectrics," *Microw. Opt. Technol. Lett.*, vol. 26, pp. 75-78, 2000.
- [14] J. Wang, Y. Li, Z. H. Jiang, T. Shi, M.-C. Tang, Z. Zhou, Z. N. Chen, and C.-W. Qiu, "Metantenna: When metasurface meets antenna again," *IEEE Trans. Antennas Propag.*, vol. 68, pp. 1332-1347, 2020.
- [15] E. J. Rothwell and R. O. Ouedraogo, "Antenna miniaturization: Definitions, concepts, and a review with emphasis on metamaterials," *J. Electromag. Waves Appl.*, vol. 28, pp. 2089-2123, 2014.
- [16] R. O. Ouedraogo, E. J. Rothwell, A. R. Diaz, K. Fuchi, and A. Temme, "Miniaturization of patch antennas using a metamaterial-inspired technique," *IEEE Trans. Antennas Propag.*, vol. 60, pp. 2175-2182, 2012.
- [17] Y. Dong, H. Toyao, and T. Itoh, "Design and characterization of miniaturized patch antennas loaded with complimentary split ring resonator," *IEEE Trans. Antennas Propag.*, vol. 60, pp. 772-785, 2012.
- [18] M. Yang, Z. N. Chen, P. Y. Lau, X. M. Qing, and X. X. Yin, "Miniaturized patch antenna with grounded strips," *IEEE Trans. Antennas Propag.*, vol. 63, pp. 843-848, 2015.
- [19] J. Zaid, M. Farahani, and T. A. Denidni, "Magneto-dielectric substrate-based microstrip antenna for RFID applications," *IET Microw. Antennas Propag.*, vol. 11, pp. 1389-1392, 2017.
- [20] X. Xu and J. Wei, "Miniaturisation design of patch antenna using a low-profile mushroom type meta-substrate tailored with high permittivity," *IET Microw. Antennas Propag.*, vol. 12, pp. 1216-1221, 2018.
- [21] X. Xu, X. Deng, and Y. Wang, "Compact and broadband stacked patch antenna loaded with

mushroom metamaterials,” in *Proc. Asia-Pacific Conf. Antennas Propag.*, pp. 1-2, 2020.

- [22] D. Sievenpiper, L. Zhang, R. F. J. Broas, N. G. Alexopoulos, and E. Yablonovitch, “High-impedance electromagnetic surfaces with a forbidden frequency band,” *IEEE Trans. Microw. Theory Tech.*, vol. 47, pp. 2059-2074, 1999.
- [23] R. B. Waterhouse, “Design of probe-fed stacked patches,” *IEEE Trans. Antennas Propagat.*, vol. 47, pp. 1780-1784, 1999.
- [24] C. A. Balanis, *Antenna Theory: Analysis and Design*. Hoboken, NJ: Wiley, 2005.



**Bei Zhang** was born in Henan, China, in 1997. She received the M. S. degree from Shanghai University, Shanghai, China, in 2022. Her research interest includes antenna miniaturization technology.



**Xiaofei Xu** received the B. S. degree in 2007 and the Ph. D degree in 2011, both from Nanjing University, Nanjing China. He is currently with the School of Communication and Information Engineering in Shanghai University, Shanghai, China.

Dr. Xu’s research areas include electromagnetics, antennas and microwave technology. He has authored over 50 papers published in

peer-reviewed journals and conference proceedings. He also serves a number of journals and society workshops as the reviewer or organizer.



**Xiao Deng** was born in Jiangxi, China, in 1995. He received the M. S. degree from Shanghai University, Shanghai, China, in 2020. His research interest includes antenna miniaturization technology.



**Yefang Wang** was born in Yangzhou, China, in 1994. She received the M. S. degree from Shanghai University, Shanghai, China, in 2019. Her research interest includes electromagnetic metamaterials and antenna miniaturization technology.



**Juzheng Wei** was born in Gansu, China, in 1993. He received the M. S. degree from Shanghai University, Shanghai, China, in 2018. His research interest includes antenna miniaturization technology and electromagnetic metamaterials.